Co-design of integrated Power Amplifier-Antenna Modules on Silicon Technologies for the Optimization of Power Efficiency

Juan Pablo Guzman Velez

To cite this version:

Juan Pablo Guzman Velez. Co-design of integrated Power Amplifier-Antenna Modules on Silicon Technologies for the Optimization of Power Efficiency. Electromagnetism. Télécom Bretagne, Université de Bretagne Occidentale, 2013. English. NNT : . tel-00794765

HAL Id: tel-00794765
https://theses.hal.science/tel-00794765

Submitted on 26 Feb 2013

HAL is a multi-disciplinary open access archive for the deposit and dissemination of scientific research documents, whether they are published or not. The documents may come from teaching and research institutions in France or abroad, or from public or private research centers.

L'archive ouverte pluridisciplinaire **HAL**, est destinée au dépôt et à la diffusion de documents scientifiques de niveau recherche, publiés ou non, émanant des établissements d'enseignement et de recherche français ou étrangers, des laboratoires publics ou privés.

N° d'ordre : 2013telb0266

Sous le sceau de l'Université Européenne de Bretagne

Télécom Bretagne

En habilitation conjointe avec l'Université de Bretagne Occidentale

École Doctorale – SICMA

Co-design of integrated PA (Power Amplifier) – Antenna Modules on silicon Technologies for the optimization of power efficiency

---

Thèse de Doctorat

Mention : Sciences pour l'Ingénieur

Présentée par **Juan Pablo Guzman**

Département : Micro-ondes

Laboratoire : Lab-STICC – Pôle : Micro-ondes, Optoélectronique et Matériaux

Directeurs de thèse : Christian Person, Michel Ney

Soutenue le 23 Janvier 2013

Jury :

Rapporteurs
M. Christophe Delavaud - Ingénieur R&D HDR, CEA LETI
M. Ronan Sauleau - Professeur, Université de Rennes 1, IETR
Examinateurs
M. Yves Quere - Maître de Conférences, Université de Bretagne Occidentale, LabSTICC
M. Eric Kerherve - Professeur, Université de Bordeaux, IMS
M. Michel Ney - Professeur, Télécom Bretagne, Lab-STICC
M. Christian Person - Professeur, Télécom Bretagne, Lab-STICC
Invités
M. Christophe Calvez - Ingénieur R&D, Autocruise-TRW, Plouzané
M. Romain Pilard - Ingénieur R&D, ST Microelectronics, Crolles

Acknowledgments

First of all, I would like to express my thanks to Christian Person and Michel Ney for their invaluable support and guidance

Next, I would like to thank all examiners for taking their time to read and evaluate my thesis.

I would also like to show my appreciation to Christophe Calvez and Shoaib Muhammad as encouraging partners who help me at some stages of my thesis and provided valuable inputs.

Prototype fabrication and measurement were also very important and for this matter I can’t skip thanking Guy Chuiton, Raymond Jezequel, Serge Pinel, Camilla Karnfelt and Pascal Coant.

I would also like to thank Nejdat Demirel, Nathalie Deltimple and Eric Kerherve from IMS Bordeaux, for their help concerning the Power Amplifier presented in this thesis and for their welcome at my short but pleasant stay at IMS labs.

And last but not least, all the people at “Département Micro-ondes”, in Telecom Bretagne and at Brest, with whom the daily life would not have been the same.

Table of Contents

Résumé .... *I*

1) Contexte et Application .... **I**

2) État de l'art des systèmes dans la bande 60 GHz .... **III**

3) Solution antenne SoC → vers l'amélioration du rendement global du système .... **IV**

4) Solution antenne SiP → vers des solutions de haut gain .... **IX**

5) Antenne doublement alimentée pour une amélioration du rendement du PA .... **XIII**

6) Conclusions Générales .... **XVI**

7) Travaux à réaliser dans le futur .... **XVII**

General Introduction *1*

Chapter 1 - State of the Art of 60 GHz Transmission Systems *1*

1) Introduction **1**

2) The 60 GHz band and its opportunities **2**

2.a) The 60 GHz band and its regulation 2

2.b) Unlicensed Band, what does this imply 3

2.c) Why the 60 GHz band? 3

2.d) Applications 5

2.e) Attenuation factors (losses in the 60 GHz band) 6

2.f) Link Budget 7

2.g) Commercially Available Solutions at 60 GHz 9

3) Generic Transmission Chain and Front End location **10**

3.a) Complete Tx-Rx Chain 10

3.b) Technological Possibilities 11

3.b.i) Silicon → Bulk or SOI (Silicon on Insulator)? 12

3.b.ii) Active Devices: the transistor 13

3.c) Passive Devices: Transmission Lines, Inductors and Capacitors 15

3.c.i) Transmission lines: 16

3.c.ii) Inductances and Capacitors 20

4) Power Amplifiers **21**

4.a) PA distortion sources 22

4.a.i) How to measure the performance of a PA? 24

4.a.ii) PA Topologies 24

4.b) Typical PA amplification curve 27

4.c) PA Stages 28
4.c.i) PA impedance matching stages 28
4.d) PA State of the Art 30
5) Antenna in the 60 GHz band 32
5.a) Antenna Performance 33
5.a.i) System on Chip or SoC 33
5.a.ii) System in Package or SiP 40
6) Front-End Transmitters (Whole Tx chain) 49
7) Conclusions 52
Chapter 2 - Integrated Silicon based antenna: toward SoC (Co-integration and Co-design Scenarios) 53
1) The 60 GHz Power Amplifier on SOI 53
1.a) PA on SOI description 53
1.b) PA Performance 54
1.c) Comprehensive analysis of the PA 56
1.d) Co-integration and Co-design scenarios 57
1.d.i) Co-integration scenario 57
1.d.ii) Co-design scenario 57
2) Antenna design for Co-Integration 58
2.a) Slot on an infinite ground plane (no substrate) 58
2.b) Lowering the input impedance 59
2.c) Slot on a finite ground plane (no substrate) 62
2.c.i) Size study of finite ground 63
2.d) Adding the substrate 65
2.d.i) W_{slot} as impedance controller 65
2.d.ii) Ground size as impedance controller 66
2.e) Final 50 Ω antenna configuration 69
2.e.i) Radiation performance 71
3) Antenna Design for Co-design with PA 73
3.a) Transistor output stage configuration 73
3.b) A 15 Ω input impedance antenna 74
3.c) Final Antenna configuration 77
4) Global energy budget 78
5) 50 Ω Antenna Measurement 79
5.a) S11 Measurement 80

5.b) Gain Measurement ... 83
5.c) Probe angle incidence ... 86
5.c.i) Probe coupling: broadside or backside effect? ... 88
5.c.ii) Probe distance ... 90
6) Co-Integration PA – Antenna (50 Ω) ... 91
6.a) Simulation of Co-integrated PA + Antenna ... 92
6.a.i) Parametric study PA – Slot distance ... 92
6.a.ii) The PA coupled resonating elements ... 94
7) Co-design of PA and Antenna (15 Ω) ... 97
8) Measuring Integrated PA-Antenna ... 98
8.a) Support Selection ... 99
8.b) S11 Measurement ... 100
8.b.i) Measurement bench description (45 to 75 GHz) ... 101
8.b.ii) S11 Measurement ... 103
8.c) Support impact on Antenna performance ... 104
8.d) Gain Measurements ... 108
9) Conclusions ... 111
Chapter 3 Dielectric Resonator Antenna: SiP solutions for enhanced performance ... 112
1) Introduction: ... 112
2) The dielectric resonator antenna or DRA ... 112
2.a) DRA state of the art ... 113
2.b) Fabrication of Dielectric Resonator Antennas ... 116
2.c) How does the DRA works ... 119
2.c.i) Resonant modes in a cylindrical DR ... 119
2.c.ii) Mode selection ... 123
2.c.iii) Resonance frequency of the TM_{11} ... 123
2.d) Selecting the excitation element ... 125
2.d.i) DR + Slot → Initial performances ... 126
2.d.ii) Finite ground plane effect ... 127
2.d.iii) The substrate effect ... 129
2.e) DRA from lossy material and CPW feeder ... 130
2.f) DRA radiation expected performance ... 132
2.g) DR Fabrication ... 133
2.h) DR Measurement ... 133

2.h.i) DR position shift impact 134
3) PA and DRA integration 136
3.a) 1st DR incorporated in Package solution 138
3.a.i) Conclusions 141
3.b) 2nd packaged solution → solving the DR alignment issue 141
3.b.i) Backside radiation measurement bench 144
3.b.ii) Measurement results 145
3.b.iii) Silicon Chip integration 146
3.b.iv) Conclusions 149
3.c) 3rd packaged solution → *completely* packaged solution 150
3.c.i) The lid effect 152
3.c.ii) The wall effect 155
3.c.iii) The CPW coupling mechanism 156
3.d) 4th solution → eliminating interconnections 161
4) Conclusions 166
Chapter 4 - Multi-feed antenna for PA-Antenna efficiency enhancement 167
1) Introduction 167
2) Multi PA solution 168
2.a) Multi-feed antenna for Multi-PA solution. 168
2.b) Coupling constraint 169
2.c) Vectorial addition 169
2.d) The impact of field rotation 171
3) DRA for multi-feed PA-antenna solutions 172
3.a) Multiple lateral DR feed configuration 173
4) Adapted feed for multi-fed DRA 176
4.a) HTCC Packaging technology 176
4.b) DR Multilayer Fabrication 177
4.c) Single Feed Waveguide Fed DR 179
4.a) Waveguide to SIW 180
4.b) Waveguide dimensioning and performance 181
4.c) Multi feed DR 186
4.d) SIW excitation 188
4.e) PA incorporation constraints 191
5) Conclusions 194

General Conclusions 195
Future Work 197
References 198
Publications 205

Résumé

1) Contexte et Application

Dans le cadre des communications numériques sans fil, la vitesse d'échange de données (débit) reste toujours une des caractéristiques qui limite la performance du système. Une diminution des temps d'échange est donc nécessaire pour l'amélioration de la performance et l'introduction des nouvelles applications. Celles comme « Wireless HD » rendent possible la transmission sans fil de vidéo non-compressée » à haute définition (débit = 4 Gbps) « Kiosk Downloading » permettrait l'échange de données à haut débit (1-2 Gbps) sur une courte portée (1 -2 m).
Selon Shannon (Eq. 1), la capacité du canal (débit) dépend du niveau de bruit dans le canal (*S/N*) ainsi que de la bande passante disponible (*B*). Prenant ce dernier en compte, une bande passante plus importante, disponible sur la bande 60 GHz (7 GHz), devrait augmenter le débit par rapport aux solutions existantes.

$$C = B \times log_2 \left(1 + \frac{S}{N}\right) \quad \textit{Eq. 1}$$

Le débit de plusieurs protocoles est montré à la Figure 1 a). On peut repérer une augmentation du débit entre différents standards; par exemple, Bluetooth (< 1 Mbps), Wifi ou 802.11 (10 – 100 Mbps) ou 802.15.3c (< 1 Gbps). En partie cela peut être expliqué par la bande passante attribuée à chaque standard: Bluetooth (1 MHz), Wi-Fi (22 MHz) et 802.15.3c (2.1 GHz). Il faut noter que cette bande passante est par canal et ne couvre pas toute la bande attribuée aux standards. Avec un débit si important, comme c'est le cas de 802.15.3c (1 Gbps), on pourrait envisager des solutions de transmission numérique de vidéo rapide. Par exemple, un téléchargement d'un film (qualité DVD ≈ 5 Gb) en quelques instants (5 s). Une nouvelle façon pour l'utilisateur d'emprunter des films. Il devra juste se rendre à un kiosque avec son PDA (Personal Digital Assistant) et réaliser le téléchargement en quelques secondes. C'est ce qu'on appelle « Kiosk Downloading » et c'est l'application visée dans ce travail.

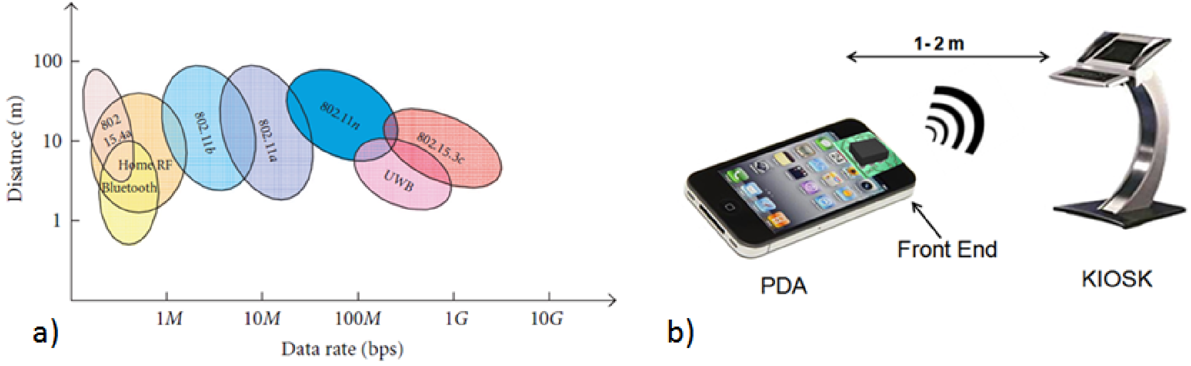

Figure 1 : a) Débits et besoins pour les standards WLAN et WPAN. [1] b) Application "Kiosk Downloading"

L'introduction de l'application visée permet de repérer les trois éléments qui constituent la liaison de communication : le transmetteur (PDA), le récepteur (Kiosk) et entre eux, l'interface aérienne. Dans cette thèse, les efforts vont être centrés sur le transmetteur, et plus spécifiquement sur les derniers éléments de la chaine de transmission (Figure 2): le PA (Amplificateur de Puissance selon l'abréviation anglaise) et l'antenne.

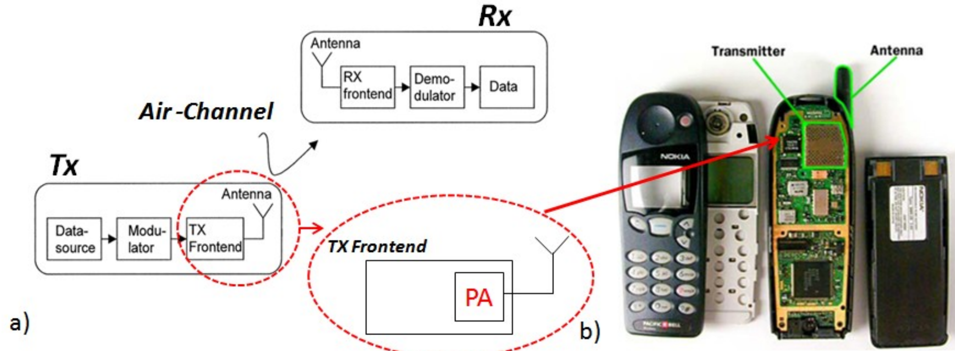

Figure 2 : a) Les trois composants de la chaine de Tx-Rx (Transmetteur – Air – Récepteur) [2] and b) Module Transmetteur-Antenne d'un téléphone portable [1]

Toutefois, les solutions PA-Antenne du transmetteur vont être soumises aux contraintes liées à l'interphase aérienne. Parmi elles, une des plus importantes pour le système transmetteur est l'atténuation de l'énergie à 60 GHz due à l'espace libre. Elle atteint – 74 dB (2 m de séparation entre récepteur et transmetteur) qui devra être compensé par le gain des éléments actifs (PA) et l'antenne. En fait, un niveau maximum de gain est imposé pour le PA de 13.7 dBm (en Europe) limitant sa contribution pour le gain du système (Tx) global et imposant un gain de 6 – 7 dBi pour l'antenne. Cette valeur a été obtenue en prenant en compte les niveaux de bruit du système ajoutés par les différents composants de la chaine (i.e. bruit thermique, codage, bruit dans le récepteur etc.).

1.b.) Choix technologique

La réalisation des éléments actifs (transistors) qui comprennent le PA ont besoin d'un substrat semi-conducteur. La sélection parmi les semi-conducteurs existants (Si, GaAs ou InP) dépend en grand partie de contraintes comme le prix et la fréquence de fonctionnement. D'un côté, le silicium offre un prix de fabrication plus bas par rapport aux autres technologies. Et cette différence de coût devrait augmenter, dû aux investissements faits ces dernières années autour du silicium [2]. D'un autre coté, la fréquence d'opération a été un des facteurs avantageant le silicium. Mais ce n'est plus le cas. Selon l'ITRS (International Technology Roadmap for Semiconductors), le silicium peut dès maintenant rivaliser avec les autres technologies même au-delà des 100 GHz [3]. C'est donc le silicium qui permettra d'obtenir une solution bas coût et également performante.
Le silicium, lui aussi, offre deux possibilités. Il existe le Si Bulk qui présente une résistivité au niveau du substrat de 10 Ω cm et le Si SOI avec 3000 Ω cm. Cette différence a un grand effet notamment sur l'efficacité du système. Comme exemple, l'atténuation d'une ligne coplanaire (CPW) est montrée dans la Figure 30. Une différence de 3 dB peut être aperçue pour la ligne entre le "Bulk" et le SOI. Par conséquent, le SOI a été choisi.

[1] http://www.electronics.howstuffworks.com

2) État de l'art des systèmes dans la bande 60 GHz

L'étude de l'état de l'art des systèmes dans la bande 60 GHz a été divisée en deux parties, une dédiée au PA et l'autre aux antennes.

2.a) Le PA : état de l'art

Un amplificateur de puissance (PA) consiste en un enchainement de plusieurs transistors (responsables de l'effet d'amplification) liés par des circuits d'adaptation d'impédance. Ces circuits permettent de transmettre un maximum d'énergie entre les différents étages d'amplification ainsi que l'entrée et la sortie. Un schéma simplifié pour un amplificateur de puissance à deux étages est montré en Figure 40. Les circuits d'adaptation amènent des pertes, dues aux éléments passifs. Ils jouent donc un rôle important dans l'efficacité du PA.
L'état de l'art des amplificateurs de puissance dans la bande de 60 GHz est résumé dans la Table 2. Les paramètres comme le PAE (Power Added Efficiency), le niveau d'alimentation (Power Supply), la dissipation de puissance (power dissipation) et le nombre d'étapes (Stages) y sont montrés.

De cette première partie, les conclusions suivantes ont été tirées.

- On préfèrera une configuration coplanaire pour les lignes de transmission.
- La taille complète du design du PA semble occuper une surface totale de 1 mm^2. (En incluant les plots de RF (Radio Frequency) et d'alimentation)
- D'habitude, les PA's ont de 2 à 3 étages d'amplification, ce qui implique 3 ou 4 circuits d'adaptation. Une augmentation d'environ 10% est observée entre le PAE de Bulk et SOI.

2.b) L'antenne: état de l'art

Deux stratégies ont été observées concernant la conception d'antennes dans la bande millimétrique. Dans le premier cas, les antennes se trouvent intégrées dans la métallisation de la technologie. C'est-à-dire que l'antenne reposera sur le substrat (Silicium, dans notre application) et sera intégrée au même moment que les circuits actifs. Ceci s'appelle « Système on Chip ou SoC ». L'antenne, dans ce cas là, se trouve affectée par les propriétés électriques du substrat comme la permittivité et conductivité. D'un autre coté, quand l'antenne est indépendante des circuits et peut être conçue comme faisant partie du boitier, on parle alors de « System in Package ou SiP ». Ce dernier permet d'avoir une plus grande souplesse au moment de choisir l'antenne mais met en évidence aussi une des problématiques des circuits à haute fréquence (60 GHz) : les interconnexions (Figure 54).

Les performances des antennes sont évaluées au moyen de plusieurs paramètres, parmi lesquels se trouvent la bande passante, le gain ou l'efficacité. Un état de l'art pour chacun des deux cas a été fait et il est montré par la suite.

2.b.i) SoC

Pour le SoC, (Table 3), les conclusions suivantes ont été tirées:

- En regardant le gain, on peut se rendre compte que des valeurs négatives sont communes. Quelques antennes montrent des valeurs positives comme 2,3 ou 4,2. Ce sont des solutions qui ajoutent un plan de métallisation à l'arrière en l'utilisant

comme un plan réflecteur. Ce qui est intéressant, c'est l'efficacité des 82 % fournie [21], due à l'utilisation du SOI. Les valeurs de gain sont toutefois insuffisantes pour notre application.

- ♣ Les antennes sur substrat semblent être bien adaptées concernant notre besoin de bande passante (8 GHz). Une bande passante de 10 GHz en moyenne peut être observée dans le tableau 2.
- ♣ Une impédance d'entrée de 50 Ω semble aussi être un cas général. Ceci est logique à cause des bancs de mesure qui imposent telle valeur. Une basse impédance (4.4 et 20 Ω) ainsi qu'une impédance complexe ont été aussi trouvées. Une configuration CPW ou CPS est surtout utilisée.

2.b.ii) SiP

Pour le SiP (Table 4), les conclusions suivantes ont été tirées

- ♣ Tout de suite, une des différences importantes est visible entre les deux approches (SoC et SiP). Une valeur plus importante de gain est obtenue pour les configurations qui prennent en compte le boitier. Les niveaux de 5, 8 et 10 dBi sont maintenant possibles. L'efficacité a tout de même aussi augmenté, essentiellement due à l'utilisation des substrats à faibles pertes.
- ♣ Malgré la souplesse donnée par les interconnexions, les pertes liées à leur incorporation dans la conception devront être étudiées afin de les quantifier. Un effet de désadaptation d'impédance peut être aussi introduit par les interconnexions.
- ♣ La bande passante reste tout à fait acceptable et maintient même un niveau supérieur par rapport aux besoins. Une valeur de 12% (8 GHz @ 60 GHz) est envisageable.

3) Solution antenne SoC → vers l'amélioration du rendement global du système

Pour cette partie de notre recherche il y a eu une coopération proche avec IMS (Laboratoire de l'Intégration du Matériau au Système situé à Bordeaux). L'amplificateur de puissance (PA) présenté dans ce chapitre a été développé par ce laboratoire. Le PA est basé sur la technologie SOI à 65 nm de ST Micro-électronics et est montré à la Figure 70. Cette technologie permet de viser une solution d'antenne de haute efficacité à cause de la haute valeur de la conductivité du substrat comme expliqué auparavant.
L'approche SoC permet seulement une « simple » intégration de l'antenne (une fois que l'impédance et le mode ont été adaptés), mais aussi lui offre de nouvelles possibilités vis-à-vis des modifications des conditions d'adaptation PA-Antenne. La puce du PA illustré à la Figure 6, montre les différentes étapes d'adaptation nécessaires pour créer le chemin entre l'entrée et la sortie en liant les transistors. Ces étapes permettent une adaptation d'impédance vitale pour une transmission maximale de puissance. Mais malgré ce rôle, ces étapes d'adaptation ajoutent des pertes provenant des éléments passifs comme les lignes de transmission. Un niveau de perte de 0.7, 1.8 et 0.8 dB est attendu pour l'étape d'entrée, milieu et sortie respectivement. Une amélioration du rendement du PA peut donc être envisagée si les pertes insérées par les étapes d'adaptation sont enlevées.

Le schéma de la dernière étape (l'étape de sortie) est montré de façon plus détaillée. Deux valeurs d'impédances peuvent être repérées dans deux endroits différents du PA : une impédance de 50 Ω (impédance vue à la sortie du PA) et une impédance de 15 + 15j (à la sortie du transistor). Cette première impédance de 50 Ω est habituellement utilisée dû à l'impédance imposée par les bancs de mesures. Mais si l'élément à la sortie ne nécessite pas une adaptation de 50 Ω, une partie du circuit peut être supprimée et on obtiendra une augmentation du rendement comme résultat. Deux antennes vont être donc montrées dans cette section : une adaptée aux 50 Ω (approche de Co-Intégration) et l'autre à une impédance plus basse de 15 Ω pour une solution plus efficace (approche de Co-Conception). A cause de la configuration de l'étage de sortie, son enlèvement complet n'est pas possible puisqu'il joue un rôle partiel sur l'alimentation du PA. De cette façon, une impédance de 15 Ω (souligné en vert dans la Figure 70), à la place de celle de 15 + 15 j Ω à la sortie du PA, devient l'impédance imposée à l'antenne.

3.a) Conception de l'antenne basse impédance (50 Ω et 15 Ω)

Pour la conception de l'antenne, deux caractéristiques importantes ont été déjà extraites : une impédance d'entrée de 50 Ω (et aussi 15 Ω) et une configuration d'accès coplanaire (CPW). Une antenne qui est habituellement utilisée sous ce genre de conditions est la fente [14], [20], [37]. A cause de la configuration coplanaire de l'accès, la fente semble l'élément rayonnant le plus adapté car il s'agit tout simplement d'une ouverture dans un plan de métallisation.

3.a.i) Modes et impédances correspondantes pour une fente

Dans la Figure 3, l'impédance pour les deux premiers modes de la fente sont montrés. Le premier a une fréquence de 60 GHz qui correspond à une valeur de $\lambda/2$ (λ = 5 mm @ 60 GHz) pour L_{slot}, soit 2.5 mm. Ensuite, le deuxième mode (≈ λ) se retrouve à 100 GHz. Une claire différence est immédiatement visible, une impédance de 500 Ω pour le premier mode qui contraste avec celle de 60 Ω pour le deuxième. C'est donc le deuxième mode qui sera utilisé. Bien sûr, L_{slot} doit être modifié pour faire descendre ce mode de 100 GHz à 60 GHz. Le substrat n'a pas été inclus dans la configuration présentée.

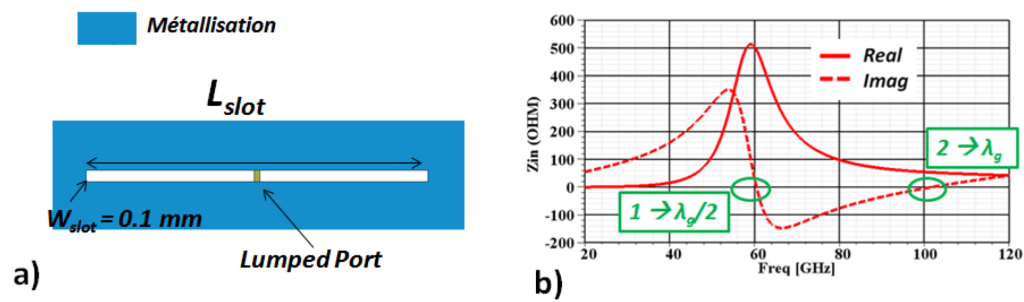

Figure 3 : a) Impédance d'entrée pour une fente (deux modes)

Cette haute impédance est expliquée par le champ éléctrique dans la fente montrée dans la Figure 73. Pour le premier mode, on peut repérer une présence maximale de champ dans la partie centrale de la fente (position du port). Maintenant, pour le deuxième mode, une absence de champ est visible au même endroit. Cette différence explique la différence d'impédance entre les deux modes.

Le rayonnement des deux modes est globalement semblable, sauf pour une différence de gain d'environ d'un dBi. Ceci peut aussi être expliqué par les champs magnétiques. On peut

observer, que pour le premier mode, le champ est lié entre les deux endroits où le champ est maximum (souligné par la flèche blanche). Ce phénomène est aussi observé pour le deuxième mode entre les champs maxima aux extrémités de la fente. Dans ce mode, un nouveau maximum au centre est aussi observé.

3.a.ii) Performances finales de l'antenne (Co-intégration et Co-conception)

L'étude présentée précédemment comprenait un plan métallique infini. Un plan de masse fini doit être introduit pour une solution réalisable. La dimension du plan de masse a un effet important sur l'impédance et aussi pour le rayonnement de l'antenne. Par exemple, dans la Figure 79, on peut observer comment, pour certaines dimensions du plan de masse, ces bords se couplent au rayonnement de la fente. En maîtrisant ces effets, et d'après l'addition du substrat, une configuration finale est obtenue et sa performance peut être observée dans la Figure 84. Une bande passante (ROS < 2 dB) de 19.8 GHz a été obtenue, avec un gain minimum de 3 dBi dans l'ensemble de la bande adaptée et une valeur maximale de 4.2 dBi (θ = 180°). Une taille finale de 2.38 mm^2 et une efficacité de 89% sont aussi obtenues par simulation. L'effet du substrat est aussi visible dans le diagramme de rayonnement. En insérant le substrat, la configuration perd sa symétrie et les valeurs du gain en θ = 180° et θ = 0° deviennent par conséquent différentes. Ces résultats contrastent avec ceux obtenus pour une configuration seulement fente (sans substrat) comme celle de la Figure 73.
Pour le cas du Co-design et comme signalé auparavant, une impédance encore plus basse est nécessaire. Une telle impédance est aussi atteignable avec la configuration « fente sur plan de masse fini ». Par conséquent, la taille ainsi que la performance de l'antenne ont été modifiées. Maintenant, pour une taille de 1.68 $mm_{2,}$ on a réussi à obtenir une bande passante de 4.8 GHz (ROS < 2 dB) et un gain maximum de 3.4 dBi @ θ = 180°. Le diagramme de rayonnement se comporte essentiellement de la même manière que celui de l'antenne à 50 Ω avec un rayonnement omnidirectionnel dans le plan H et avec des zéros à θ = 90° et θ = -90° dans le plan E.

3.b) Mesures de l'antenne à 50 Ω

Puisque les dimensions de l'antenne sont vraiment importantes pour une résonnance à 60 GHz et une bonne adaptation, un procédé de coupage a été demandé à l'usine. Cependant, les dimensions obtenues sont différentes de celles attendues. Ce changement fait décaler la fréquence de résonance de 7 GHz, soit une résonance à 67 GHz. L'antenne fabriquée, ainsi que ses réponses en adaptation pour deux mesures sont montrées dans la Figure 93. Malgré la modification de taille, une résonance à 60 GHz est toujours obtenue. Pour pouvoir expliquer le décalage par rapport aux résultats de simulation (qui prennent en compte les nouvelles dimensions), un autre élément doit être introduit dans la configuration de la simulation : la sonde de mesure.
La sonde est maintenant incorporée dans la simulation. Le couplage avec l'antenne peut être observé dans la Figure 96. Le champ autour de la sonde montre que le couplage a lieu par-dessus comme par-dessous. Il va donc transformer le rayonnement de l'antenne. D'une part, le diagramme de rayonnement change particulièrement autour de θ = 80°, où une augmentation de niveau est observée de plus de 20 dB par rapport au niveau de la configuration «antenne seule». Cette relocation d'énergie va, par conséquent, modifier le diagramme de rayonnement. Une baisse d'intensité de 2 et 3 dB selon θ = 180° (arrière) ainsi que une variation plus importante vers la direction normale (10 et 20 dB respectivement pour θ = 0° et θ = 10°). D'autre part, une augmentation de la polarisation croisée est aussi observée entre les deux configurations. Les mesures montrées dans la

Figure 99, concordent avec les modifications induites par la présence de la sonde. C'est-à-dire, une diminution de la puissance dans la direction normale est obtenue et un haut niveau de polarisation croisée a été aussi mesuré (non montrée). Ces mesures ont permis de valider l'antenne.

3.c) Co-intégration PA – Antenne (50 Ω)

Après la conception de l'antenne et sa validation, on remarque que la taille de l'antenne (1.86 x 1.61 mm^2) fait plusieurs fois celle du PA (0.614 x 0.565 mm^2). Pour limiter la taille globale du système (PA-Antenne), le PA est incorporé dans la métallisation de l'antenne. Cette opération est possible grâce à la configuration coplanaire du PA qui rend une grande partie du PA comme métallisation et par conséquent compatible avec la configuration de la métallisation de l'antenne. Une ligne de 50 Ω est utilisée pour lier l'antenne au PA et elle permet d'avoir un certain degré de liberté pour la position du PA par rapport à la fente rayonnante. Pour la simulation, l'agencement du PA a été inséré dans la métallisation de l'antenne et cette configuration est simulée par un simulateur électromagnétique 3D. Ce simulateur ne peut pas prendre en compte l'effet des transistors, c'est-à-dire, l'amplification du PA. Pour le prendre en compte, un simulateur de circuit est nécessaire mais il ne permettra pas d'évaluer l'interaction électromagnétique entre les deux parties. Pour notre étude, cette interaction est primordiale. Par conséquent, la configuration pour le simulateur 3D a été choisie.

Malgré la compatibilité de la disposition de la métallisation entre le PA et l'antenne, des effets de couplage sont trouvés par simulation. Le niveau de couplage diminue avec l'augmentation de la distance entre le PA et la fente. Cette réduction est visible dans les courbes du gain réalisé. Pour comprendre le couplage, le courant surfacique dans la métallisation est montré à 50 et 74 GHz. On peut repérer un fort niveau de courant dans des éléments du PA. Les plots et lignes du PA entrent en résonance et génèrent une composante destructive pour le rayonnement de l'antenne. Une chute de 16 et 9 dB est observée dans le gain respectivement à 50 et 74 GHz (Figure 106).

3.d) Co-conception PA - Antenne (15 Ω)

De la même façon que pour l'antenne de 50 Ω, la réalisation a débouché sur une augmentation de la taille totale de l'antenne. L'impédance d'entrée a donc été modifiée. Une impédance de 25 Ω a été obtenue au lieu de celle attendue de 15 Ω. Le changement en adaptation, ainsi que la configuration PA-Antenne sont montrés dans la Figure 111. Un décalage vers le bas de la fréquence de résonance (la résonance à 60 GHz est maintenant à 57 GHz) et une diminution de l'adaptation sont montrés par la courbe du S11. Le layout du PA est ensuite incorporé et le S11 également montré. Une nouvelle résonance est immédiatement observée à 72 GHz. Comme précédemment, il s'agit d'une résonance provenant des éléments du PA. Malgré ces changements, un gain de 3 dB est obtenu dans toute la bande.

Ces derniers résultats nous ont permis d'obtenir les réponses pour les deux configurations de PA -Antenne. L'influence du PA, ainsi que la taille de l'antenne ont été étudiés. Maintenant, les résultats de mesures seront présentés.

3.e) Mesures: S11 et gain

Dans la Figure 112 a, le circuit d'alimentation DC du PA est montré. Ce circuit comprend le connecteur DC, les capacitances de découplage, le substrat de support et finalement des fils de connexion en or. Ces derniers sont montrés en détail dans la Figure 112 b. Une colle non-

conductrice et de basse permittivité est utilisée pour fixer la puce au support. Le support va permettre aussi de tenir le circuit pendant les mesures, rendant possible la position de la sonde d'une façon fiable. La réponse d'adaptation est d'abord mesurée pour les deux cas : Co-intégration et Co-Conception.

La mesure et la simulation du S_{11} du PA isolé, c'est-à-dire sans aucune stratégie de co-intégration, est montrée à la Figure 114. Un décalage est observé d'autour de 6 GHz pour une fréquence de résonance visée de 60 GHz. Même avec une modification du modèle du transistor qui a rapproché les résultats de simulation de ceux des mesures, une fréquence de résonance de 62 GHz est obtenue. Ce décalage est tout de suite observé dans les mesures de Co-intégration et de Co-conception. Une fréquence de résonance de 65 GHz est obtenue. Ces résultats nous ont permis de valider le fonctionnement correct du circuit d'alimentation DC. Ce décalage aura un grand impact sur les mesures de gain présentées ensuite.

A cause du décalage obtenu en fréquence, l'analyseur utilisé jusqu'à présent (fréquence maximal de 65 GHz) a été remplacé par un autre analyseur qui opère jusqu'à 75 GHz. Les résultats de simulation inclus prennent en compte le support, la sonde, les fils de connexion et le support. La structure simulée peut être observée dans la Figure 112 b) pour le cas de la co-intégration.

D'après les résultats du gain présentés dans la Figure 4, le transfert d'énergie du PA à l'antenne est évident. Une augmentation du gain d'environ 15 dB a été mesurée pour le cas de la co-intégration à 65 GHz. Une valeur plus faible est obtenue pour la co-conception. Ceci est expliqué par les résultats de simulation et aussi par la position finale de la puce par rapport aux parois du support. Elle se trouve en contact avec le support et la frontière de l'antenne est modifiée selon les caractéristiques du support comme sa permittivité. Cette nouvelle position est soulignée dans la Figure 4.

Une chute inattendue est aussi observée dans les deux cas au moment de l'amplification maximale du PA.

Un niveau de 15 dB est immédiatement suivi par une descente de gain atteignant2 ou 3 dB. On peut constater que le gain «mesuré » de l'antenne (PA Gain – Measurement: ligne orange) et la simulation (ligne verte) montrent une plus grande divergence entre 65 et 70 GHz. Bien qu'on voie une différence entre gain du PA (ligne rouge) et mesure (ligne bleue), cette chute importante n'a pas pu être précisément expliquée.

Une des explications possibles vient peut être du fait que la simulation simultanée des éléments passifs et actifs n'est pas possible, comme mentionné auparavant. L'existence des transistors est négligée et leur réaction à la présence d'un champ électrique extérieur comme celui de l'antenne n'est pas pris en compte. À mesure que le PA transfère l'énergie à l'antenne, elle est davantage rayonnée et, par conséquent, il aura plus de champ externe sur les transistors. Ceci pourrait expliquer les résultats obtenus en mesure. Les valeurs simulées et mesurées retrouvent leurs concordances dans la partie haute de la bande (70 à 75 GHz) pour les deux cas.

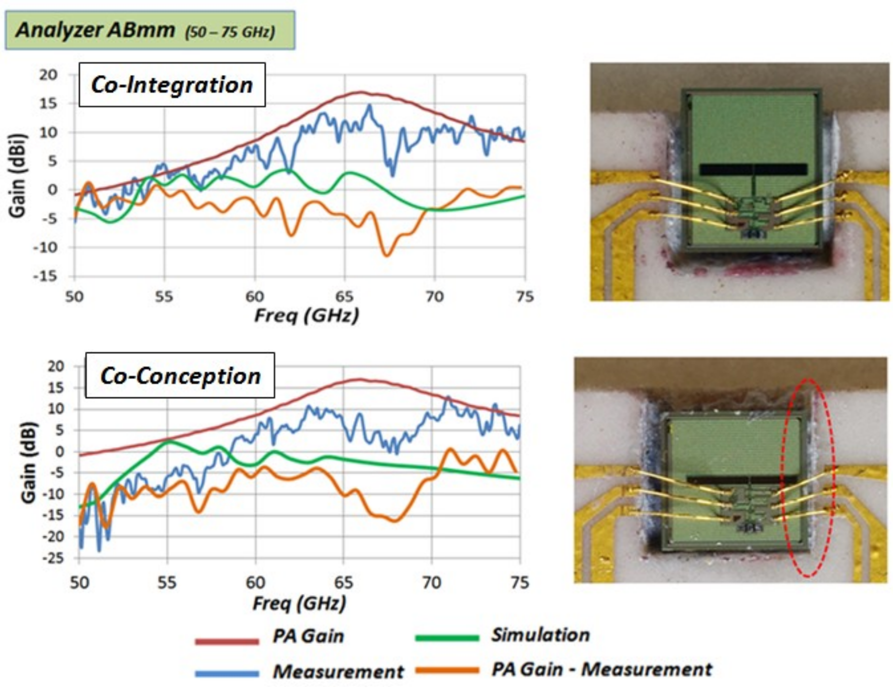

Figure 4 : Mesure de gain pour la Co-Intégration et la Co-Conception (50 - 75 GHz) Vue détaillée de la puce collée et connectée par fils.

Ces résultats présentent la dernière étape de notre travail par rapport aux solutions SoC. Les limites de simulation des éléments passifs et actifs on été exposés. Une amélioration du rendement a été aussi obtenue avec une stratégie de co-conception. Les pertes liées à l'étape de sortie ont été diminuées, passant de 0.8 dB à 0.4 dB et par conséquent une amélioration de 11% pour les pertes totales liées aux éléments passifs du PA. Par contre, le niveau de gain visé pour notre application (6 dBi) est toujours inatteignable avec cette stratégie SoC (4 dBi obtenu) et c'est pour cela que les solutions SiP vont être poursuivies et présentées plus tard.

4) Solution antenne SiP → vers des solutions de haut gain

D'après les solutions présentées dans l'état de l'art pour des systèmes SiP, une solution semblait être intéressante due aux possibilités de haut gain et aux compatibilités avec des technologies de « packaging ».

4.a) L'antenne basée sur le résonateur diélectrique ou DRA

L'antenne basée sur résonateur diélectrique ou DRA d'après l'abréviation anglaise (Dielectric Resonator Antenna) est donc choisie. Une DRA est composée de deux éléments : le résonateur diélectrique et l'élément d'excitation. Celui-ci va transférer de l'énergie guidée (par exemple par une ligne coplanaire) pour générer les champs électromagnétiques dans la cavité. Le rayonnement de l'antenne est obtenu grâce à la distribution des champs qui déborde à l'extérieur de la cavité. Les champs peuvent s'exprimer par des modes qui ont un rayonnement propre. Dans notre cas, le mode TM_{11} a été choisi car il possède le facteur de qualité le plus bas et, en conséquence, la plus large bande passante.
Le champ H du TM_{11} (pour une cavité cylindrique) est montré dans Figure 137, ainsi que l'élément excitant. L'excitation du mode du DR se fait à partir d'une fente non résonante qui partage la distribution du champ magnétique (distribuée linéairement tout au long de sa

longueur) avec celle du DR. De cette façon, la fente doit être mise sous le DR au centre pour une correcte excitation. Cette excitation a été déjà validée dans [100] and [101].

4.b) DR Fabrication et mesures (Validation du DRA)

Neuf échantillons ont été fabriqués au laboratoire et peuvent être observés dans la Figure 146. Trois épaisseurs différentes du substrat disponible ont permis d'obtenir trois groupes de cavités diélectriques avec des hauteurs différentes (h = 0.508 mm, 0.635 mm et 1 mm). La fréquence de résonance de la cavité dépend de son rayon comme de sa hauteur. Une diminution du rayon est nécessaire pour garder la même fréquence de résonance si la hauteur augmente. Une valeur de 0.1 mm pour W_{slot} et de 0.9 mm pour L_{slot} ont été utilisés pour les mesures. Après l'usinage par laser, une forme conique a été trouvée à la place de la forme cylindrique attendue. Cette conicité provoque une diminution de la fréquence de résonance de 3 ou 4 GHz en simulation. Les résultats de simulation ont été corroborés par des mesures comme le montre la Figure 5. Seules deux mesures d'un des échantillons de 0.508 mm de hauteur sont montrées. Des oscillations sont visibles sur les mesures de gain produites par des réflexions sur le banc de mesure. Une haute valeur de gain est obtenue malgré ces réflexions avec valeurs entre 5 et 6 dBi dans la bande adaptée (S11 < -10dB). Le gain est aussi mesuré par une fréquence fixe pour une variation de 0° à 60° dans deux plans orthogonaux. Un niveau plus faible est trouvé pour le plan E par rapport à celui du plan H et est expliqué par la présence de la sonde millimétrique dans ce plan. Un bon accord entre les mesures et la simulation est observable pour la co-polarisation comme pour la cross-polarisation dans les deux plans. Par conséquent, le DR est ainsi validé.

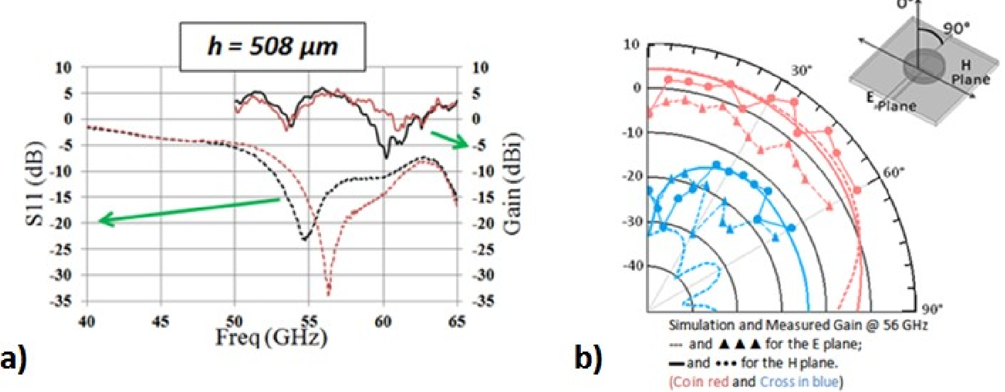

Figure 5 a) Adaptation et gain pour deux échantillons de 0.508 mm et b) diagramme du gain @ 56 GHz.

4.c) Intégration du PA et DRA

Après la validation du DR, l'intégration avec le PA doit être étudiée. Dans les sections suivantes, plusieurs configurations sont présentées dans lesquelles différentes possibilités d'interconnexion et « packaging » sont explorées.

4.c.i) 1ere Solution: Incorporation du PCB et ses interconnexions

Cette configuration est illustrée dans la Figure 152. La configuration proposée est basée sur l'intégration d'élément excitant (la fente) dans la structure de la technologie SOI. La puce sera introduite dans une cavité faite au niveau du substrat d'alumine. Une fois insérée, le DR est positionné par-dessus. Ici, on profite de la taille réduite de la fente grâce à la haute permittivité du silicium qui permet d'atteindre une surface comparable à celle du PA (0.5 µm x 0.6 µm). Ensuite, le PCB est aussi introduit au moyen des interconnexions. Ces sont des « solder balls » qui permettent d'envoyer le signal DC pour l'alimentation du PA ainsi que le

signal de 60 GHz. Une solution quasi encapsulée est donc présentée. Pour compléter l'encapsulage, comme on verra plus loin, une protection de l'environnement est nécessaire.
Cette solution a été validée par simulations et quelques conclusions ont pu être tirées. Premièrement, le DRA conserve toujours ses bonnes performances : un haut gain (6dBi) et une assez large bande passante (6 GHz @ ROS <2) malgré le changement de la position de la fente par rapport au DR. Deuxièmement, l'impact du PCB sur le rayonnement est visible pour lequel, dépendant de la hauteur des « solder balls », une quantité importante est rayonnée vers le substrat diminuant ainsi le gain. Finalement, le DR comme élément indépendant de la configuration ajoute une difficulté au moment de l'aligner avec la fente. Par conséquent, un décalage en fréquence ainsi qu'une chute de gain peuvent être générés par un défaut de positionnement. Une seconde solution est donc présentée pour contourner le problème ci-dessus.

4.c.ii) 2ème solution: une solution DR-fente auto-alignée

Pour maximiser le couplage et le transfert d'énergie de la fente au DR, l'alignement doit être assuré. Une nouvelle solution est donc présentée, où le DR et la fente sont fabriqués par le même procédé d'élaboration. De cette manière, le positionnement est assuré par la méthode de fabrication et non au moment de mesurer la configuration. Le procédé est montré à la Figure 155. Une fente miniature est gravée à l'arrière du substrat où le DR sera usiné ensuite par laser. Les échantillons obtenus sont aussi montrés. Une ligne coplanaire de 50 Ω est aussi gravée dans la métallisation utilisée par la fente.
Avec cette solution, une nouvelle configuration d'intégration du PA doit être introduite car la fente fait maintenant partie du DR. La Figure 156 montre cette configuration. La puce est maintenant connectée à la fente par le moyen de « μ-solder balls » (hauteur h=90μm). Ils servent à établir la connexion pour le signal de 60 GHz. D'autres « solder balls » d'une hauteur plus importante sont utilisés comme support et pour l'alimentation DC. Une bonne isolation électrique est attendue entre l'antenne et la puce grâce au plan métallique de la fente qui se trouve entre les deux.
Comme auparavant, la forme finale cylindrique attendue du DRA a été modifiée et une forme conique la remplace. Cette fois-ci, un décalage en fréquence vers le haut est obtenu. Les mesures et la simulation dans la Figure 159 montrent un bon accord avec une bande passante de 6.4 GHz et un gain maximal de 5.4 dBi . Un rendement minimum de 59% est obtenu aussi dans la bande adaptée de l'antenne avec une valeur maximale de 95% @ 61.3 GHz. Six échantillons ont été mesurés pour déterminer la répétitivité et la fiabilité de l'usinage par laser. Le coefficient de réflexion de ces six échantillons montre une différence maximale de 0.6 GHz avec un rayon minimal de 1.54 mm et maximal de 1.59. Ces valeurs peuvent être réduites si d'autres techniques de fabrication sont utilisées comme par exemple un usinage par laser à haute puissance ou des techniques de moulage par injection.

4.c.iii) Pertes des interconnexions

Pour l'intégration de la puce, comme présenté dans les pages précédentes, les interconnexions sont faites au moyen des "μ-bumps". Cette interconnexion présente un changement d'impédance et un mode pour la liaison entre les deux lignes coplanaires. Un changement d'impédance et de mode ajoute des pertes au système. Pour quantifier le niveau de pertes qu'on pourrait attendre, la configuration montrée dans la Figure 160 est proposée. Les deux lignes coplanaires (sur alumine et sur silicium) exhibaient des pertes respectivement de 0.15 dB et de 0.4 dB. Ensuite, une simulation des deux lignes liées par les "μ-bumps" est faite. Aujourd'hui, le pitch des "μ-bumps" selon [40] atteint les 50 et 100 μm

pour des diamètres respectivement de 25 ou 50 µm. Pour obtenir les pertes ajoutées par l'interconnexion, les pertes de lignes sont déduites de la valeur du S21 obtenue pour la configuration complète. Un niveau de perte de 0.44 et de 0.24dB est donc obtenu pour des diamètres respectivement de 100 et 50 µm.

4.c.iv) 3ème solution: solution complètement encapsulée

Dans les solutions présentées antérieurement, la puce ne se trouve pas dans une configuration complètement encapsulée. L'utilisation des "bumps" comme support mécanique ne remplit pas la définition d'une solution intégralement encapsulée. Selon [41], l'encapsulage pour des circuits intégrés doit assurer une connexion électrique, un support mécanique, une protection environnementale et un chemin de conductivité thermique pour la dissipation de la chaleur. Dans les solutions précédentes, la connexion électrique et aussi le support mécanique sont intégrés aux configurations. Dû à la basse puissance de travail, la dissipation de puissance peut être négligée. Par contre, la protection environnementale n'a pas été toujours prise en compte. Pour ceci, une nouvelle solution est maintenant présentée et montrée dans la Figure 6. L'antenne devient une partie de l'encapsulage.

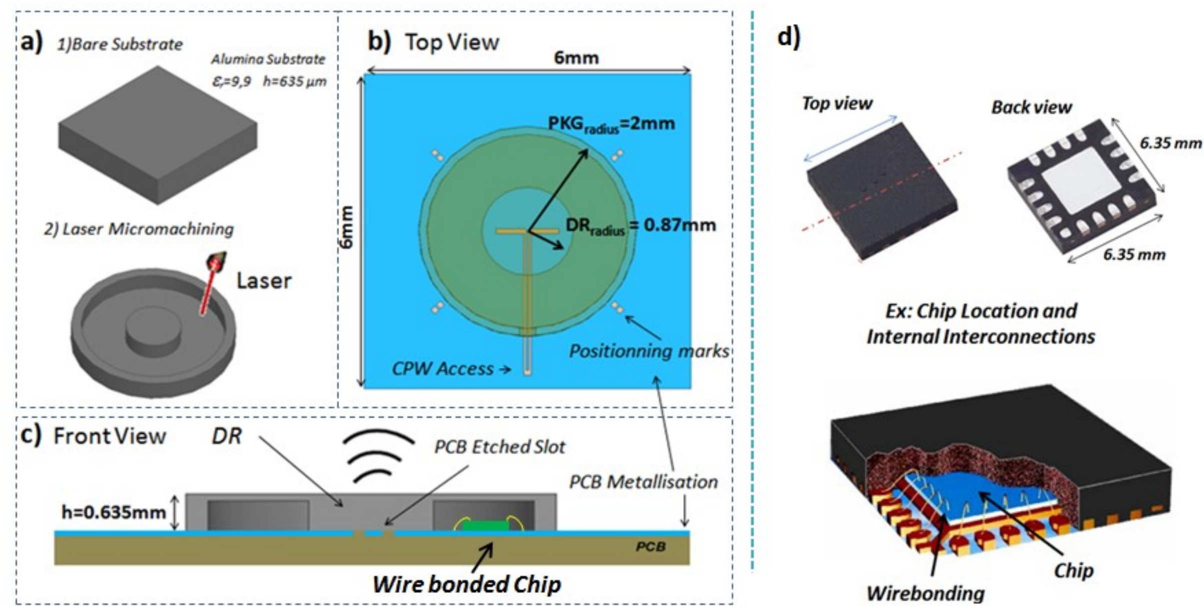

Figure 6 : a) Procédé de fabrication b) Vue d'en haut c) Vue de face (PCB, Antenne et intégration de la chip) et d) exemple de mise en boîtier QFN (utilisation industrielle[2],[3])

L'antenne et le package sont usinés par laser en même temps à partir d'un substrat d'alumine. Le package est donc « flip-chipped » sur le PCB où une fente a été gravée précédemment. L'antenne-boitier pourra ensuite héberger la chip qui peut être interconnectée au CPW de la fente par bonding (comme montré dans la figure) ou par des µ-bumps. On peut comparer cette mise en boîtier à celle QFN d'utilisation industrielle où les interconnections électriques ainsi que la protection environnementale se font de manière similaire. Comme avantage, notre mise en boîtier inclut l'antenne. L'ensemble fait

[2] http://www.pcb-3d.com/models/

[3] http://www.obs.u-bordeaux1.fr

maintenant une taille globale de 36mm^2, une taille comparable aux QFN qui mesurent 40 et 57 mm^2 [42]. L'antenne et le boîtier usinés sont montrés dans la Figure 174.
Comme nous l'avons vu, l'usinage du boitier par le laser a modifié la forme du DRA et les parois externes. Ces modifications ont été prises en compte par retro-simulation et les résultats sont montrés dans la Figure 175. Un assez bon accord est trouvé entre la simulation et les mesures. Un décalage en fréquence de 3 GHz est visible pour la réponse du S11. Il peut être expliqué par le désalignement de la fente par rapport au DR. De fortes ondulations sont aussi repérées, probablement produites par des signaux réfléchis par le banc de mesure. Pourtant, un bon niveau de gain (> 5 dBi) est trouvé dans la bande adaptée. Le problème de désalignement de la fente par rapport au DR est de retour dans cette solution et c'est pour cela qu'une nouvelle configuration est présentée ci-après.

4.c.v) 4ème solution: Réduction de l'impact du désalignement fente-DR et les pertes des interconnections

Dans la solution précédente, une très haute précision est nécessaire pour le positionnement de la fente et le DR. Un décalage en fréquence de 3GHz peut être attendu avec une séparation de 5 µm entre le plan métallique de la fente et le DR. Ce résultat montre l'importance de l'interphase d'air entre les deux éléments. Une excitation latérale est maintenant introduite, où la fente d'excitation reste intégrée dans le silicium mais positionnée à coté du DR, générant ainsi un couplage latéral. Cette configuration est montrée à la Figure 177. La position de la fente doit être assurée de telle façon qu'elle corresponde au champ magnétique du mode TM^{11} (Figure 178).
La même stratégie de boitier est utilisée malgré le changement de forme (circulaire à rectangulaire). Cette configuration présente aussi un avantage au niveau des interconnections où, à la différence du cas précédent, la fente et le PA n'ont pas besoin de connexions. Une connexion sur le silicium est suffisante et de cette manière les pertes par interconnexion peuvent être réduites.
L'interaction entre la fente et le DR est visualisée à la Figure 179. Le champ magnétique est montré dans un plan qui coupe la structure par la zone de champ maximum. Une concentration significative du champ est trouvée dans le DR et contribue de façon significative au rayonnement global de la configuration. L'effet du DR et du boitier est aussi évident dans les courbes de gain. Trois configurations ont été étudiées : i) fente seule, ii) fente + DRA et iii) fente + DRA + boitier. Dans cette configuration la fente passe d'un état non-résonant à un état résonant; pour cela une partie du rayonnement proviendra de la fente et peut être visualisée pour une haute valeur de gain avec la première configuration. À mesure qu'on ajoute les autres éléments, la bande passante s'améliore, passant de 2 à 6 GHz. Ce comportement est aussi présent pour le gain, qui pour la configuration complète arrive à avoir un niveau de 6 dBi dans toute la bande.

5) Antenne doublement alimentée pour une amélioration du rendement du PA

Dans la section 4, les éléments passifs ont été repérés comme une des sources des pertes du PA. Mais elle n'est pas la seule. Dans la Figure 183, la courbe du gain du PA est montrée par rapport à la puissance d'entrée. Deux régions d'amplification sont montrées par la courbe mauve. Une région de gain linéaire jusqu'à 3W de puissance d'entrée et après un gain asymptotique qui fait que la courbe de gain (courbe verte) descend à mesure que la

puissance d’entrée augmente. Cette baisse dans le gain dans la deuxième région est due à l’effet de la saturation du PA qui ajoutera des harmoniques supérieures au signal de sortie. L’énergie totale sera donc redistribuée dans les différentes harmoniques et le signal d’intérêt aura moins de puissance à mesure que les harmoniques augmentent. Ce sont, en fait, ces signaux supplémentaires ajoutés à la saturation du PA qu’on visera à réduire en utilisant l’antenne en plus de son rôle d'élément rayonnant.

5.a) Multi PA solution

Pour éviter la saturation, le PA est limité à travailler dans la région linéaire. De cette façon, une réponse de haut gain et haute linéarité est possible. Le seul problème avec cette région d’opération est la basse puissance de sortie. Une augmentation de cette puissance de sortie peut être envisagée si, à la place d’utiliser un seul PA, un deuxième PA est ajouté à la configuration. Deux PA en parallèle de puissance réduite mais fonctionnant dans la zone linéaires vont s’additionner pour avoir un seul signal de sortie de haute puissance et toujours en fonctionnement linéaire, évitant ainsi les harmoniques. L’antenne sera dans ce cas, non seulement un élément rayonnant mais elle fera aussi l’addition des signaux des deux PA indépendants.

5.a.i) Contraintes et conséquences d’une alimentation multiple

Une configuration initiale d’un patch multi-alimenté est présentée à la Figure 7 qui permettra d’établir les possibles conséquences et contraintes pour les antennes multi-alimentées. Les PA vont donc partager la même antenne et à partir de là, un problème d’isolation entre les sources devient évident. L’isolation entre les multiples alimentations de l’antenne devient désormais une des contraintes de la configuration. L’isolation, elle, sera montrée par des paramètres S de transmission de l’antenne et une valeur de -20 dB devra être assurée. Dans le cas de patchs, une valeur de -23 dB est obtenue dans la fréquence de résonance (61 GHz).

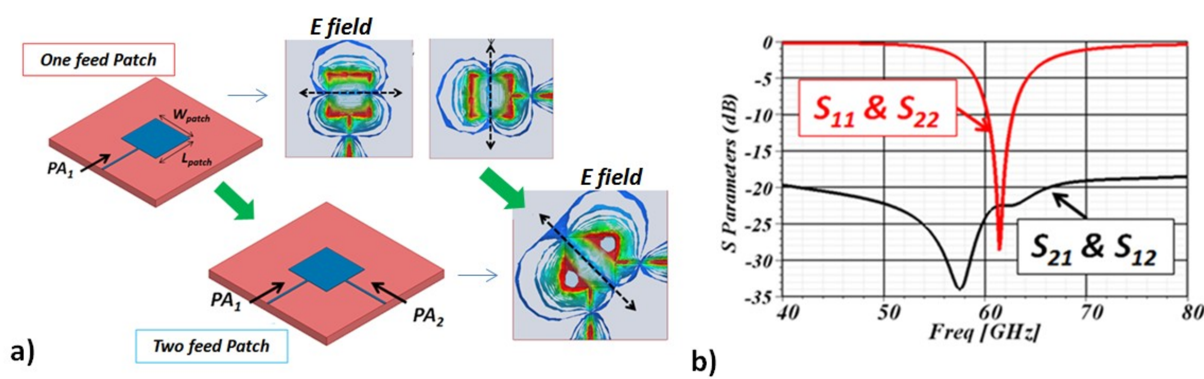

Figure 7 : a)Passage d’une seule alimentation à deux alimentations et le champ E dans le substrat. b) S Paramètres pour la configuration des deux alimentations

Un deuxième changement est visible aussi dans la polarisation de l’antenne. Il est illustré par la rotation du champ E dans le substrat dans la Figure 184. Initialement, les champs sont montrés pour des configurations d’alimentation simple où une orthogonalité entre les deux cas est observée. Au moment d’alimenter simultanément l’antenne par les deux ports, l’addition des champs produit une rotation du champ de 45° qui se traduit par une rotation de la polarisation linéaire de l’antenne.

En identifiant maintenant les contraintes que peuvent avoir les solutions d'antenne à multiples alimentations, une technologie de mise en boîtier sera introduite et les possibilités pour la réalisation d'un DRA de multiple alimentation présentées.

5.b) Technologie de mise en boîtier HTCC et ses possibilités pour l'usinage du DRA

LTCC ou HTCC (Low or High Temperature Co-Fired Ceramics) est une technologie pour la mise en boîtier en région millimétrique. Elle permet l'intégration de circuits actifs avec des éléments passifs. Elle offre donc des possibilités intéressantes pour nos solutions PA et antenne. Ces technologies consistent en l'empilement de plusieurs couches de céramique qui peuvent ou pas être métallisées. Pour le cas du HTCC, la céramique offre une permittivité de 8.6 et un tan $\delta = 0.0021$ @ 60 GHz. Ces valeurs permettent de penser à la fabrication de l'antenne à partir du matériel même, par exemple une antenne DR. Un des inconvénients pour l'usinage d'une DRA (par exemple celle de la section 5 avec une excitation par-dessous) c'est l'imposition d'une liaison entre tous les éléments pour chacune des couches dans lesquelles est divisée la structure. Pour certaines couches du DR, le cylindre restera isolé du reste de la structure et sa position finale ne pourra pas être assurée lors de l'empilement final. C'est pour cela qu'une nouvelle excitation pour le DR est présentée. Cette fois-ci, une excitation latérale du DR est réussie par le moyen d'une guide d'onde (Figure 8 a). Le guide d'onde montré est impossible à usiner dans la technologie multicouche dû à l'impossibilité d'élaborer la métallisation verticale pour les parois de la guide. Un guide d'onde dont les parois sont construites par des trous métallisés (« vias »), aussi nommé SIW (Substrate Integrated Waveguide), peut être utilisé tel que présenté à la Figure 8 c).

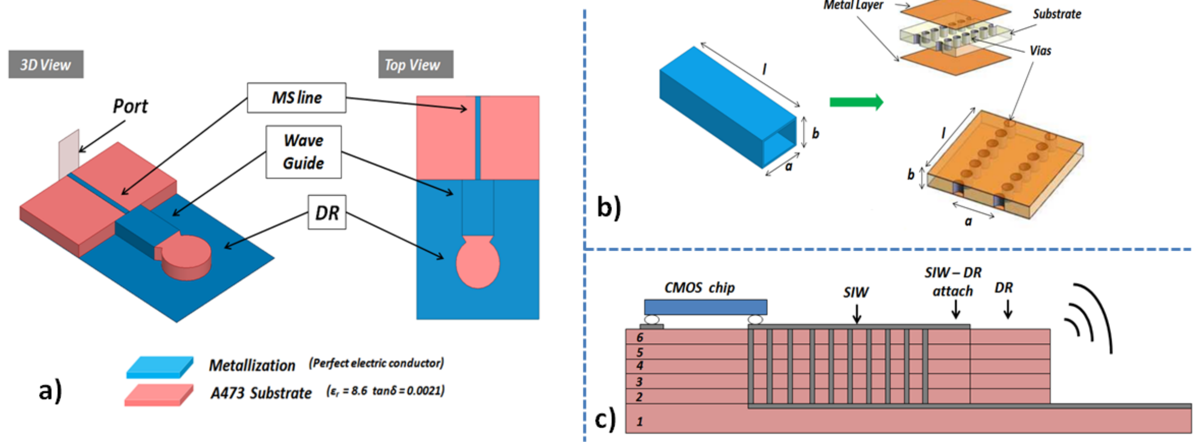

Figure 8 : a) DR excité latéralement par un guide d'onde, b) Guide d'onde et SIW (Substrate Integrated Waveguide) et c) Solution d'intégration

5.c) Double alimentation pour un DR

Maintenant, en reprenant l'idée d'une alimentation multiple, une deuxième excitation est ajoutée à la configuration comme le montre la Figure 204. Le DRA exhibe avec cette excitation une bande passante de 10 GHz, plus que suffisante. Mais elle montre un niveau de couplage de -15 dB qui doit être amélioré. Un gain d'une valeur de 7.1 dBi est quand même obtenu. Dû à l'excitation latérale, une inclinaison du champ est observée, le maximum ne se trouvant plus à $\theta = 0°$ mais à $\theta = 50°$. Des éléments parasites pourraient être ajoutés à la configuration pour faire revenir le champ dans la bonne configuration.

Deux autres modifications doivent aussi être faites à la configuration à cause de l'excitation du guide d'onde et aussi sa position. Comme le montre la Figure 213, une excitation appropriée du guide d'onde doit être ajoutée pour une compatibilité avec la sortie du PA. Dans ce cas, une excitation avec une ligne CPW est utilisée. Comme montré auparavant, l'interconnexion entre la puce et le guide peut être réussie au moyen de bumps. Une deuxième problématique porte sur la distance (L) qui sépare les deux excitations. Pour une solution qui minimise la puissance globale du système, une seule puce devrait être utilisée. Donc, les excitations doivent être rapprochées de la puce qui, dans ce cas, aura les deux PA. Pour ça, un guide d'onde courbé sera utilisé (Figure 213).

6) Conclusions Générales

Un système a été étudié pour le transfert des données à haut débit dans la bande de 60 GHz. Plusieurs solutions sont présentées pour ce genre de système, plus précisément pour l'amplificateur de puissance et l'intégration avec l'antenne. Premièrement, la technologie sur silicium a été choisie et ce choix est basé sur les trois points suivants. i) une baisse du coût de fabrication semble être la tendance grâce aux importants investissements de la part de l'industrie et du gouvernement. ii) une possibilité plus importante d'intégration grâce à une haute capacité de production comparée aux autres technologies et iii) la technologie SOI présente une haute valeur de résistivité du substrat (3000 Ω cm). Cette propriété rend les éléments passifs comme les condensateurs, inducteurs et lignes de transmission plus efficients. Donc, la technologie CMOS silicium semble le choix le plus adapté pour des solutions à bas coût, à haute intégration et à haute efficacité.
Le prochain point était de rendre l'intégration de l'antenne du transmetteur plus efficace.
Deux stratégies d'intégration ont été considérées : SoC et SiP.
En incorporant l'antenne sur la puce, une augmentation de 12% de l'efficacité a été observée en utilisant une sub-stratégie de SoC. Cela démontre les possibilités offertes par « intégration sur puce » quand l'impédance typique de 50 Ω à la sortie et entrée du PA sont utilisées. Cette même impédance d'entrée de l'antenne peut être modifiée et adaptée au besoin.
Bien que l'intégration de PA et antenne sous une stratégie SoC offre de bonnes possibilités d'augmentation de l'efficacité, la conception devient plus complexe à cause de la réduction de la taille du système. Premièrement, le PA et l'antenne peuvent interagir au détriment de la performance du système. La distance du PA par rapport à l'antenne devient donc un paramètre-clé dans ce genre de stratégies. Deuxièmement, les éléments introduits en mesures (sonde et support) n'ont pas d'effets négligeables. L'interaction de la sonde avec l'antenne a été étudiée par des simulations et vérifiée par des mesures. Une interférence destructive est donc ajoutée sur la performance de l'antenne par la sonde. Et troisièmement, les frontières de la puce, c'est-à-dire son boîtier, deviennent importants pour des solutions de taille réduite.
Les solutions SiP, quant à elles, offrent une souplesse plus importante du point de vue de l'antenne. D'une solution d'antenne de haut gain basée sur le résonateur diélectrique plusieurs configurations montrent les possibilités d'utiliser le DRA pour des solutions efficaces d'antenne dans la bande des 60 GHz. Grâce à un substrat de faibles pertes, une antenne avec une performance de haute efficacité peut être envisagée. À partir d'ici, des solutions originales basées sur le résonateur ont été usinées par laser. De cette façon, une

première « semi -packaged» solution a été présentée. Le rôle et l'impact des interconnexions ont été mis en évidence. Particulièrement, l'efficacité (liée aux pertes introduites par les interconnexions) et la bande passante de l'antenne sont principalement affectées. Deux configurations finales pour des solutions intégrales de mise en boîtier sont ultérieurement présentées. Ces solutions partagent le même boitier basé sur le DR, où le boitier et le DR sont usinés dans la même étape de fabrication par laser. Une large bande passante est finalement obtenue (10 GHz) et un gain minimum de 5 dBi dans toute la bande adaptée. Ainsi, les besoins imposés par notre application ont été remplis.
En gardant à l'esprit le but de cette étude, une autre stratégie pour l'augmentation de l'efficacité est proposée et validée par simulation. Il est donné à l'antenne un rôle supplémentaire à celui du rayonnement. L'antenne précédente, alimentée par une seule entrée, devient maintenant un élément à multiples entrées. De cette manière, deux PA à faible puissance mais opérant dans une zone linéaire vont remplacer l'unique PA à haute puissance mais moins linéaire. L'antenne sera désormais en charge d'additionner les deux signaux en provenant des deux PA. Du point de vue de l'antenne et de ses performances de rayonnement, deux conclusions sont tirées. Premièrement, le couplage entre les deux sources devient une contrainte supplémentaire pour le système. Deuxièmement, une rotation du champ (et de la polarisation) augmente la probabilité d'un niveau fort de polarisation croisée. Après l'identification des ces contraintes, des nouvelles solutions ont été proposée en incluant l'utilisation des technologies industrielles pour le « packaging », e.i. la technologie multicouche HTCC. Des contraintes d'usinage ont été détectées et résolues. Les résultats de simulation montrent des performances prometteuses pour l'intégration de PA et antenne.

7) Travaux à réaliser dans le futur

D'après les résultats précédemment présentés, plusieurs axes peuvent être identifiés pour continuer ces recherches.
Premièrement, les outils de simulations sont en constante évolution et offrent de nouvelles opportunités pour des co-simulations entre antennes et circuits.
Comme nous l'avons vu auparavant, certains aspects des solutions de PA et antenne ne peuvent pas être pris en compte par la simulation. Les solutions de la co-intégration et de co-conception montrent des perturbations quand la puissance maximum du « PA output » a été atteinte. Ces perturbations ne sont pas visibles lors des simulations et n'infirment que quelques phénomènes qui semblaient expliquer les résultats. En ayant cela à l'esprit, de nouveaux outils de simulation pourraient offrir de nouvelles possibilités pour décrire la chaine complète de PA et antenne, et l'interaction entre elles.
Deuxièmement, la technologie multicouche (HTCC) est idéale pour les antennes basées sur les résonateurs électriques. La relativement forte permittivité des bandes de ruban céramique permettent à la taille du résonateur d'être compatible avec les appareils fonctionnant en millimétrique. Elle offre aussi un fiable angle de perte qui permet un accroissement de l'efficacité de l'antenne. L'usinage de l'antenne, même en prenant en compte les contraintes de fabrication, peut offrir une solution complète pour un PA et antenne mis en boîtier. Hors de l'intégration du « front-end », la flexibilité du procédé de fabrication permet l'expérimentation sur l'antenne. Par exemple, la forme cylindrique du DR peut être modifiée (rectangulaire, ovale) et pourrait améliorer ses performances. La

frontière de l'antenne pourrait aussi être modifiée en ajoutant des éléments parasites métalliques arrivant à des solutions d'antenne – PA blindées.
Finalement, et comme mentionné précédemment, des études complémentaires doivent être faites sur la technologie SIW pour confirmer la compatibilité de l'alimentation du DR et des contraintes qui pourraient surgir de la conception du PA (deux PA dans une seule puce).

General Introduction

The discovery and study of the electromagnetic waves has allowed the communication between human beings to change drastically. Theoretical studies and practical work dating from 1820's, from physicists like Faraday set the bases for the telegraph. With this invention, the electrical energy started to be used as means of transmitting information. Then, Maxwell and Hertz developed the theory of electromagnetic waves, which predicted the possibility of using the air as the transmitting medium. The radio at first, being the first wireless device, covered several miles at the beginning crossing the English Channel between England and France in 1899. Years later, communication between continents was demonstrated when America and Europe were united by a radio transmission in 1901.[4] Since then, a much wider frequency range has been exploited and other application have been developed using the electromagnetic waves over a very large spectrum (Figure 9).

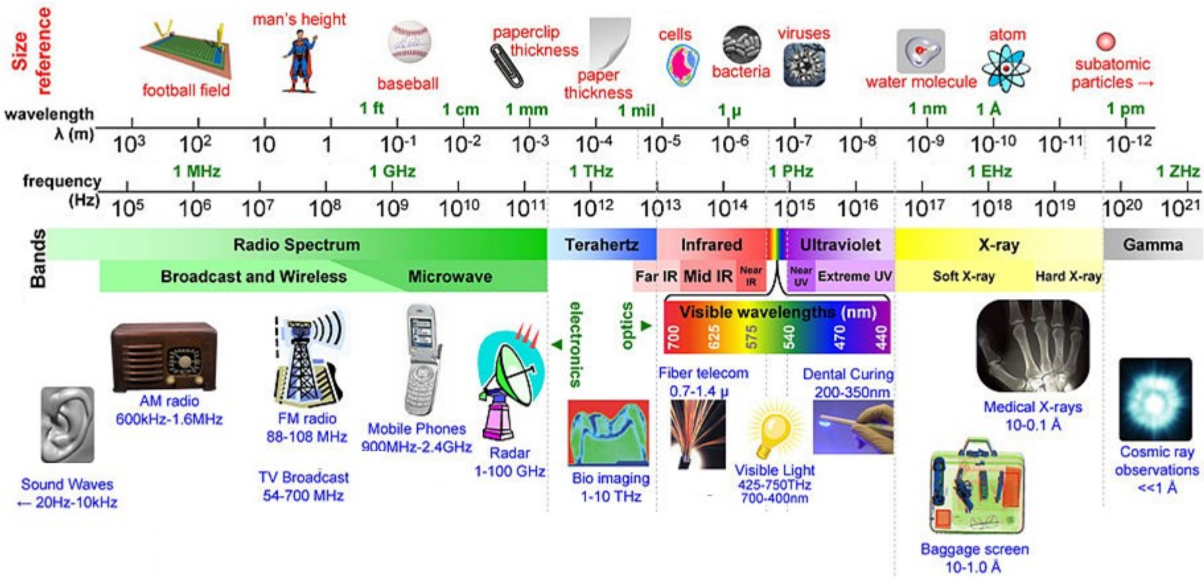

Figure 9 The electromagnetic spectrum and applications[5]

One of the key factors has been the technological improvement, as for example the appearance of the transistor. It allowed the miniaturization of devices which has led to the mobile phone and the PDA (Personal Digital Assistant). As its name clearly states it, the PDA

---

[4] http://www.clemson.edu

[5] http://www.nsu.ru

assists the user with digital information and the transfer of this information should be done as fast and reliable as possible. For this purpose a decrease in downloading time regarding existing solutions (like the WiFi standard at 2,4 GHz) is expected by selecting a higher frequency band like the 60 GHz band. This band offers a bandwidth of 7 GHz that would allow transfers of up to 2 Gb/s, much faster than WiFi or UWB. (A more thorough comparison is presented in chapter 1).

To take advantage of this high data rate possibility, the design of compatible antenna and transmitter has to be made at 60 GHz. And this constitutes the motivation for this thesis. The transmitter and the antenna of a mobile phone are illustrated in Figure 10. The transmitter includes the modulation and amplification stages of the transmission chain. It is this last part, the amplification stage or the power amplifier (PA), where our work will concentrate. New integration strategies will be presented for PA and antenna connection.

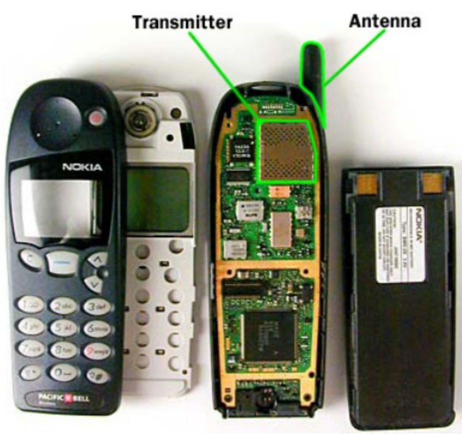

Figure 10 Transmitter module and antenna [6]

The outline of this thesis is shown below:

In chapter 1, the 60-GHz band and its regulation are described, leading to the application requirements and constraints. The benefits of the SOI technology are presented. A state of the art of 60-GHz systems is presented. Special attention is given to the PA and antenna solutions. Two strategies (System on Chip (SoC) and System in Package (SiP)) for PA and

---

[6] http://www.electronics.howstuffworks.com

Antenna are described giving room to introduce interconnections. Conclusions end the Chapter 1.

In chapter 2, the SoC solution is developed and presented. Then, PA performances and interconnection with the antenna are discussed. The substrate impact on On-Chip antenna regarding gain and efficiency is studied. The boundary specifications for Antenna and PA integration (impedance and line topology) are determined. Co-integration and Co-design strategies are explained and solutions for each one are described. Simulation, measurement results and conclusions end the chapter.

In chapter 3, the SiP approach is explained. The choice of the Dielectric Resonator Antenna (DRA) as solution is justified. Then, a short state of the art and DRA feeding schemes are presented. Radiating principle of the DR and fabrication methods are described. Validation of the first DR and other packaging solutions based on the DR are then described. Measurement and simulation results precede the conclusions of the chapter.

In chapter 4, a PA-Antenna energy efficient configuration is presented. The importance of a linear PA response is explained and how the antenna can be used for other purpose than the radiating element. The antenna could be thought of a multi-fed element. More precisely, two low power but linear PA can add their signals by means of the antenna. Thus, the antenna acts as a radiator and coupler. Simulation results concerning antenna elements are finally presented.

A general conclusion and future work terminate the manuscript.

Chapter 1 - State of the Art of 60 GHz Transmission Systems

1) Introduction

Communications are becoming mobile. In 2011, mobile devices sales overtook fixed mostly thanks to the development of Smartphones which grew by 256% in 2011 (Figure 11 a). This means that wireless data transfer is increasing and the amount of information exchange should continue to increase.

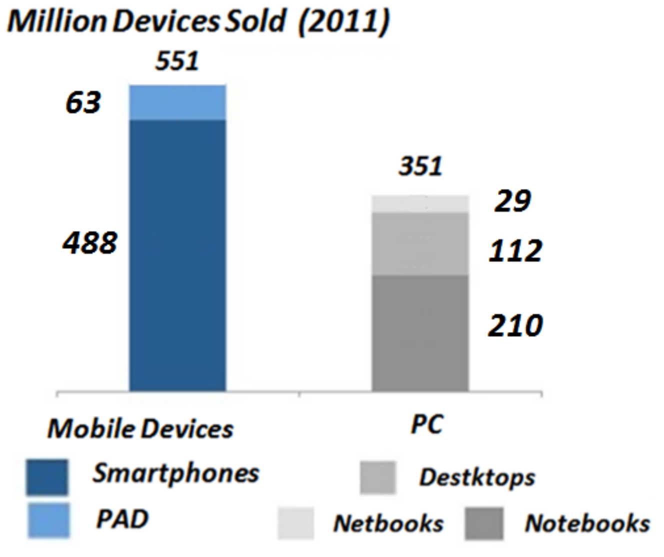

Figure 11 a) Devices Sold in 2011[7]

With this in mind, not only the demand of wireless data exchange is increasing but also a *fast* wireless data transfer performance is expected. The 60 GHz band is a good candidate to solve the fast short range wireless exchange.

[7] www.*Marketing-Webmobile.fr*

2) The 60 GHz band and its opportunities

2.a) The 60 GHz band and its regulation

The "recently" released unlicensed band around 60 GHz opened a new world of opportunities and challenges. In 2001, the United States Federal Communications Commission (FCC) released 7 GHz of bandwidth for unlicensed use; other governments have similarly allowed portions of the 60 GHz band to be used. The IEEE 802.15 Task Group 3C, has been working since 2003 in the definition of the standard that will try to seize this 60 GHz band for wireless communication. At the end of 2009, they released the latest update to the final regulatory document in which recommended use and definitions are stated. But of course, these recommendations are not always followed by all regulatory entities around the world and some modifications can be seen. For example, the frequency range stated in [1] allocates a 9 GHz frequency range between 57 and 66 GHz but is not the same as for example the 7 GHz for the FCC mentioned before. Frequency allocation according to geographic region can be seen in Table 1 [2].

Geographic location	Frequency Allocation (Bandwidth)	Regulatory Entity
US - Canada	57 – 64 (7 GHz)	FCC (US)
Europe - China	57 – 66 (9 GHz)	ETSI (Europe)
Japan	59 – 66 (7 GHz)	Ministry of Public Management
Australia	59.4 - 62.9 (3.5 GHz)	

Table 1 Frequency Allocation and Bandwidth according to geographic location

Another important consideration is the channel allocation and the bandwidth given to each channel. According to the 802.15 Task Group 3C, a 1728 MHz bandwidth has been given to each of the four channels in which the 7 GHz band has been divided as seen in Figure 12. This is very important as it will play a fundamental role in the determination of the budget link that is presented later.

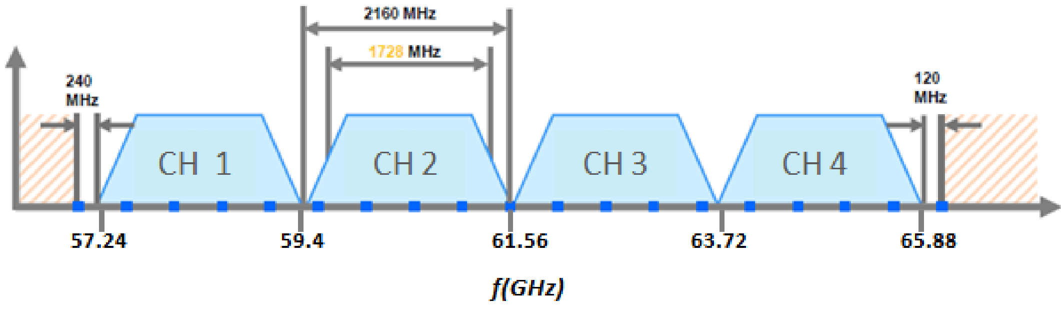

Figure 12 Frequency channel allocation according to the 802.15.3c [1]

2.b) Unlicensed Band, what does this imply

The electromagnetic spectrum has been divided into different regions by governments all over the world to be able to control its use. Apart from dividing it, they also decide the conditions for its use; they decide which portions of the spectrum will be licensed or unlicensed. For a licensed band, a fee is charged to operate at this frequency, unlike for an unlicensed band where the use of a certain frequency band is free. One of these regions is the 7 or 9 GHz band around the 60 GHz frequency and it has been declared as unlicensed. No cost has to be considered regarding its use and although it could be thought to be a positive aspect, this also means that anyone can use this band, thus increasing the possibilities of interference as the number of users increases. And this is one of the key characteristics to be taken into consideration for the regulatory entities defining the 60 GHz standard: a set of rules will have to be established to resolve or mitigate the possible interference coming from multiple number of users. [3]

2.c) Why the 60 GHz band?

To be able to obtain a higher data rate (C), according to Shannon's theorem (1), one has only to increase the frequency bandwidth (B) maintaining the same Signal-to-Noise ratio (S/N); we can see how around 60 GHz, there are more bandwidth available than for a 2.4 GHz on

today's WLAN network. For instance, one can compare the 9-GHz bandwidth at 60 GHz to the about 76 MHz available for the Wi-Fi standard. Note that we obtain a wider spectrum for the 60-GHz signals which is about a 12%. If we assign the same percentage to the 2.4-GHz signal we obtain 288-MHz bandwidth. This demonstrates, that for the same relative bandwidth (in our case 12%), a wider frequency range is achieved when increasing the operating frequency.

$$C = B \times log_2 \left(1 + \frac{S}{N}\right) \qquad Eq.\ 2$$

Another way of obtaining a higher data rate is by using modulation schemes that take advantage of the inherent information of an electromagnetic wave like phase and amplitude to represent digital information. This, of course, comes with computing costs that will be translated into power consumption. The use of this unlicensed band and its bandwidth allows one to decrease the computing burden used for complicated modulation schemes. For example, to transmit 1 Gb/s, with 1 GHz of bandwidth, we only need 1 Hz/bit. Using 100 MHz of bandwidth we would need 10 bits/Hz that obviously needs to be modulated to transmit the 10 bits in one Hertz. Without the need of complex constellations and modulation schemes, lower power consumption will be achieved thanks to fewer base-band circuits that are needed to process the information. As a result, lower power/bit consumption can be obtained [4]. Figure 13 shows a comparison of data rate possibilities with the use of different standards and how 60-GHz operation should give solutions for data communication up to 5 Gbps. This is not possible, for example, with the 802.11 WiFi standard or UWB (Ultra wide Band).

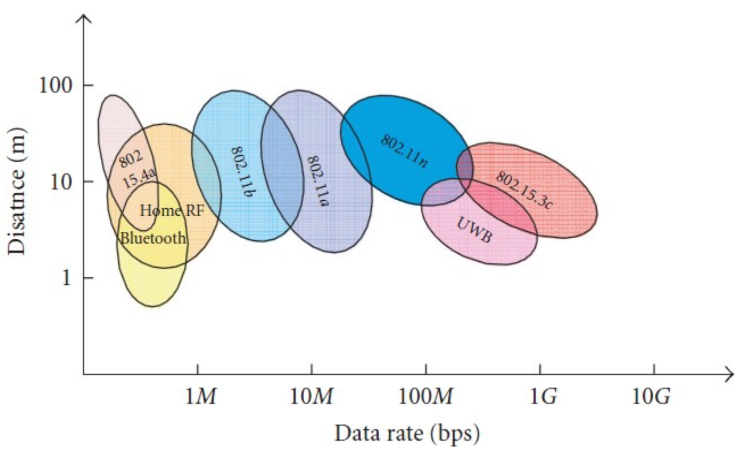

Figure 13 Data rates and range requirements for WLAN and WPAN standards and applications. [5]

2.d) Applications

With the above mentioned high data rate, several new applications can now be foreseen like Wireless HD TV, high data rate wireless, wireless desktop docking, desktop point to multipoint connections and kiosk downloading. The later application will be dealt with in the present thesis.

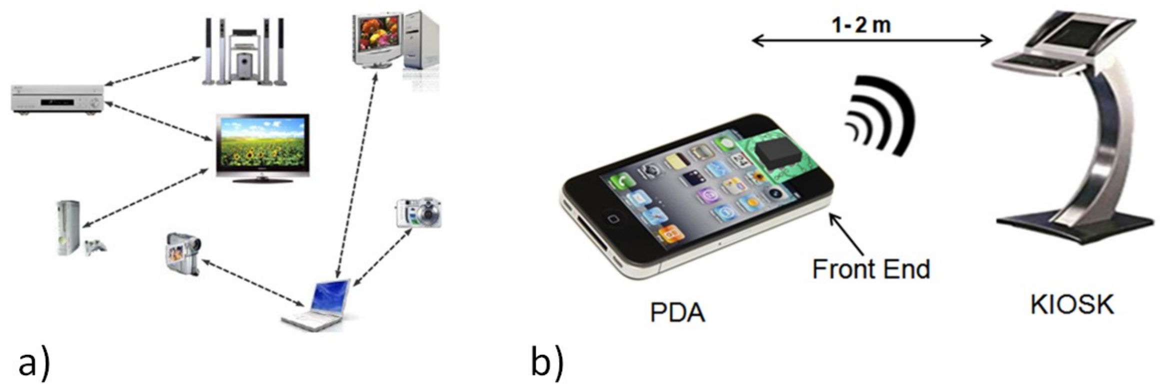

Figure 14 Application for the 60 GHz band a) Wireless HD TV, high data rate and point to multipoint connection [6] b) kiosk downloading

To be able to cover the above applications, the standard IEEE802.15.3c has defined three different physical (PHY) configurations [6]:

- Single Carrier (SC) → Typically for Line of Sight (LOS) Scenarios. 2 to 5.2 Gbps
- High Speed Interface (HIS) OFDM → Typically for No Line of Sight Scenarios (NLOS). 5.7 Gbps
- Audio/Video (A/V) OFDM → Typically for NLOS (uncompressed HD) with 5.7 Gbps

For kiosk downloading application, due to the configuration of the environment between the receiver and transmitter, that is a LOS scenario can be expected at any time, a SC PHY configuration has been adopted.

Other standards exist as well for the 60 GHz band. Different groups and organizations have started working, somewhat after the IEEE 802.15 Task Group 3C, on their own standards as for example the IEEE 802.11ad, which foresees a WLAN application. A summary of these groups and forums, with their respective applications and status can be seen in Table 2. [7]

Group (Forum)	**Status**	**Max. Data Rate**	**Applications**
ECMA-387	2nd version released: Dec 2010	6.35 Gbit/s per channel, 25.4 Gbit/s (4 channels max.)	- High-data-rate WPAN transport for both bulk data transfer and multimedia streaming
IEEE 802.15.3c	Released: Oct. 2009	5.8 Gbit/s	-High-data-rate WPAN specification -Focus on point-to-point applications -Basis for Wireless HD specification
Wireless HD Specification 1.1	released: April 2010	7.14 Gbit/s per channel, 28.6 Gbit/s (4 channels max.)	- Specification for wireless high-definition digital interface WVAN for uncompressed A/V streaming and high-speed media transmission
IEEE 802.11ad PAR	approved, release: Dec 2012	> 6.8 Gbit/s	- WLAN in the 60 GHz band - Fast session transfer between 60 GHz and 2.4 GHz/5 GHz
Wireless Gigabit Alliance (WiGig)	Common standardization with IEEE 802.11ad		- Global wireless ecosystem of interoperable, high-performance devices (CE, PC, IC, handheld) - Multi-gigabit-speed wireless communications in the 60 GHz band

Table 2 Different Groups defining different standards for the 60 GHz band

2.e) Attenuation factors (losses in the 60 GHz band)

Why short range communications? If one considers the power budget link between a transmitter and receiver, one observes that there is an attenuation of the received power due to the decrease of the free-space wave power density. This factor (Free Space Path loss or FSPL) increases with both the frequency and the distance as shown by figure 4.

$$FSPL_{att} = 10\ log\left(\frac{f4\pi d}{c}\right)^2 \qquad Eq.3$$

Where f is the frequency (Hz), d is the distance between transmitter and receiver (m) and c is the free-space light velocity (m/s; ≈ 300000000).

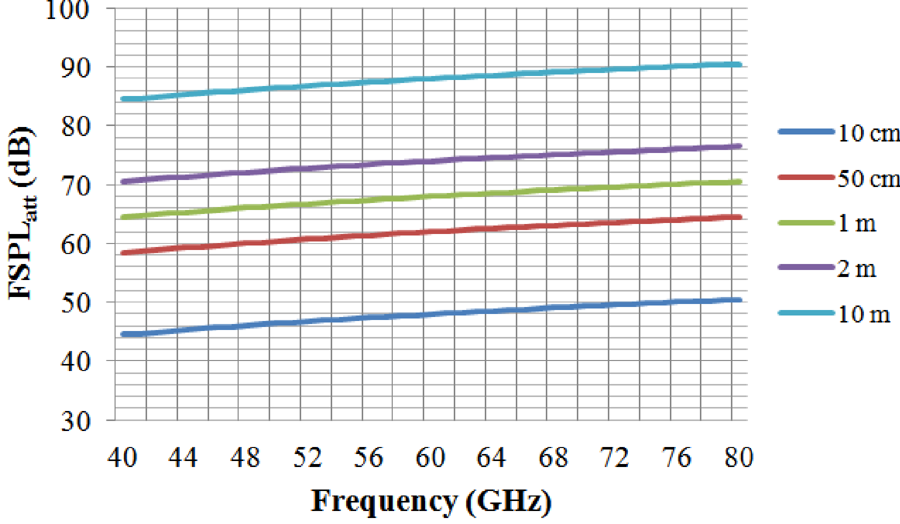

Figure 15 Free-Space Path attenuation (dB) due to frequency and distance

For example, at 60 GHz, -74- dB free-space attenuation can be expected for a wave when the receiver and the transmitter are separated 2 meters from each other. It is important to note that any loss due to the propagation medium (rain, fog, mist, etc.) will produce an additional attenuation. The total attenuation of the received signal will define the characteristics of the antenna and amplifiers for a given application.

2.f) Link Budget

For our investigation, that is, finding an antenna solution for a kiosk downloading environment, the minimum transmitting gain of the antenna is one of the key parameters to be established. This will be done through the link budget calculation that takes into account all the factors that contribute to the signal power level at the receiver access. (Friis Transmission relation [8].)

$$\boldsymbol{P_R = P_T + G_T + G_R - FSPL_{att}} \qquad \textit{Eq.4}$$

It states that the power received by the receiving antenna P_R (dBm) is equal to the addition of the transmitted power P_T (dBm), the gain of the transmitting and receiving antenna, G_T (dB) and G_R (dB) respectively, and minus the free space attenuation factor.

Now, if we include losses deriving from environmental and implementation issues as thermal noise (k is the Boltzmann's constant (1.38×10^{-23} J/K), T the temperature (290 K), B the bandwidth), carrier-to-noise ratio *C/N* (depends on the PHY configuration selected: LOS in our case and it is the minimum signal to noise ratio necessary for the receiver to work), the noise introduced by the receiver *NF* and implementation loss in the transceiver L_I (losses in the transmission chain e.g., PA or Mixer) we will now have:

$$\boldsymbol{C/N = P_T + G_T + G_R - FSLP_{att} - 10\, log\ (1000kTB) - NF - L_I} \qquad \textit{Eq.5}$$

Furthermore, information about the transmission channel modeling has to be incorporated. The FSLP factor is slightly modified. According to the 802.15.3c group, for a LOS environment, a reference value (P_L) for a 1 m distance (between transmitter and receiver) and a logarithmic distance dependent factor is added. A path loss exponent is also defined (n) to account for shadowing and antenna radiation properties (directive or omnidirectional).

$$FSPL_{att} \rightarrow P_L + 10n\log(d) \qquad Eq.\ 6$$

The link margin (M) that is the difference between the receiver sensitivity (minimum power at which the receiver will stop working and the actual received power) is also added. Finally we have

$$C/N = P_T + G_T + G_R - 10\log(1000kTB) - NF - L_I - P_L - 10n\log(d) - M \quad Eq.\ 7$$

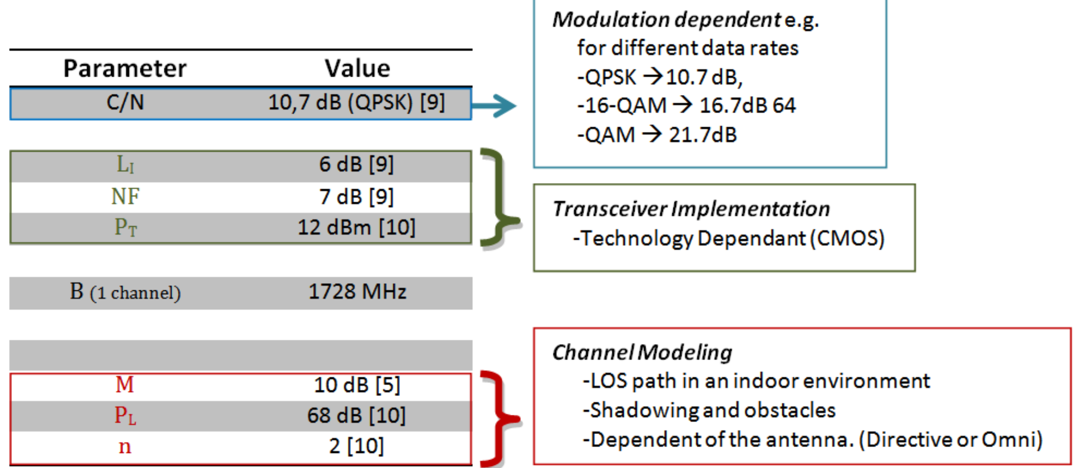

Parameter	Value
C/N	10,7 dB (QPSK) [9]
L_I	6 dB [9]
NF	7 dB [9]
P_T	12 dBm [10]
B (1 channel)	1728 MHz
M	10 dB [5]
P_L	68 dB [10]
n	2 [10]

Table 3 Parameters and Values of the budget link

By replacing all the values in Eq. 6, and leaving the distance as an unknown parameter, we can find a relationship between the gain of the antenna and the maximum distance for a reliable communication link that can be established. Furthermore, if we assume that the gain of the receiving and transmitting antenna is the same, we clearly have the minimum gain that should be fulfilled by the antennas to cover a specific range (7).

$$G_T = -1 + 20\log(d) \qquad Eq.8$$

The antenna gain needed for distances of 1 m up to 6 m can be seen in Figure 16. A value of 6 dBi is imposed to assure a link for a 2 m separation between transmitter and receiver; which applies to our application.

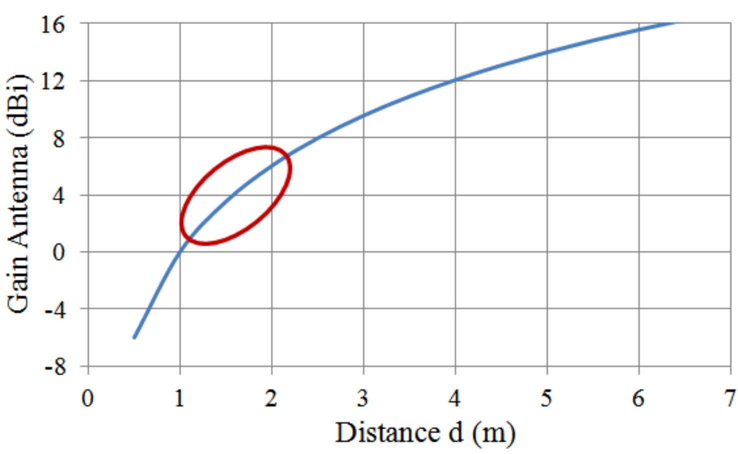

Figure 16 Antenna Gain according to distance between Transmitter and Receiver

Regarding the transmitted power (in our case P_T), a limitation exists such as frequency allocation and it depends of the regulatory entity as shown in Table 1.

Geographic location	Max Transmit Power (mW, dBm)	Max Antenna Gain (dBi)	EIRP (dBm) Transmit Power(dBm) + Antenna Gain (dBi)
US - Canada	10, 10	Not Specified (NS)	43
Europe	20, 13.1	37	57
Japan	10, 10	47	NS
Australia	10, 10	NS	150W (Tx Power (W)*Gain ant (dBi))

Table 1 Maximum Transmit Power according to geographic location [5]

2.g) Commercially Available Solutions at 60 GHz

Since the accepted standard for the IEEE 802.15 Task Group 3C at the end of 2009, several electronic manufacturers have started working in adding to their products the ones for fast data transmission rates, now made possible thanks to the 60 GHz standards.

For example, by the end of 2009, Panasonic had already incorporated a Wireless HD module to one of its TV set. The same is true for LG Electronics that realized in January 2012 its LG's LH85. Toshiba and Funai achieved products with the same performances. [9]

In May 2011, Qualcomm Incorporated and Wilocity, leading developers of 60 GHz multi-gigabit wireless chipsets for the mobile computing, consumer electronics and peripheral markets, announced the AR9004TB. It is the first chipset capable of supporting a wide range of applications, from I/O to video to networking, at the same speeds as equivalent wired connectivity technologies. [10]

3) Generic Transmission Chain and Front End location

Having defined the gain and bandwidth for the antenna, (two of the most important parameters), it is now time to locate the antenna and identify its role in the Transmission Chain.

3.a) Complete Tx-Rx Chain

If we follow the flow of a signal through a wireless communication chain, one can identify three major system components: The transmitter, the air channel and the receiver. The transmitter converts the information given by any data source into energy capable of using the air channel as the propagation medium. This air channel is now the link between the transmitter and the receiver. It may modify the traveling signal, depending on its characteristics. At the other end, we find the receiver which detects the energy that arrives through the air channel and recuperate the initial data as shown in figure 6.

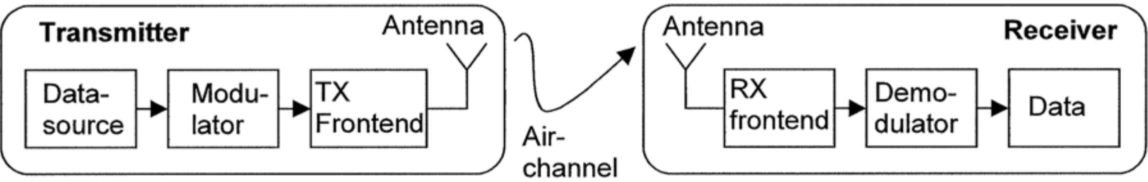

Figure 17 Three components for the Tx-Rx Chain Transmitter – Air - Receiver [11]

As it can be seen in the link budget, all three components play a vital role in defining the required performance of the antenna. However, even though our work concerns only the transmitter, it was important to begin by taking them into consideration.

Now, living aside the air channel and the receiver, we will focus on the transmitter component. This part of the communication channel can also be divided into several subsystems. It consists of a high frequency generator (VCO), a modulator (Mixer), a Power Amplifier and the Antenna. They can be clearly identified in Figure 18. These four stages have their own characteristics and it is not the aim of this thesis to enter in the details of each component.

-**Generic** Transmission Chain and Front End location

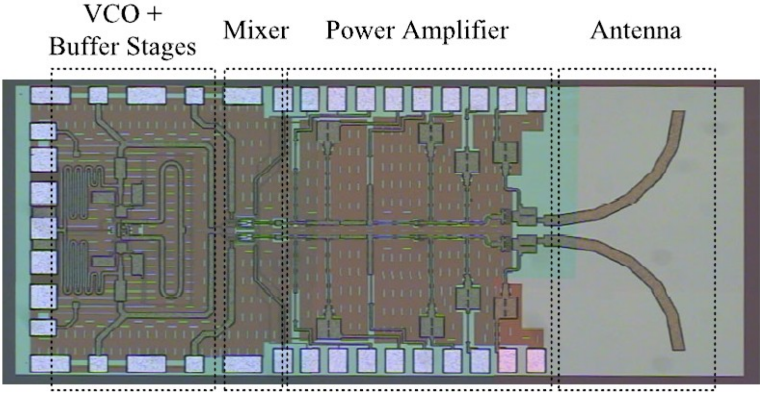

Figure 18 Example of a Transmission Circuit and its Building Blocks [12]

The transmitter presented above operates at 60 GHz and it has been fabricated in 0.18-μm SiGe BiCMOS technology. This gives rise to two topics that will be discussed in the next pages. The first one is the technology choice (why silicon?) and the other one deals with a peculiar feature that can be seen in figure 7, i.e., the antenna size (@ 60 GHz → λ = 5mm) is comparable to that of active devices. This will have some important impact when trying to meet the gain requirement established before.

3.b) Technological Possibilities

Several advantages make silicon the possible semiconductor solution for the present high frequency application. Other candidates, like GaAs and InP, were ready to undertake the task of the radio frequency (RF) solution @ 60 GHz. Yet, one may wonder why silicon remains the best choice. First of all, it is cheaper than any other technology and its price continue to decrease due to the great investment (from industry and government) that it benefits (mostly CMOS). [11] Secondly, silicon has a much higher integration possibility contrasting with the low manufacturing yield (capability of die production) of the other semiconductor technologies. This allows a greater flexibility for the manufacturer giving a greater efficiency on the production process. For example, with III/V semiconductors, only ASK modulation scheme has been possible. With silicon, other more complex and efficient modulation schemes are possible and have already been tested [4]. One of the hurdles for silicon CMOS that prevents its use at 60 GHz, was the limited frequency of operation compared to the other technologies. It is no longer the case as seen in figure 1 with the

projection of the CMOS scaling according to the ITRS [13],[14]. We have clearly reached by now, the possibilities of manufacturing at the 45 and 32 nm regions, hence providing solutions at much higher frequencies at the same or even lower power levels. [11]

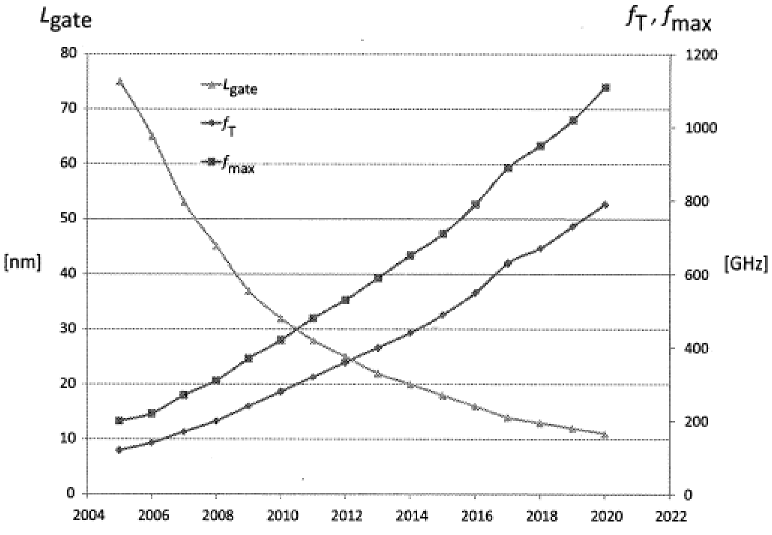

Figure 19 CMOS Ft and Fmax trend according to ITRS 2006

3.b.i) Silicon → Bulk or SOI (Silicon on Insulator)?

So, silicon CMOS seems the best choice to obtain low cost, high integrability and high efficiency solutions for RF applications. However, there are two different types of silicon technologies that exist; one known as bulk silicon and another one known as Silicon on Insulator or SOI. There are two major differences between bulk and SOI. One of them is the insertion of an insulating layer in the silicon bulk substrate (silicon oxide or sapphire) and the other is the elevation of the substrate resistivity that rises from 12 Ω/cm to 3000 Ω/cm. One of several existing fabrication processes is shown in Figure 20.

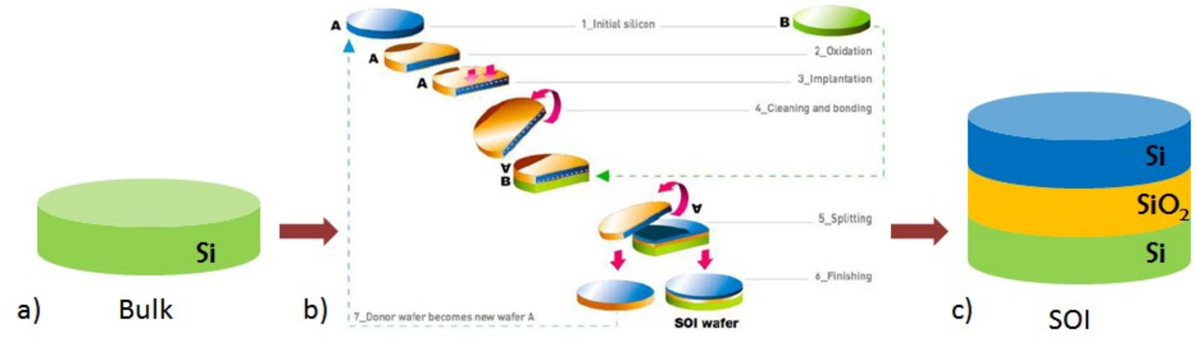

Figure 20 a) Bulk wafer b) Smart Cut SOI wafer fabrication process [15] c) SOI wafer (not to scale)

-**Generic** Transmission Chain and Front End location

To compare their performance, a division of a RF circuit into its active and passive devices is done to see the impact of the technological choice in each type of device. Active devices are constituted mainly by the transistors. They can be seen highlighted in Figure 21, where a 60-GHz PA in 90-nm CMOS technology is shown. This is a two-stage PA (two amplification stages). In this case, each one depends on only one transistor. Between these two, and between the IN and OUT signals, only passive elements exist. Here, the passive elements are transmission lines and capacitors. Inductors and transformers are also frequently found in literature ([14], [16], [17]) as part between the input and output stage.

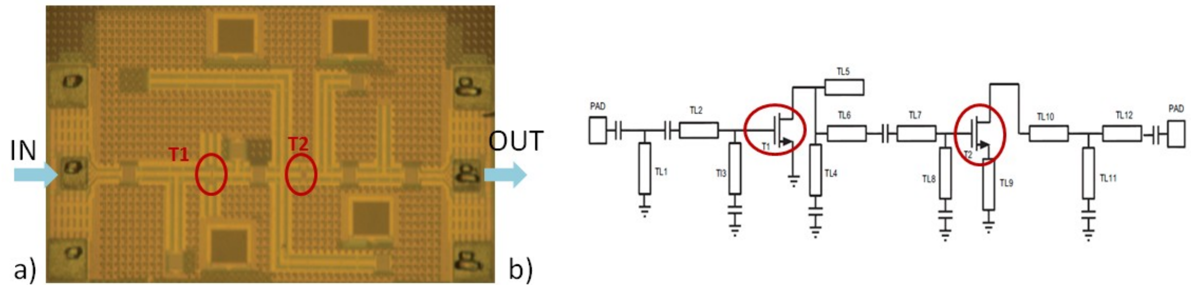

Figure 21 a) Photograph of PA (highlighted transistors) b) Schematic of PA [13]

3.b.ii) Active Devices: the transistor

Let us begin by taking a look at the active devices and their differences for the bulk and SOI cases, i.e., the difference between bulk based transistors and SOI based transistors. These two cases are illustrated in Figure 22 where the insulating layer (BOX: Buried Oxide Layer) for the case of SOI can be seen.

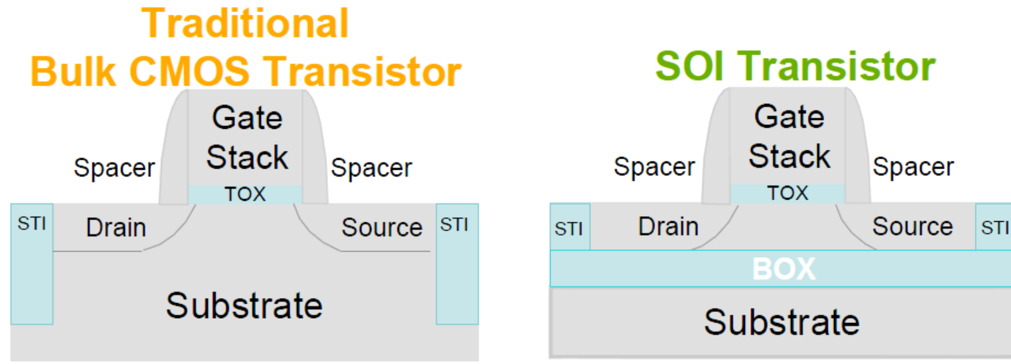

Figure 22 Transistors on Bulk Si and SOI [18]

The following are some of the new possibilities when a SOI technology is employed regarding its bulk Si counterpart.

-**Generic** Transmission Chain and Front End location

- Electric Isolation → Higher Efficiency and Greater Integration Possibilities

This concept is tied up to the «latch up » phenomenon that arises in the normal CMOS bulk processes. This phenomenon describes the current paths that can be created between the N and P wells of two neighboring transistors through the substrate. This effect lowers the transistor's performance due to consumption of unusable energy that will also heat up the device. Due to this, in CMOS bulk process, some special rules have to be followed concerning the distances between the different elements of the transistor. This makes it difficult to integrate many transistors in a small space. In SOI, the transistors are naturally independent. No current paths will be created among the different transistors. All of this is due to the SiO2 layer (vertical isolation) and to the STI (Shallow Trench Isolation) technique that isolates transistor horizontally from its neighbors. [19]

- Lower Parasitic Capacitances → Higher Frequency of Operation

Capacitances between the different regions of the transistor will always exist. As seen in Figure **23**, these capacitances in SOI have a different dielectric material giving a different response due to the lower permittivity of the Si02 (ε_r=4) compared to that of Si (ε_r=11.9).

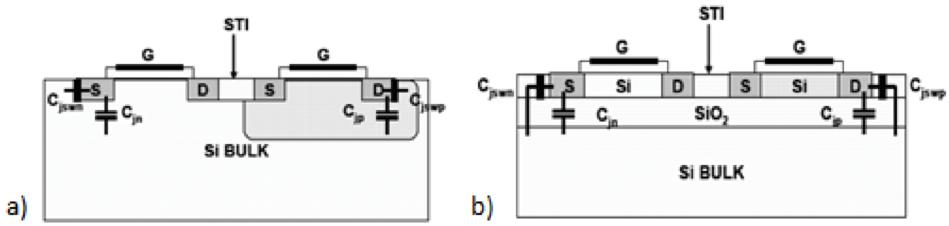

Figure 23 Parasitique Capacitances Si Bulk and SOI [20]

The value of these capacitances is related to the maximum frequency of operation of the device. The limit of the frequency of operation is tied up to these parasitic capacitances and can be described by the f_T (transition frequency) and f_{max} (maximum frequency) frequencies:

f_T → frequency at which the current gain of the transistor is equal to 0dB.

f_{max} → frequency at which the power gain of the transistor is equal to 0 dB.

The frequency f_T is inversely proportional to the gate source and gate drain capacitances and f_{max} will be inversely proportional to the square root of the same capacitances. [20]

- High Resistivity Silicon → Digital and Analog Integration

-**Generic** Transmission Chain and Front End location

On classical bulk CMOS, the substrate resistivity is typically in the order of 12 Ω/cm. This is due to a high doping strategy to prevent the latch-up effect. Due to the inherent protection against this phenomenon related to the SOI configuration, less doped substrates can be used and thus, a higher resistivity can be achieved (3kΩ/cm). This allows the integration of digital and analog components in the same die as digital noise that can couple to analog devices becomes negligible. [19]

There are also some drawbacks that limit the performance of SOI-based transistors. They are briefly mentioned below.

Auto heating: due to the isolation effect of $Si0_2$ that leaves no path to the heat to be dissipated by the substrate

Feed Noise: Since the capacitances that limit the operating frequency are now smaller, noise that could appear from the energy feed is less filtered.

Bipolar Transistor Effect: a parasitic bipolar transistor exists in the design of any circuit, for example, an inverter. It creates a high parasitic source current. The inconvenient is that on SOI the threshold voltage to activate this transistor is lower than that in the CMOS in the circuit.

Capacitive Coupling: due to the isolation given by the $Si0_2$ layer, a greater capacitive coupling exists between interconnections and/or metallic elements.

Kink Effect: At low frequencies, an excess of current can be seen in the I_{ds} / V_{ds} graph due to the accumulation of charges in the transistor. [20]

3.c) Passive Devices: Transmission Lines, Inductors and Capacitors

Before giving the description of passive devices, the description of the technology should be done to locate the different elements on the semiconductor substrate. For the SOI case (ST Microelectronics technology), the technology has a 7-metal layer deposition process on top of the SOI wafer mentioned before. Levels M1 to M6 made of copper and AP a top aluminum layer. The different metal layers are connected with vias. As no empty spaces can be left and due to mechanical constraints, a layer of Silicon Oxide is introduced between the metal and vias from M1 to M6 layers. At last, a passivation layer is deposited surrounding

the AP layer. The stack-up of the different layers, or back end of line (BEOL), can be seen in Figure 24. Metal deposition may be different concerning their layer thicknesses. A detailed illustration is shown in b), where it is clear that the M6 and AP are much thicker than the other layers.

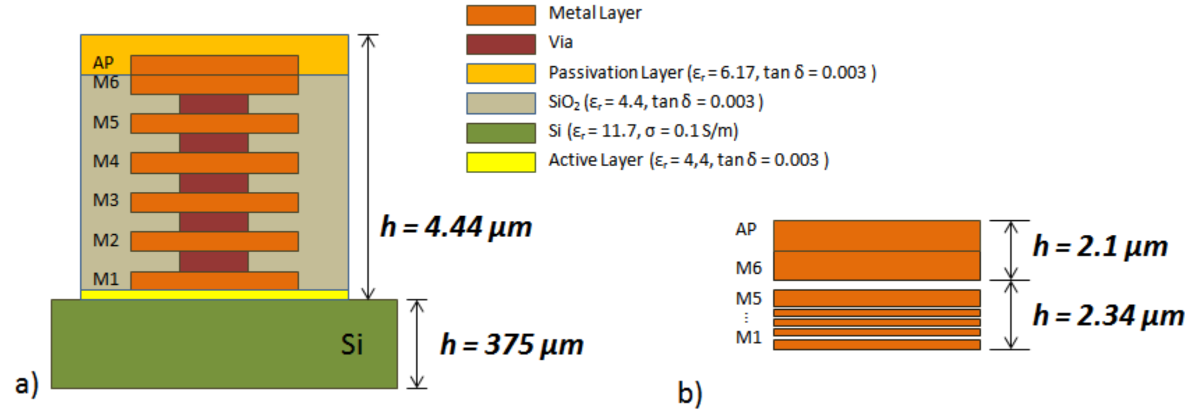

Figure 24 a) Metallization for the 65 nm SOI technology b) Real thickness values for Metal Layers

3.c.i) Transmission lines:

An example of a transmission line (TL) and a capacitor is seen highlighted in Figure 25. As we can see from the schematic, there are several transmission lines used for the realization of the PA, as well as for the capacitors. This is usually the case where the passive elements constitute most of the die area. Due to their high number, some global performance improvement should be obtained if the performance of passive elements is also improved. Passive devices are essential as they allow us to interconnect different elements that constitute the transmitter. And that is the case of SOI based passives (TL's, inductors and capacitors), that will take advantage of the high resistivity of the substrate.

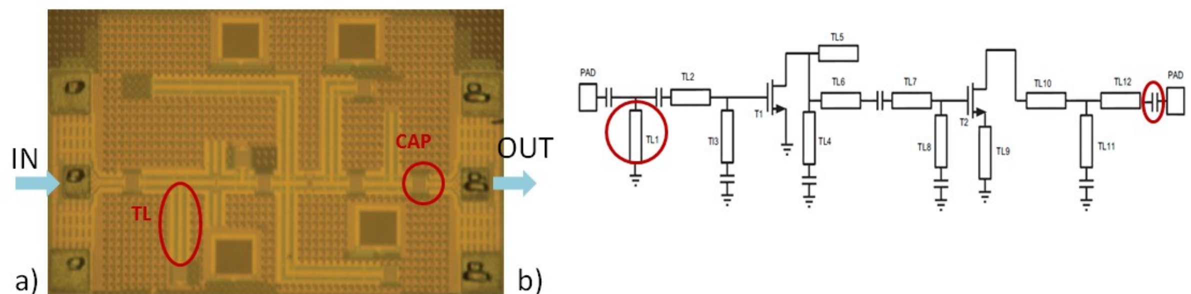

Figure 25 a) Photograph of PA (Transmission Line and Capacitor highlighted) b) Schematic of PA [13]

-**Generic** Transmission Chain and Front End location

Typical TL configurations found for 60-GHz transmitters are depicted in Figure 26. Each configuration has its own loss and impedance characteristics, depending on the dimensions of their components like substrate height and metal or gap strip width. Also, different modes can be established for each of the transmission line schemes considered. That is, different distributions of the electric and magnetic fields can be found. (e.g. CPW TEM Mode in Figure 27). Each of the modes presents different characteristic impedance and attenuation constant; the later will be explained further as it will become the key difference between SOI and bulk substrates for transmission lines.

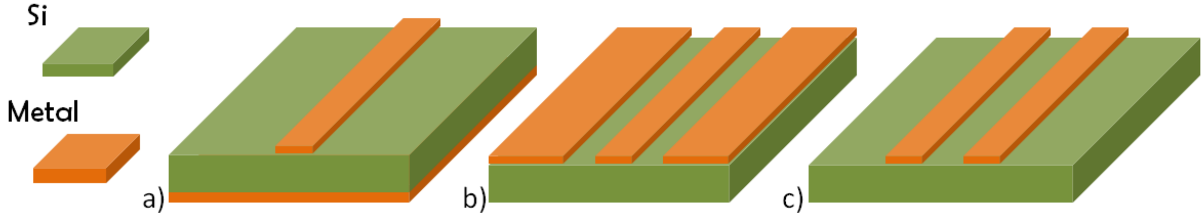

Figure 26 Transmission Line configurations a) Microstrip b) Coplanar Waveguide (CPW) and c) Coplanar Stripline (CPS)

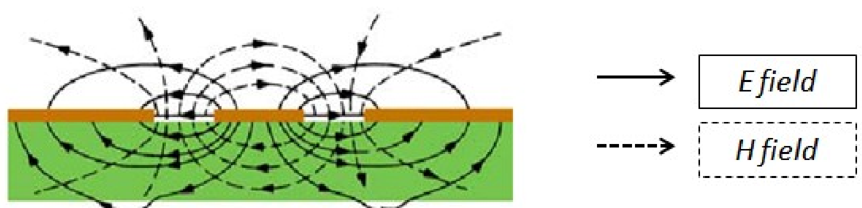

Figure 27 TEM Mode of a CPW line (transversal view) [21]

As mentioned before for SOI, the silicon resistivity is higher than that of the bulk case. This will play a vital role when losses added to a circuit, due to the presence of transmission lines, are calculated. This is one of the criteria for quantifying the performance of a transmission line.

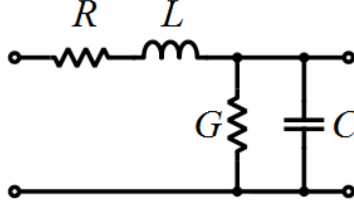

Figure 28 Transmission Line Lumped Model

A loss study of this type of elements through the use of the TL lumped model can be a fairly good way to evaluate their properties and the importance of the substrate resistivity. The following model of the transmission line (Figure 28) has proven to give a really good physical insight of the type of losses, to locate their source and describe their nature. Note that the model components R, L, G and Z are in fact infinitesimal linear components R'*dz*, L'*dz*, G'*dz* and C'*dz*.

There are two kinds of losses that can be found in a transmission line: conductor losses related to *R*, and dielectric losses related to *G*.

Conductor Losses *(R)*: These losses concern the heat generated in the metal conductors due to the existence of electrical current. The electrons in motion that generate the current will not always find a clear path to travel, crashing into atoms and other electrons transforming the electromagnetic energy into unusable heat. In the case of alternating current, the region in the conductors where the current exists (its volume distribution) depends on the frequency and this lossy phenomenon that increases with frequency is known as the skin effect.

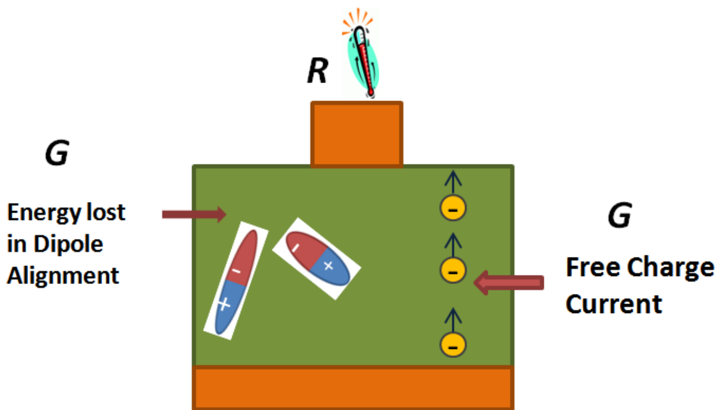

Figure 29 Different phenomena that contribute to the total loss in a MS Line.

Dielectric Losses *(G)*: Dielectrics are materials that can be polarized by the presence of an electrical field. Two kinds of charges will react to the presence of the electrical field: bound and free charges. These two charges are considered in the Maxwell's curl equation for the magnetic field intensity H:

$$\nabla \times H = j\omega\varepsilon\overline{E} + J \qquad Eq.\ 9$$

where (E) is the electrical field and (J) the free-charge volume current density. The permittivity (ε) is related to the bound charges and J to the free charges. When a dielectric is polarized, the bound charges will tend to align their dipole moment with that of the external field applied. The alignment process is not a "clean" process. Energy will be lost when neighboring charges try to align and bump with each other. In the case of the free charges, they will generate a useless current inside the dielectric. To consider the bounding charge effect, the permittivity is defined as a complex variable and the J define in terms of the electrical field.

$$\boldsymbol{\varepsilon = \varepsilon' - j\varepsilon''} \qquad \textit{Eq. 10}$$

$$\boldsymbol{\bar{J} = \sigma\bar{E}} \qquad \textit{Eq. 11}$$

By considering the curl equation and replacing all the above variables yields:

$$\boldsymbol{\nabla \times H = j\omega\left(\varepsilon' - j\varepsilon'' - j\frac{\sigma}{\omega}\right)\bar{E}} \qquad \textit{Eq. 12}$$

With this new equation, the tangent loss factor can now be introduced. It relates the real and imaginary parts of the permittivity including the conductivity factor. [22]

$$\boldsymbol{\tan\delta = \frac{\omega\varepsilon'' + \sigma}{\omega\varepsilon'}} \qquad \textit{Eq. 13}$$

To quantify these losses, the case of a 50 Ω CPW is considered. The attenuation regarding the resistivity (inversely proportional to the conductivity) of the substrate is plotted in Figure 30. Clearly, as the resistivity of the substrate increases, the attenuation constant increases as well. That is, the energy lost to the substrate is reduced when a line is implemented in high resistivity substrates (SOI) as compared to low resistivity substrates (Si bulk). A difference of 3dB/mm can be expected when using SOI instead of Si bulk for a SOI CPW line.

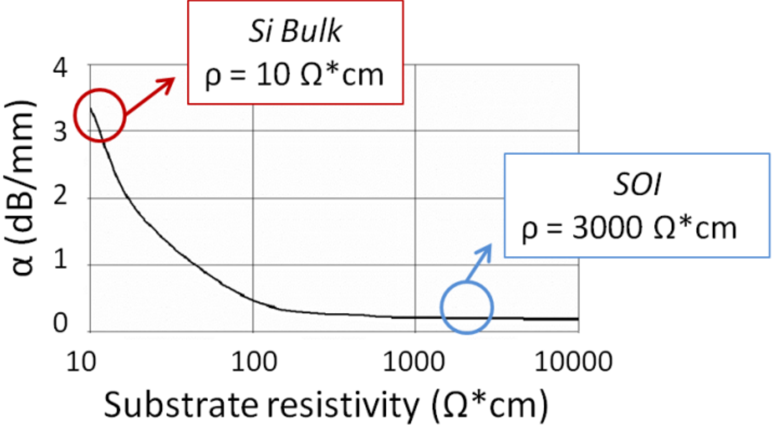

Figure 30 Attenuation constant for a CPW @ 50 GHz [21]

3.c.ii) Inductances and Capacitors

Inductances also benefit from high resistivity substrates. One way of characterizing inductances is by their Q factor. This factor expresses a relation between the energy an element can store and the energy lost during the storage. The energy loss for the inductors, as in the case of transmission lines, depends mainly on the losses of the substrate (G for the case of the TL seen before). As explained before, the substrate losses decrease with a higher resistivity substrate for G which explains the higher Q of the inductor. Another positive characteristic is the reduced size of the inductor that can be obtained in SOI. One way of reducing losses for Bulk is to avoid the use of the metal layers closer to the substrate; that is to use for example only layers 6 and AP. If this technique is no longer necessary, several stacked layers can be used to form the inductor. In this way, for the same electric path, a smaller region is needed in a multilayer strategy. Q improvement and size reduction can be seen in Figure 31.

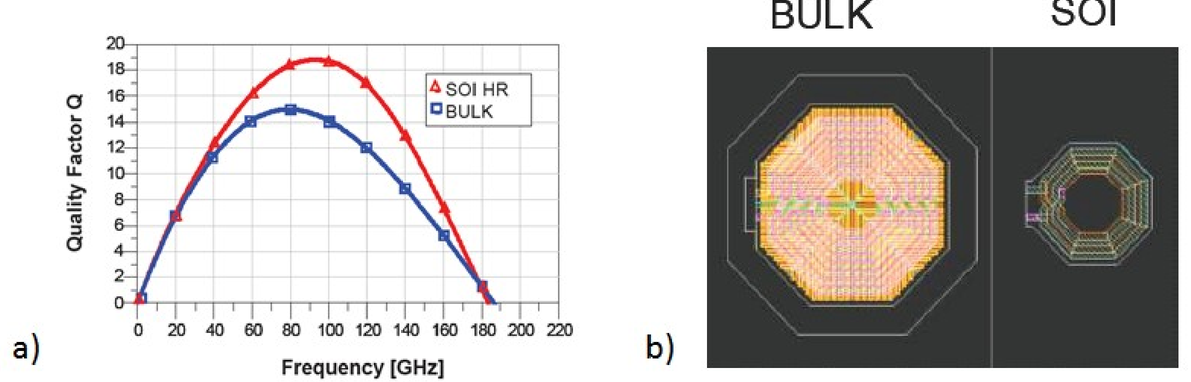

Figure 31 a) Q factors for SOI and Bulk and b) Size Comparison of Inductor for a given Q [19]

For the case of capacitors, the possibility of using all the layers is also beneficial. A size reduction due to the higher integrated density is achievable. A MOM (Metal-Oxide-Metal) capacitor, which is made from inter-digitated elements, achieves a higher capacitance for a smaller area on SOI in comparison with its similar on Bulk (30% decrease in size [23]).

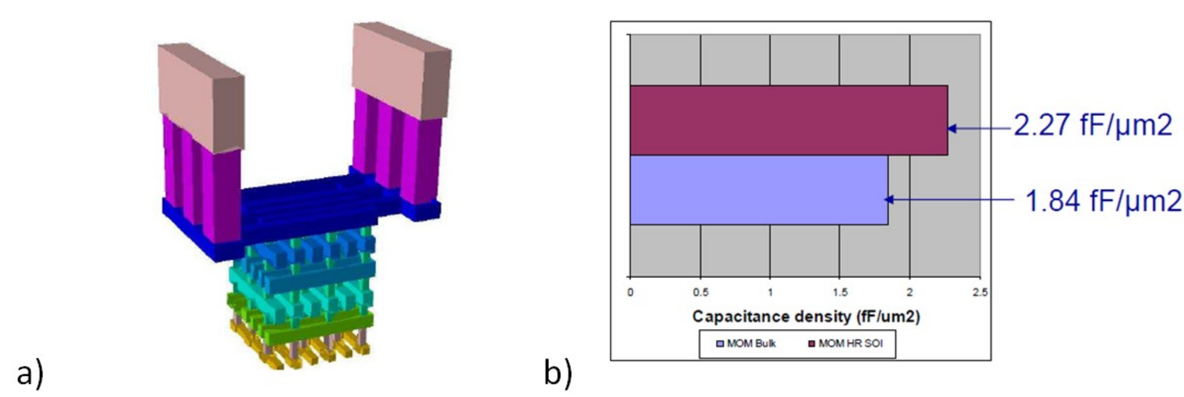

Figure 32 a) Integrated SOI MOM capacitor b) Bulk and SOI capacitance/size comparison

4) Power Amplifiers

After taking a look at the different elements that constitute a transmission front-end (VCO, Mixer, PA and Antenna) and the discrete elements that they are made with, we now enter more in detail into those that concern us the most: the PA and Antenna. First of all, we will take a look at this last active device of the front-end (in most cases) of the TX chain, the PA.

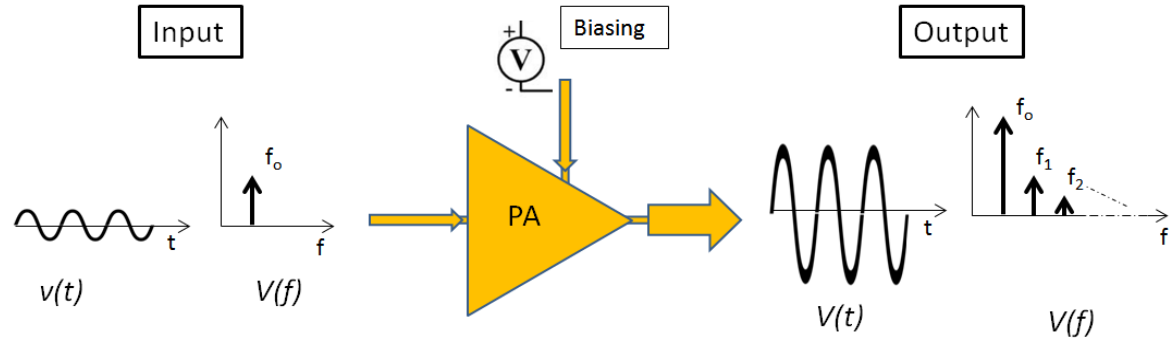

Figure 33 PA's Input and output signals in a PA (time and frequency domain)

4.a) PA distortion sources

The power amplifier has the task of inserting energy to the modulated signal. In Figure 33, the PA takes the energy from a biasing source and adds it to the input signal to obtain an amplified output signal. But along with power amplification, a distortion of the input signal is also witnessed in most of PA configurations. This distortion produces higher frequency harmonics due to the nonlinear characteristic relating amplifier input and output. When trying to model this non ideal amplification response, a good start is to separate the different harmonics contained in the output signal by introducing a nonlinear relationship with second and third order terms. The graphical representation of these non linear responses can be seen in Figure 34. Starting from the ideal response, in which the same amplification level is maintained throughout the whole voltage variation of the input, we pass to a second and third order response. These, now will change the shape of the input signal (as in d), where the input and output of a third order amplification response is shown. A clear cut to the sine wave is evident and this translates to third order harmonic generation. If we add both, the second and third term, a frequency response containing the second and third harmonics could be expected. In [24], ideal voltage and current signals are compared to cases where the second and third harmonics, respectively, have been tuned (have been eliminated). We can see how the discrepancy in the current case (red line) between both signals is more evident, compared to that of the blue line.

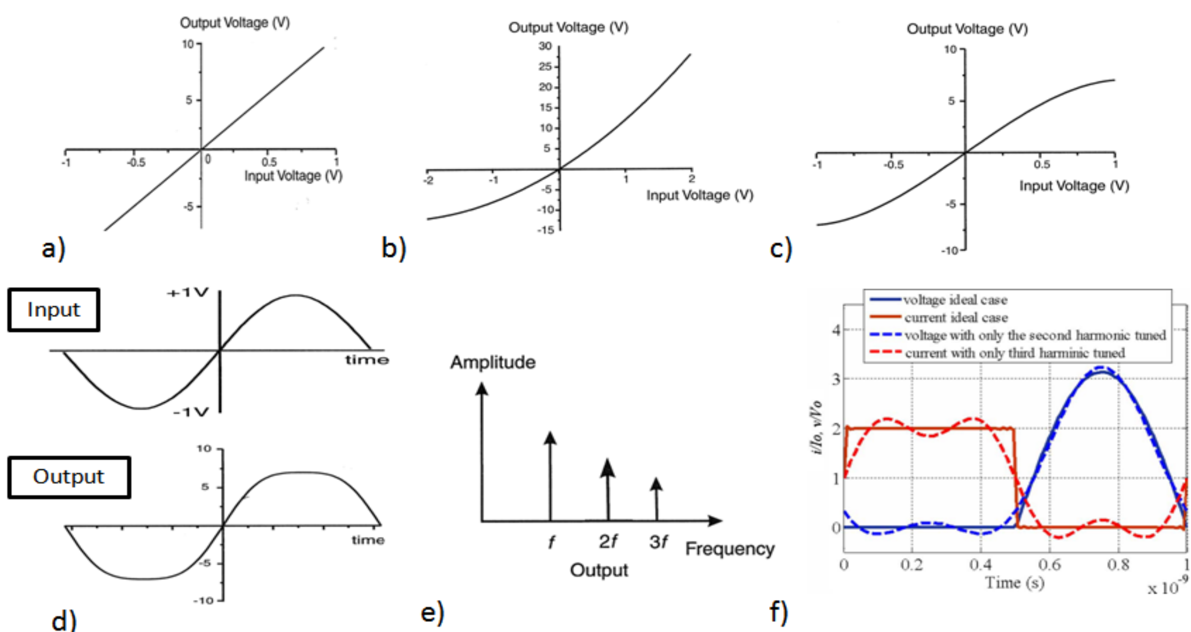

Figure 34 PA Amplification curve a) Ideal b) Second order term added c) Third order term added (without second term) d) Input and Output response for a third term response e) Higher order harmonics f) Second and third harmonic tuning [24].

This is the common case, where the second harmonic has much more energy compared to the third harmonic, thus, having a greater impact in the output response. This can also be seen in the frequency response in Figure 34 e).

Another source of harmonic generation results from the finite biasing of the amplifier; this is called clipping. When the amplifier reaches its maximum level of amplification, that is, when the input signal level is such that the amplifier cannot amplify it further, the maximum values of the amplified signal are cut (or clipped) at these high voltage values. This result in an output similar to that of Figure 34 d and can also be seen in Figure 35. The clipping effect also generates, much in the same way, high order harmonics.

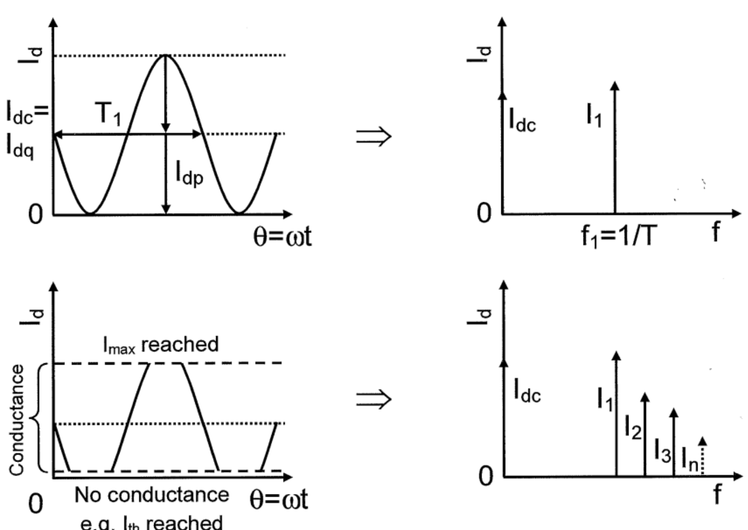

Figure 35 Clipping of a signal and harmonic generation [25]

4.a.i) How to measure the performance of a PA?

The efficiency of a PA is an important parameter. It indicates how much power spent in the amplification process is really delivered to the signal. Typically, the efficiency (η) defined in Eq. 13 or the Power Added Efficiency (PAE) defined by Eq. 14 are employed to measure the efficiency of the PA. The PAE is the ratio of the output radio frequency power (only including fundamental frequency power) minus the input radio frequency power by the power delivered by the biasing DC source.

$$\eta = \frac{P_{RFout}}{P_{DCin}} \qquad \textit{Eq. 14}$$

$$PAE = \frac{P_{RFout} - P_{RFin}}{P_{DCin}} \qquad \textit{Eq. 15}$$

4.a.ii) PA Topologies

Given this PA characteristics, different topologies exist. Also, different ways of treating the input signal for its amplification, lead to different efficiency and linearity values. PA classification can be done by their linearity and efficiency performance. First of all, we have classes A, B, AB and C, which depend on the conduction angle, i.e., how much of the 2π sine wave period the transistor amplifies.

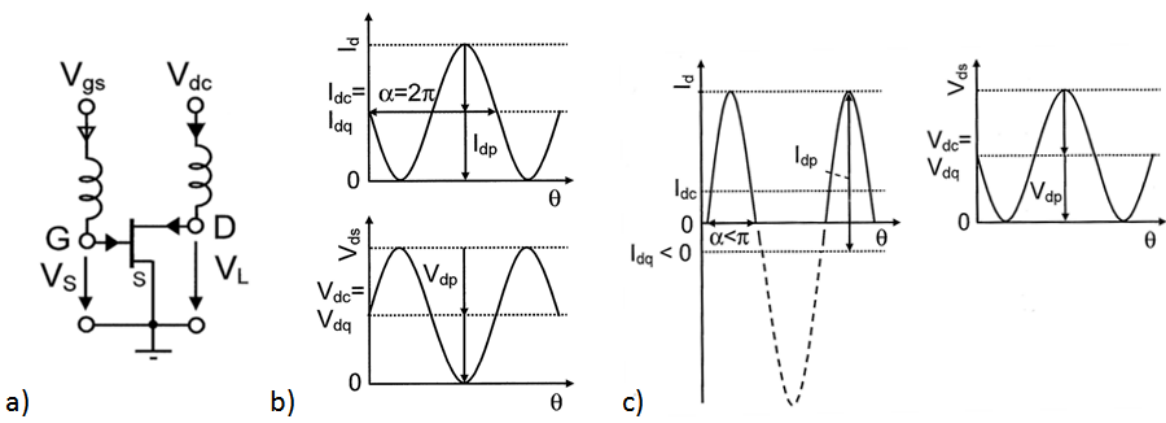

Figure 36 a) Common source biased transistor, b) Class A amplification scheme and c) Class C amplification scheme [25]

For the class A response, as seen in Figure 36 b), the current flows during the whole period of the signal. As a result, the transistor (Figure 36 a) is always in the ON state. This leads to a current passing through the transistor and directly going into ground; this means that some energy will not be recuperated. For this kind of configuration, 50 % efficiency is expected. Although a low efficiency is obtained, there are many applications for this kind of configuration due to a 100% linearity response. A common strategy to increase the efficiency is based on changing the biasing level for the current response setting the transistor in OFF state for part of the cycle. In this way, no current will flow unnecessarily through the transistor. This is the case for the B, AB and C classes. An example is shown in Figure 36, where the voltage and current curves for a C class amplification scheme are depicted. A conduction angle (α) of less than π is used, setting the transistor to OFF state for more than half the cycle, improving the efficiency. But as we can see in Figure 37, the reduction of the conduction angle has some drawback, as the linearity of the PA is compromised due to the extra clipping of the signal. The generation of harmonics is amplified and as α moves towards 0°, energy delivered to the fundamental and higher order harmonics reaches the same level. This shows one of the constraints of PA design where high efficiency leads to low linearity and vice versa.

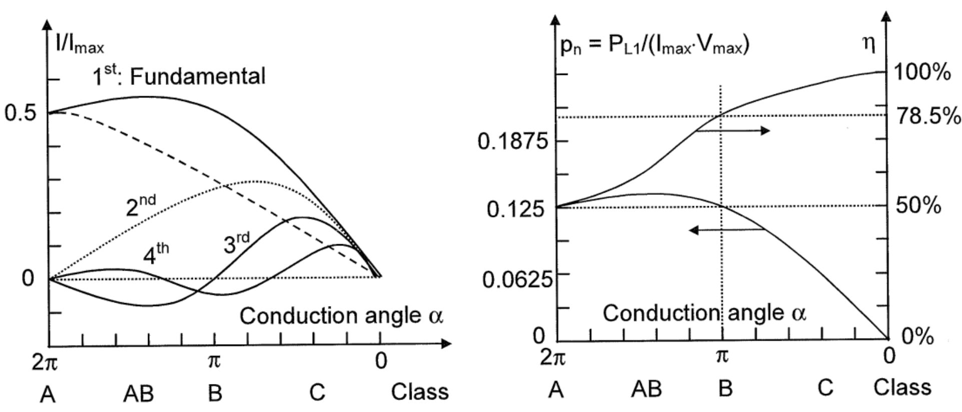

Figure 37 Linearity and Efficiency by class [25]

Other configurations exist, where the transistor is switching between ON and OFF state. That is, either the current through the transistor or the voltage between drain and source is zero. In this way, a theoretical 100% efficiency should be achieved. Of course, this cannot be achieved because of the delay in the commutation. Between the OFF and ON regions (Figure 38 a), the transistor passes through the whole working state and thus consumes power. Output waveforms of the current and voltage can be seen in Figure 38 b). This is a typical output seen in switching amplifiers. To obtain a sinusoidal signal, a filter stage is needed at the output where, depending on the configuration, voltage or current sinusoidal signals are obtained. This is the operating strategy of classes E, D and F; where a much higher efficiency is obtained as compared to non-switched classes. Other configurations such as the Doherty's or Khan's are obtained from these switching classes where the linearity is improved while maintaining a high efficiency. We will not enter into details of these classes. A comparison between all amplification classes can be seen in Figure 38 c) regarding their linearity and efficiency.

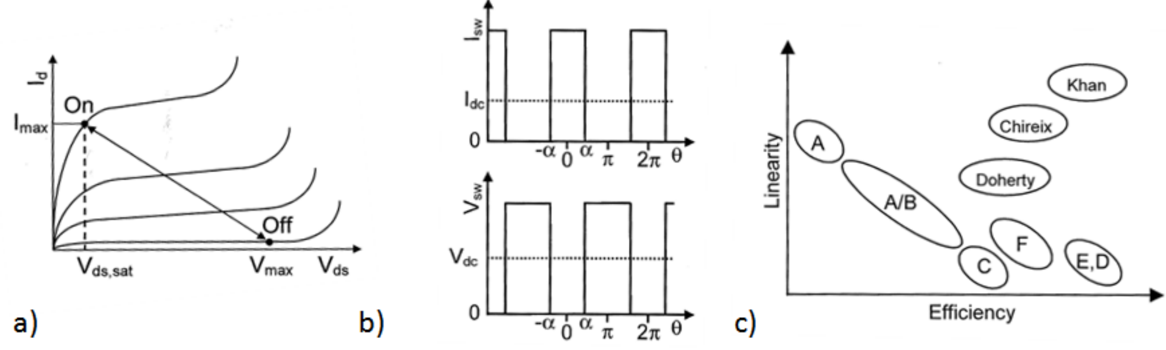

Figure 38 a) ON and OFF Transistor regions, b) Output current and voltage waveforms c) Classification of PA by linearity and efficiency [25]

4.b) Typical PA amplification curve

But what are the consequences of these high order harmonics? We can see them in the amplifier gain curve in Figure 39. The ideal amplification path that a PA should follow is outlined by the pink trace that corresponds to a slope of the same value as the gain of the PA. As the input power increases, the same amplification ratio should exist and thus, a straight line will relate the input and the output power. A constant gain level is then achieved. But this is the case for only a small portion of the PA amplification curve, the actual operating characteristic of the PA follows the purple curve. The constant gain response is no longer obtained and the gain of the PA starts to decrease. This is called gain compression (clipping region). As the gain of the amplifier starts to drop, it will soon reach values 1 or 2 dB below the max gain value, points at which the PA has its P1dB or P2dB compression points. This is another operation parameter of the PA. In the figure, P1dB is found to be at 5W, where a gain of 12-dB instead of the 13-dB gain is obtained. The linearity of the PA will be measured with help of the P1dB and P2dB points extracted from the Gain curve. So, as we increase the input signal level, a lower gain is achieved for the signal at the frequency of interest. That is, more energy is delivered to the higher order harmonics and less to that of the fundamental frequency.

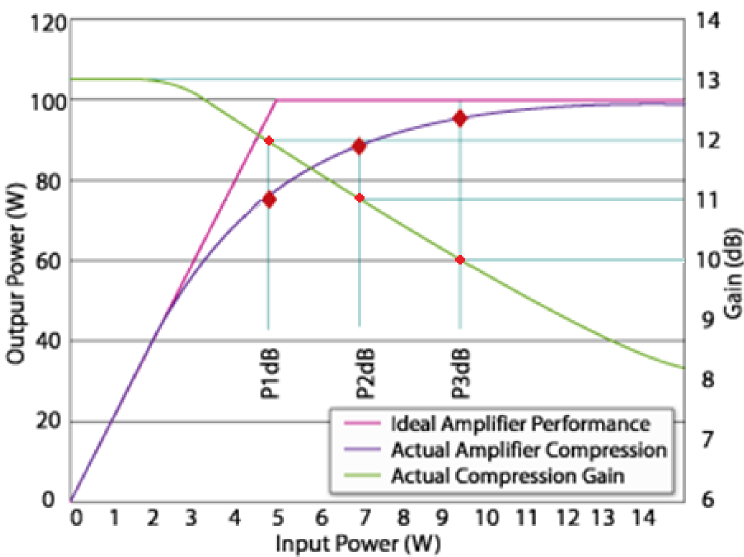

Figure 39 Typical PA response (Input Power vs Output Power and Gain)

4.c) PA Stages

Typically, more than one amplification stage is used for a power amplifier. They are typically divided into two types: driver and power stages. Driver stages are found at the beginning of the amplification chain and the power stage at the end as seen in Figure 40. The driver stage is generally design for gain, that is, it increases the voltage level of the signal. The power stage will add power to these signal, thus an increase in current appears. As seen, inter-staged elements are also included in the PA input-output chain. These are matching passive elements, necessary to match the impedance at every stage. This impedance matching is very important as it allows the maximum power transfer. Without these elements, some energy returns back to the source due to impedance mismatch.

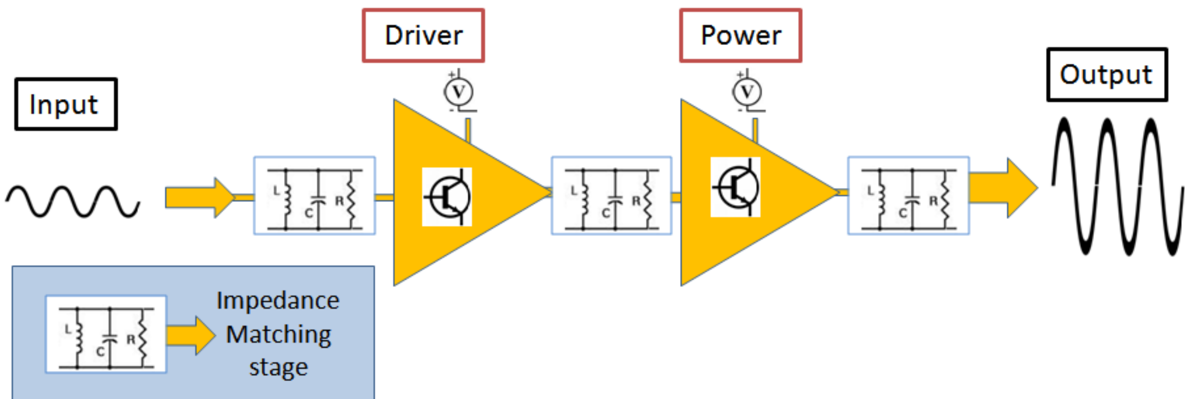

Figure 40 Stages of a Power Amplifier

4.c.i) PA impedance matching stages

Since we are concerned with the matching stages, exactly with the output stages of the PA, some examples are given next. In the example depicted in Figure 41, the driver stage is used as gain control and impedance match between the driver and power stage is achieved using planar inductors. The inductors in this case are used to compensate the high capacitance value seen at the input of the power stage. An output stage is also seen where low input impedance is matched to the 50 Ω output impedance. Due to the nature of the power stage, (high current output) a low output transistor resistance is expected. According to [26], a value between 10 and 15 Ω allows a maximum power transfer depending on the biasing for the P1dB compression point.

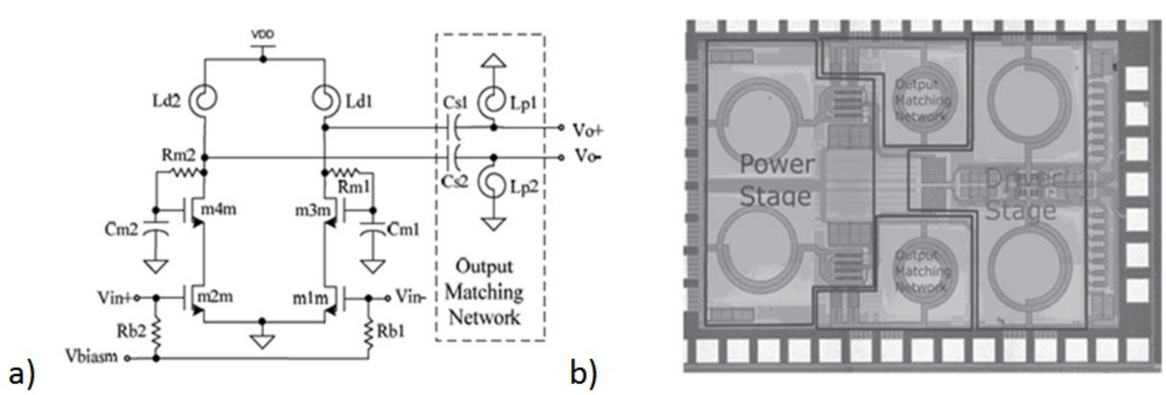

Figure 41 a) Schematic of Power and Output matching stage and b) PA Circuit in CMOS [26]

Switched output matching networks can be also found. They are used to match the PA to the load even under frequency varying conditions; the matching network now has a wide bandwidth behavior. The use of diodes or transistors can be seen Figure 42. The circuit in Figure 42 below, shows that four different impedances can be obtained thanks to both switches. They modify the total capacitance value given by C1 and C4 or by C2 and C3.

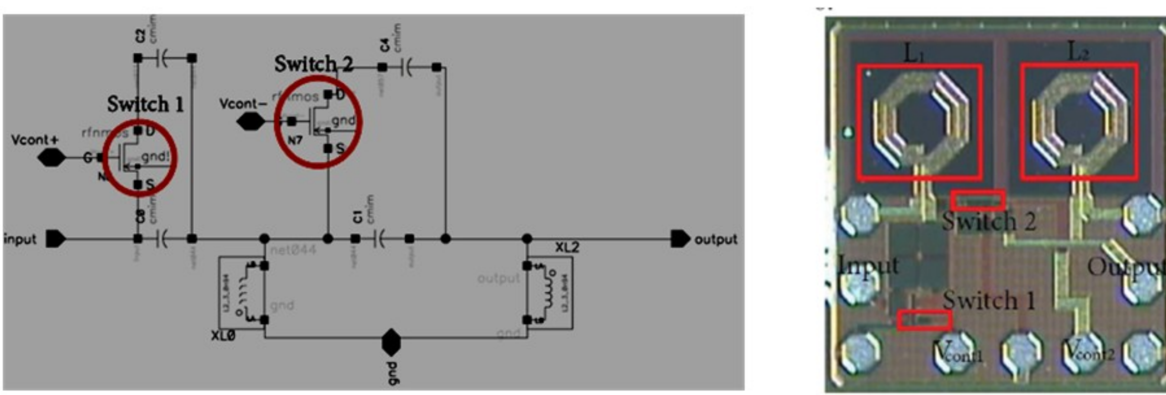

Figure 42 Switched Impedance matching configuration a) Schematic and b) Circuit (0.25µm-SiGe HBT technology) [27]

In [28], the use of transformers eliminates the need for AC coupling capacitors and RF chokes. In addition, differential operation reduces the amount of bypass capacitance needed (Figure 43). Both of these configurations can be seen in figure 32. High reverse isolation between output and input is necessary to mitigate the effects of antenna mismatch, to limit unwanted interference between circuit blocks on-chip and to enhance stability [29].

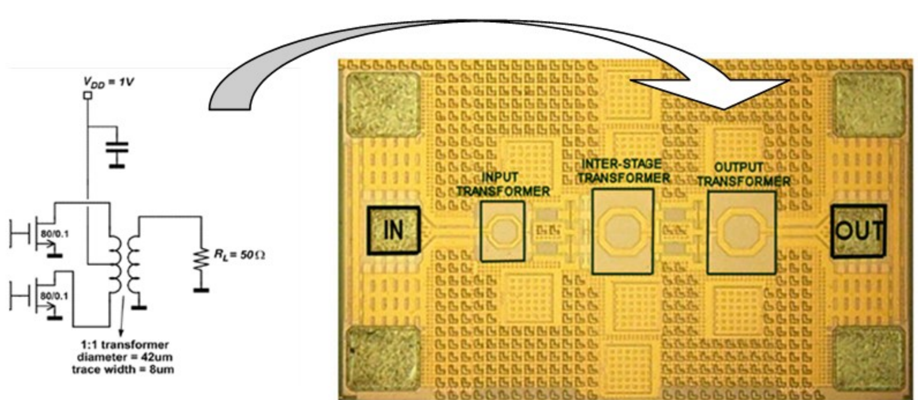

Figure 43 Transformers as matching stages a) Schematic and b) circuit [28]

In [30], all matching networks have been realized using coplanar waveguide transmission lines with 51-Ω characteristic impedance and length varying between λ/20 to λ/6. Bypass and coupling caps are custom-designed finger capacitors. Together with input and output pads, they were modeled and incorporated as part of the matching networks. The output transistor is also degenerated through a small transmission line to add a degree of freedom in the stability-power gain trade-off. To obtain higher power in this design, the output matching network converts the load to a lower impedance of 15 Ω using a transmission line matching network (Figure 44).

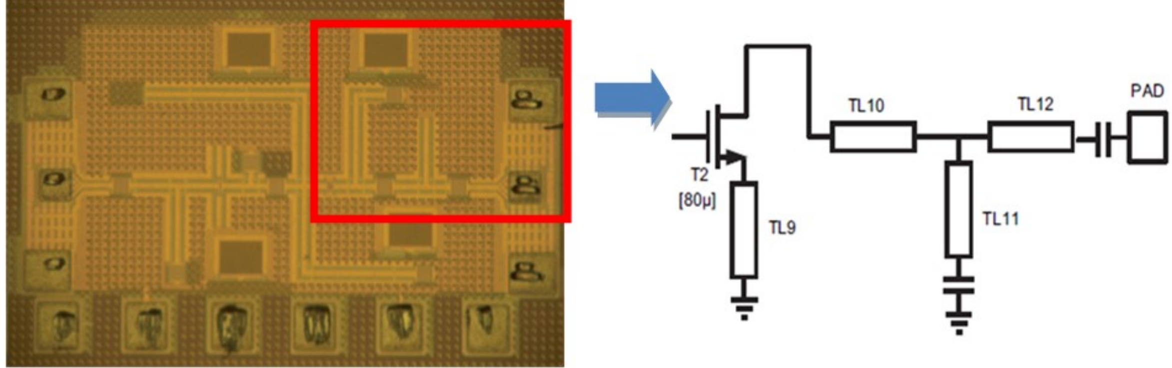

Figure 44 Transmission lines used as impedance matching network a) circuit and b) schematic. [31]

4.d) PA State of the Art

Next, a state of the art for 60-GHz Power Amplifiers in CMOS is shown (Table 2). Some performance values are shown for some PA's like their PAE, power dissipation and supply

voltage. This will help us to narrow down some characteristic values for 60-GHz power amplifiers.

Ref.	Technology	Year	Stages - Class	Power Gain (dB)	Supply (V)	Dissipation Power (mW)	$P_{1\,dB}$	PAE (%)	Sat. Output Power (dBm)	Output Impedance	Size mm^2
[31]	CMOS 90nm	2007	2	9,8	1	23	6,7	20	N/A	15	N/A
[32]	CMOS 90nm	2008	3	17	N/A	54	5,1	6	8,4	N/A	0,99
[32]	CMOS 90nm	2008	3	17	N/A	30	2	5	4	N/A	2,6
[33]	CMOS 45nm	2009	3 - AB	13	1,2	7,8	N/A	16	6,1	50	0,21
[33]	CMOS 45nm	2009	3 - AB	18	1,2	14,4	N/A	19	7,9	50	0,21
[34]	CMOS 90nm	2009	5 - A	9,6	1,2	183	5	N/A	N/A	100 diff.	N/A
[35]	CMOS 65nm	2008	2	8	0,9	10	N/A	11	N/A	50	0,288
[36]	CMOS 65nm	2009	3	15,4	1	43.5	N/A	11	11,5	N/A	0,053 w/o pads
[37]	CMOS 90nm	2009	3	N/A	1,2	170	N/A	14	N/A	N/A	N/A
[38]	CMOS 90nm	2009	3	10	1	213	8,8	7	12,2	N/A	0,64
[28]	CMOS 90nm	2008	2	5,6	1	N/A	9,7	9	12,3	50	0,25
[39]	0,16um SiGe	2006	1 - B	18	4	248	13,1	13	20	N/A	0,975
[40]	CMOS 65nm	2008	2	8	0,9	64	8,9	11	13	50	0,228
[41]	65nm SOI	2009	2	16	1,8	77	12,7	25	14,5	50	0,57
[41]	65nm SOI	2009	2 – A,AB	14	1,2	22	7,1	22	10,5	50	0,57
[42]	CMOS 90nm	2007	3	25	1,5	109	5	7	8	50	1,13
[43]	CMOS 90nm	2008	4	N/A	1,2	228	8,2	N/A	10,6	50	N/A
[44]	CMOS 90nm	2008	3	13,3	1	N/A	10,5	7	8,4	N/A	1,5
[45]	CMOS 90nm	2009	3 - A	30	1,8	188	10,3	13	13,8	N/A	0,33
[45]	CMOS 90nm	2009	3 - A	32,4	3	405	12	15	18	N/A	0,33

Table 2 PA References and Performances

From all of these topologies and the state of the art we can make several conclusions:

- Due to the high current expected at the output, low output impedance seems to be the trend for the power stage. For the only reference found that did not include an output matching stages, a 15 Ω output impedance was obtained. A common output impedance matching stage for a final 50 Ω is thus seen for all the other cases.
- Coplanar configurations are preferred. Either differential or common mode topologies are commonly found. This is expected, due to the metallization configuration of the technology.
- Complete PA designs tend to occupy an area less than 1 mm^2 (includes RF and Biasing Pads)
- Maximum saturated output power as high as 18 dBm has been obtained. Due to output power limits (13.1 dBm max according to the regulation of the 60-GHz band), improving PA configurations focuses rather on efficiency and linearity issues.
- Typically, 2 and 3 amplifying stages are found which imply 3 and 4 impedance matching stages. As a result, losses in passive circuits contribute the PAE. Comparing this parameter between CMOS bulk and SOI, a considerable increase in efficiency is obtained, almost 10%.

5) Antenna in the 60 GHz band

After the output matching stage of the PA, the antenna element is found. Due to the operating frequency, which leads to a wavelength of 0.5 cm, antenna is reduced 25 times in size for example in comparison to a λ/2 dipole at the WiFi standard (2.4 GHz). A λ/2 dipole will now measure 0.25 cm instead of 6.2 cm. Due to this size reduction, antenna and PA are now size compatible (PA ≈ $1mm^2$), i.e., antenna implementation in the substrate is now feasible. Moreover, by taking into account the substrate permittivity (11.7 for silicon), the size of the antenna reduces by a factor related to the square root of the permittivity. Due to the metal configuration of the technology, planar antenna configurations are compatible and its integration is somewhat simple. The antenna, the same way as for the PA, needs in most cases a matching stage due to its typical high value input impedance. Frequently, λ/4 transformers and stubs can be found in configurations for impedance matching (Figure 45 a,b).

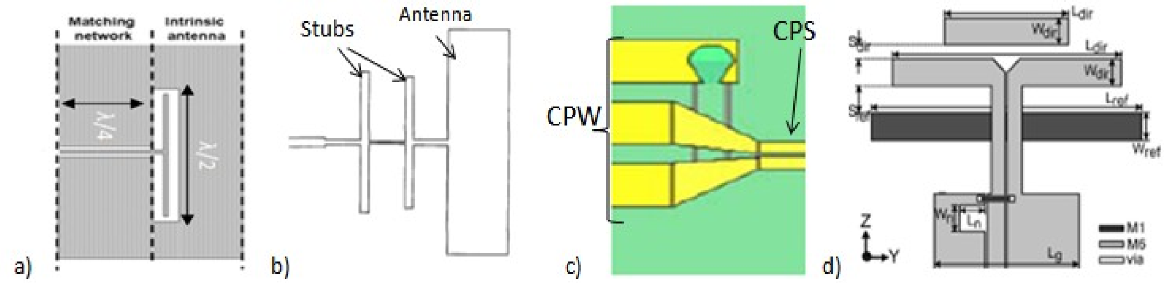

Figure 45 a) and b) Impedance Matching networks ([46] and [47]; c) and d) balun for mode conversion and Yagi with balun ([48] and [49])

The feeding strategy of the antenna is another issue that one has to keep in mind. Not only impedance match has to be ensured, but also the transmission-line mode compatibility has to exist. For coplanar configurations two common dispositions are found as seen before: the CPW and the CPS (Figure 45 c). For a good power transfer, the mode distribution has to be kept when passing from the PA to the Antenna. In some configurations, the antenna has a CPS feed while the PA has a CPW output. Transitions have to be incorporated for a smooth mode transformation. As seen in Figure 45 c) and d), a balun is inserted between the incompatible CPS and CPW lines. All of these elements will play a vital role when integrating

antenna with PA as they have some important impact on bandwidth and size, as well as losses.

From Figure 45c and 34d, another remark can be made by taking a closer look to the antenna and balun configuration: Multilayer metallization has been employed. For the Yagi configuration, the reflector is added at a lower level regarding the feeding and radiating elements. For the balun, an underpass from ground to ground of the CPW line is incorporated using lower metallization layers in both cases. For some antenna configurations, this multilayer availability can be useful.

5.a) Antenna Performance

The antenna performance is evaluated through several parameters such as bandwidth, gain and efficiency, for instance. To give a comprehensive and objective state-of-the-art for antenna performances, a division between PA-antenna integration strategies has to be made. Because of the radiation nature of the antenna, the environment or near surroundings have some strong influence on the antenna operation. As a result, different antenna performances will be obtained when the antenna is incorporated into the Si metallization level or if it remains as a single element interconnected to the PA by external elements. This distinction gives rise to two strategies that exist when interconnecting PA and antenna: the System on Chip (SoC) or System in Package (SiP). Both of them will be studied next as we progress through the antenna state-of-the-art.

5.a.i) System on Chip or SoC

As mentioned before, due to the antenna size and the technology description, antenna and PA could be thought of co-existing on the same substrate. After impedance and mode matching between the output of the PA and the input of the antenna, the design is achieved. No extra stage at factory level is needed and a PA-Antenna operating design is elaborated. Input signal can be injected to the PA input and radiating energy can be obtained from the antenna. But what are the expected performances for On-Chip antennas?

5.a.i.1 On chip Antenna Theoretical Performance

As seen before, the high resistivity of the substrate decreases the losses in passive elements. For on-chip antennas, radiation efficiency should also increase. But we still have to deal with the high permittivity offered by the substrate. We can start by taking a look at some results

- **Antenna** in the 60 GHz band obtained from theoretical analysis and the effect of the substrate permittivity. As an example, a microstrip rectangular patch antenna is investigated.

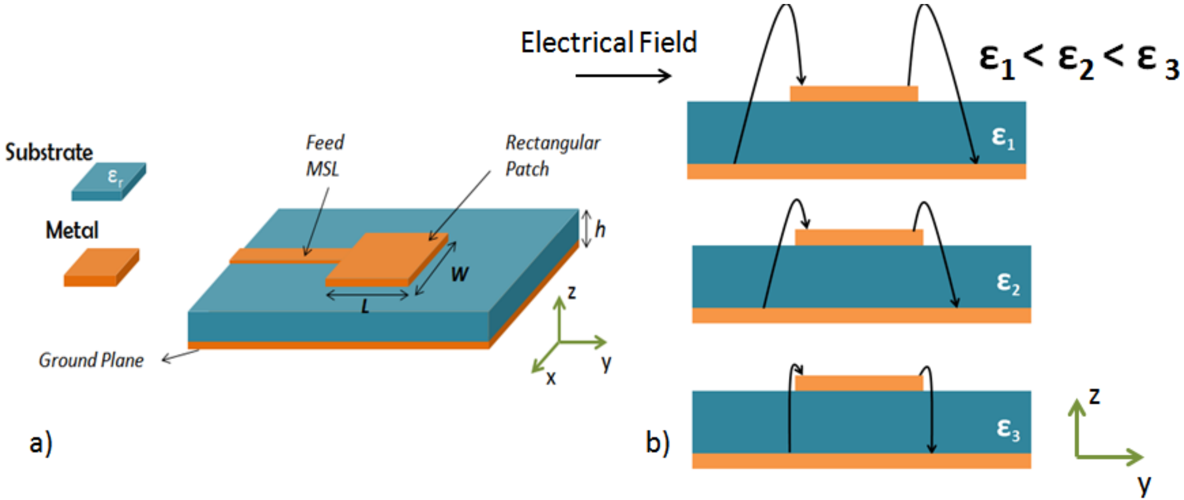

Figure 46 a) Microstrip fed rectangular patch and b) Radiation mechanism of the patch at 3 different permittivities

For a microstrip patch, fringing electrical fields are ideally generated only at two opposite edges of the patch (Figure 46). Generally it will be the edge from where it is fed (MSL in Figure 46 a)) and its opposite edge. The patch can be seen as two-radiating slots fed by fringing fields.

A theoretical study was conducted in [50] and seen in Figure 47, where the radiation efficiency and bandwidth is calculated for different permittivities and substrate thicknesses. It can be concluded that the radiation efficiency increases as the substrate height (h) increases and the substrate permittivity decreases. As h increases and ε_r decreases, a larger amount of energy is concentrated in the patch fringing fields, thus a higher radiation efficiency is obtained as graphically seen in Figure 46 b).

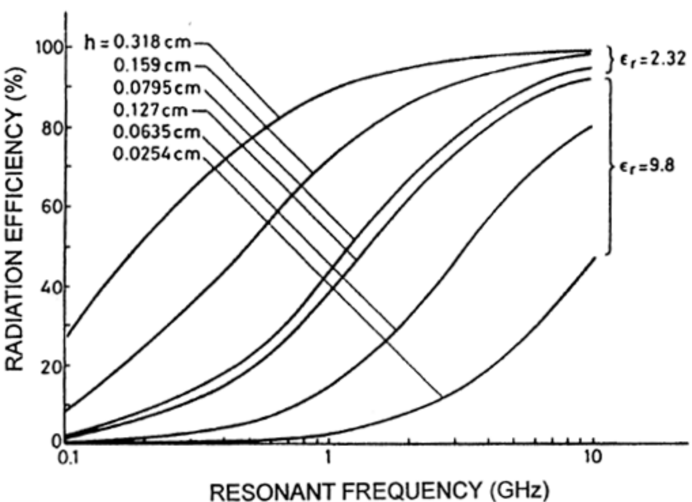

Figure 47 Theoretical radiation efficiency performance for a rectangular patch. Resonating Mode TM_{10} with L = 1.5W, σ = 5.8 x 10^7 S/m, δ = 0.0005. (No substrate wave loss is considered). [50]

The radiation efficiency calculated before was obtained from the quality factor study done for the patch. That is, the patch is seen as two parallel plates that dissipate and store energy. Up until now, the dissipated energy or losses taken into account are dielectric (δ = 0.0005), conductor (σ = 5.8 x 10^7 S/m) and radiated losses. But there is still one more factor to take into account: the surface wave energy. Due to the dielectric presence, modes on the dielectric can be established. The patch will couple to these modes and less energy is devoted to radiation. The radiation efficiency shown in Figure 48 accounts for these surface waves. In fact, only losses coming from radiation and surface waves are used to calculate the efficiency. For example, by assigning a 1 to the substrate permittivity, no surface wave will be generated and 100% efficiency should be obtained. It can also be concluded, that as the dielectric thickness or the permittivity increase the efficiency decreases; higher energy transfer to the surfaces waves is seen. Finally, for an efficient patch design, a compromise between radiation and surface energy has to be made.

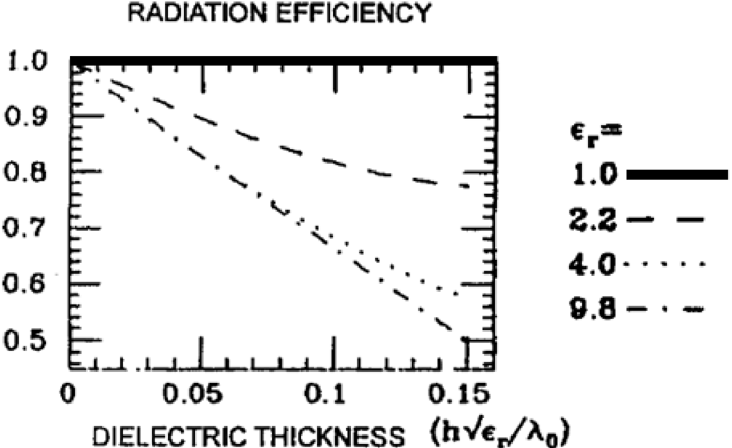

Figure 48 Theoretical radiation efficiency for a Rectangular patch. Permittivity and thickness as free parameters. [50]

To be able to quantify the losses of planar antennas, a literature research has been done and some examples are given next: (Performance of the following examples as well as a more thorough antenna research is given at the end of the section)

5.a.i.2 On Chip Antenna

This first example shows a differentially fed dipole on Silicon, with a lambda/4 impedance transformer and CPW to CPS balun needed for measurement. A gain of -8 dBi is obtained for a 300 µm thick substrate. Figure 49 shows the different samples fabricated for different resistivity substrates as well as calibration and de-embedding structures. These allow eliminating the effect of balun and transformers from the measured data. In this way, the raw data of the antenna structure is obtained.

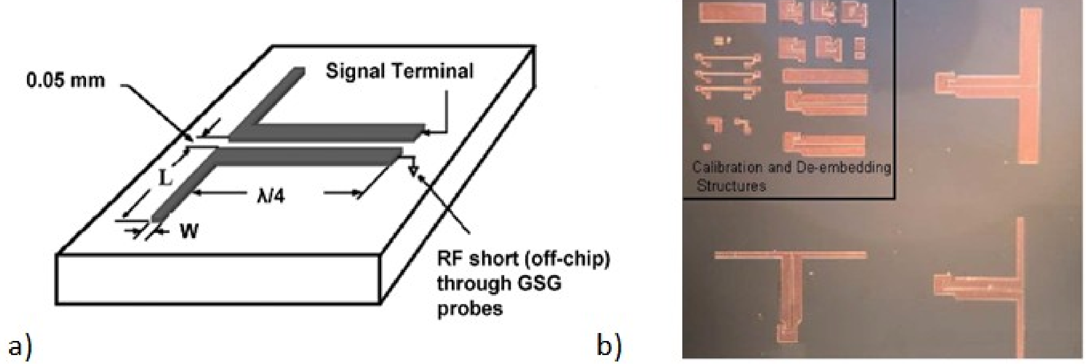

Figure 49 Dipole@ 24GHz a) 3D view b) Top view of fabricated dipoles [51]

Microstrip antennas are also seen, using only the metallic layers from the technology. In this case, metals 1 to 5 are considered as the ground plane while Metal 6 and AP are used for the

- **Antenna** in the 60 GHz band

patch (Layer description similar to SOI description presented in Figure 24). This configuration allows the ground plane to shield the antenna radiation from the substrate. Although, due to the distance of 4um between patch and ground in this microstrip configuration, a low efficiency is obtained with only 22%.

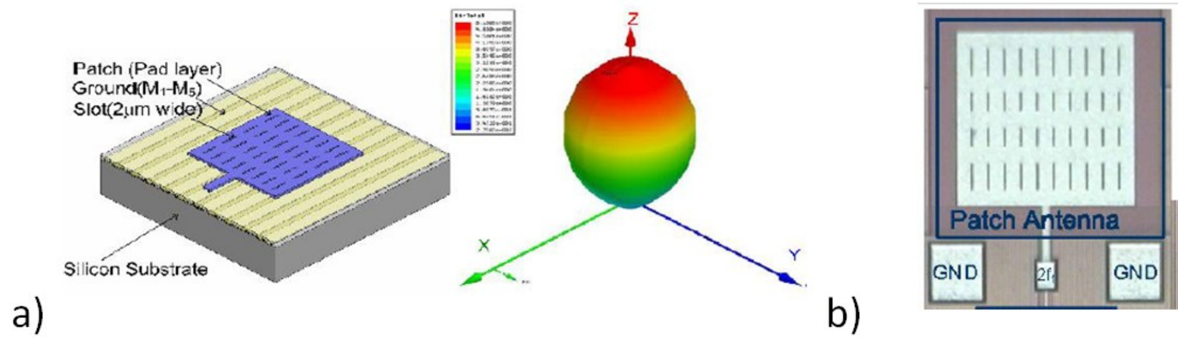

Figure 50 Microstrip Square Patch @ 410GHz a) 3D View b) Fabricated antenna and Measuring Pads [52]

Figure 51 presents an On-chip triangular monopole antenna fabricated with TSMC 0.18-mm CMOS process. The chip size is 1.00 × 0.81 mm^2. Measured gain was -9.4dBi with a low simulated efficiency of -12%. Bandwidth control is possible in this configuration by properly dimensioning the flare angle (α in Figure 52 a). A 15-GHz (S11 <-10dB) bandwidth was measured.

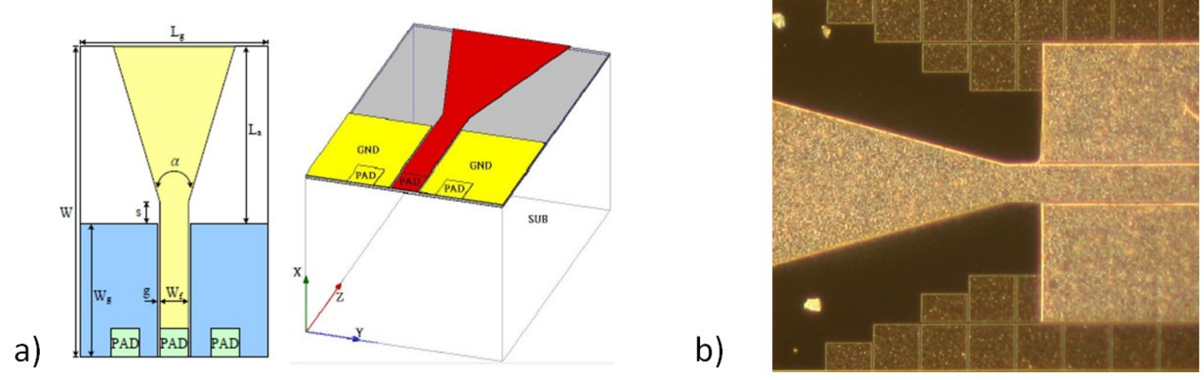

Figure 51 Triangular Monopole a) Top and 3D view b) Top view of fabricated antenna [53]

The fabrication was realized with the back-end-of-line process of silicon substrates with low resistivity 10 cm*Ω. Measurement results show that the inverted-F antenna yields a gain of --19 dBi at 61 GHz, where the maximum matching level is obtained.

- **Antenna** in the 60 GHz band

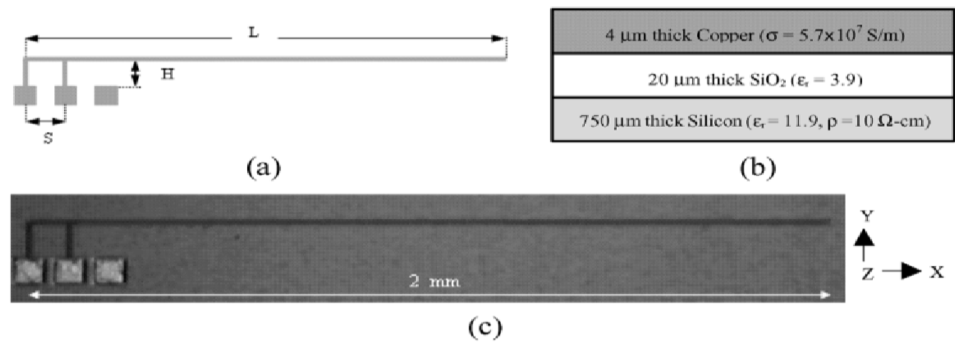

Figure 52 Inverted F antenna a) Layout Top view b) Cross Section Technology description and c) Top view fabricated antenna [54]

An on-chip dipole-based antenna was implemented using WIN 0.15 um pHEMT process. The fabricated antenna has a compact size of 0.9 mm^2, including test pads. The antenna comprises a half-wavelength dipole element and two tilted and slotted dipole elements to realize a wider impedance bandwidth than conventional wire dipole antennas. No efficiency performance is though reported.

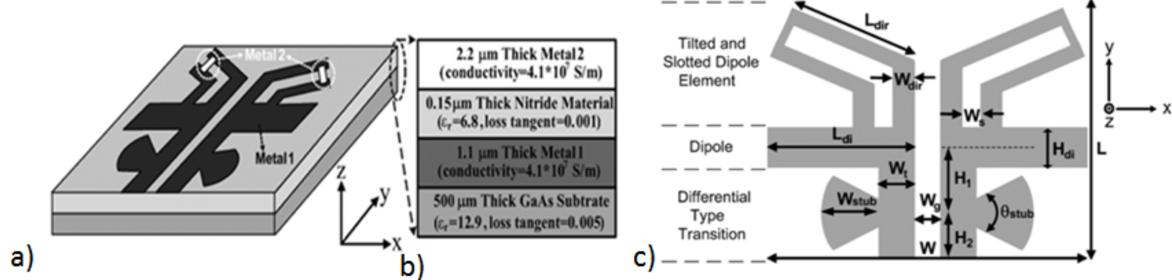

Figure 53 Multi-element dipole based antenna a) Layout 3D View b) Technological description and c) Top view antenna

More detailed performance oriented information can be found in the following table. It presents a state-of-the-art for on-chip antennas.

Ref.	Antenna Type	Freq. (GHz)	Technology	ρ (Ω*cm)	Gain (dBi)	Effic. %	BW (GHz)	Feed	Imp. (Ω)	Subs h (µm)
[51]	Dipole	24	CMOS	10	-8	N/A	N/A	CPS	4.4-j12	300
[55]	Folded Dipole	24	CMOS	N/A	-22	N/A	13.5	CPS	N/A	N/A
[56]	Slot Dipole	24	GaAs ε_r=12.9	N/A	2	N/A	1.4	CPW	50	420
[57]	Zig Zag Dipole	24	CMOS 0.13µm	20	-7	25	N/A	CPS	35+5j	670
[58]	Zig Zag Dipole	24	CMOS 0.13µm	N/A	N/A	10	N/A	CPS	40-j100	250
[54]	Inverted F	60	CMOS	10	-19	3.5	12.5	CPW	50	750
[54]	Quasi Yagi	60	CMOS	N/A	-12.5	5.6	9	CPS	50	N/A
[52]	Slotted Patch	410	CMOS 45nm	N/A	N/A	22	N/A	GCPW	50	N/A
[59]	Folded Patch	5.7	BiCMOS HRPS	10k	N/A	58	0.05	GCPW	50	N/A
[60]	Dipole	60	SiGe: BiCMOS	20	2.35	78.43	7	CPS	30+j30	N/A
[61]	Dipole	60	CMOS 0.18um	10	-6.7	9	N/A	CPS	50	N/A
[61]	Yagi two elem.	60	CMOS 0.18um	10	-3.55	15.8	8	CPS	50	750
[61]	Rhombic	60	CMOS 0.18um	10	-0.2	85	N/A	CPS	50	110
[61]	Loop	60	CMOS 0.18um	10	-1.2	77	N/A	CPS	50	700
[62]	Zig Zag	24	CMOS	20	1.5	13	N/A	CPS	30	670
[49]	Yagi	60	CMOS 0.18µm	N/A	-10	10	10	CPW to CPS	N/A	N/A
[53]	Triangular Mono	60	CMOS 0.18µm	N/A	-9.4	12	15	CPW	N/A	N/A
[63]	Dipole	60	CMOS 0.13µm SOI	1k	4	85	8	CPW to CPS	50	350
[64]	Dipole	40	BiCMOS 0.25um	N/A	-12	N/A	N/A	CPW to CPS	50	N/A
[64]	Patch	60	Glass Process	N/A	2.3	N/A	N/A	CPW	N/A	N/A
[65]	Dipole	40	HCMOS SOI 120nm	1k	-2	N/A	10,0	CPW	50	N/A
[66]	Double Slot	52	BICMOS 130nm	15	N/A	N/A	10,0	CPW	33	N/A
[66]	Double Slot	52	SOI 130nm	1k	N/A	N/A	10,0	CPW	N/A	N/A
[66]	Patch	40	SOI 130nm	1k	2,3	N/A	N/A	CPW	N/A	N/A
[67]	Spiral	60	SOI	N/A	4,2	82	15	CPW to CPS	50	N/A
[68]	Dipole Based	60	HEMT 0.15 um ε_r =12,9	N/A	3,6	N/A	15	CPS	50	500
[69]	Double Slotted	67	SOI	1k	N/A	N/A	19	CPW	36	N/A
[69]	Fractal	67	SOI	1k	N/A	N/A	23	CPW	52	N/A

Table 3 Antennas Performance for SoC configuration

From this data, some conclusions can be extracted.

- From the gain parameter, as we scroll down through the different values for the different antennas, we soon realize that basically a negative value of gain is obtained. A value that does not fulfill the requirement of our application (6dBi gain). High gain values are though attainable since 4 or 4.2 dBi are reported in [63] and [67] respectively. In these cases, a back side radiation metallization is used that serves as a reflector. What is interesting is the high efficiency values reported: 85 and 82%. These values are far from those obtained for low resistivity substrates where 10 or 20 % are common values.
- On-chip antennas seem to be well adapted to our bandwidth requirement. An average of 10 GHz can be observed in Table 3, which is more than sufficient for our need (8 GHz).

- Input impedance of 50 Ω seems to be the most common one; logically due to measuring test benches that have a 50-Ω fixed input impedance. Low (4.4 and 20 Ω) as well as complex input impedances are listed in Table 3. CPW and CPS feeding mechanisms are found to be commonly used.

5.a.ii) System in Package or SiP

For antennas presented for the SoC configuration, no packaging has been taken into account. To have a complete solution, a package has to be foreseen due to the presence of the PA. The packaging element should protect the active device, isolate it from other circuits, interconnect it to other external elements of the transmitter (that is connection to the PCB and other chips), provides a physical support and, in some cases, it should contribute to heat evacuation process. To pass to a packaged from an on-chip point of view, the antenna should first become an independent element of the system.

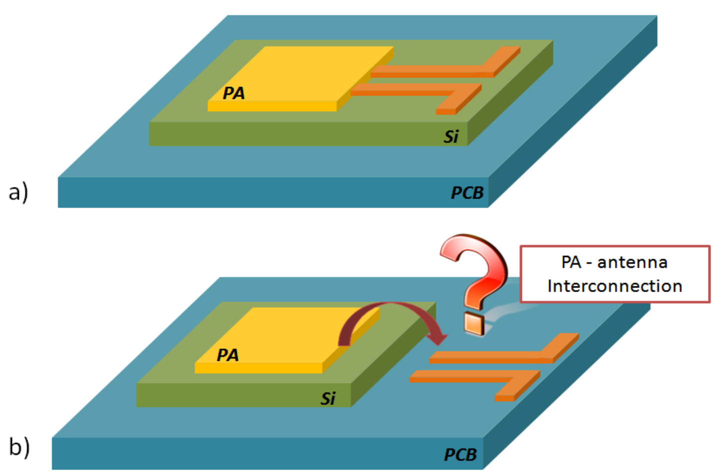

Figure 54 a) On chip antenna solution and b) Chip and antenna interconnection issue

As we convert the antenna into an external element, that is taking the antenna from the Silicon chip, a problem of interconnection arises. As seen in Figure 54, the antenna needs now an interconnection element to be able to receive the signal from the PA. These out-of-chip interconnections are commonly found in the semiconductor industry for PCB-chip and In-Package interconnections. As seen in Figure 55, there are two major interconnecting topologies: wire bonding and flip-chipping. As a first interconnection strategy, the antenna could be elaborated from the metallization of the PCB and connected directly to the chip using the interconnections mentioned before.

5.a.ii.1 Interconnection and first level Packaging

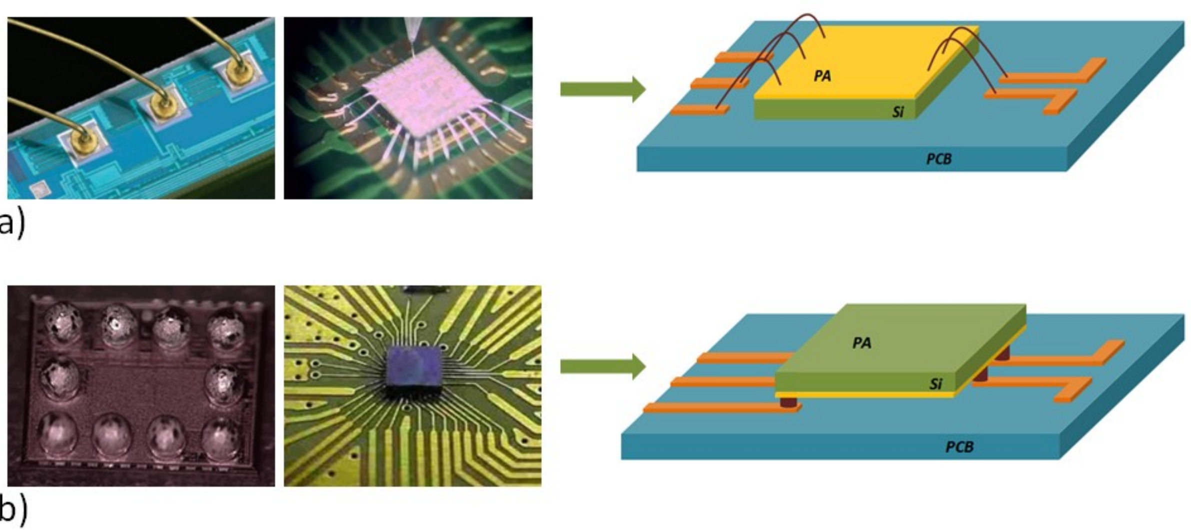

Figure 55 Interconnection schemes a) Wire-bonding [8] b) Flip chip through bumps[9]

Strictly speaking, no package has been considered up to this point. Only interconnection from the chip to the PCB has been described. For some applications, this will just be sufficient. This is commonly known as Direct Chip Attach or DCA, in which the bare die is attached to the PCB (glued for the wire-bonding case or by way of flip chip). A protective resin is added to offer some environmental protection to the interconnections and chip. For the wire-bonding case (seen in Figure 56 a), glob top deposition was made. The material properties and temperature curing time are very important to achieve a zero air bubble finished assembling. Another technique is also available, where a surrounding wall (dam) is placed before the deposition of the resin. It is then filled in the same way as the glob top case. Dam and fill processes allow one to control the covered area more precisely than the glob top process. These filling agents are also found for the flip chip scheme, where the resin penetrates under the chip, filling up the void spaces left between the PCB and the chip. The same considerations for material properties and temperature curing have to be taken into account.

[8] http://www.keyence.com & http://minneapolisstpaul.ebayclassifieds.com

[9] http://www.maxim-ic.com & http://www.microbonding.com

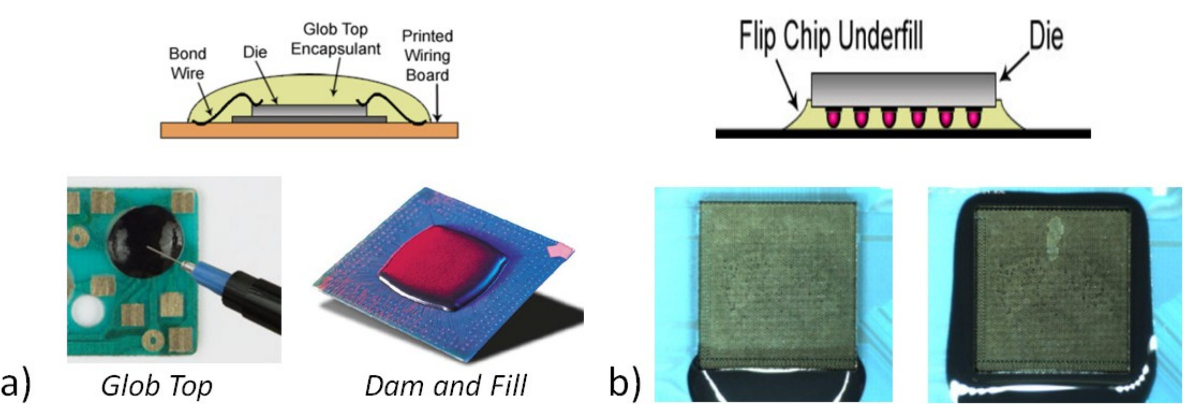

Figure 56 a) "Glob Top" and "Dam and Fill" b) Underfill examples [10]

5.a.ii.2 Second Level Packaging

Another way of interconnecting and protecting a semiconductor chip is by packaging it. Package can be thought of a DCA strategy with one additional interconnection stage. This additional stage will allow the die to be ready for soldering to PCB. No chip interconnection or environmental housing is then needed for a packaged chip as they are already included. As many types of package exist nowadays, only a few of the mostly used packages will be presented next.

A first classification could be made for these packaging technologies depending on their way to interact with the PCB, i.e., the way of interconnecting the output of the package to the PCB. Through hole technology (THT) and surface mount technology (SMT) are described next.

[10] http://www.masterbond.com & http://flipchips.com

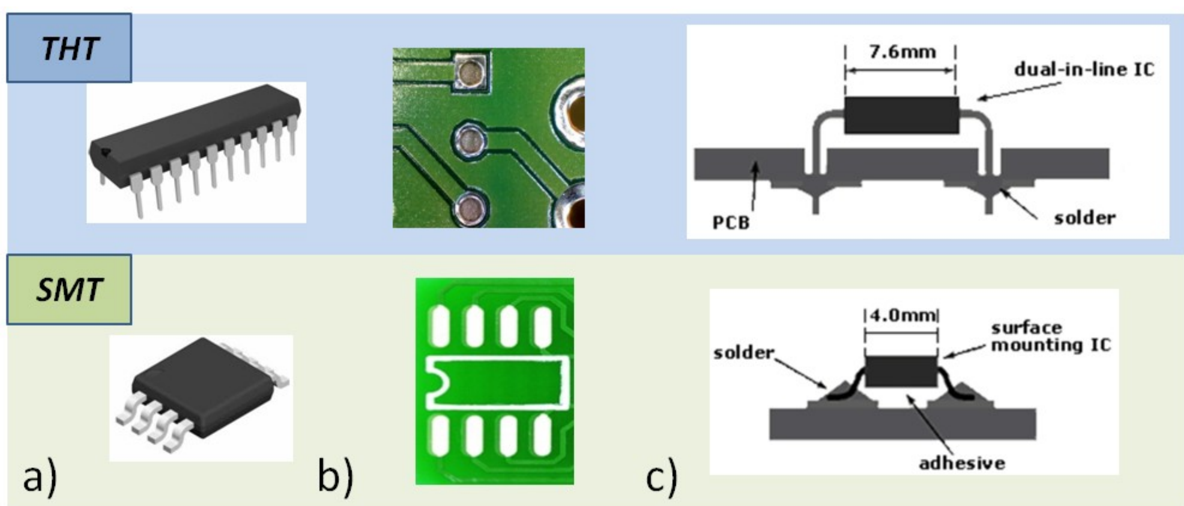

Figure 57 THT and SMT (SOIC) packaged examples a) Component[11] b) PCB layout [12] and c) resistor example [13]

The main reasons to consider implementation of SMT include

- reduction in circuit board size, as well as its weight
- single layer PCB needed
- reduction in electrical path length which decreases the parasitic components and allows a higher frequency of operation

Due to the reduction of size, one consideration has to be bear in mind when thinking of SMT: the temperature evacuation. The heat generation will continue to be the same, but this time it will be dissipated in a smaller area. This could be problematic for circuit life time and performances.

From the above described SMT, other packaging schemes were developed. One of these, the QFN, is described next and it will also allow us to enter into the first level interconnections or the interconnections inside the package.

[11] http://www.national.com

[12] http://www.eurocircuits.com

[13] http://www.ami.ac.uk

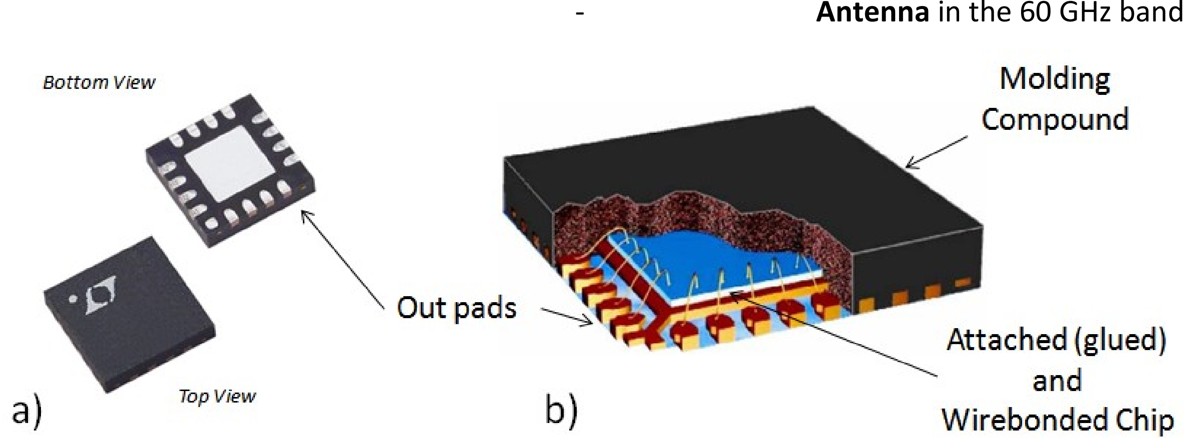

Figure 58 QFN package a) 3D view[14] and b) first level interconnections [15]

An even more compact design for a packaged chip is the QFN. In this case, the connections seen for example for the SMT (SOIC: small-outline integrated circuit) of Figure 57 are suppressed and landing pads are placed under the package. A 4x4 QFN package is shown as example in Figure 58. At the beginning of the QFN packaging process, the metallization for the output and central pad is carried out through etching. The chip is then glued with thermally conducting adhesive to the center of the package. Wirebonding interconnection comes next, allowing the chip to be connected to the external pads. Package molding then takes over and finishes the packaging of the device by covering the chip and the interconnection with a molded material. Typically more than one packaged chip is elaborated in the process. Consequently, a sawing (or singulation) stage comes at last, to separate each package.

5.a.ii.3 SiP Antennas

Some SiP examples are given next to clarify and discus the possibilities of using the above interconnections coupled to packaging technologies. The presence of the antenna and its interconnection is emphasized. Performances are summarized in Table 4.

The wireless chip set proposed by IBM depicted by Figure 59 was packaged together with a 7-dBi cavity-backed folded dipole antenna using a DCA (Direct Chip Attach). PCB finished process can be seen in Figure 59 b) where a glob top finishing stage was used. Under fill

[14] http://www.digikey.com

[15] http://www.obs.u-bordeaux1.fr

technique and molded materials are used. The antenna differential excitation was interconnected through a flip chip process.

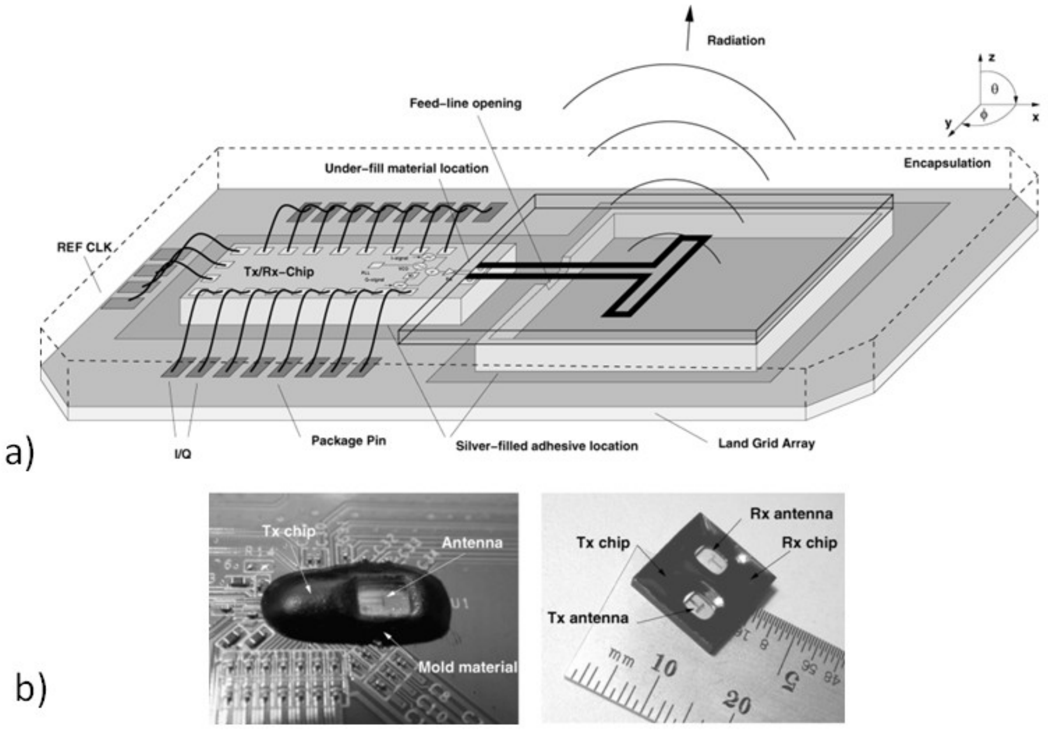

Figure 59 Completely packaged solution a) Wire-bonded chip and flip chipped antenna b) Molding material to complete the package. [70]

The integration of a CMOS power amplifier (PA) and antenna in printed circuit-board (PCB) technology is shown in Figure 60. A ROGER® based package enables the implementation of a high-efficiency antenna due to the low-loss materials. A differential excitation is used and the interconnection between the PA and the antenna is realized with flip-chip technology. The multilayer technology provides some opportunity to have different elements of the antenna distributed vertically. The vertical distribution can be controlled depending on the thickness of the substrates used. This is not possible to achieve with on-chip antennas.

- **Antenna** in the 60 GHz band

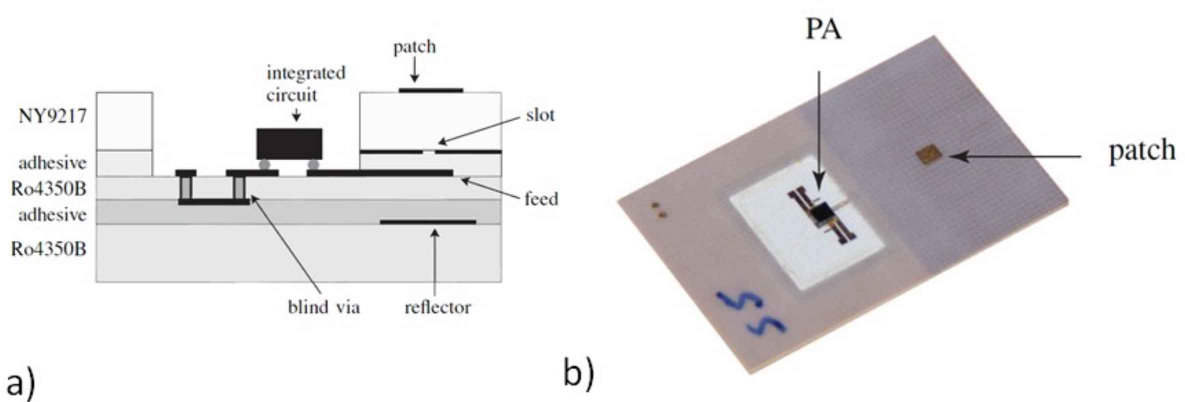

Figure 60 PCB based integration by flip chip a) Antenna and Chip cross section b) Fabricated Sample [71]

Two AiPs (Antenna in Package) are shown next. They are based on ceramic packages using low temperature co-fired ceramic (LTCC) technology for 60-GHz radio. LTCC process can embed high-quality passive elements in low loss ceramic substrates, while allowing active devices to be mounted on/in them. No adhesive is necessary between layers. A stage of pressure and temperature (850°C) will unify all the different layers into one single element. Between each layer, an etched metallization layer is possible when needed. Vias are also possible for communication between layers, rendering LTCC technology ideal for versatile packaging. The LTCC process produces mechanically strong, hermetically sealed, thermally conductive, chemically inert, and dimensionally stable structures with high yield.

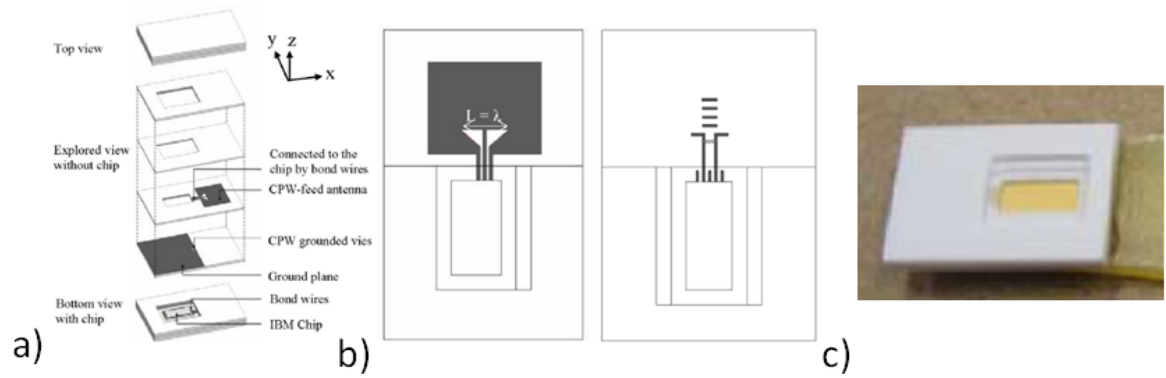

Figure 61 LTCC Packaging Technology a) Fabrication and Layers b) Slot and Yagi Antennas c) Fabricated sample [72]

Antenna in Package and wire-bonding as the interconnection for chip and antenna is foreseen in this example. A lid and no molding phase is used to cover the chip and bonding. Bumping in BGA (ball grid array) technology is used for the package second level

- **Antenna** in the 60 GHz band

interconnection. The package is based on a multilayer low cost organic material. Four metallization layers are also possible. The antenna is based on an open ended SIW (Substrate Integrated Waveguide) which provides an end-fire radiation; i.e., a radiation direction parallel to the PCB. Feeding transition is also needed to be able to excite the SIW mode of the antenna with a GSG configured probe.

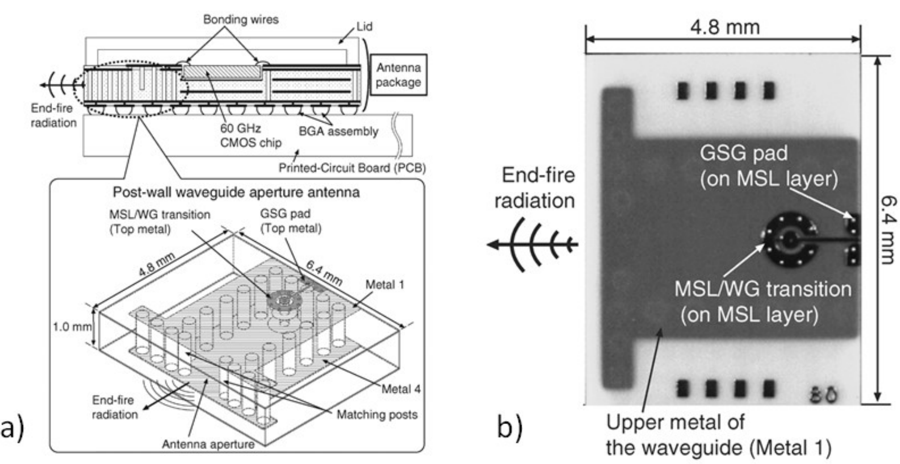

Figure 62 Open waveguide Antenna a) cross section and 3D (package schematic) and b) Top View fabricated sample [73]

Infineon's embedded wafer level ball grid array (eWLB) is employed as packaging technology. It consists of an organic molding stage and a second level interconnection of solder balls. The difference with other technologies is its RDL (Re-Distribution Layer) as the first level interconnects. It allows an efficient spacing of the solder balls beneath the chip and no wire-bonding or bumping is necessary. A dipole antenna (made from the RDL) in an 8x8 mm^2 eWLB package is presented. The low loss and low permittivity of the substrate makes it ideal for high efficiency antenna. To achieve broadside radiation, the antenna was designed taking into account a metallic shield acting as a reflector introduced into the PCB.

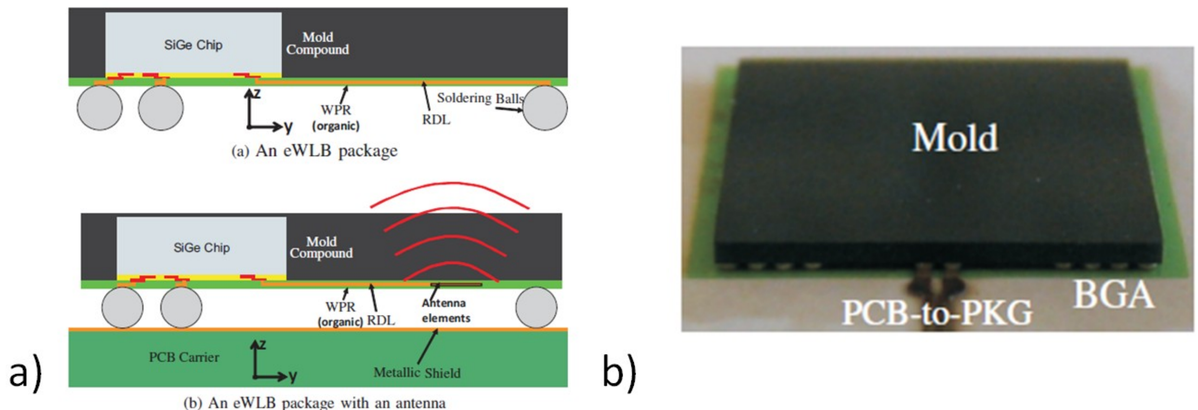

Figure 63 a) Package description and Antenna in Package (made from the RDL (Re-Distribution Layer)) b) Fabricated Antenna in Package [74]

A full-silicon based package is seen in Figure 64. A silicon carrier for the SiGe based chip is used as the first level interconnection interface. Antenna and chip are connected through the carrier. The flip chipped wafer is then connected at a second level to the PCB by bumps. Through wafer, vias are also incorporated as part of the interconnection scheme. This renders possible to bump the package to the PCB. The antenna is fabricated from a 1.2 µm thick Cu film with silicon process. To maximize antenna performance, the Si wafers were thinned after processing from 725 µm to 150 µm using a back-side grinding process. A cavity made by a micromachining process is used to produce a broadside radiation pattern. The antenna is connected to the 100-Ω coplanar strip line through a quarter wavelength transformer. A coplanar open loop is used to suppress the surface waves in the silicon substrate.

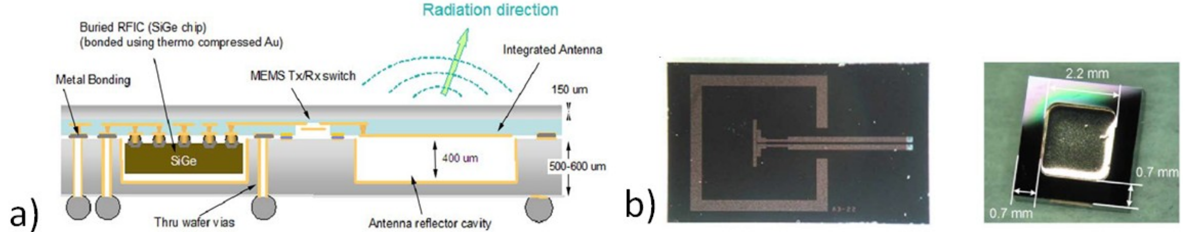

Figure 64 a) Cross Section of Package, interconnection and antenna b) Top view of fabricated antenna and cavity. [75]

As mode and impedance matching are vital to assure a maximum power transfer, the interconnection elements (wire-bonding and bumps) at mm-wave frequencies become important due to their size and configuration. Impedance and mode continuity will not always be possible. Some energy loss is expected. A new parameter called Insertion Loss (IL)

has to be introduced to quantify this type of losses. IL of 1.8 dB, 2 dB and 0.6 dB were reported in [76], [70] and [77] respectively.

The following table presents a state of the art for In-Packaged Antennas:

Ref.	Antenna Type	F. (GHz)	Technology	Gain (dBi)	Effic. %	BW (GHz)	Feed	Imp. Ω
[78]	4x Dipole Array	77	SiGe BiCMOS 120nm	2	N/A	2	CPS	45
[71]	Aperture Coupled Patch	60	CMOS 65nm	7	75	7.8	CPS	100
[79]	Circular Stacked	2.1	N/A	5.1	N/A	0.6	Microstrip	50
[80]	Circular Stacked	2.4	N/A	5.1	N/A	0.6	Microstrip	N/A
[81]	Patch	720	N/A	3.8	54.9	13.3	CPS	N/A
[82]	Post Supported Patch * 2	60	N/A	9.9	94	8.7	CPW	100
[70]	Cavity-backed dipole	60	SiGe 0.13 µm	7	90	18	CPS	50
[83]	Folded dipole	60	SiGe	8	90	8.4	CPW to CPS	150
[83]	Folded dipole * 2	60	SiGe	8	90	7.8	FGCPW	100
[72]	Triangular Slot (LTCC)	60	SiGe $\varepsilon_r = 5.9$	N/A	93	9.3	CPW	50
[72]	Yagi (LTCC)	60	SiGe	7	93	9.4	CPS	50
[75]	Dipole	60	N/A	6. 8	90	N/A	CPS	80 & 100
[84]	DRA	5	N/A	5.9	N/A	18%	Microstrip	N/A
[85]	Horn Antenna	60	N/A	14.4	N/A	6.3	CPW	N/A
[76]	SIW	60	CMOS 90nm	10.6	N/A	5	CPW	N/A
[86]	DRA	2.4	N/A	4.6	N/A	25%	Microstrip	50
[87]	Patch	60	N/A	4	68	15	CPW	N/A
[88]	Folded Dipole (eWLB)	77	N/A	7	N/A	8	CPS	100
[73]	Open End Wave Guide	60	CMOS	6	N/A	5	MS to CPW	50
[74]	Rectangular Slot	77	N/A	6	N/A	8	CPW	N/A
[77]	Rectangular DRA	36	N/A	5.5	95	12.5%	MS to SIW	50

Table 4 Performance for antennas in SiP based systems

- ♣ When comparing both SoC and SiP approaches regarding the performance of antennas, a clear increase in gain is visible for Sip configurations. Values of 5, 8 and 10 dBi in gain is now possible for antenna. Antenna radiation efficiency values have also increased, basically due to the low-loss substrates used.
- ♣ Although interconnections render the packaging and antenna design more flexible in terms of antenna and chip location, IL should be investigated as high loss and impedance mismatch may appear.
- ♣ Bandwidth of more than 8 GHz or 12% (7 GHz @ 60 GHz) is possible with In-Packaged Antennas, which is well suited for our application.

6) Front-End Transmitters (Whole Tx chain)

Although our investigation is focused on PA and Antenna interaction, a succinct state-of-the-art for the complete front-end is presented next. Input signals are now digital information that are amplified and modulated by the transmitter. On-Chip and In-Package antennas have been found in literature as seen in Figure 65. Wirebonding are commonly found for injecting the digital and bias signals to the front-end input (Figure 65 a).

- **Front-End** Transmitters (Whole Tx chain)

a) 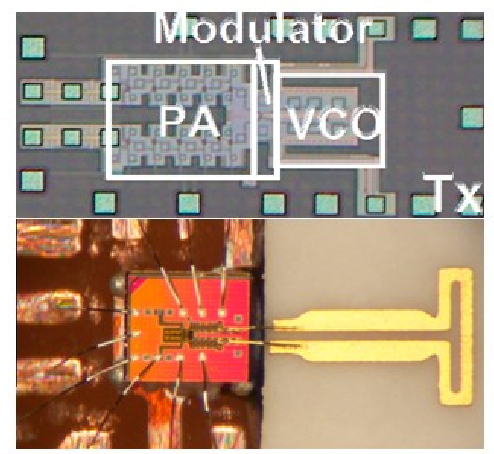

b) 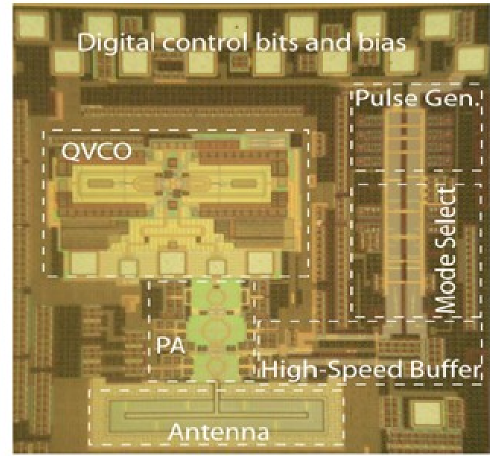

c) 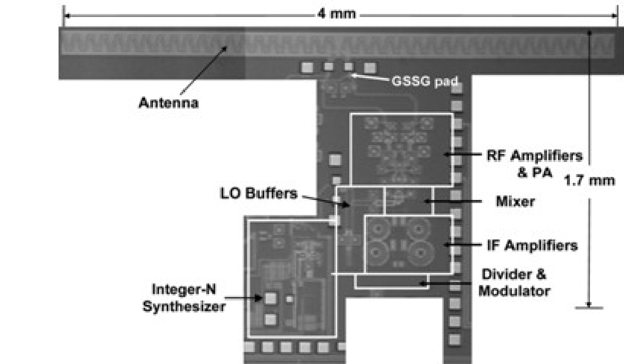

Figure 65 a) Transmitter modulator and PA with wire bonded off chip antenna, b) Transmitter with on-chip antenna c) Transmitter with Zig-Zag dipole incorporated in on-chip antenna

Table with state of the art for the Transmission Front End:

Ref	Year	Frequency	Source	Technology	Consumption	Gain	Size	Input Voltage
[89]	2009	60GHz	UC Califor.	90nm CMOS	78mW w/o PA	16dB	0.2mm^2	1,5
[90]	2009	60GHz	NTU, Taiwan	90nm CMOS	183mW	9,6dB	0.43 mm^2	1,5
[91]	2010	90GHz	Berkeley	0.13µm SiGe	739mW	12.25dB	1.2 mm^2	N/A
[92]	2008	60GHz	NEC, Japan	90nm CMOS	N/A	10.3dB	1.5 mm^2	1
[93]	2008	60GHz	Georg. Tech	90nm CMOS	173mW	17dB	2.65 mm^2	N/A
[94]	2008	60GHz	IBM	65nm Bulk CMOS	N/A	4.5dB	3 mm^2	N/A
[95]	2009	60GHz	Berkeley	90nm CMOS	170mW	14dB	6,8 mm^2	1,2

Table 5 Front-end transmitter performances

If the whole transmitter is thought to be fabricated in the same technology and in the same chip, the SoC strategy becomes even more attractive. The antenna size is now comparable to the space taken by active devices.

One characteristic of packaged solutions, beyond that one of increasing the performance of antenna, is the solution cost. The packaging stages have been found to be the cost

- **Front-End** Transmitters (Whole Tx chain)

differentiator for any given solution[23]. As the cost depends on the number of units to be fabricated, an initial packaging cost is difficult to determine. But cheaper solutions will have a clear advantage and cheaper solutions, in many cases, means cheaper materials.

Up until now, antenna and PA characteristics in the 60 GHz band have been presented. A thorough state-of-the-art study has been presented. Two different approaches, for PA-Antenna integration have been identified; SoC and SiP. Antenna performance (gain and bandwidth) for these two approaches, are presented as well.

In the next chapter, the SoC approach is explored. PA performances and interconnection with the antenna are presented next. Two different configurations are study with the aim of augmenting the efficiency of the PA-Antenna configurations. Simulation and measurements are shown.

Concluding remarks now follow for this introductory chapter.

7) Conclusions

The recently realized 7 GHz bandwidth around the 60 GHz frequency offers a great opportunity for developing fast (2GBps) wireless (1-2 m) data transmission. The silicon technology has also matured and transceiver silicon -based solutions have already been conceived. One question stills remains though, how to manage the transmitter antenna integration? The state of the art research shows that both On-chip and In-Package configurations are worth exploring.

From one hand, antenna gain and efficiency for On-chip antenna configuration, should improve regarding the state of the art due to the high resistivity substrate (SOI). Low interconnection loss should also be expected as mode and impedance matching can be achieved without the need of external elements. Study of the output matching stage should offer some insight into co-designing techniques to increase the energy transfer from PA to Antenna.

Secondly, high gain antenna solutions already exist for a packaged point of view. For the antenna, the independence from the silicon environment renders more flexible the antenna design. Different antenna topologies can be foreseen as for example the Dielectric Resonator Antenna (DRA). Note, that the antenna externalization adds a new constraint in the design as it is the 60 GHz chip – antenna interconnection.

To conclude, antenna-on-chip and antenna-in-package based solutions are to be explored. With this, a more detailed performance comparison of each configuration can be given.

Chapter 2 - Integrated Silicon based antenna: toward SoC (Co-integration and Co-design Scenarios)

1) The 60 GHz Power Amplifier on SOI

For this part of our investigation, there has been a close cooperation with IMS Bordeaux (Laboratoire de l'Intégration du Matériau au Système), as they are the designers of the PA. The PA was realized in CMOS SOI 65 nm technology from ST Microelectronics, giving us the opportunity to aim for a high efficiency antenna solution due to the high resistivity characteristic of the substrate as explained before. The description of the PA is given next.

1.a) PA on SOI description

The PA considered consists of a two amplification-stage scheme (Driver and Power). The driver stage is based on a cascode transistor design while the power stage has a common source design. Transistors are highlighted in Figure 66. A size of 565 x 614 μm^2 (including pads) is obtained. Capacitors and transmission lines are also found in the input and output matching stages.

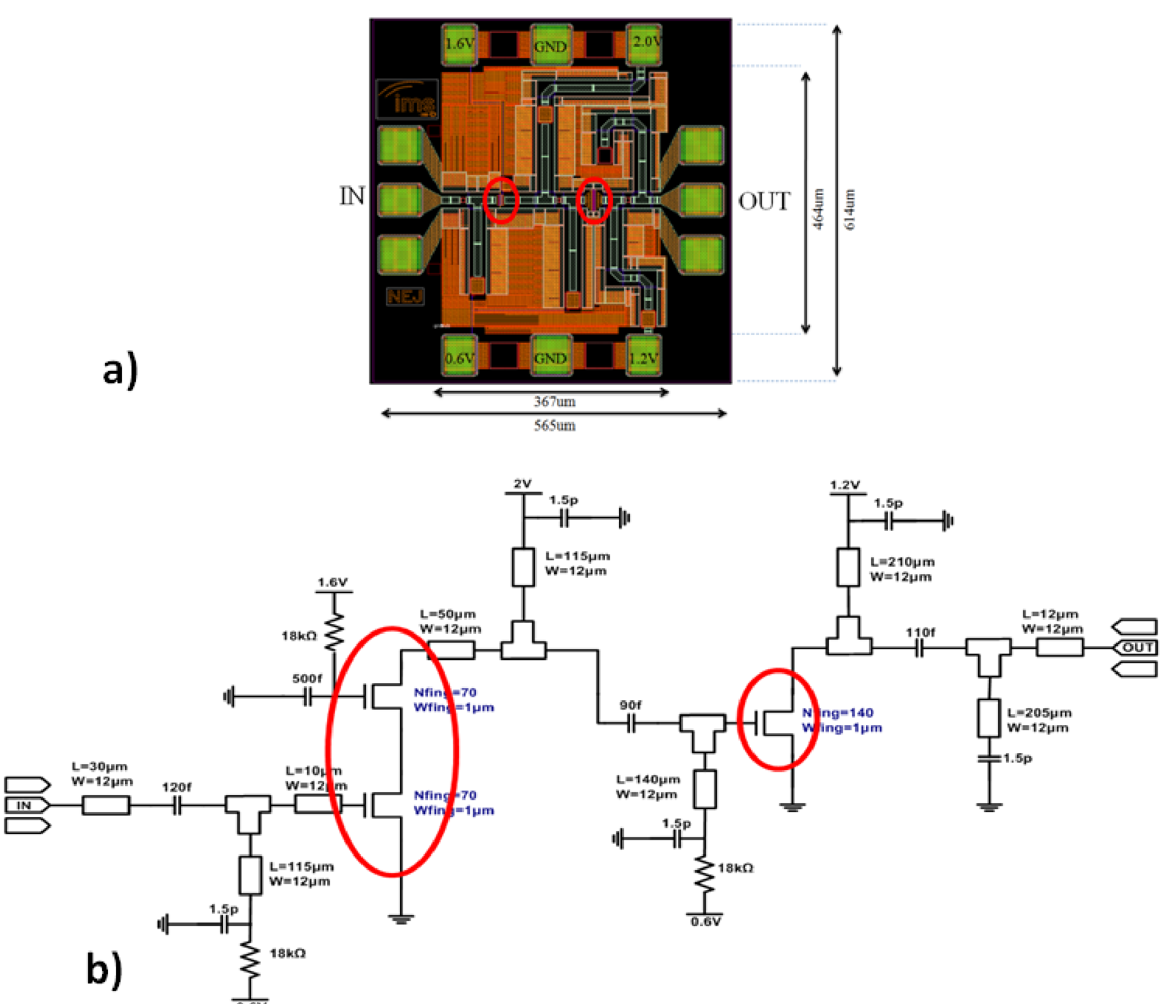

Figure 66 a) Power Amplifier layout and b) Schematic. Transistors are highlighted

1.b) PA Performance

The PA performance is shown in Figure 67 for small signal and in Figure 68 for large signal study. For the case of the small signal study, (that is, in the linear region) the results have shown a frequency shift of 5 GHz from expectation (maximum S21 level at 60 GHz), with a maximum gain at 65GHz. The transistor model has been modified but the simulated response remains still 3 GHz below the measured values. This frequency shift could be related to the modeling of the transistor inherent parasitic capacitances (It hasn't been tested yet). The frequency shift has a high impact on the large signal behavior shown next.

Figure 67 S21 and S11 response (Simulated and measured) of the SOI based PA

For the large signal study, the gain of the PA is tested for different values of the input power RF signal. This study exhibits the performance of the PA in its linear-region as well as in the non-linear region of operation. After the transistor model modification, a maximum power gain of 17dB (at -12dBm input power) and a maximum PAE (Power Added Efficiency) of 23% is expected at 62 GHz (Figure 68). Measurements are also shown at 65GHz to be able to account for the frequency shift. A reduction in "Power Gain" is observed, from 17 dB in simulation to 16 dB in measurements. This drop in gain is also seen in the small signal response. The differences between simulation and measurements can be explained by line and capacitors modeling differences.

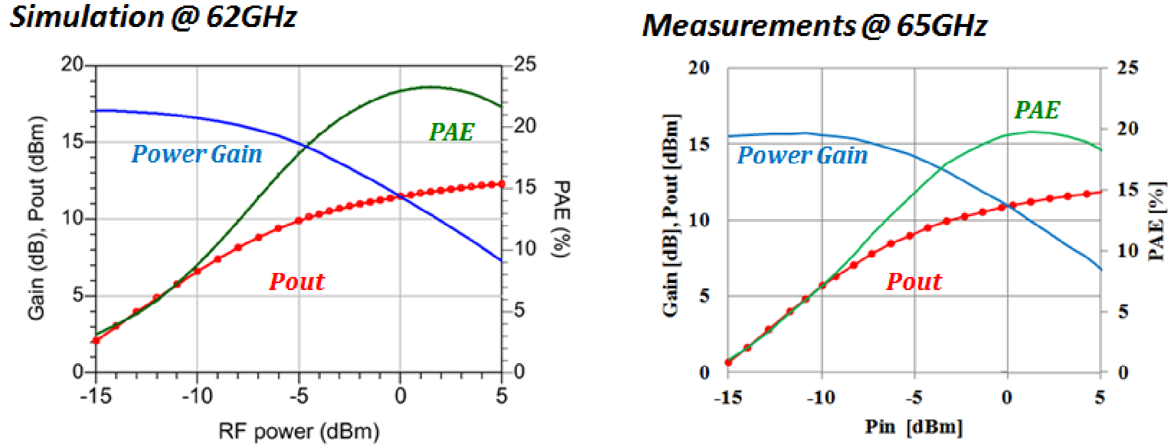

Figure 68 Gain, Output Power and Power Added Efficiency (PAE) % for SOI PA.

1.c) Comprehensive analysis of the PA

The PA on SOI is based upon a hybrid integration combining lumped R,L,C structures and CPW lines. The coplanar line configuration is used to link the transistors between each other (characteristic impedance Z_c = 50 Ω) and the Input and Output PA parts. The lines serve also as impedance transformers that will guarantee the maximum energy transfer through the different stages of the PA. For example, the driver output impedance is set to 36 + j44 Ω while the input impedance of the power stage is equal to 5 + j13 Ω. Matching between the different stages is achieved by the use of integrated capacitors and CPW lines. The study of the CPW line allows testing the simplification process needed for the EM simulator. All CPW lines share the dimensions reported on Figure 69b. All metal layers, as well as the vias, have been replaced by a single metallic element. Passivation, and SiO_2 layers, active and silicon layers remain for the simplified model. Comparison between the measured and simulated CPW characteristic impedance Z_c are compared in Figure 69c; a good agreement is observed. A small capacitive effect can be observed from measurement at 50 GHz and beyond. This may come from the TRL (Through-Reflect-Line) calibration process used for measurement. This procedure is used to remove the effect of the measuring probe and landing pads associated to the line for probe-CPW line access port dimensions accordance.

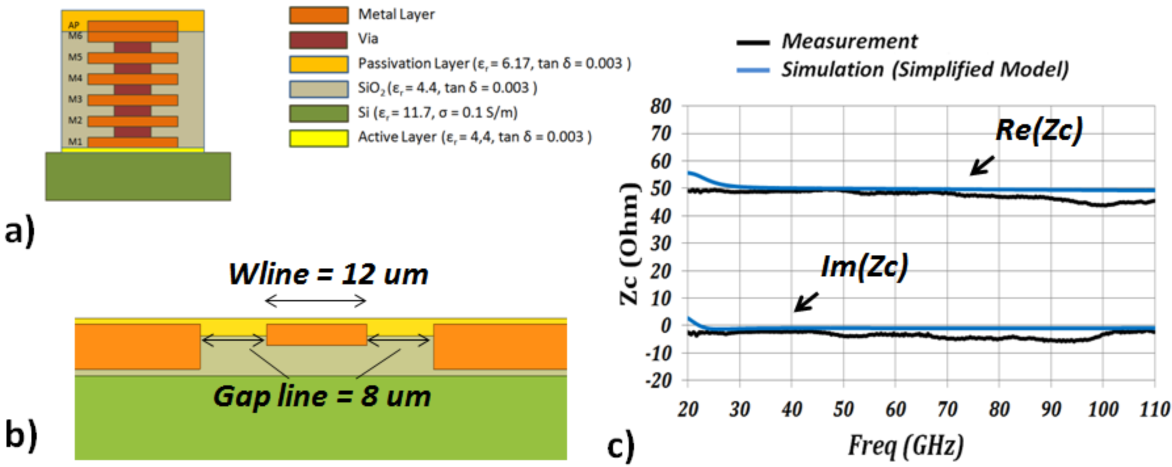

Figure 69 a) SOI 65nm SOI technology layer distribution, b) Simplified CPW line and c) Simulated and Measured CPW line results

Nevertheless, the reproducibility of the probe-pad contact is not completely ensured, thus explaining some differences.

1.d) Co-integration and Co-design scenarios

Although the matching stages permit a maximum energy transfer, losses arise from them due to the lossy materials employed. As we saw before, the SOI technology diminishes the loss of the line but will not eliminate it completely. Loss levels of 0.7, 1.8 and 1 dB are expected for the Input, Inter and Output stage respectively (highlighted stages shown in Figure 70a). This corresponds to the measured 0.8 dB/mm measured for such CPW line at 60 GHz.

1.d.i) Co-integration scenario

The antenna design of the transmission takes into account the integration with the PA output stage; that is, typical 50 Ω output impedance, thus conditioning 50 Ω input impedance for the antenna. In a 50 Ω approach, the antenna and the PA can be easily co-integrated. The PA output line configuration (CPW) has to be maintained, though, to ensure the mode compatibility between PA and Antenna; thus adding a constraint to the antenna design. The technological simplification mentioned before will also be applied during the antenna design process. This allows one to foresee the planar antenna design on one metallic layer only.

1.d.ii) Co-design scenario

For the co-design scenario, a different approach is taken. As mentioned before, transistors impedances are different from 50 Ω. The output impedance of the power transistor, for the considered technology described before, is 15 + 15j Ω. The antenna can therefore be designed with an input impedance complex conjugate presented by the transistor avoiding the need of any output matching stage. Loss of this last matching stage can thus be suppressed, which should increase the efficiency of the PA. The antenna and PA are now co-designed. These two cases can be seen in the schematic of the output stage in Figure 70b.

For the considered SOI-PA designed above, loss levels of 0.7, 1.8, and 1 dB are introduced by the input, inter and output stages at 60 GHz respectively. A 31 % improvement in passive loss could be expected by suppressing the output matching stage. As it will be discussed later, this percentage is lower due to the boundary conditions imposed by both the output stage and antenna.

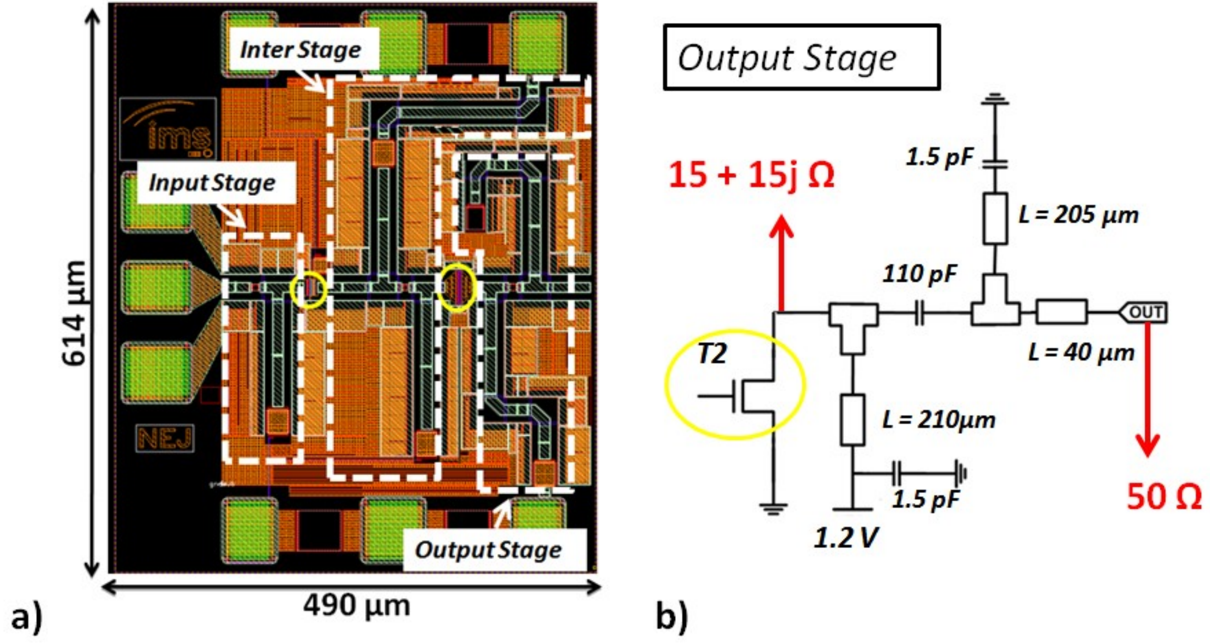

Figure 70 a) Highlighted - Matching stages (white) and - transistors (yellow) and b) Output stage Schematic

2) Antenna design for Co-Integration

For the antenna design, two important characteristics have been already extracted: the input impedance (50 Ω) and the feeding line configuration (CPW). A first design has been made from a typically CPW fed antenna , considering a slot configuration [56], [64], [66]. Due to CPW configuration, the slot seems to be the most adapted radiating element to be connected as it simply consists of an aperture in a metallization plane.

2.a) Slot on an infinite ground plane (no substrate)

A first simulation has been done where the slot is excited in the center by a lumped port. No CPW line is used for the moment. An initial simplified environment is simulated, no substrate, only air. A perfect conductor is used for the metallization and an infinite plane condition is selected in the simulator. This way, the possible impact of the finite ground plane is avoided and the slot performance can be isolated. For the first resonance of the slot, the length of the slot (L_{slot}) should be set to λ/2 (or 2.5mm in the absence of substrate → ε_r = 1 for the air) at 60 GHz frequency. The actual length is somewhat smaller due to the width W_{slot} (0.1 mm). L_{slot} was varied and the input impedance is shown in Figure 71c. As expected, the resonance frequency shifted from 48 to 69 GHz for a sweep of L_{slot} from 3 to 2 mm

respectively. An important value that can also be extracted is the magnitude value of the impedance, a high value of 500 Ω, far from the value of 50 Ω needed. This high impedance value is explained later. The radiation performance is seen in Figure 72. Omnidirectional radiation is observed on the E Plane.

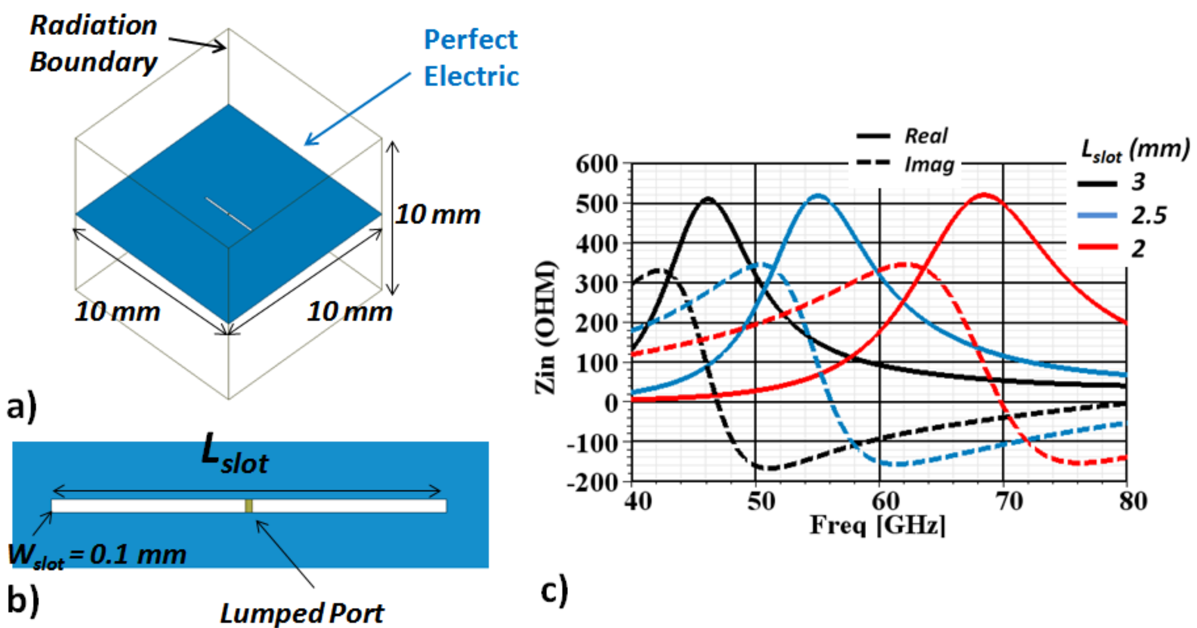

Figure 71 a) Air slot b) L_{slot} dimension of the slot (w_{slot} = 0.1 mm) and c) Real and Imaginary Input impedance seen at the port

For the moment, 50 Ω - input impedance is out of reach. If this antenna configuration should be used, matching stages are necessary at the input of the antenna. Previewing an increase in system efficiency by decreasing the matching elements, it will be counterproductive to add them to be able to match the antenna. A different strategy is pursued for the antenna to achieve a lower input-impedance.

2.b) Lowering the input impedance

Retaking the infinite ground plane slot, the input impedance is shown for a wider frequency range (20 to 120 GHz) in Figure 72. The slot length has been adjusted to 2.3 mm for a 60 GHz resonance. This frequency corresponds to a $\lambda_g/2$ resonance. By increasing the frequency range, another resonance is seen at 100 GHz (≈ λ_g). At this frequency, the real input impedance value is 55 Ω. A max gain of 3.3 dBi achieve regarding the 2.3 dBi gain at 60 GHz. The gain increase can be explained by the increase in the antenna aperture area. The aperture or effective area is related to the antenna “ability” to capture (or in the same way,

radiate) radiated power. As we increase the frequency (from 60 to 100 GHz) and maintain the same slot dimensions, the electrical size or slot area has increased regarding the resonant wavelength. The aperture of the antenna is proportionally related to the directivity [8]. Since no losses have been considered until now, the directivity has the same value as the gain. And as the slot aperture is related to the slot size, an increase in gain is the outcome. The gain increase produces a decrease in the beamwidth; this can be seen in the H plane patterns.

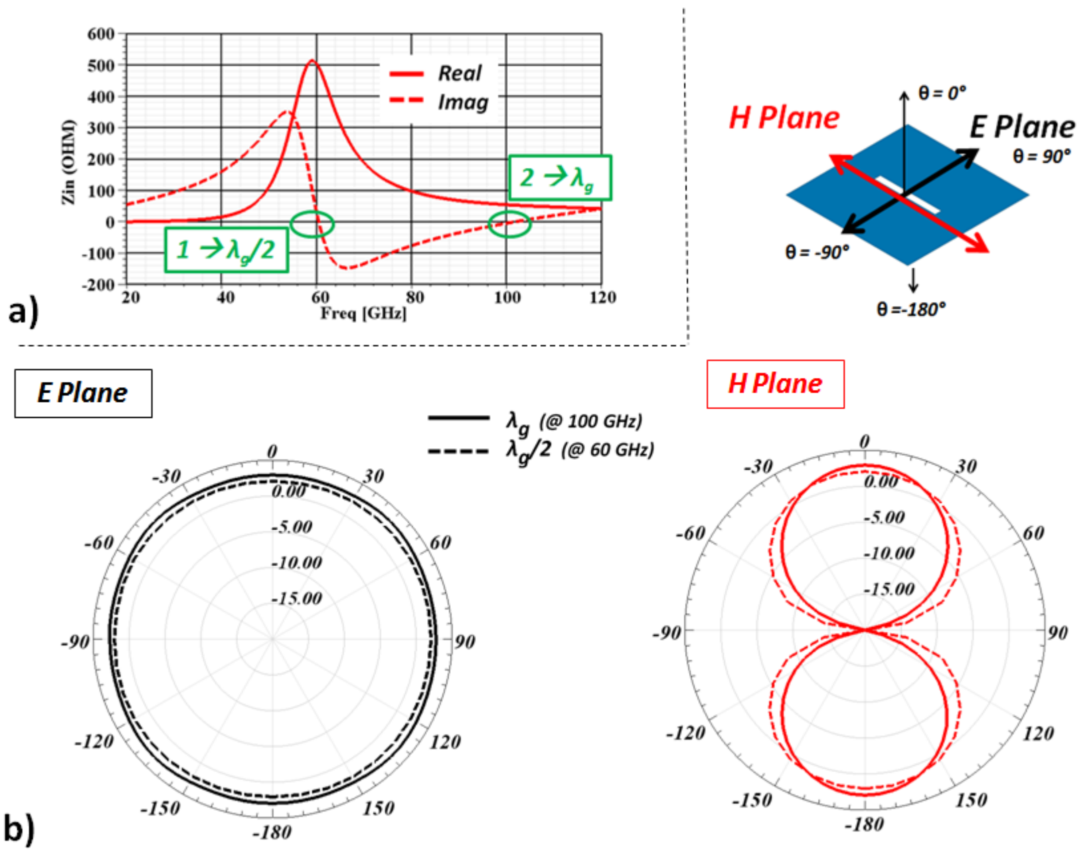

Figure 72 a) Input impedance and b) Gain pattern @ 60 and 100 GHz.

The resonant frequency for the second mode is brought down by increasing the length of the slot. The value for L_{slot} is now 4 mm and corresponds to a λ_g resonance at 60 GHz. The increase of the slot length has modified also modified the input impedance and is now of 38 Ω. It can also be observed, that the radiation patterns for both resonances are identical if the gain increase is not taken into account. To explain this, the vector H field for the two modes is shown in Figure 73 b. For the first mode ($\lambda_g/2$), the field distribution shows how the field concentrates on the borders of the slot and completes a semi cycle (black dashed arrow) in

the upper hemisphere of the structure (-90° < θ < 90°). The fields are directed from one edge to the other. A complete cycle is seen when taking into account the whole structure. For the second mode (λ_g), the same behavior is seen for the fields maxima at the edges of the slot. The same radiation pattern is thus obtained. The difference is the addition of a complete second cycle at the center of the structure that is 180° out of phase. This central cycle is completely independent from the external one and no contribution on the radiation is seen.

The lower impedance for the second mode can be explained by taking a look at the E field distribution in the H plane. The impedance is related to the ratio of the electric and magnetic fields seen by the port. Due to the centered port position on the slot, the magnitude of the E field changes from a maximum value for the 1st mode to a minimum for the 2nd mode, as seen in Figure 73. In this way, for a low E field value, lower impedance is achieved. The theoretical Z_{in} = 0 is not obtained at the center of the structure due to difference seen between the external and central E field magnitude minima. The magnitude of the central E field concentration is not the minimum field value found in the structure, thus allowing a higher electric field and consequently higher impedance.

This higher resonating mode (λ_g) achieves a higher gain, low input impedance and a wide bandwidth (13.4 GHz for 38 Ω port input impedance). The slot size has increased by 42%.

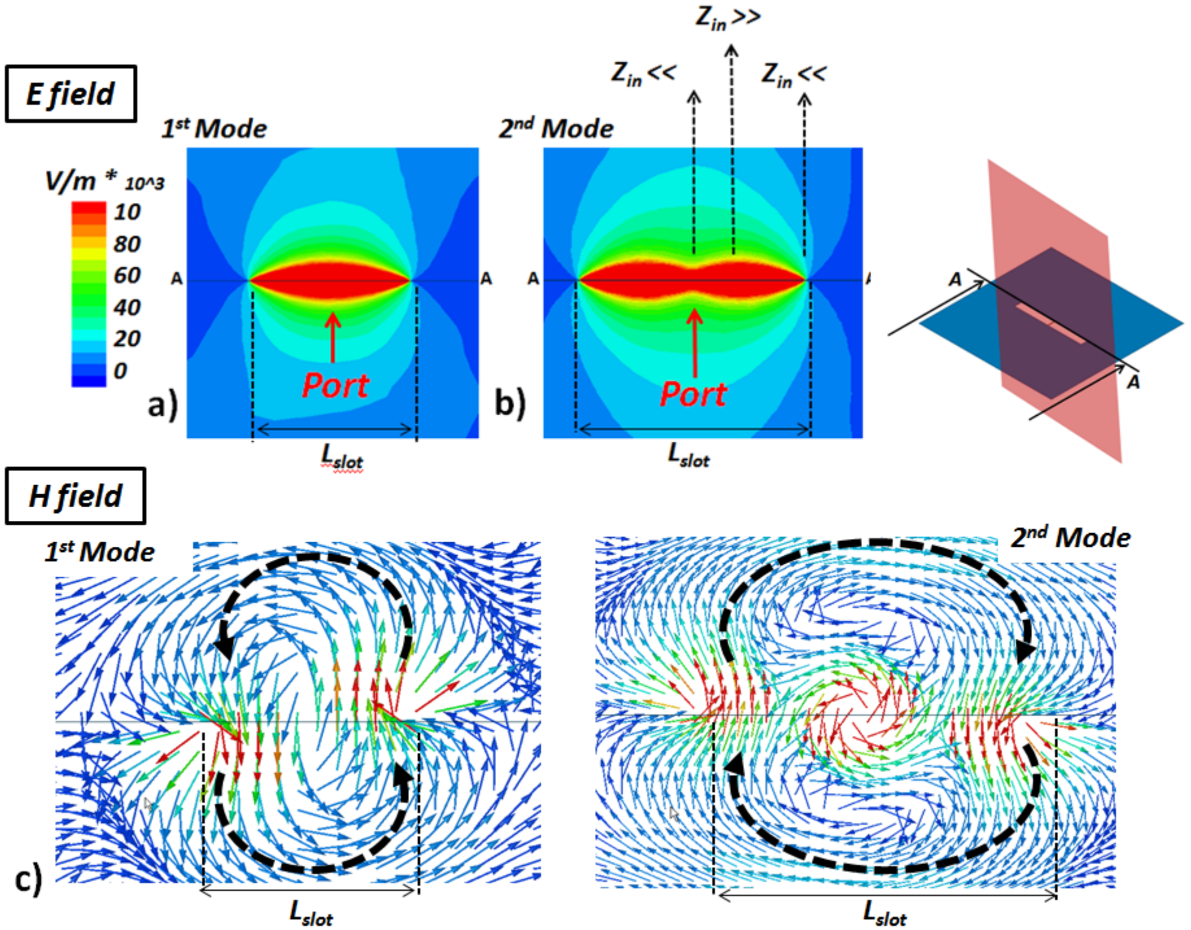

Figure 73 E field on H plane @ 60 GHz for a) L_{slot} = 2.3 mm b) L_{slot} = 4 mm and c) the corresponding H vector fields for the two modes

2.c) Slot on a finite ground plane (no substrate)

The infinite ground plane used until now is replaced by a slot on a finite ground plane configuration. This is done by leaving fixed the size of the metallization (10 mm x 10 mm) and enlarging the size of the radiation boundary to 14 mm x 14 mm (Figure 74). The input impedance remains mostly constant. It decreases only by 7 Ω obtaining down to 31 Ω. Electric fields in E plane are described for both configurations. The importance of the edges of the ground plane is evidenced. The field interacts with the edges of the ground plane (highlighted by the red dashed circle) and a diffraction effect takes place, also witnessed in [96].

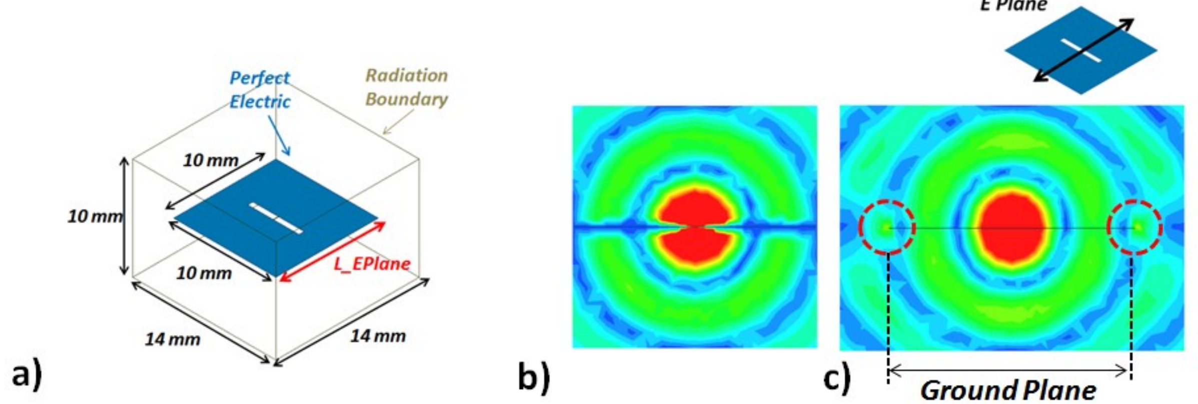

Figure 74 a) Finite ground configuration, b) E field E plane Infinite Ground and c) Finite Ground (slot dimensions not to scale)

Consequently, the field configuration is modified. A high impact is seen on the radiation characteristics of the antenna. It has been observed by simulation that the radiation behavior is highly modified by the ground plane length along the E Plane (L_EPlane in Figure 74a). The impact of the ground size is shown next.

2.c.i) Size study of finite ground

Two parametric studies are done to study the impact of the ground plane size. First of all and as seen in Figure 75, the longitudinal dimension along the E plane (L_x) is fixed while L_y takes 5, 10 and 50 mm values. The E plane radiation remains almost constant throughout the sweep of L_y. As expected from this last, radiation on H plane for θ = 0° and 180° remains constant as well. The radiation impact of L_y size reduction is only on the metallization plane (θ = 90° and -90°) and is more evident for the lowest L_y value (5mm). The effect of approaching the metallization to the slot will be studied in more detail further down.

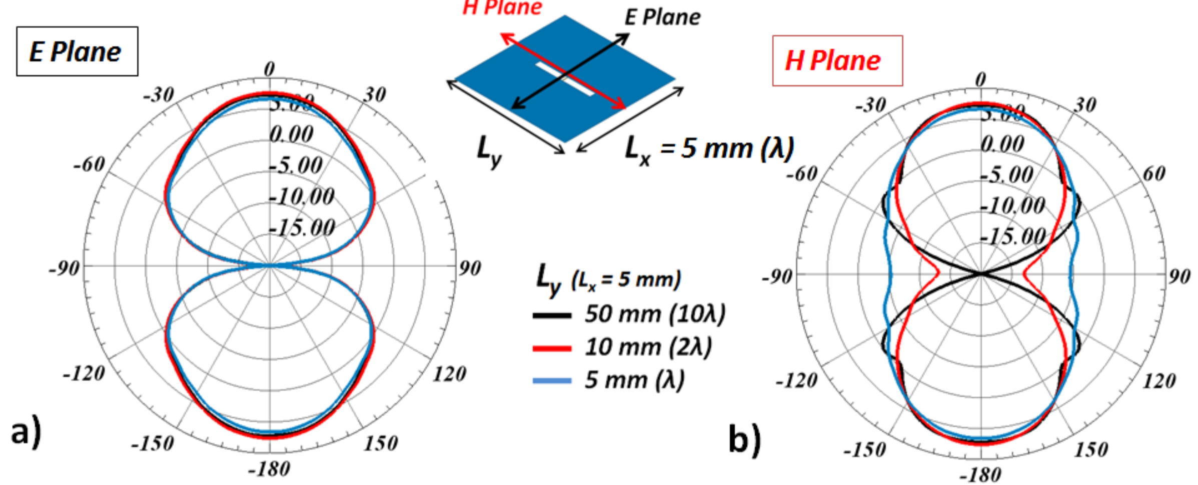

Figure 75 Slot ground plane size impact: L_y parametric study (L_x = 5 mm) a) E Plane and b) H plane

Secondly, longitudinal dimension along the H plane (L_y) is fixed while L_x takes 5, 10 and 50 mm values (Figure 76). For large ground planes (L_X > λ), the diffraction effect mentioned before has a high impact on the antenna radiation on the E plane. Once this distance is reduced (L_X = λ), the radiation of the slot changes and a broadside radiation is obtained. This behavior is maintained for all small L_X values (L_X < λ). Note, that the previously omnidirectional radiation on the E Plane is replaced by a directive radiation due to the absence of the metallization. A higher gain is achieved. The energy redistribution for a high broadside directivity seen for the small size ground plane (L_X = λ) is also evident on the H Plane.

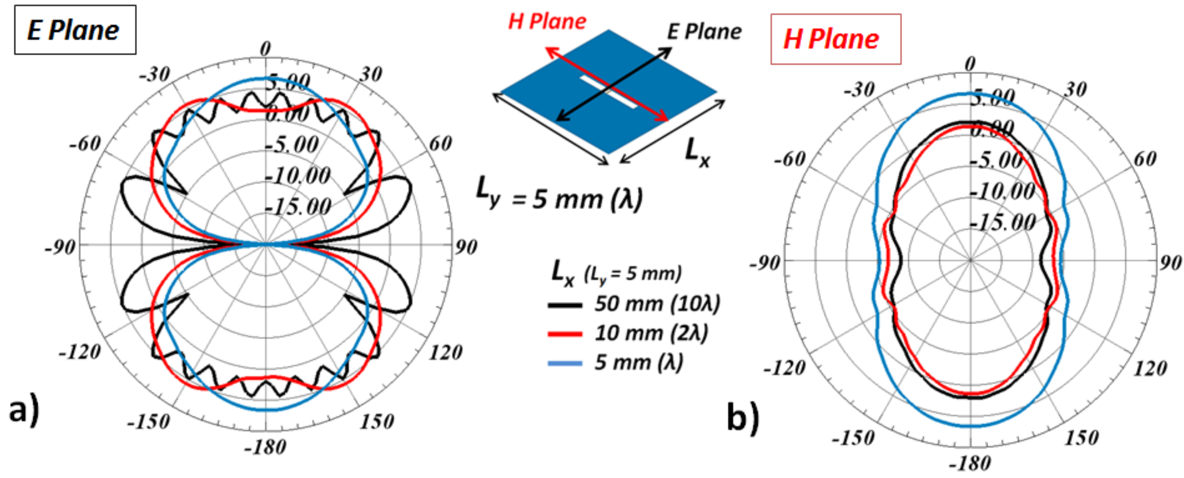

Figure 76 Slot ground plane size impact: L_x parametric study (L_y = 5 mm) a) E Plane and b) H plane

The input impedance for both parametric studies is also shown (Figure 77 Input impedance for ground plane size variation a) L_x fixed and b L_y fixedFigure 77). A higher impact is observed for the fixed L_x configuration as expected from the radiation pattern results shown before. Slight modification of the impedance curve (Figure 77 b) throughout the frequency band shows the effect of the edge diffraction. No significant change is however observed for the real and imaginary values at 60 GHz.

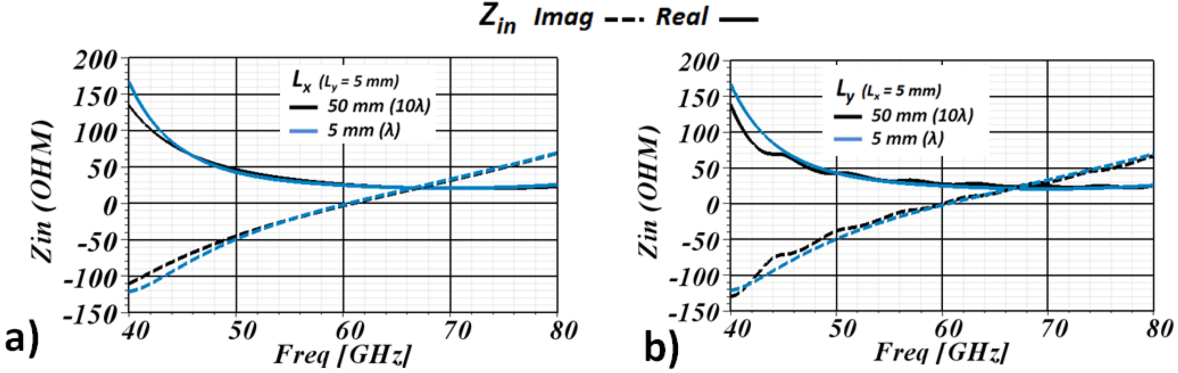

Figure 77 Input impedance for ground plane size variation a) L_x fixed and b L_y fixed

2.d) Adding the substrate

The substrate is now added. In this case, due to the substrate height (0.25 mm) and high permittivity (11.7), the slot length decreases to a value of 1.55 mm for a 60-GHz λ resonance. The substrate has a high impact in the input impedance; it is now of only 5 Ω. Impedance control is given priority due to the low impedance obtained until now.

2.d.i) W_{slot} as impedance controller

Typically, the slot width (W_{slot}) is used to control the input impedance of the antenna. As the width increases, the impedance of the antenna increases. An infinite ground plane and no substrate configuration is used for the next analysis. An increase from 36 to 84 Ω for the real component of the input impedance is obtained for a W_{slot} variation of 0.1 up to 0.5 mm (Figure 78 a) at 60 GHz.). This can be explained by taking a look at the magnetic field at the slot plane (Figure 78 b)). As before, a variation of field level changes the impedance seen by the port. An inductive component is also added to the input impedance as W_{slot} increases. This can be seen on the imaginary component. In fact, there has always been a capacitive component linked to the slot due to the small separation of its longitudinal edges: edges

along the L_{slot} dimension. As the separation between these edges start to increase, the capacitive component decreases resulting in an increase of Z_{in} imaginary component. As consequence, a frequency shift is observed, passing from 60 to 44 GHz for Wslot 0.1 and 0.5 mm respectively. A 2 dB decrease on gain is also seen, which adds a limitation to the impedance control by dimensioning of W_{slot}. Another strategy is now pursued by taking advantage of the ground size and its impact on the antenna performance.

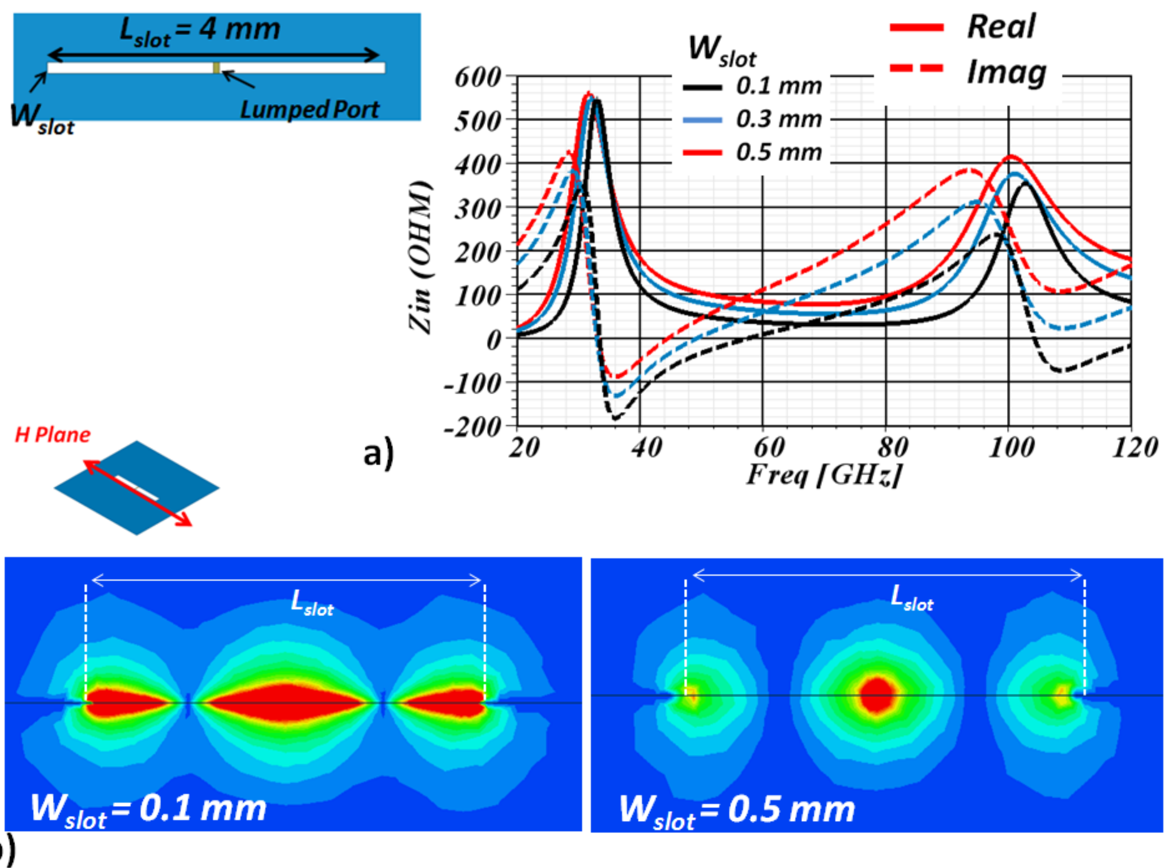

Figure 78 Wslot impact on input impedance a) Real and Imaginary values of slot input impedance b) Magnetic field on H plane for W_{slot} = 0.1 and 0.5 mm.

2.d.ii) Ground size as impedance controller

In our case, due to the finite ground size, the ground dimensions (L_y and L_x) will also allow to control the input impedance. L_x is studied first by decreasing its value from 5 mm to 1 mm for several values of L_y. A value for L_x is found, where highest impedance value is achieved for each configuration. To study the source of this high impedance ground size value, the E field is shown next (Figure 79). A coupling phenomenon is observed on the ground borders cut by the E plane. The same effect is seen in Figure 74 for a “No Substrate” configuration.

In this case, due to the high permittivity of the substrate, this phenomenon occurs for a smaller size ground plane value (L_x = 2 mm). Backward radiation (θ = 180°) is not impacted by the ground plane size for these configurations as seen in Figure 79 b. This phenomenon has though a high impact on the input impedance as seen before.

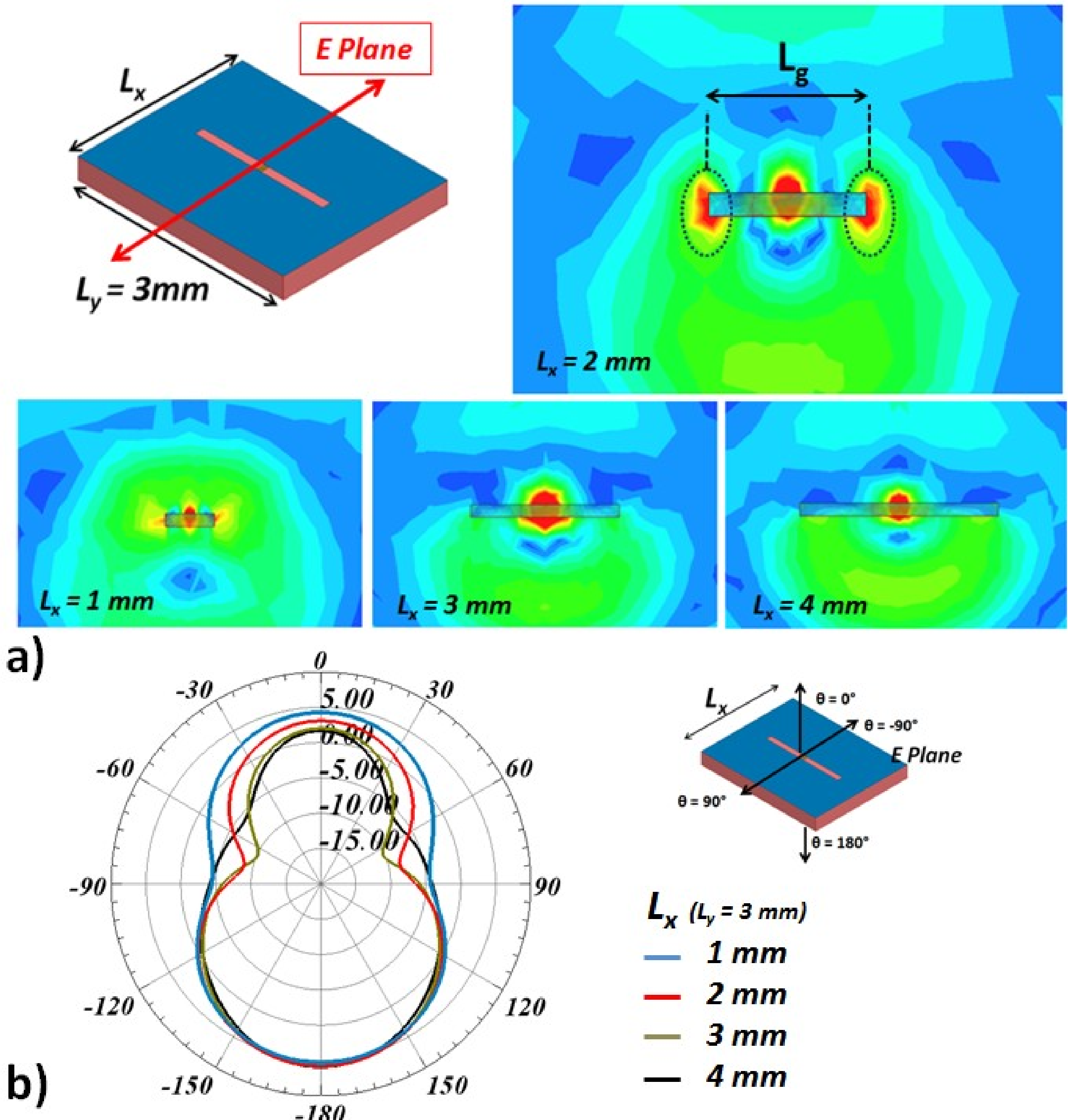

Figure 79 L_x impact. a) E field for Lx = 1, 2, 3 and 4 mm. and b) Gain pattern for L_x values

It can also be observed (Figure 80), that the lowest value of L_y (2 mm) is also responsible of the highest impedance (15 Ω). Taking this information as the starting point (L_x = 1.7 mm and L_y = 2 mm), a parametric study is now done for $W_{slot.}$ As seen in Figure 80b, higher impedance reaching up to 38 Ω is obtainable when having a 0.4 mm wide slot. As also seen, the resonant frequency decreases as the slot width is increased. This is logical as it is the slot perimeter (2*L_{slot} + 2*W_{slot}) that fixes the frequency.

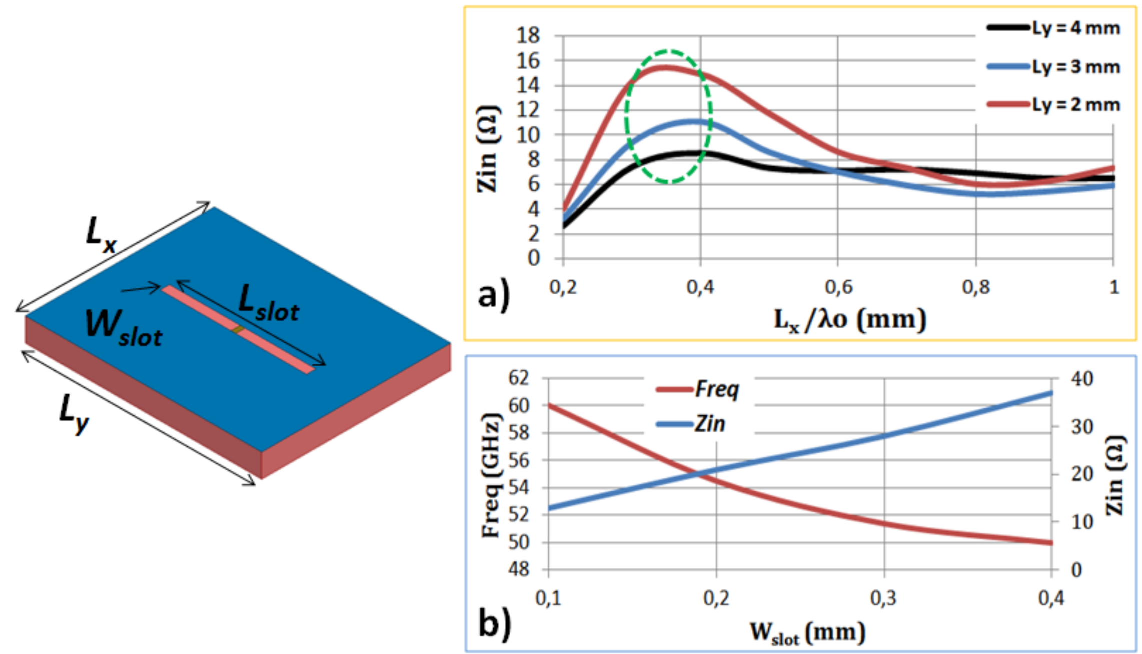

Figure 80 Slot parameters for impedance control a) Parametric study of L_x and L_y (L_{slot} = 1.55 mm and W_{slot} = 0.1 mm) and b) Parametric study of W_{slot} (L_x = 1.7, L_y = 2 mm and L_{slot} = 1.55 mm)

To regain the 60-GHz resonant frequency and keep elevated impedance, the slot length is reduced. Bearing this in mind, an optimization process is done. Antenna dimensions are then optimized for 50-Ω input impedance and 60-GHz resonant frequency solution. Final values are L_{slot} = 1.15 mm, W_{slot} = 0.18 mm, L_x = 1.7 mm and L_y = 1.4 mm. As the impedance, the antenna radiation is impacted by the dimensions of the ground plane. Radiation characteristics are shown next for small ground plane dimensions (L_x and L_y < 2 mm). A sweep of L_x from 1 to 2 mm with a fixed L_y = 2 mm value is done first. The effect of a small Lx value is clearly seen on the E plane radiation pattern. The high gain levels at the metallization plane (θ = 90° and -90°) seen before for $L_x > \lambda$ start to decrease. The metal absence renders the radiation of the antenna somewhat directive. This was already observed in Figure 76. Still, high gain is maintained at θ = 0° for any Lx value. An analogue effect is seen for the H Plane as L_y decreases. It is explained in the final configuration section.

The influence of the substrate is also visible. Broadside (θ = 0°) gain values diminish, passing from 5 to 2.5 dBi for L_x = 1 mm. This is the effect of the high permittivity of the substrate.

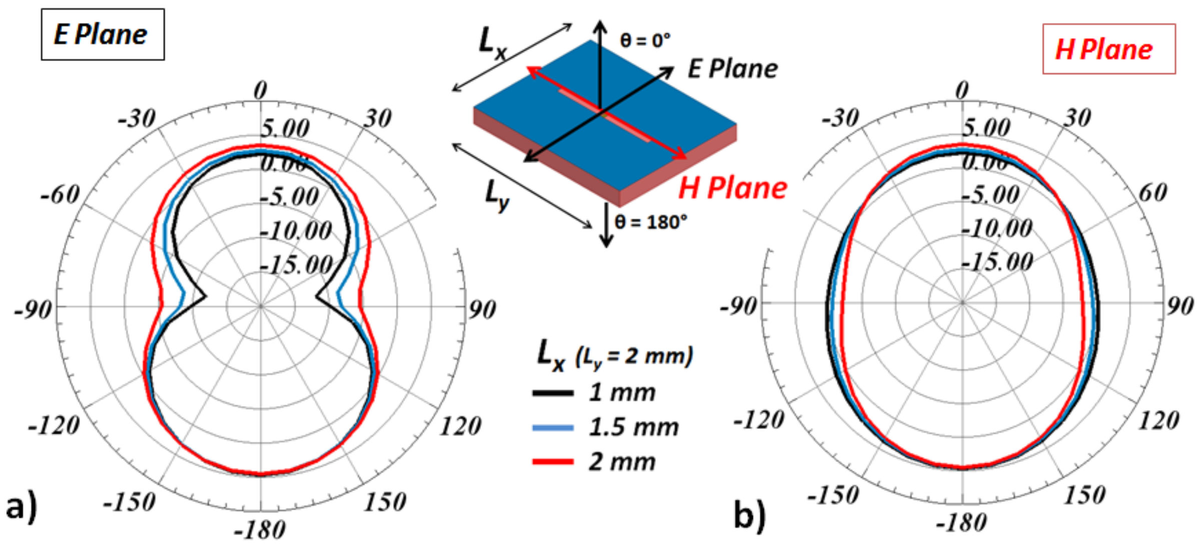

Figure 81 L_x reduction impact on the gain pattern (E and H Plane shown)

2.e) Final 50 Ω antenna configuration

In the optimization process, the antenna CPW feed line has been included. Dummies (metalized isolated regions) have also been included in the slot position to comply with the metal density constraint from the SOI fabrication process. No CPW, short and long CPW and With Dummies configurations are compared next. At first hand, the effect of including the CPW line (0.05 mm) has a large impact in the input impedance of the antenna. The S11 values show a shift of 6 GHz between both responses. This is due to the current path increase added by the incorporation of the central CPW line. The path increase is highlighted in red and seen in Figure 82.

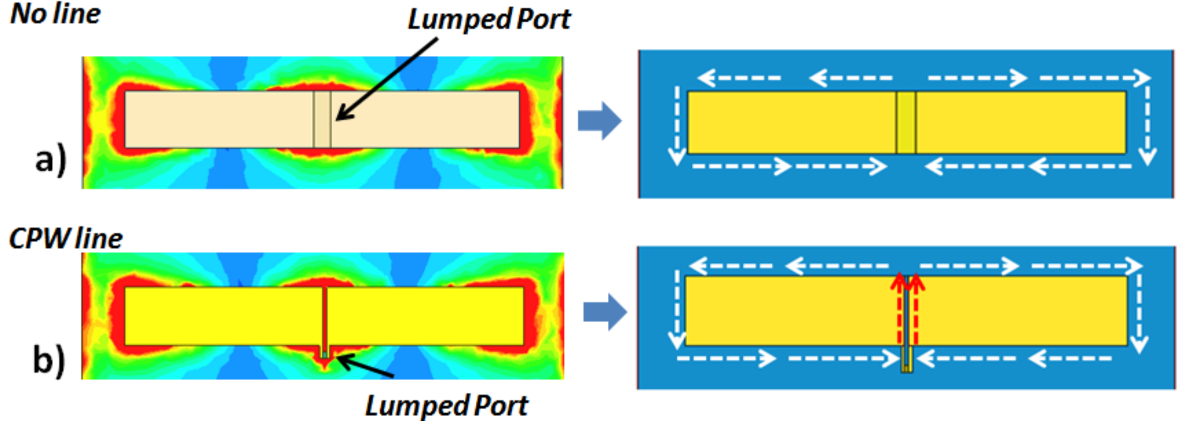

Figure 82 Surface currents paths around the slot. a) No Line and b) CPW lumped port fed configurations.

For the other configurations, extending the CPW (for example; CPW line 0.05 mm to 0.6 mm), has almost no impact on the S11 response. Nevertheless, a drop of 0.2 dB is witnessed in the gain response. The configuration "dummies & 0.05 mm CPW" shows an almost equal bandwidth to the CPW configuration with a 60 GHz resonance frequency. A matching improvement is seen, that suggests a slight impact on the input impedance at resonance. No effect on the radiation performance is witnessed; this is due to the isolated nature of the dummies and their small size (15 x 15 µm) regarding the resonant wavelength.

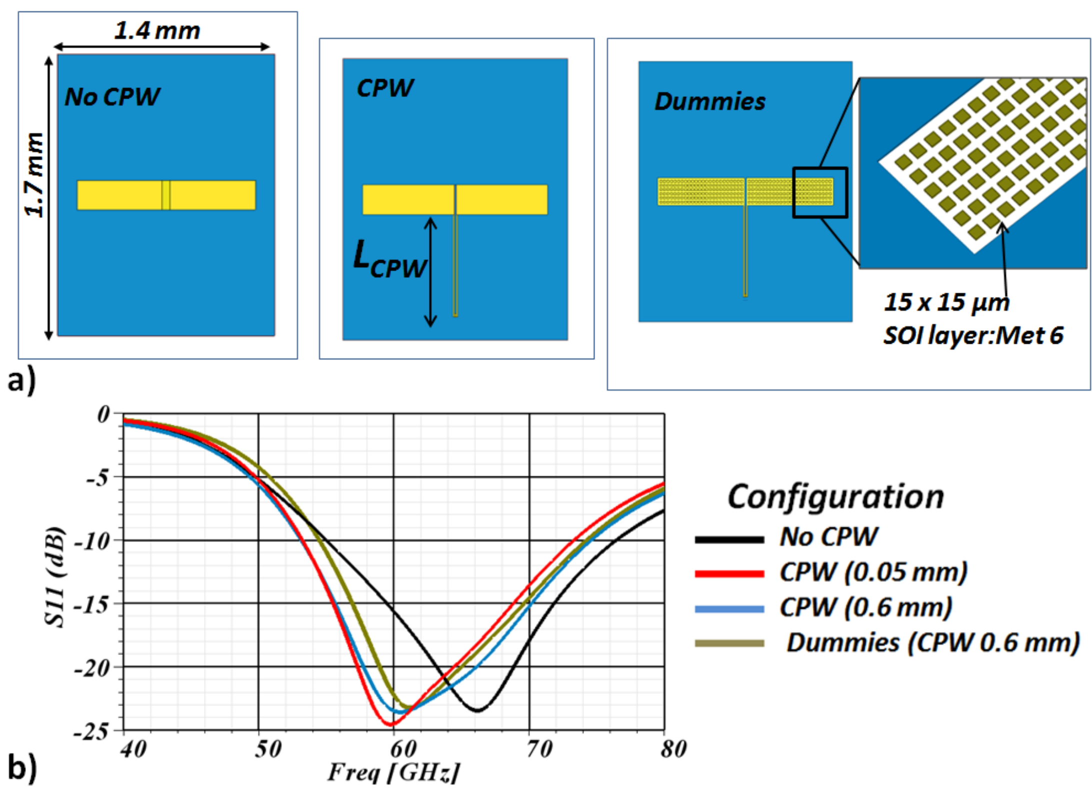

Figure 83 a) No CPW, CPW and dummies included configurations b) S11 response

The final antenna performance (including 0.6 mm long CPW+ dummies) is seen in Figure 84. As expected, a wide band is covered (19.8 GHz), with a minimum gain of 3 dBi on the matched band and a maximum value of 4.2 dBi. An 88% efficiency simulated value is also obtained @ 60 GHz. The high efficiency value is mostly due to the high resistivity values of the substrate. The effect of the high permittivity substrate is also seen, as a backward θ = 180° directed gain is obtained. The radiation of the antenna is concentrated towards the θ = 180° value (Figure 84 b), i.e. through the Si substrate.

2.e.i) Radiation performance

A major difference regarding the infinite plane ground configuration (Figure 72b) is the radiation pattern. The E field and H field patterns behave differently. In Figure 84 a, the two patterns can be seen. The gain pattern on the E Plane for the final configuration tends to follow the gain pattern on the H Plane for the Infinite ground plane configuration. Likewise, the gain on the H plane for the final configuration has the same pattern as the gain on the E plane for the infinite plane.

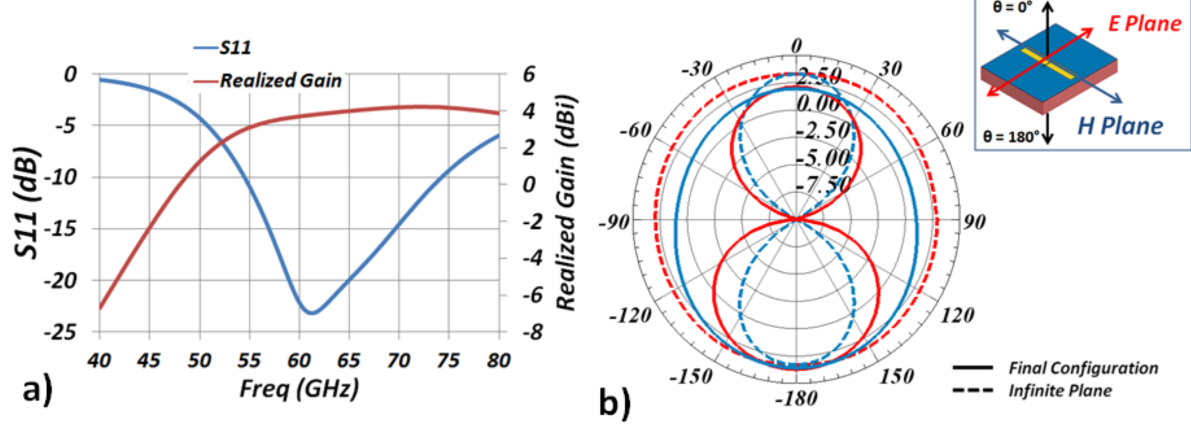

Figure 84 Final performance antenna a) S11 and Realized gain (Theta = 180°) and b) Gain pattern for final configuration and infinite plane @ 60 GHz

The E fields in the H plane are plotted in Figure 85. Two values for Y (distance between the slot and the Si frontier) are taken. The typical E field configuration for the infinite plane is seen for Y = 1.5 mm. A minimum gain value (highlighted by the black dashed circle) is seen due to the presence of the metallization. This is corroborated by the gain pattern for the infinite plane in Figure 84 b, where a minimum is found at θ = -90°. As the slot edge approaches the edge of the ground plane (Y = 0.3), the fields are no longer entirely separated by the metallization. The fields interact beyond the edge of the ground plane. An quasi omnidirectional pattern is obtained. (H plane Gain pattern for final configuration, Figure 85 c).

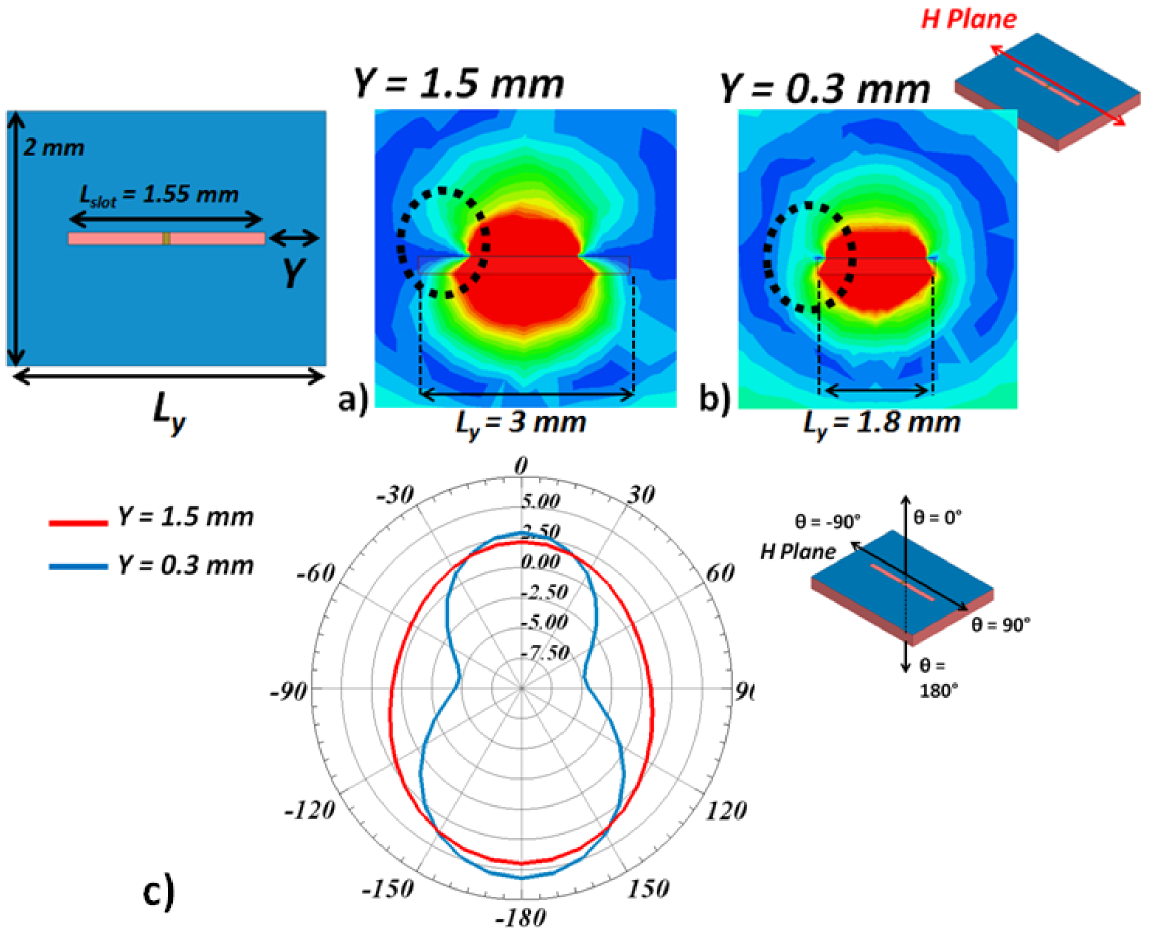

Figure 85 Impact of Y value. E Fields on H Plane for a) Y = 1.5 mm and b) Y = 0.3 mm

This phenomenon has not only a high impact on the radiation characteristics of the antenna, but it also helps controlling the frequency of resonance. When the Si substrate edges are close the slot, the fields extend beyond the length of the slot and the frequency of resonance is no longer entirely controlled by the slot dimensions. The frequency of resonance decreases as Y decreases. Z_{in} is maintained unvaried. This is useful as it allows to diminish the length of the slot and the size of the chip, and to remain centered at 60 GHz.

The different phenomena of a radiating slot integrated in a finite ground plane have been shown. The modification of the radiation pattern and the interaction of the slot radiation with the ground plane edges have been studied. Taking advantage of this last, the slot based antenna is modified for the Co-design scenario.

3) Antenna Design for Co-design with PA

3.a) Transistor output stage configuration

For the co-design scenario, the input impedance has been defined in Figure 70. A complex value of 15 + 15j Ω is found at the output of the second transistor. But this is not the value that the antenna will encounter. The transistor (T2) biasing conducts to match in a different place and consequently to a different impedance value. The biasing circuit and source (1.2V, Figure 86b) cannot be removed; the transistor would not be properly biased. Note, that the power transistor biasing configuration could be modified to obtain a direct access to the transistor output for a future design. This places us before the 110 pF capacitor highlighted in green. As we intend to use the CPW fed slot antenna, the presence of the capacitor is very important. As seen in the schematic of the output stage, if the antenna would be place before the capacitor, a direct DC path would result for the 1.2 V DC source and ground from the slot. This would create a short circuit for the biasing of the transistor. The capacitor is subsequently added with a small 12 µm length line that will allow connecting the antenna. At this moment, the input impedance does not have any inductive component. Entirely real impedance is obtained.

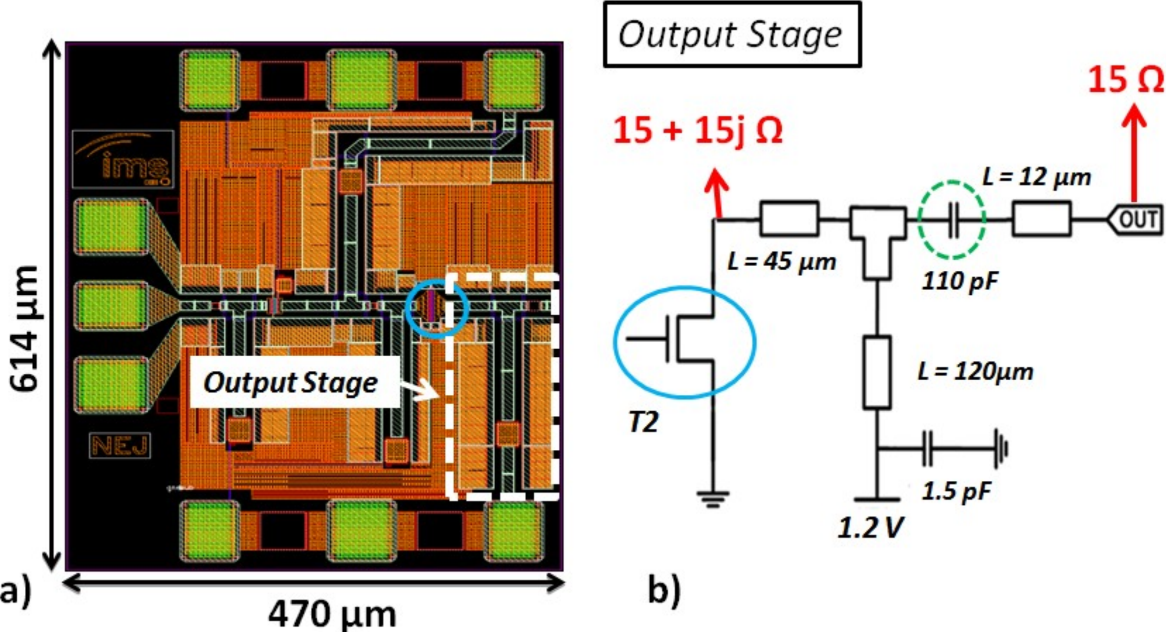

Figure 86 Modified transistor layout for a 15 Ω match a) Highlighted - Output stage (white) and - transistors (yellow) and b) Output stage Schematic

As commented before, some of the output stage elements (transistor biasing and DC decoupling capacitor) could not be removed from the transistor output. Consequently, the 1 dB passive loss mentioned before for this 50 Ω configuration output stage cannot be completely eliminated. Passive elements considered here are CPW lines and capacitors of the input, inter and output stages. But an efficiency increase is still achievable due to a partial suppression of output passives stage. For the initial 50 Ω configuration, a total of 3.5 dB loss is obtained taking into account all stages. With this partial output stage elimination, a 0.4 dB reduction is achieved resulting in a total of 3.1 dB passive loss due to matching stages. A 11.5 % efficiency increase for the PA operation only is therefore expected.

3.b) A 15 Ω input impedance antenna

As shown before, low input impedance values can be achieved when using the second resonant mode of the slot. We have already obtained low impedance values (15 Ω) as seen in the parametric study in Figure 80. (Dimensions 2 mm (L_y) by 1.7 mm (L_x) and W_{slot} = 0.1 mm). This results in a 3.4 mm^2 size solution. Regarding the PA size (0.5 mm x 0.6 mm), which gives a total area of 0.3 mm^2, the antenna is ten times the size of the PA and evidently not optimally miniaturized for a low cost solution. The PA + Antenna configuration is shown in Figure 87.

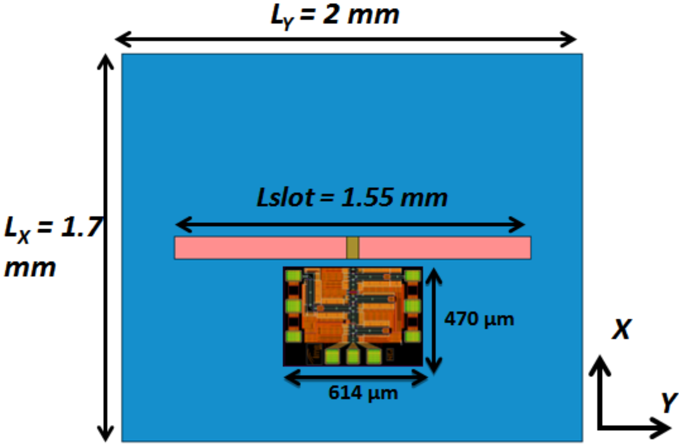

Figure 87 PA and slot dimensions for 1st 15 Ω solution

A solution for obtaining low input impedance could be obtained with $\lambda_g/2$ resonant slot. It would, however, require an additional adapting stage for lowering the high input impedance seen for the $\lambda_g/2$ resonance. An additional stage implies separating the PA from the slot,

consequently increasing the antenna size and adding an additional source of loss due to passives. The low input impedance of the λ_g is thus further investigated for a size compact and low input impedance solution.

Retaking a look at the parametric ground-size study of Figure 80, we can deduce that a low input impedance solution can be found for lower values of L_y and L_x. If we take a lower L_x value than that taken for the 50-Ω solution, lower impedance values can be obtained. In fact, a minimum value for L_x has been chosen to allow the incorporation of the PA. An important characteristic of the integration scenario is the low output impedance (< 50 Ω) and 50 Ω characteristic CPW. Due to this configuration, the PA has to be placed as close to the slot as possible to avoid a large CPW feed line and consequently mismatch. L_x has now a value of 1.3 mm that allows the positioning of the 470 µm long PA and ensures the smallest L_x value.

L_y is also reduced, and as consequence, L_{slot} has to be also reduced. As mentioned before, the perimeter of the slot determines the resonant frequency of the slot. As the slot is reduced, a higher frequency is obtained. This frequency cannot be regained by enlarging the width of the slot as it would displace the PA and L_x would need to increase. It would also increase Z_{in} which would be counterproductive. Rather, the phenomenon depicted in Figure 85 and explained before is used in part to decrease the resonant frequency as well as L_{slot}. A minimum 65 GHz resonance is achieved by taking advantage of the slot and chip edge. Dimensions are now 1.4 mm (L_y) by 1.3 mm (L_x) and W_{slot} = 0.1 mm. As expected, a smaller size solution with only 1.87 mm^2 has been achieved, having a reduction ratio of 2 with respect to the initial configuration (Almost half as that taken as initial configuration).

A different strategy is taken to achieve a 60 GHz resonance. Due to the small size of the PA, one has certain freedom regarding the position of the PA in the Y axis as depicted in Figure 87. This means that the feeding port position of the slot can be displaced. The slot shift will have a high impact in the frequency of resonance of the antenna.

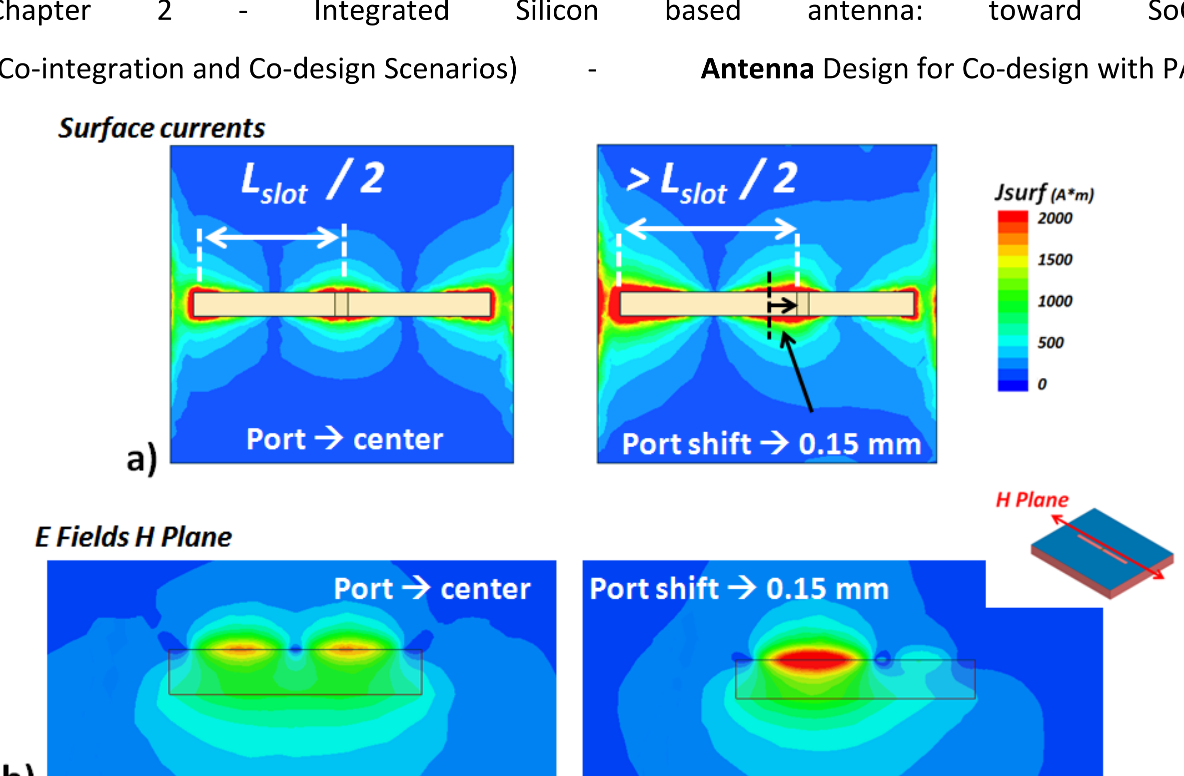

Figure 88 Surface currents for a) port at the center @ 65 GHz and port at 0.15 mm @ 62 GHz and b) Electric fields in the H plane for both configurations

As seen in Figure 88, the surface currents are compared for a centered fed slot and a shifted fed slot. Our undisturbed resonant mode is seen in a) where a distance of $L_{slot}/2$ is obtained between the currents maxima. As the port is shifted, the two maxima start to move away and a lower frequency of resonance is obtained. The antenna passes from a 65 GHz to a 61 GHz resonance for 0 and 0.15 mm shift respectively (Figure 89 a). The impact on Z_{in} is minimal for low impedance values. A 1 or 2-Ω shift is enough for a 10-dB shift in the matching value. As we can see, as the port moves, the maximum current center region moves along, keeping the port always at a high field level which ensures an almost equal impedance level.

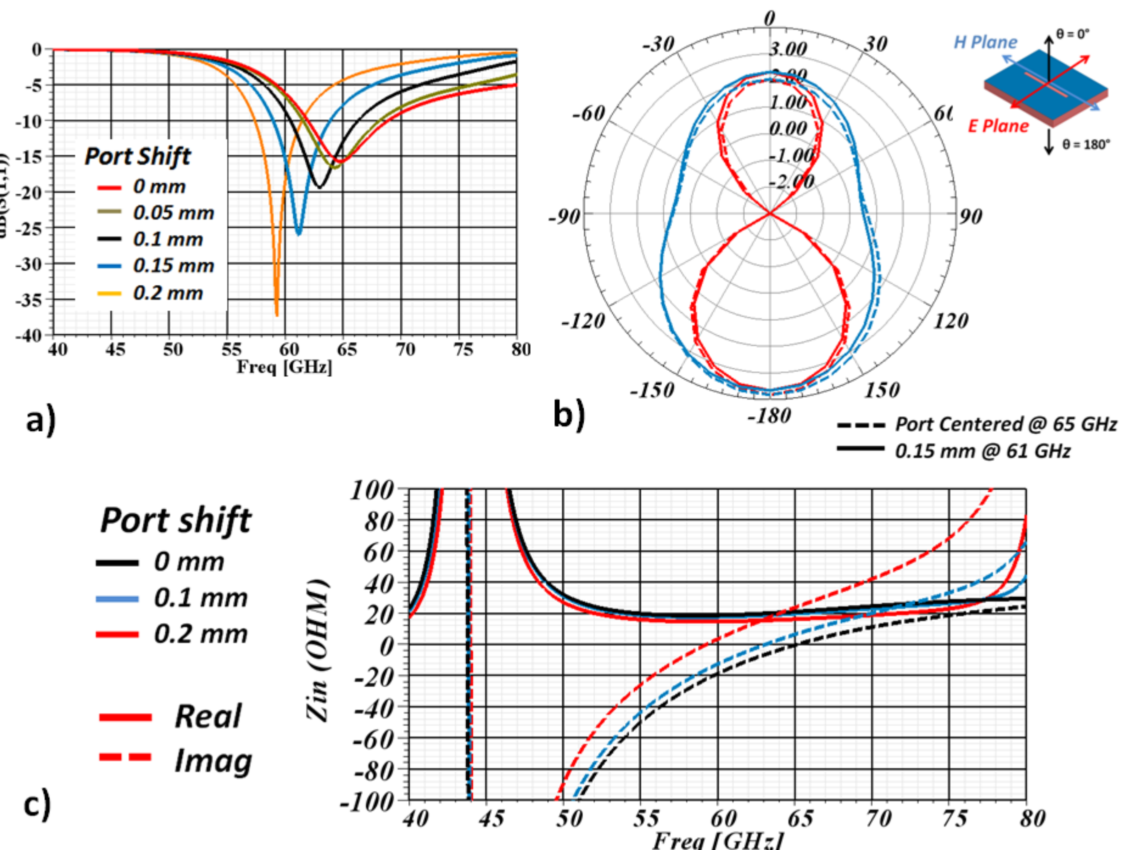

Figure 89 Port shift study a) S11 response b) Gain Pattern for Centered Port and 0.15 mm shift and c) Z_{in}

The electric fields for 0 mm and 0.15 mm slot feed position are also shown (Figure 88 b). A redistribution of the electric field can be observed, passing from two symmetrical high field regions to a one asymmetrical high field concentration. This causes a slight gain pattern modification. A decrease is seen for the F/B. Note that the gain values at θ = 180° maintain the same level. The F/B ratio decreases due to the increase at θ = 0°. The port shift seems to favor the radiation of low θ values. The asymmetric configuration also impacts the radiation symmetry seen before, and a slight tilt is seen on the H Plane.

3.c) Final Antenna configuration

From this 0.15 mm shift position value, the CPW line is added. As seen before for the 50 Ω case, the excitation of the slot is not the same for the only port excitation (port configuration used until now) as it is when a CPW is added. A decrease of the resonant frequency is also observed. A value of 57 GHz is obtained. Note that by decreasing the port position shift, the 60 GHz frequency can be obtained again. This is what has been done, but instead of shifting

the excitation, the slot is displaced with respect to the silicon substrate edge maintaining the port at the same relative location. Final configuration is seen next (Figure 90) as well as the bandwidth (4.8 GHz @ VSWR < 2) and gain (max gain = 3.4 dBi @ θ = 180°).

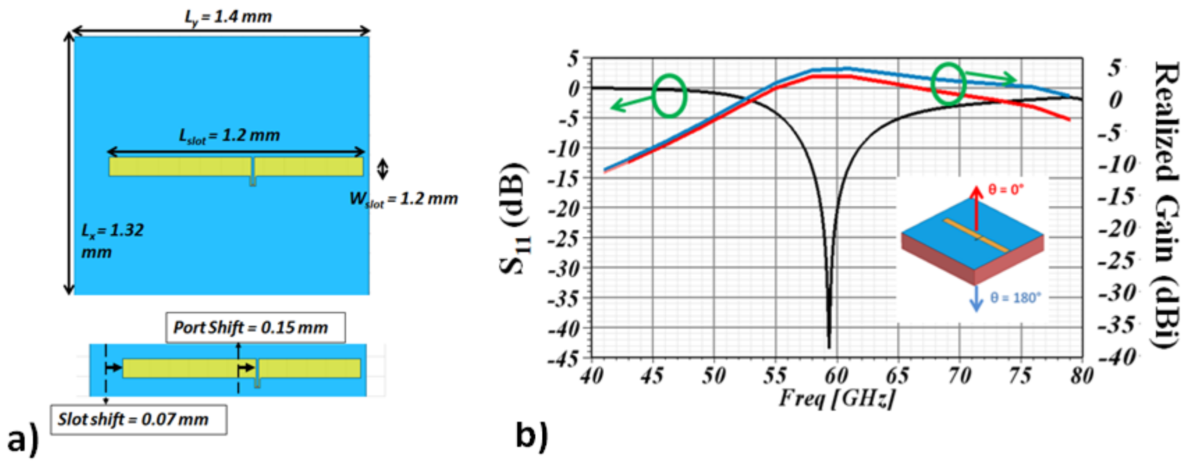

Figure 90 a) Final 15 ohm slot configuration and b) Performance expected for S11 and realized gain

For the 50-Ω as for the 15-Ω final configurations, a bidirectional radiation is observed. This is clearly not suited for our application where a single radiation direction should be obtained to remain compatible to a LOS (Line of Sight) scenario. To solve this, an additional metallization layer acting as a reflector can be added to the configuration. It can be part of the telephone PCB circuit or can be integrated in the packaging element. A λ/4-distance between slot and reflector should be ensured for a constructive field addition. As a counter effect, the antenna gain bandwidth is reduced due to the single frequency value at which the "λ/4" distance is ensured. An additional optimization procedure is thus needed, as the antenna input impedance and resonant frequency will surely be modified.

After the antenna design for Co-integration and Co-design scenarios, a global (PA – Antenna) energy assessment is presented.

4) Global energy budget

A global energy budget is now possible by taking into account the passive loss of the PA for both configurations (Co-integration and Co-design) and the antenna efficiency. These values are shown in Figure 91. A difference of 0.4 dB is obtained by the co-design strategy which offers an efficiency increase of 8.5 %. Next, the antenna performance is added to obtain a

global energy view of the system. The 88 and 90 % antenna efficiency values for the co-integration and the co-design scenarios show that the global efficiency gain comes mainly from the PA passive reduction strategy. Even more, the 88 % efficiency of the co-integration case will increase if the CPW line lengths for both antennas are made the same. A 0.6 mm long CPW line has been included for the co-integration simulation. This should reduce the global energy gain to 8.5 %. A size reduction of 24 % is though still obtained.

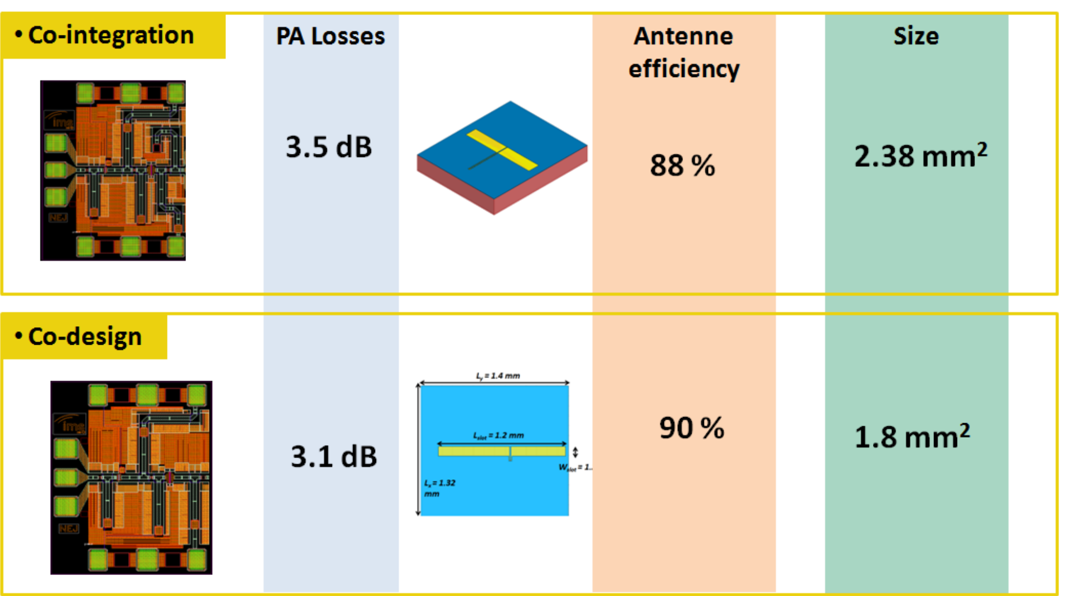

Figure 91 Global energy budget: PA losses (due to passives), antenna efficiency and total solution size

5) 50 Ω Antenna Measurement

Because the boundaries of the antenna have an important impact on its performance, a dicing (cutting) procedure was requested after its fabrication. After dicing, the obtained antenna dimensions obtained were different from those expected. The same band is still covered (55 to 75 GHz) although a 7 GHz shift (from 60 to 68 GHz) for the optimal matching point is observed. The obtained dimensions and matching responses are depicted on Figure 92. A frequency shift toward higher frequencies is seen and explained by the increase of L_Y (from 1.4 mm to 1.61 mm).

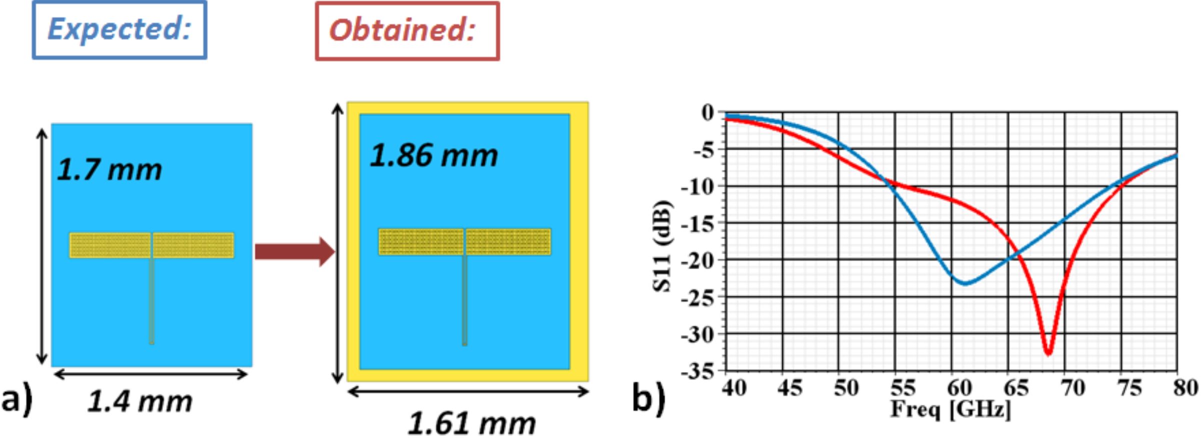

Figure 92 Change in antenna dimensions after cutting a) Dimensions expected and obtained b) Matching response

5.a) S11 Measurement

The matching response of the antenna was then measured. A 60 GHz central frequency was obtained as seen in Figure 93 (green curves). Two measurements were done and the same response was achieved. A new element had to be included to explain the shift in the antenna response: the measuring probe. The mm probe and the landing pads on the antenna were included in the simulation. Description of the probe and pads are seen in Figure 94. The new result is also compared in Figure 93 (red curve).

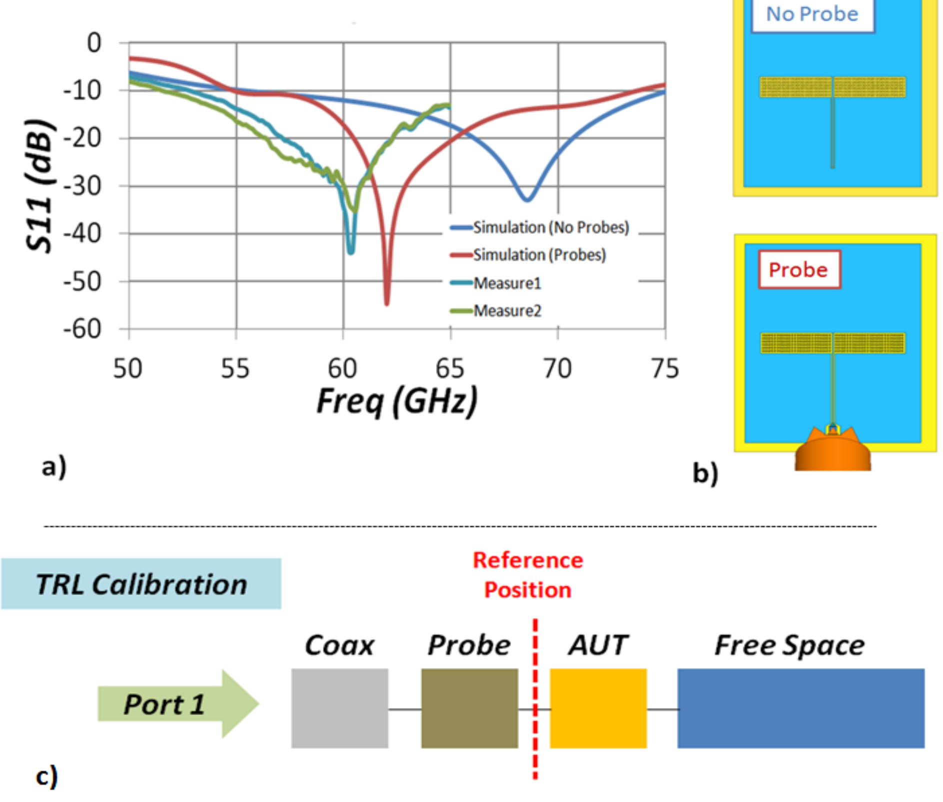

Figure 93 Matching results and simulation configuration a) measured vs. simulated results b) Probe – No Probe scenarios and c) TRL calibration

From the configuration where the probe is included, two questions arise to explain the new response. Not only the probe presence justifies the difference between the 2 situations (Probe vs No Probe). The port position has also been modified. It no longer excites directly the CPW but excites rather the same mode at the tip of the probe that is connected to the CPW by way of the pad (see Figure 94). These two configurations are studied to be able to determine the origin of the frequency shift. First of all, we have excluded most of the probe body from the simulation. Only the probe tip remains; it contains the port that excites the structure. On the other hand, we have included all the probe body but changed the position of the port; it now excites directly the CPW. The probe tip touches the metallization of the CPW to assure electrical continuity resulting in the same configuration as when the port is placed on the probe. These two configurations can be seen in Figure 95.

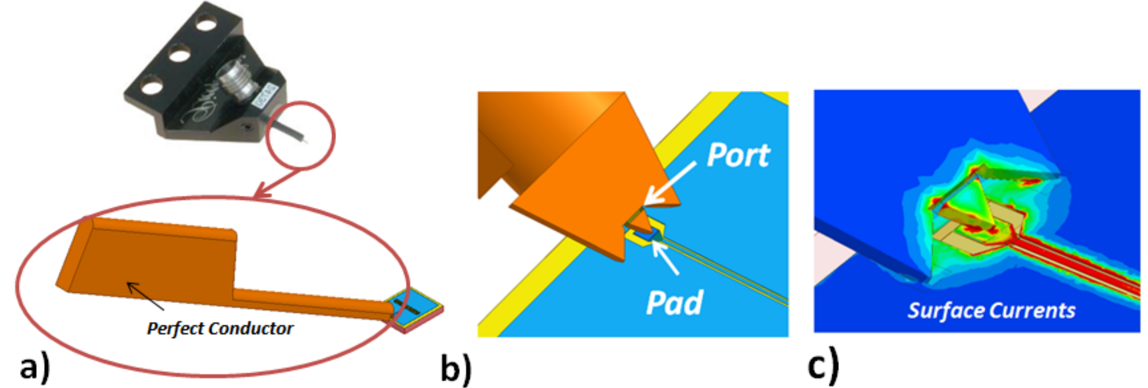

Figure 94 Probe description a) Only Tip of the probe (Pico Probe 67A) b) Port and Pad and c) Surface currents after simulation (62GHz)

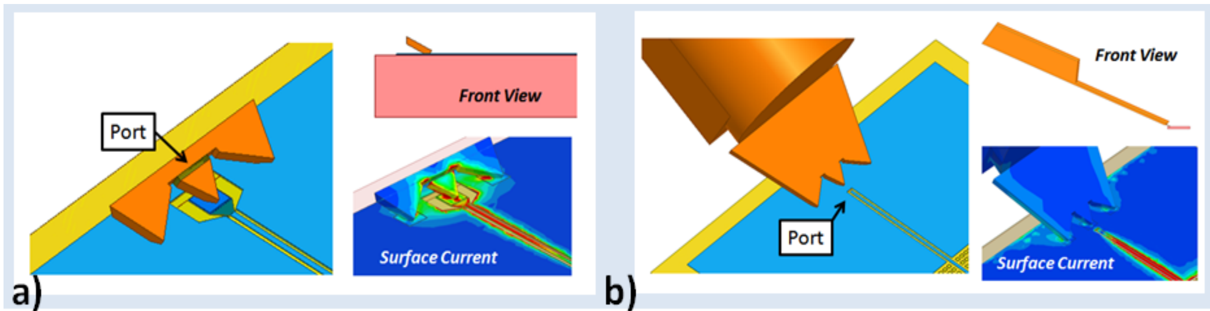

Figure 95 Configurations for a) Only probe tip with excitation and b) Not excited probe (Port on the CPW) (Front view and Surface current shown also

The matching response is now compared between the previous two configurations and the "No Probe – Probe" configurations of Figure 93. Starting from the "No Probe" configuration, we find the "Only Probe Tip" configuration follows in most part of the frequency band the "No Probe" response. Note that a 1 GHz shift is seen between these two responses in the matched portion of the band this is. With the addition of the probe (maintaining the port on the CPW "Probe (Port on CPW)") a 4 GHz shift is seen approaching the 62 GHz resonance of the "Probe (Port on Probe)" configuration. The S11 response for the "Probe (Port on CPW" also reproduces more closely the "Probe" (Port on Probe) response in the lower and upper part of the band. Clearly, we can see that the presence of the probe, rather than the position of the port, impacts in a mayor degree the response of the antenna. The electrical fields for the "Only Probe Tip" and "Probe" (Port on CPW) are also depicted in Figure 96. It is observed a good symmetry of the electrical fields for the "Only Probe Tip". In comparison, this symmetry is broken when the probe is added. Due to a high field concentration on the

edge of the substrate where the probe is positioned during measurement, the presence of the probe will clearly have an impact on the performance of the antenna.

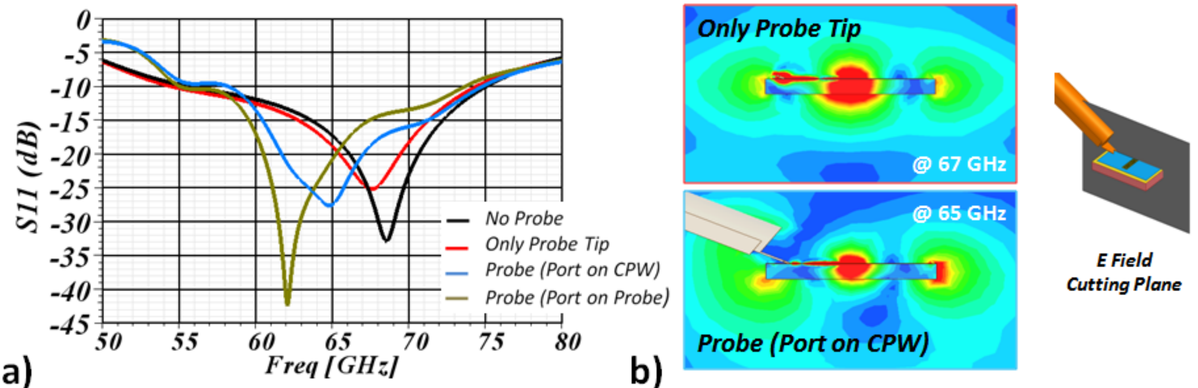

Figure 96 a) Matching response comparison for port placement and probe presence study and b) E field distribution for only probe tip and Probe (port on CPW) configurations

5.b) Gain Measurement

The presence of the probe can also impact the radiation properties of the antenna. Retaking the “Probe” and “No Probe” scenarios of Figure 93, the Realized Gain Pattern for both can be seen in Figure 97. The probe impact is immediately seen when taking a look at the E Plane simulation results. A high level gain (9 dBi) is observed at θ angles between 70° and 85°. This contrasts with the -10 dBi gain that the antenna should have and is observed in the “No Probe” radiation pattern (red dashed line). Lower gain levels are seen at θ = 0° and 180°. A decrease from a 4 dBi to an approximate 1.5 dBi is observed. This can be explained by taking into consideration the amount of energy that is now exciting the structure through the side (θ ≈ 75°) where the probe is located. Matching level is ensured for both the “Probe” and “No Probe” configurations and no energy is lost in the Probe as it consists of a PEC material (Perfect Electric Conductor). The energy is now relocated differently due to the presence of the probe.

A second but less evident effect can be also observed on the E Plane. The field for the Probe scenario can be thought of being tilted regarding the “No Probe” configuration. In the “No Probe” configuration, maximum values at each hemisphere (top hemisphere -90° < θ < 90° passing through 0°, bottom hemisphere -90° < θ < 90° passing through 180°) were at θ = 0° and 180°. By adding the probe, an inclination of the field toward the positive θ values for the

upper hemisphere is observed. In this same way, the “No Probe” maximum radiation direction (θ = 180°) has now shifted and appears at θ = -110°. One can see a higher gain at this value for the “Probe” configuration as for the “No Probe” configuration. Probe impact is also much higher in the E Plane that in the H Plane. Taking a look at the cross polarization in both planes, we notice the cross polarization level for both configurations differ greatly for both planes. While in the H plane, cross polarization levels remain almost the same, a 20 dB difference can be found at some angles in the E plane. This is just logically due to the presence of the probe in this plane.

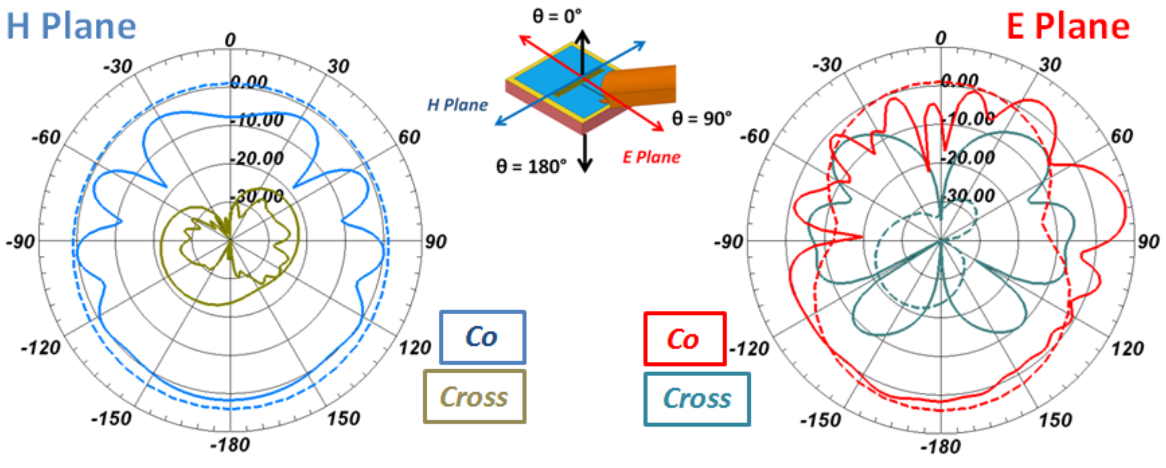

Figure 97 Realized Gain patter for H and E Plane. Dashed Line for No Probe (@67 GHz) and Continuous Line for Probe (@ 62 GHz) Scenario. Cross polarization levels are also shown.

Gain measurements were done for broad and back side radiation configurations. The test bench description is seen in Figure 98. A more complete description of the back side radiation measurement setup is done in Chapter 3. In both cases, a 10 dBi Rx Horn antenna is used.

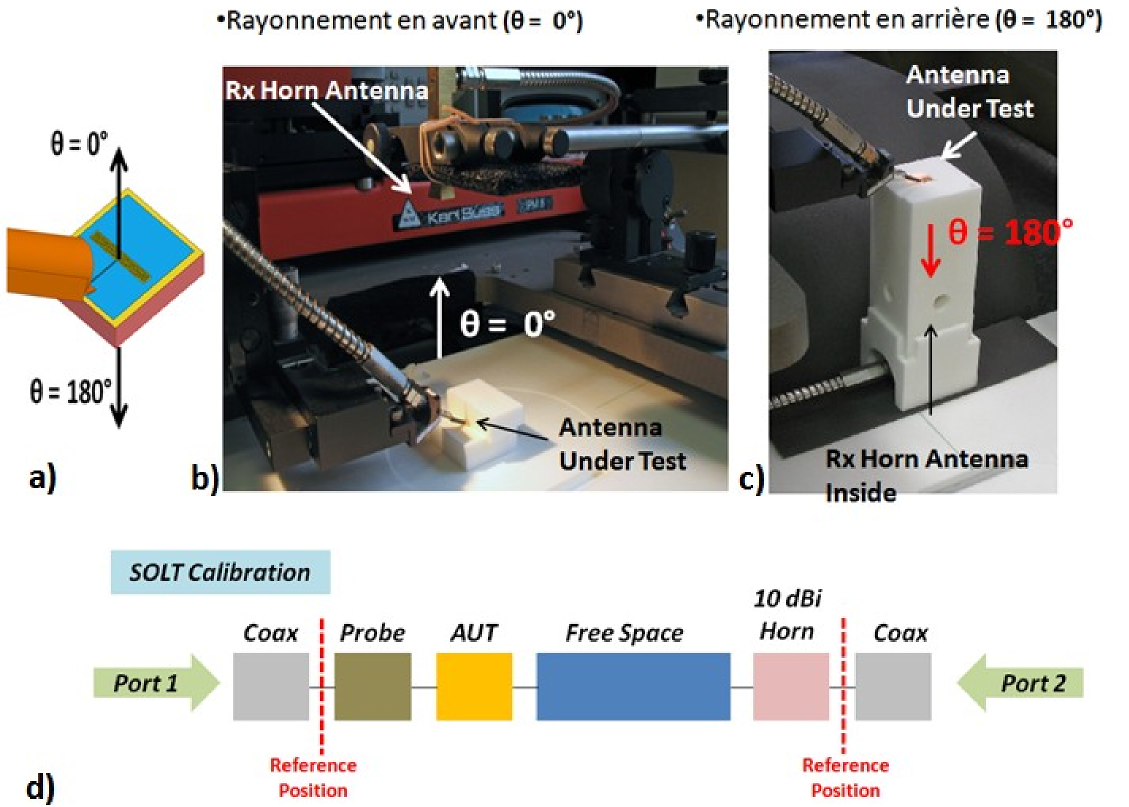

Figure 98 Test Bench for Gain Measurement a) θ = 0° and θ = 180° b) θ = 0° Configuration c) θ = 180° Configuration d) Test bench calibration

Measurement for Co and Cross polarization are shown in Figure 99. Good agreement is seen for the Co polarization response at θ = 180° (or backside radiation). This was not the case for the broadside radiation measurement (θ = 0°). However, by taking a look at the broadside radiation on E Plane (Figure 97), we can see that for an aperture angle of 20° (-10° < θ < 10°), gain values can vary from -20 to -5 dBi. A much more accurate response is then found at 10° (green dashed line). The measurement test bench cannot assure a θ = 0° positioning. Cross level values show also a good agreement although more important noise component is observed due to the lower energy levels measured. The 10° shift was also taken into account for the θ = 0° measurement. “No-probe” simulated gain values are also shown. As expected from the gain pattern, a decrease in gain is seen for the backside levels, in this case almost throughout the band, from 3.4 dBi down to 1dBi. For broad side radiation, the effect of the probe is even more evident. Difference in levels of up to 10 dB is seen. For the case of the cross polarization, the probe clearly increases the level of cross polarization. This can be seen by the difference between the simulated responses of “Probe” and “No Probe”

configurations, with almost 20 dB difference at some frequencies. The measured levels of cross polarization are in good agreement with those of simulation that include the probe.

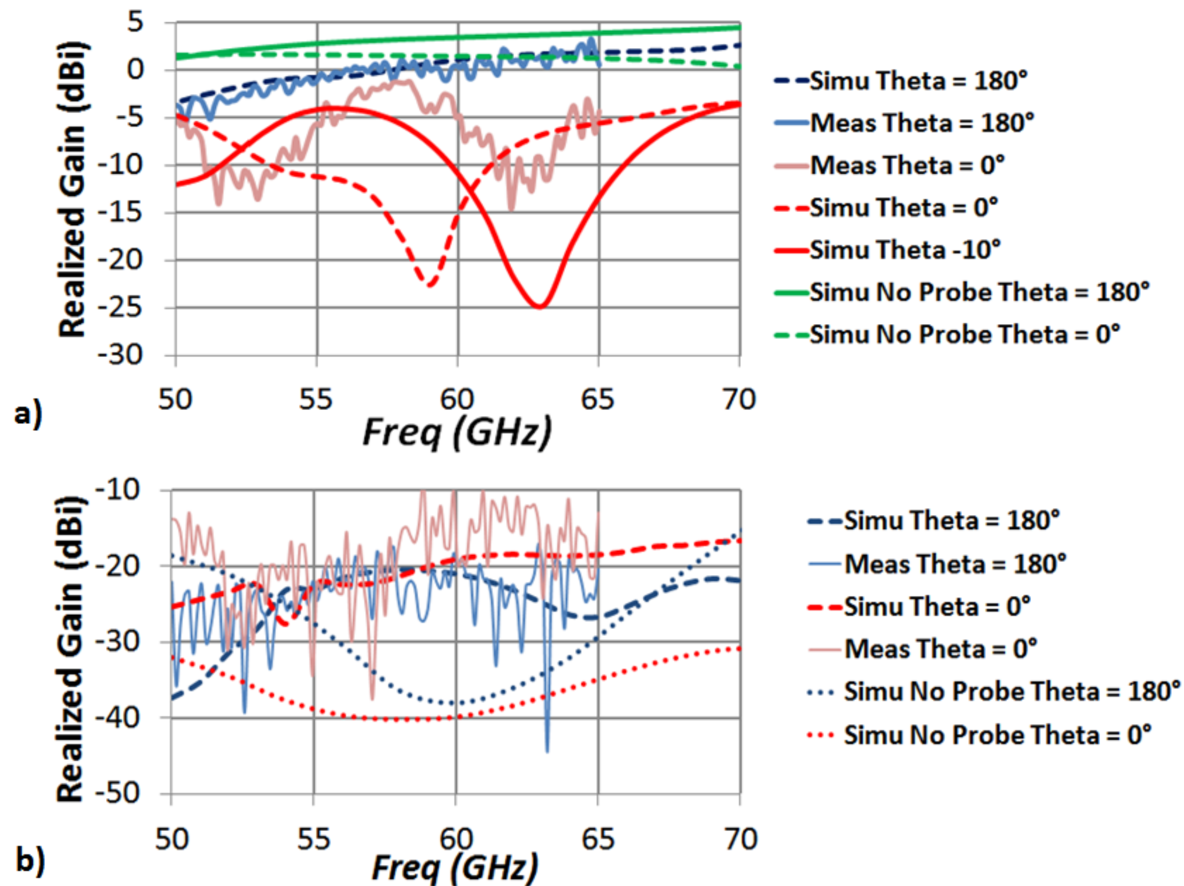

Figure 99 Realized Gain Measurements vs Simulation for Broad and Back side radiation a) Co-Polarization and b) Cross-Polarization (No PAD de-embedding was done)

The effect of the probe coupling to the antenna is studied in more detailed manner next. For instance, the impact of the probe presence is different if the angle of the probe changes. One can also try to identify if the coupling happens from the broadside or the radiation side of the antenna. Another parameter is the distance of the probe to the antenna. What could be the distance at which the influence of the probe can be neglected?

5.c) Probe angle incidence

The impact of the probe angle is studied next. Figure 100 shows the sweep done by the probe through simulation. S11 responses are compared, one with the antenna without the probe, and three different values of θ: 40°, 60° and 80°. The probe is in direct contact with the metallization of the antenna for all angles.

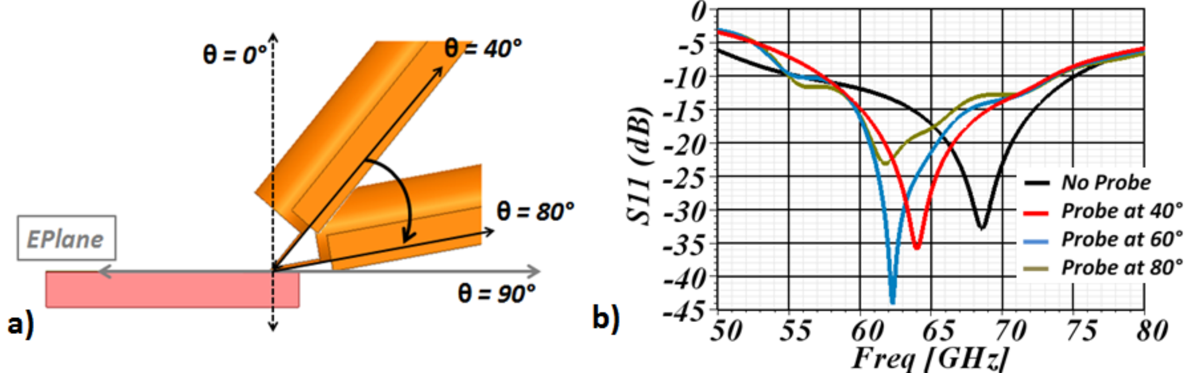

Figure 100 Probe inclination a) 40°, 60° and 80° probe angles covered b) S11 response for the covered angles

Beginning from the "No Probe" configuration with a resonance at 67 GHz, one can see that the impact on the antenna grows stronger as the probe reaches the 90° axis. The new frequencies of resonance are now 64, 62.5 and 62 GHz for probe angles 40°, 60° and 80° respectively. That is, the steeper the probe, the lower the coupling to the antenna. Not only the frequency of resonance shifts, but disturbances (ripples on the S11 curve) at several position angles can be seen, for example at 80° probe position where they become more notorious. This is confirmed by the gain pattern seen in Figure 101. The coupling is highlighted in all the figures by use of a green arrow. The coupling, as it can be expected, will change depending on the angle of the probe. Different maximum gain values are also seen at these coupling angles. 7, 8.5 and 9.5 dBi values are seen for 40°, 60° and 80° respectively. As expected, a maximum is then seen for the 80° probe angle. One can observe also the tilt of the radiation pattern mentioned before. The yellow arrows, that mark the presence of a maximum in the opposite direction of the field coupled to the slot, also rotate as the probe rotates. What is interesting to observe, is that the arrows (green and yellow) will always be rotated by 180°, just as the maxima seen for the "No Probe" configuration in Figure 101 a) marked by the black arrows. The rotation angle is also marked by the dashed line. The manufacturer assures a 60° for the Picoprobe™ probe and 50° for the case of Cascade-Microtec™ probe. This angle, of course, can vary depending on the pressure put on the probe at the moment of positioning and making contact on the antenna under test. Certain flexibility is ensured by the probe manufacturer.

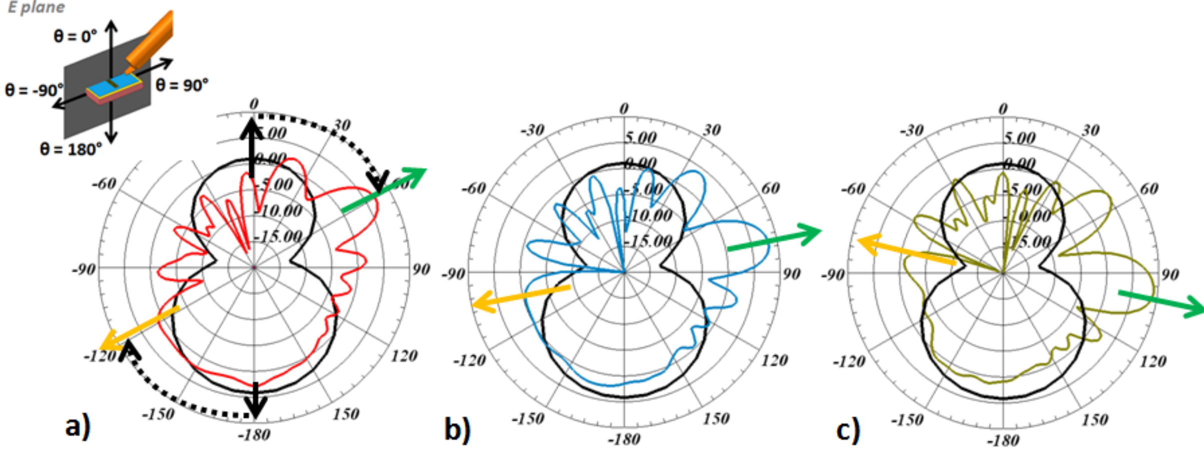

Figure 101 Gain pattern @ 63 GHz for a) 40° b) 60° and c) 80°

5.c.i) Probe coupling: broadside or backside effect?

Although the antenna has a higher gain at θ = 180° (4dBi), it does radiates in the opposite direction, θ = 0°, with considerable energy (gain 1dBi). From this, one can conclude that there are two possible coupling sources for the antenna and the probe. A phase study has been done and is shown in Figure 102 for a probe angle of 60° to be able to locate the coupling source. It can be observed that from 0 to 135° phase, the probe couples to the broadside radiation. This is logically due to the position of the probe within the broadside region of the antenna. Although this coupling exists, there seems to be another source that couples to the bottom part of the probe. This coupling has a stronger effect based on the color scale. The E field magnitude is higher on the back part of the probe regarding the E field magnitude on the top part. This is particularly visible for Phase 0° and Phase 135°. This "bottom" coupling has to do with the propagation of the energy through the substrate to the edges. As seen in phase 45°, a central and unique radiation source is responsible for the energy leaving the structure. As the phase changes, that is, as the energy propagates away from this central radiation source and arrives to the edges of the structure. At one of the edges, the energy will couple to the probe.

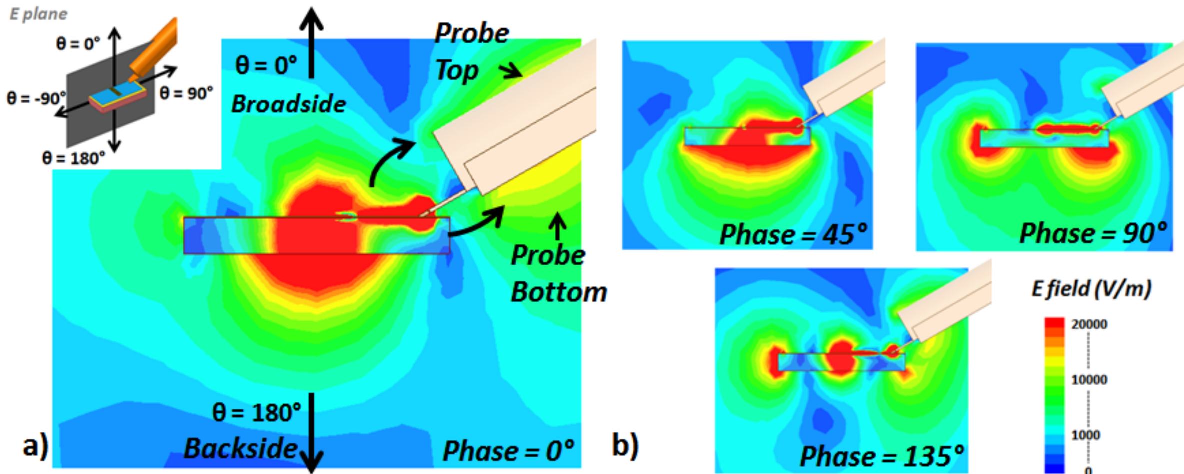

Figure 102 E field @ 63 GHz for Probe angle = 60° for phases = 0°, 45°, 90° and 135°

Antenna radiation without the probe is compared with two different probe angles in Figure 103. We can see that the antenna normally has a concentration of energy near the edges on the E Plane.

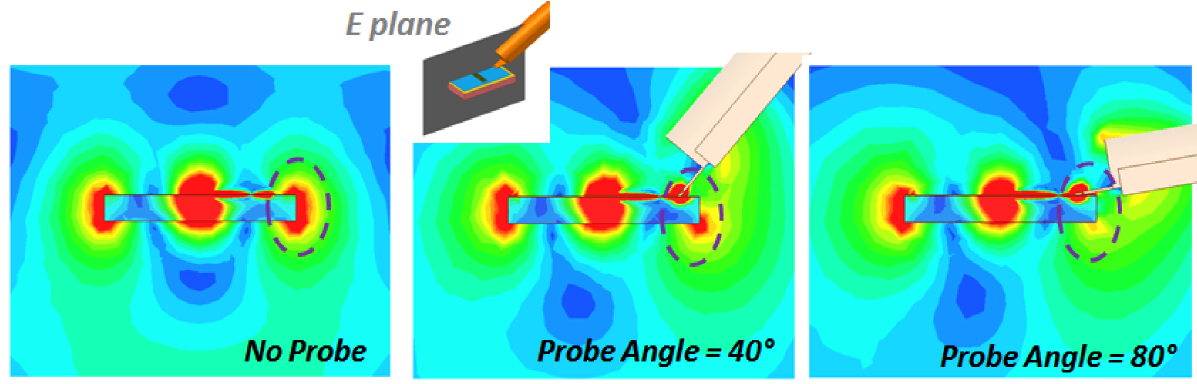

Figure 103 E field @ 63 GHz and Phase 135° for No Probe and Probe angle 40° and 80°

When the probe is added (40°), the field is no longer concentrated entirely at the edge but is now spread into a much wider area and coupled to the probe. When the probe reaches 80°, the field has almost completely disappeared from the edge. This should help understand the tilt effect. With the presence of the probe, one of the edges decreases its contribution to the whole radiation of the structure. The balance that the structure had when the two edges radiated is jeopardized. Now, one of the edges will radiate in an end-fire fashion (through the side) while the other will couple to the probe. Coupling from both “top” and “bottom” is seen. These two coupling phenomena come from the energy propagation (Phase 135°) once the slot has reached its peak at Phase 0°.

5.c.ii) Probe distance

The distance between the probe and the antenna is now studied. This should allow determining a “safe” measuring distance for the probe location. An intermediate transition interconnection could be added to the Probe-Antenna configuration to separate the probe body from the antenna.

First of all, a distance study of probe means a disconnection of the probe from the antenna. For this, the effect of leaving the probe as a floating element in the configuration is first studied. A first comparison between the “No Probe”, “Contact Probe” and a “Raised Probe” configuration is seen in Figure 104c. No distance has been added (L remains = 0), just a small shift on the Z position of the probe. As seen in the S11 response (Figure 104b), rendering the probe a floating element has a non negligible effect. Between the “Contact Probe” and “Raised Probe” responses, a 5 GHz shift is seen. The electrical path for the antenna generated current to reach the probe no longer exists. The antenna is now an isolated element and should approximate to the “No Probe” configuration. First, the S11 response shows only a 1GHz shift between the “Raised Probe” and the “No probe” configuration. Secondly, *“*Contact” and “Raised probe” Gain pattern response show a lower coupling at θ = 75° and an increase in gain at θ = 180° approaching the “No Probe” Gain value of 4dBi.

The distance between the probe and the antenna has also been studied. Three values of L are depicted in Figure 104d, where a decrease in probe coupling can be seen. The S11 response shows that for a 1 mm distance, the 68 GHz resonance frequency has been reencountered. With the same behavior for all the other values of L. (not shown for clarity)

Taking all this into account, we can conclude that the presence of the probe and its position will have a non negligible impact performance of the antenna. Note that the coupling of the probe depends greatly on the antenna radiation. Should the antenna under test radiate differently, the coupling to the probe will surely change. Separating the probe from the antenna under test, should allow measuring the antenna element and not the antenna-probe configuration.

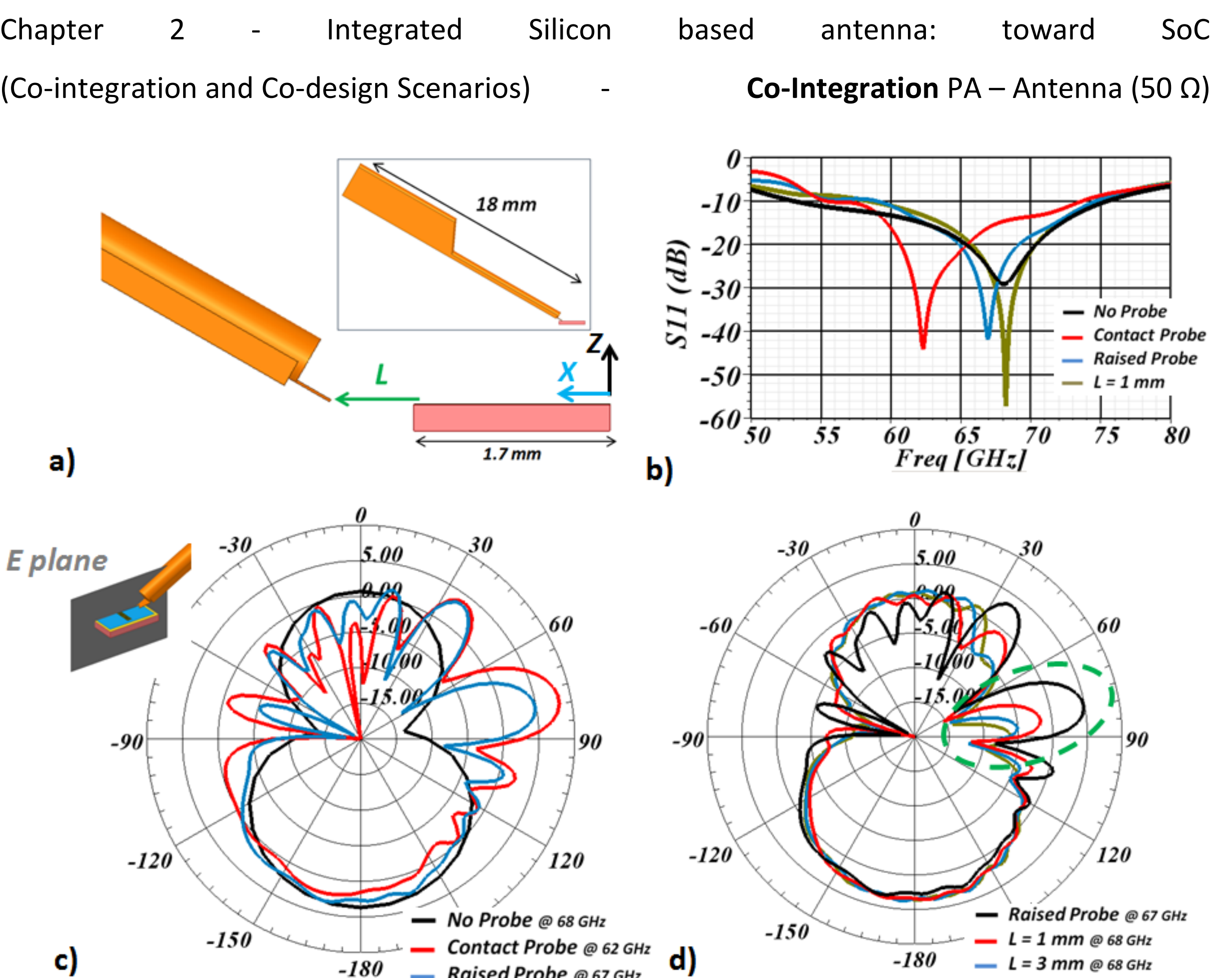

Figure 104 Separating the probe from the antenna a) Definition of L (distance parameter) b) S11 response c) Gain Pattern for Contact and Raised Probe and d) Gain Pattern for the distance study

6) Co-Integration PA – Antenna (50 Ω)

After the validation of the 50 Ω slot antenna, the integration with the PA comes next. Although the antenna has been designed taking into account the small size of the PA, it is several times bigger that the PA (PA size = 0.614 x 0.565 mm^2 and Antenna size = 1.86 x 1.61 mm^2).To limit the PA-Antenna size, the PA has been included in the metallization of the antenna. This is possible due to the CPW configuration of the PA that renders a great portion of the PA as metallization. In this way, the metallization of the antenna should not be disrupted or affected greatly. Due to the 50 Ω-input-impedance antenna, a crucial flexibility is achieved in terms of PA position (distance of the PA to the slot). No need for matching stages is required. Just by extending the 50 Ω CPW line, matching between the PA output and Antenna Input is ensured for any PA-Antenna separation. In fact, the separation of the PA and the antenna slot has an important impact as it will be shown next.

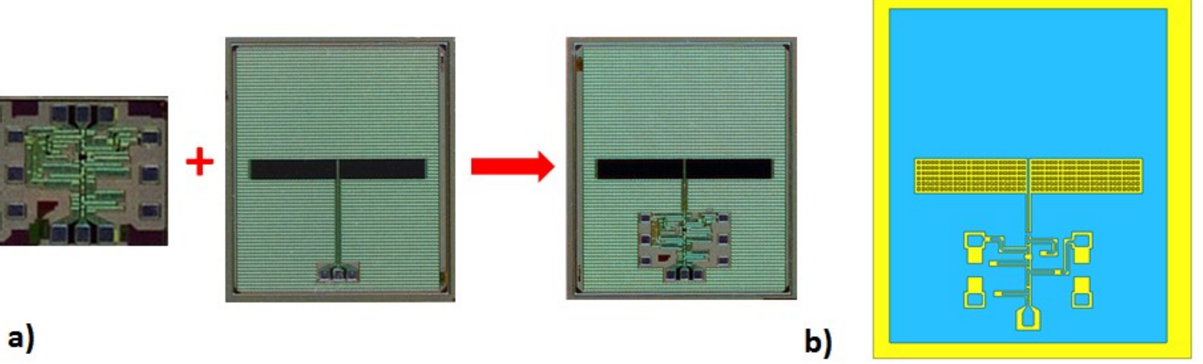

Figure 105 a) Fabricated PA + SOI based 50 Ω based antenna = Integrated PA and Antenna b) Layout of PA incorporated to the antenna design (Configuration for EM Simulation).

The final fabricated configuration is seen in Figure 105a.

6.a) Simulation of Co-integrated PA + Antenna

The Co-integrated PA-Antenna configuration adds new challenges from the simulation point of view. The different nature of the circuit simulator needed for the PA and the 3D Electromagnetic (3DEM) simulator needed for the antenna induces difficulties for the "Co-Simulation". The circuit simulator, which includes transistors and line models, cannot take into account the radiation effect of the antenna. The antenna can only be included as a model with certain impedance characteristics. With analogue constraints, the 3D EM cannot include the transistors presence or the antenna radiation impact on active devices. The complete circuit-antenna simulation is not possible.

Although the entire simulation is not possible, the impact due to the PA presence (without the electrical presence of transistors) can be taken into account with the 3DEM simulator. For this purpose, the layout of the PA -i.e. metallic parts only- has been included in the antenna 3D simulated design. By doing this, a parametric study the PA presence can be done. The layout includes the CPW lines and the DC and RF pads. The final PA-Antenna ready for simulation is seen in Figure 105 b.

6.a.i) Parametric study PA – Slot distance

Three separation distances of PA and Slot were simulated and compared to that of the antenna without PA. In all of them, the port exciting the CPW was maintained at the same distance (0.05mm) for all configurations (Figure 106). That is, a 0.05 mm long CPW fed the

slot in all cases. In this way, the PA coupling to the slot could be studied independently from the PA coupling to the CPW. As first results, one can see on the S11 response that the PA position has a high impact on the matching of the antenna. Matching levels change passing from -60 dB at 0.05 mm and reaching -26 dB at 0.25 mm. Although the antenna remains matched for at least over a 15 GHz band in all cases, a bandwidth reduction is observed regarding the “No PA” response with its 22 GHz bandwidth. This variation of the S11 response is also visible in the gain response. Drop in gain levels from 10 to 6 dB are seen at 50 and 74 GHz respectively. It can also be observed how the gain drop is stronger as the PA approaches the slot. This leads us to think that the antenna is somehow interacting with the PA or with some of its components (CPW line or Pads).

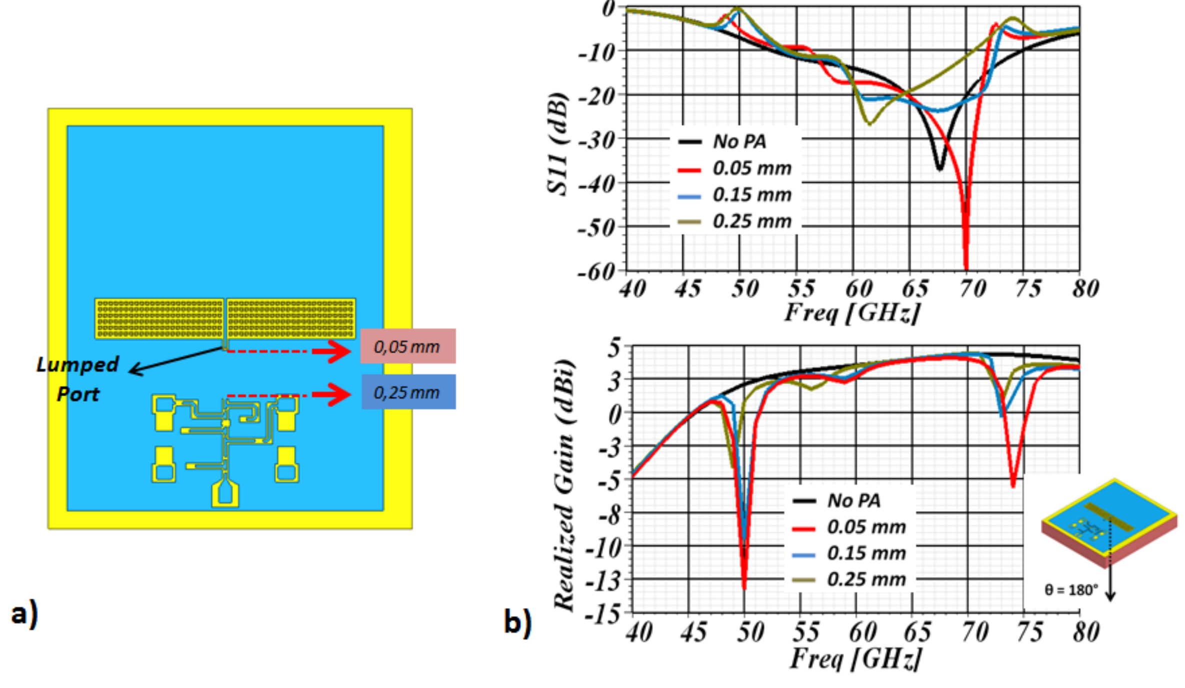

Figure 106 Distance of PA – Slot study a) Distance covered by the PA and b) S11 response for 0.05, 0.15 and 0.25 mm

Surface currents are shown to see if they will give some insight into what is happening. For all four cases, No PA, 0.05, 0.15 and 0.25 mm surface currents at 67 GHz are shown. Coupling to one of the PA lines is observed (highlighted). As seen before, stronger coupling is seen as the PA moves closer to the slot. First of all, a “slight” impact due to the PA presence is seen on the S11 (still matched). A small variation on the input impedance is witnessed. The coupled line can now be considered as a stub. It is a CPW line segment open ended that adds an impedance component to the total input impedance seen by the port. And at

second hand, the gain response remains almost constant at this frequency (67 GHz). Level between 4 and 4.2 dBi are seen and explained by the different in matching level (S11). Thus, the line does not contribute to the antenna radiation.

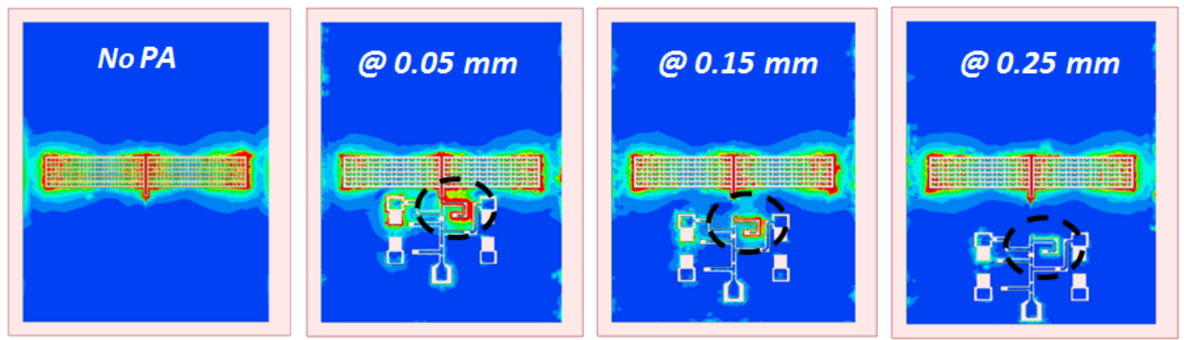

Figure 107 Surface currents @ 67 GHz for all four cases: No PA, and 0.05, 0.15 and 0.25 mm PA distance.

6.a.ii) The PA coupled resonating elements

For 50 and 74 GHz cases, the same procedure is considered. Surface currents are depicted in Figure 108. Here, other coupling phenomena are observed. For the two cases, some of the PA components seem to resonate together. At 74 GHz, one of the pads and a line couple to the slot. For the 50 GHz case, two pads show the same behavior. This resonant-elements separation is shown by "***L***". An increase in the electric resonance length can be seen when comparing the 74 and 50 GHz cases. This is a normal behavior for a resonant element when the frequency increases. One concludes that the elements coupling to the slot form a resonating structure. The electric field is now plotted for both 74 and 50 GHz and compared to the No-PA configuration. As the resonating elements enter in resonance, no radiation from the slot is observed anymore. At 74 GHz, the pad-line configuration radiate by itself modifying completely the radiation performance of the antenna. The pad-pad configuration at 50 GHz shows the same behavior. These resonating structures are responsible for the radiation disturbance seen in Figure 106.

Figure 108 Surface Currents and Electric fields for 74 and 50 GHz.

The PA is now positioned at 0.2 mm from the slot. The CPW line is extended to reach the output of the PA. This is the final CPW and PA configuration. The PA presence has also an important impact in the cross-polarization levels. Using this last configuration, the cross-polarization of the antenna is studied. Three configurations are compared in Figure 109 to determine the origin of high cross polarization levels. First of all, a “No-PA” with a short CPW line (0.05 mm) is shown to quantify the normal level of polarization for the antenna alone. Cross levels oscillate around -60 dB’s. In second hand, the same configuration with a longer CPW (0.2 mm) is shown. This is the length of the line that the antenna will have once the PA is introduced. The cross polarization increase related to the line is normal. As we stand outside of the antenna matched band, the impedance seen at the input of the antenna is different from the 50 Ω value. This creates a resonance on the CPW due to the stationary wave created by the reflected energy. Higher cross pol can be seen at the lower and higher part of the band.

After this, the PA is added to the configuration. An increase of 50 dB is suddenly obtained. The cross polarization levels are even higher at the aforementioned PA-Slot coupling frequencies (50 and 74 GHz). It is also evident at 58 GHz where a decrease in Co-Polarization is seen for all PA distances in Figure 106. This last decrease corresponds also to the coupling of PA components; in this case and as for the 50 GHz case, two pads enter into resonance.

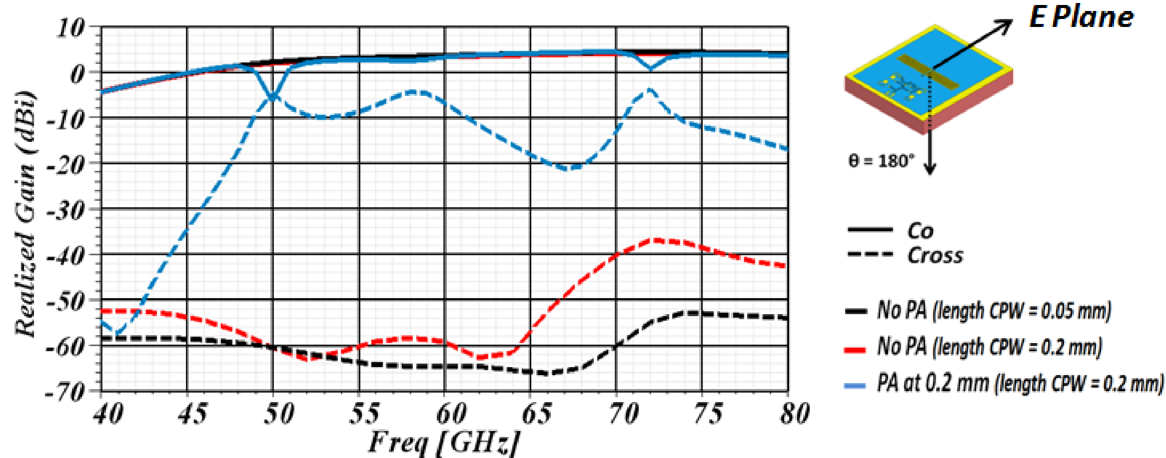

Figure 109 Co and Cross polarization levels for No PA and PA included slot @ θ = 180°

To explain the high level of cross polarization, the electric and magnetic field distributions for the slot and dipole are shown in Figure 110d. Clearly, our antenna behaves as a CPW fed slot. The H field and the E field components are parallel to the Y and X axis respectively. For the dipole, maintaining the same reference plane, the H and E components are parallel to X and Y axis respectively. If we assume now that the resonating mechanism of the coupled structures of the PA resonate as a dipole, one can conclude that the E and H field components of one structure (e.g. the slot) are perpendicular to those of the coupled PA elements (e.g. two pads @ 50 GHz). A lower Co level and higher Cross level is the result. The same situation is observed for the resonant structure at 74 GHz. A slightly different situation is seen for the 58 GHz coupling, where the coupling elements are not parallel to the slot axis (Figure 110a). This rotation decreases the H and E field components in the perpendicular plane to the slot plane. This explains the increase of cross polarization at this frequency and the lower impact on the Co-polarization levels regarding the 50 and 74 GHz cases.

•Surface Currents @ 58 GHz

Figure 110 Final configuration 0.2 mm PA-Slot distance a) Surface currents @ 59 GHz and d) Slot and Dipole E and H field distributions

Expected gain and matching performance have been obtained for the PA-Antenna 50 Ω configuration. The same study is also done for the 15 Ω antenna to obtain the expected performance of the PA-Antenna at Co-design.

7) Co-design of PA and Antenna (15 Ω)

The new size of the antenna is shown in Figure 111. As expected, the change in size has drastically modified its performance. A 25-Ω input impedance has now replaced the lower 15 Ω matching condition as well as incorporating a frequency shift of 2.5 GHz. As we are dealing with low impedance values, the matching performance of the antenna becomes more sensitive to an impedance change. Compared to that of the 50-Ω antenna, a change of 10 Ω represents a 20 % variation (10 Ω difference of the ideally 50 Ω), while it represents a 66 % for the 15-Ω case. Although the matching conditions are not optimal, gain still shows good performance and maintains levels of 3 dBi. As we add the PA, the matching performance is slightly affected with a drop of several dBs in the lower band (40 – 67GHz). However, as we reach the top part of the band, a similar situation has been found with the 50 Ω antenna. A resonating element has been introduced with the PA. The cross polarization level at 70 GHz for the New Size + PA curve clearly indicates the presence of a radiating element that find itself in an orthogonal position regarding the position of the slot.

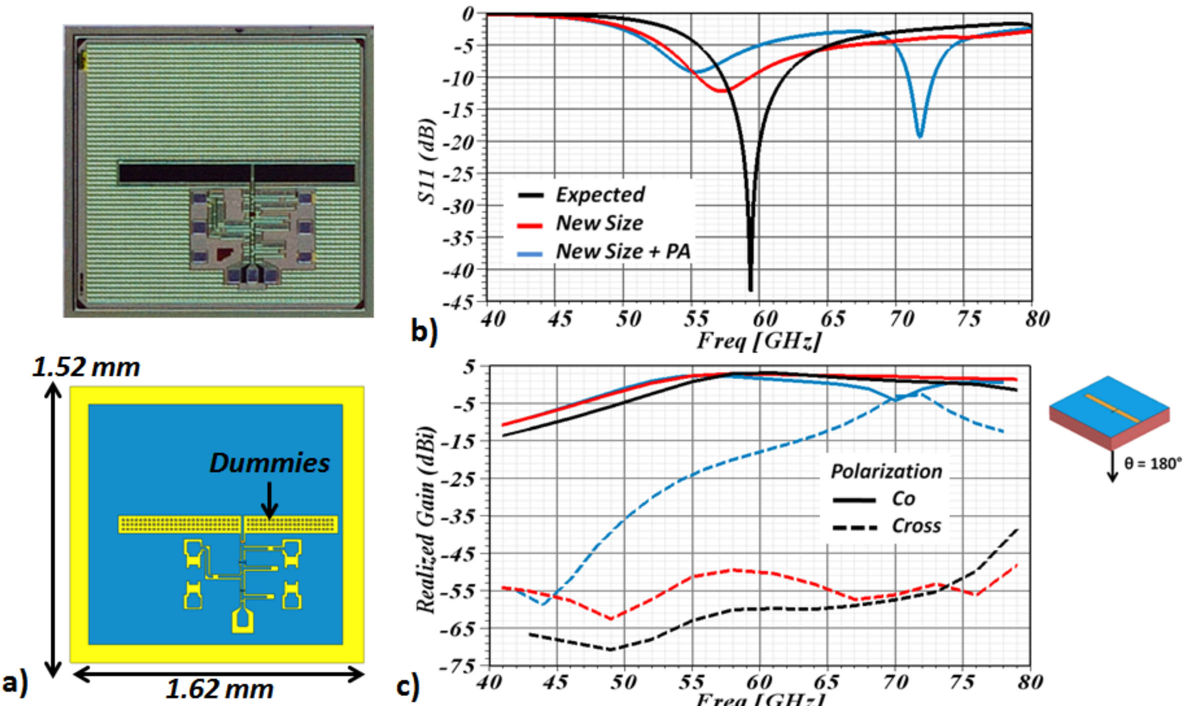

Figure 111 Final antenna design (New size and PA) a) Real chip and Simulated design b) S11 response and c) Realized Gain (Co & Cross) for θ = 180° of expected, New Size and New Size with PA.

The previous simulation studies have permitted us to obtain the expected matching and gain response of both PA-Antenna configurations. The PA presence has been studied and its influence on the antenna has been determined. In both cases, resonant PA element coupled to the slot generating a high cross-polarization. Chip sizes were seen to have high impact on the input impedance and resonance of the antenna. These effects should be visible in the measuring stage which is presented next.

8) Measuring Integrated PA-Antenna

After seeing what can be expected from the PA-Antenna integrated configuration, a supporting device has to be designed for measurement. This module should allow ensure biasing of the PA (insertion of DC signals) and support the antenna. The DC circuit has to include the decoupling capacitors needed for filtering the DC signal. These capacitors and their position in the designed circuit are shown in Figure 112. Wirebonding is used to deliver the signal from the DC routing circuit to the On-Chip pads of the PA.

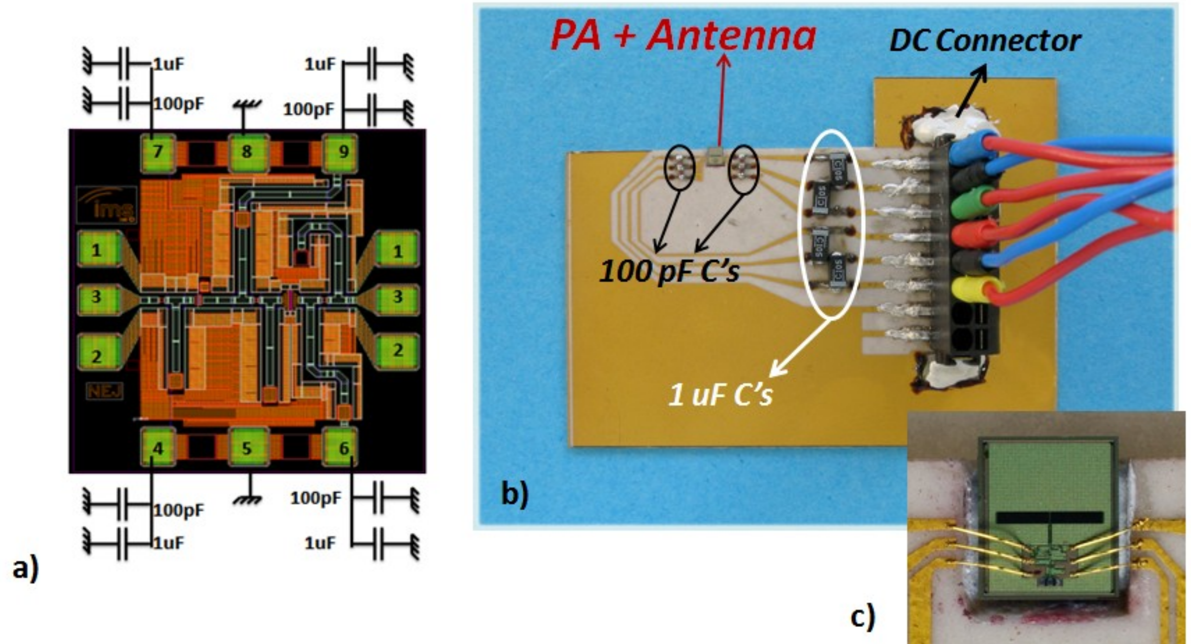

Figure 112 a) Decoupling DC capacitors and b) designed DC routing and support circuit (Surface mount capacitors) and c) Wire bonding close up

8.a) Support Selection

The support should remain as transparent to the circuit and mm-wave signal as possible. In an ideal case, neither the support nor the DC circuit should modify the performance of the circuit under test. For us, this will not be the case as the circuit includes an antenna. The radiated energy will inevitably interact with the elements nearby; i.e. the support and the DC circuit. As seen on Figure 113, the radiation of the antenna can be observed for different phases at 65 GHz. The radiation of the E plane changes from being concentrated at the center (Phase 0°) to being distributed in the edges (Phase 135°). On the H plane, something similar is also witnessed; take for example cases Phase 135° and 45°. As the antenna will lie on the support, this last will undoubtedly impact the radiation of the antenna.

For the choice of the support, more specifically the substrate, two options were available: alumina (ε_r = 9,9 and tan δ = 0.0001) and cordierite (ε_r = 4,9 and tan δ = 0.0026). These materials allow for gold deposition needed for the bonding. Both of them can be considered as low loss materials due to their low loss tangent. The 50-Ω antenna has been inserted on both substrates as support (Height of 0.635 mm for both substrates). For the alumina case, a

10 dB drop in gain is obtained for θ = 180° in simulation. Only 2 dB loss is observed with the cordierite substrate. The cordierite substrate is then chosen as the material for the support.

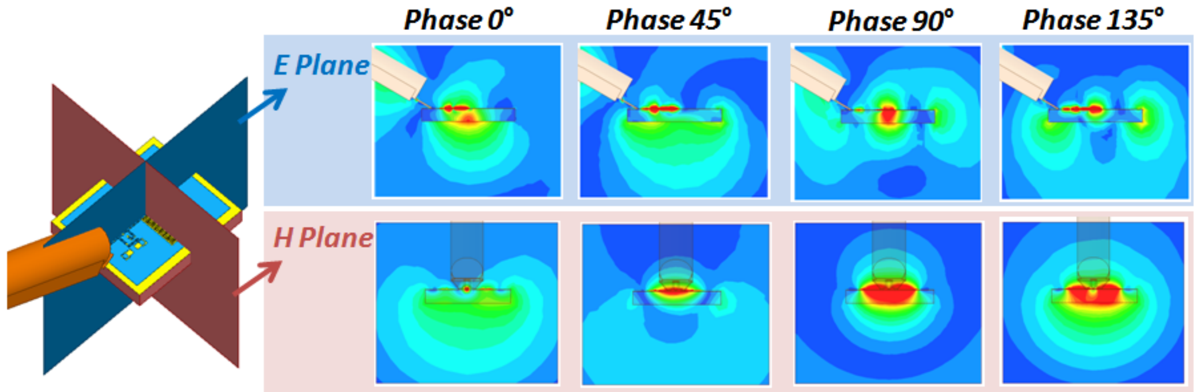

Figure 113 E field on E and H Plane @ 65 GHz for half a cycle (Phase 0 to 135°)

8.b) S11 Measurement

A first measure of the matching response of the PA was done. A Vector Network Analyzer Anritsu (VNA 37397C) was used for this first measurement. The measured responses are seen in Figure 114. The frequency shift seen is evident with the 65 GHz resonance. The measurements correspond to those obtained at IMS laboratory who had designed the PA and shown in Figure 114c. Although a good response is obtained for both co-integration and co-design circuits, the analyzer has a maximum frequency of operation of 65 GHz which limits us for the matching as well as for the gain measurements. A short description of the second analyzer that covers the V band (45-75 GHz) is done next.

Figure 114 S11 for Co-Integration and Co-design b) Measurements Telecom Bretagne and c) Simulation and Measured IMS

8.b.i) Measurement bench description (45 to 75 GHz)

The ABmm works on base band from 8 to 18.3 GHz Figure 115 a). With a coaxial output, low loss can be expected at these frequencies. A complementary converter module is then needed to increase the frequency. This module is shown in Figure 115b. It is a band-specific module (in our case, V band (45 - 75 GHz)) that will allow multiplying the frequency of signal (multiplicators seen in Figure 115c) and deliver it in a wave guide mode.

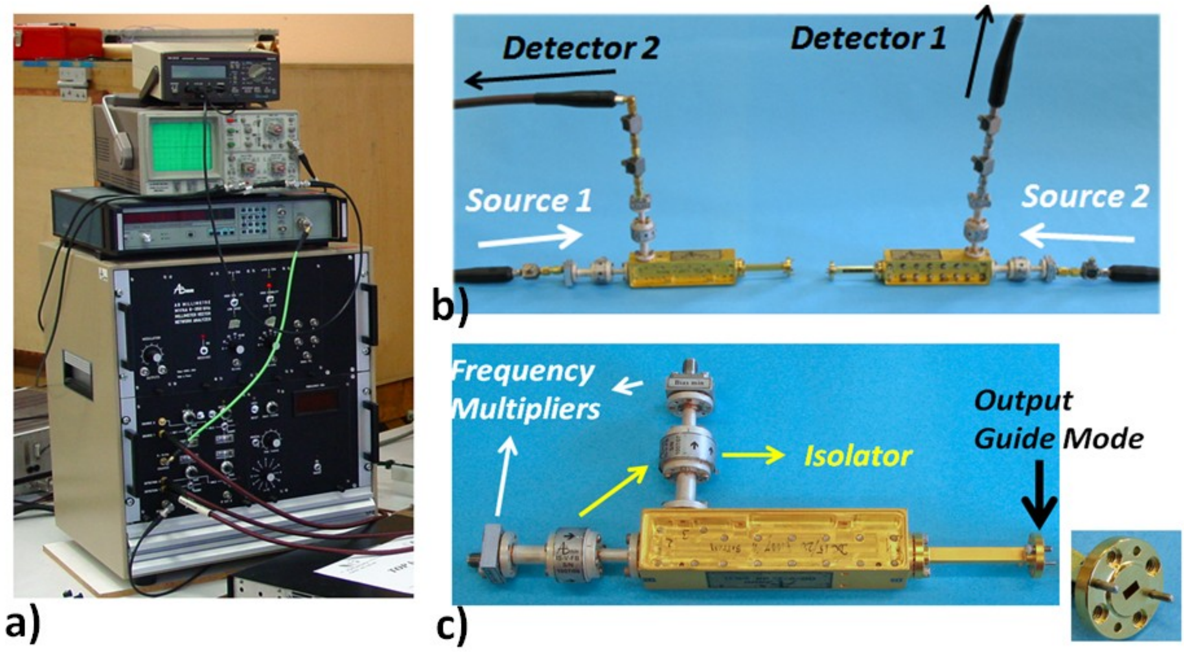

Figure 115 V band (45 - 75 GHz) test bench description a) Analyzer (ABmm) b) V band left and right modules (Tx and Rx on each) and c) Frequency multipliers and isolators for the left module. Emphasis done on the output: Guide Mode

The coaxial input of the probes required the use of coaxial cables. According to the coaxial cable manufacturer, for the Anritsu Semi-Rigid (ref: 3670V50-2), the maximum frequency of operation is 65 GHz. Due to this, the coaxial cable was tested on a wider band to assure its functionality. In fact, all the elements added (coax-guide trans., coaxial cable and probes) from the output guide up to the probe were tested. A wider frequency band (45-90 GHz) was chosen to observe the maximum working frequency, if any, of the added elements.

An initial transmission measurement is done with a direct link configuration (Figure 116a). This will position the reference plane at the output of the V band module and loss of this module will be accounted for. From here, each element is cascaded while doing a measurement systematically referenced. Note that the two modules (left and right) must be used to obtain the transmission response. Two transitions are used to create the link. As well, two coax cables and two probes are needed for a complete path to be established. They are joined by a "through" element for which the losses are neglected.

From the results obtained (Figure 116c), we can observe that the coaxial cable is the lossiest element in the chain. A difference of about 3 dB is obtained regarding the transition and probes. A mostly steady response of about -4 dB is obtained for the coaxial cable up to 65 GHz, the maximum operation frequency stipulated by the manufacturer. From then, a 1 dB

loss increase is obtained until 76 GHz. Still, good response from the coax cable and up to this frequency, the measurement configuration is validated. Around 77 GHz a sudden drop of 10 dB is witnessed. This is probably due to a new mode excitation inside the coaxial cable which establishes the operational limit for the bench. Besides the coaxial cables, a degradation of the bench response is seen. For example, for the Direct Link, a noise factor is added from 80 GHz forward. This effect is amplified for the transitions and probe at these final part of the band. In this way, the coaxial cables have been tested for a wider frequency range than that stipulated by the manufacturer.

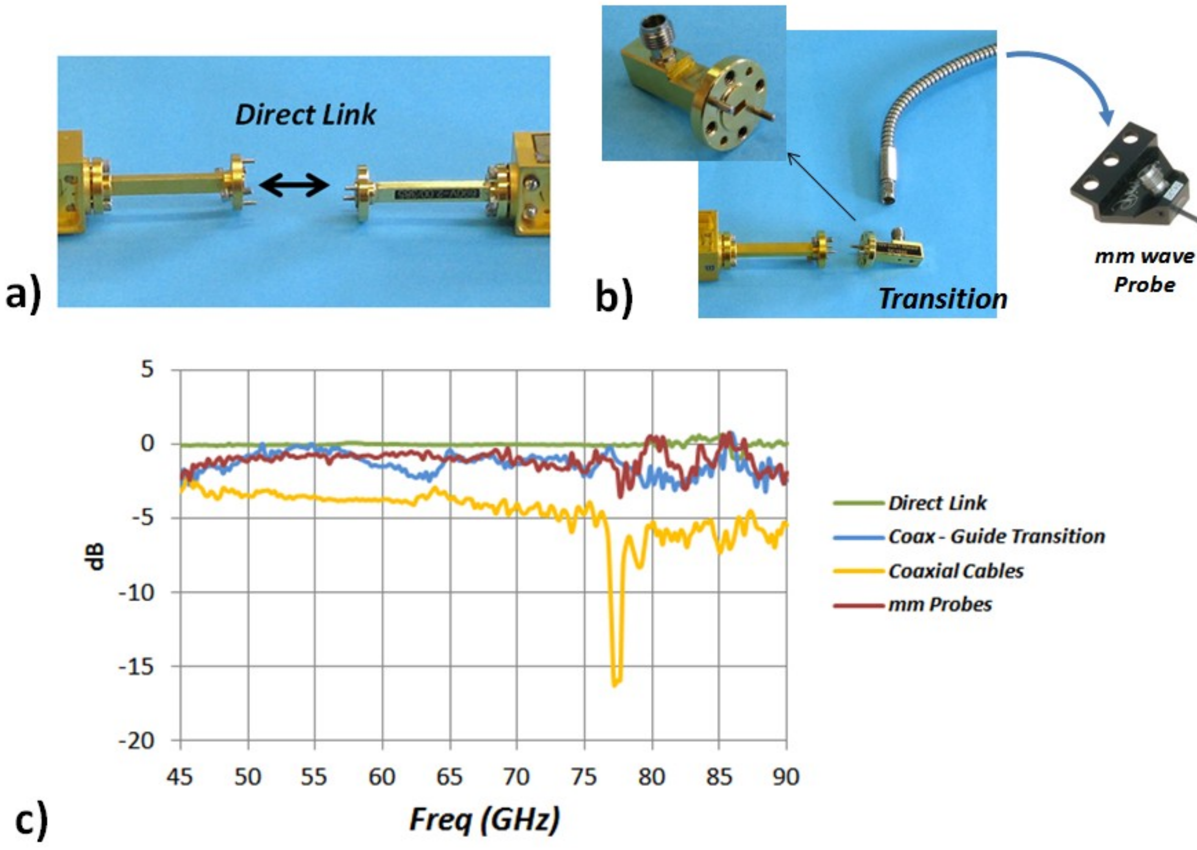

Figure 116 Testing at higher frequencies a) Direct link configuration b) Transition, Coax cable and mm probe and c) Losses expected for each independent element

8.b.ii) S11 Measurement

On this new band, 50 - 75 GHz, the S11 response for both, co-integrated (50 Ω) and co-design (15 Ω) PA-Antenna configurations, can be seen in Figure 117. Similar responses are seen with those measured before and shown in Figure 114. A 65 GHz first resonance is seen for both Co-Integration and Co-Design. A higher frequency matched response is maintained in agreement with the simulation of the PA response (Figure 114). A noise signal is added

though to measurements on the upper half of the band, also visible on a 50 Ω probe kit load. This noise signal starting at the 65 GHz is added by the coaxial cables as can be seen in Figure 116.

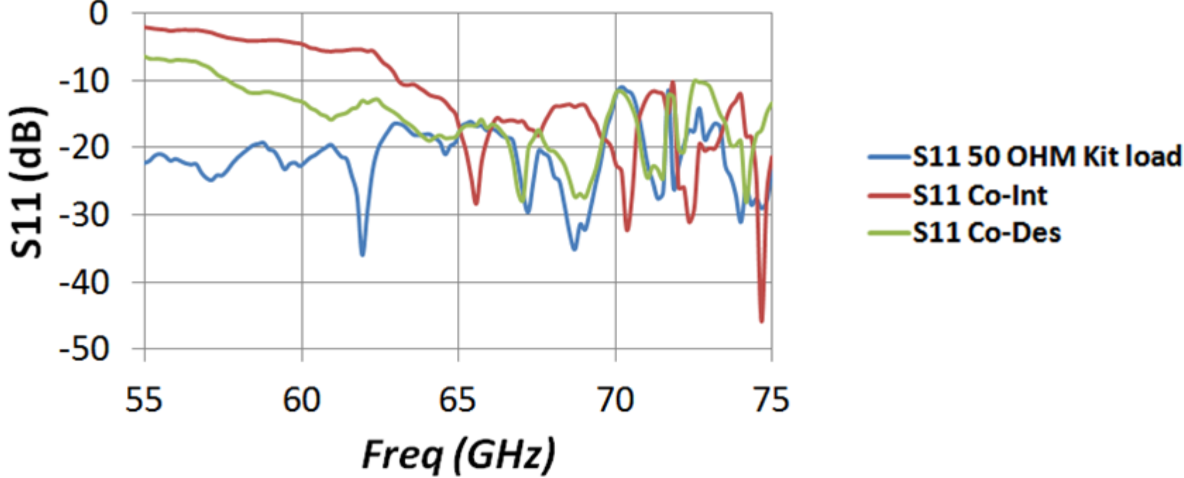

Figure 117 S11 response for a 50 Ω load (probe calibration kit), Co-integrated and Co-designed PA-Antenna

8.c) Support impact on Antenna performance

As mentioned before, the support will modify the behavior of the antenna. Both, the radiation properties of the antenna and the matching performance will be impacted. For the proper PA – antenna energy transfer, the PA relies on matched output impedance. The support is now included in the simulation. The support includes the mm probe, bonding and DC routing metallization. This will allow perceiving the impact of the support on the antenna input impedance. The two circuits, 50 and 15 Ω are described next.

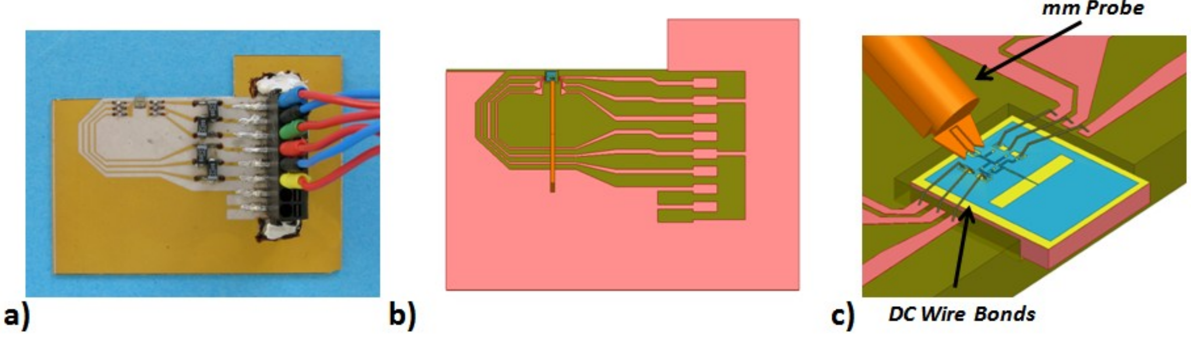

Figure 118 Simulation of the whole structure a) Fabricated Circuit b) Simulated Circuit and c) Close up on the chip, wire bonds, mm probe included (Ex: 50 Ω antenna)

Two configurations are compared, without support (blue) and with support (red), in Figure 119. A matching level reduction is seen at 68 GHz resonant response accompanied by a bandwidth reduction passing from 17 to 11 GHz. In fact, the slot resonant frequency has decreased towards 64 GHz as expected due to the presence of the probe. At 67 GHz, we observe a new PA – Slot coupling phenomena. In fact, it is the same phenomena seen in Figure 108, found at 74 GHz. Surface currents are depicted by Figure 120. The same PA elements still resonate. Although it is the same coupling seen before, it behaves in a different manner regarding the PA-antenna configuration matching response. It seems to offer the same 50 Ω input impedance as the slot, thus, maintaining a matched response. Nevertheless, a destructive radiation behavior is observed at this point: drop in co-polarization is seen.

Another resonant mode appears in the lower part of the band which does not contribute to the radiation. In fact, the increased cross-polarization level at this frequency shows that as before, another resonant radiating element is excited.

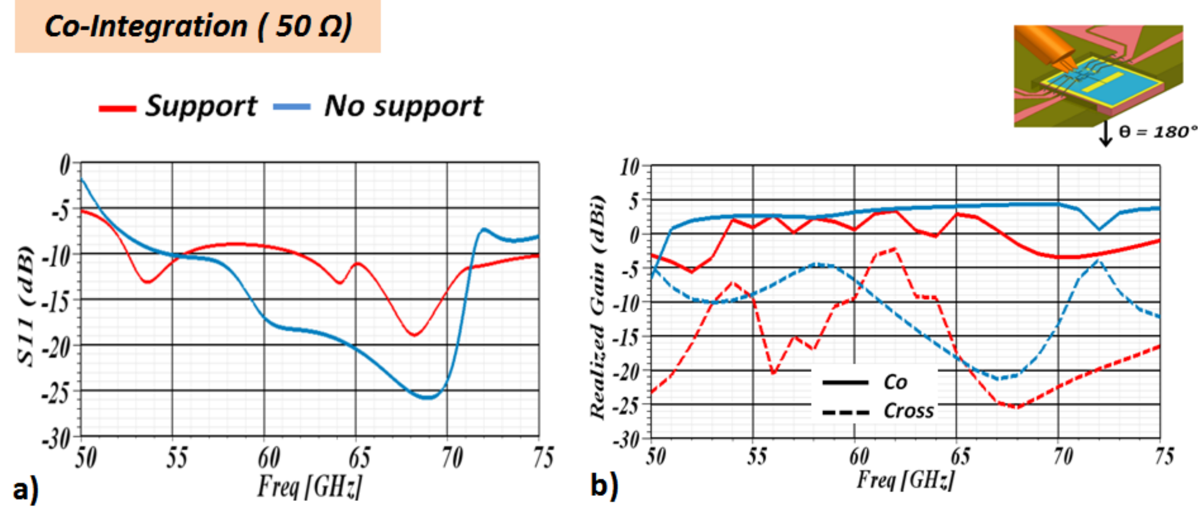

Figure 119 Co-Integration: Support Impact on antenna a) S11 b) Gain responses (θ = 180°): Co and Cross Pol

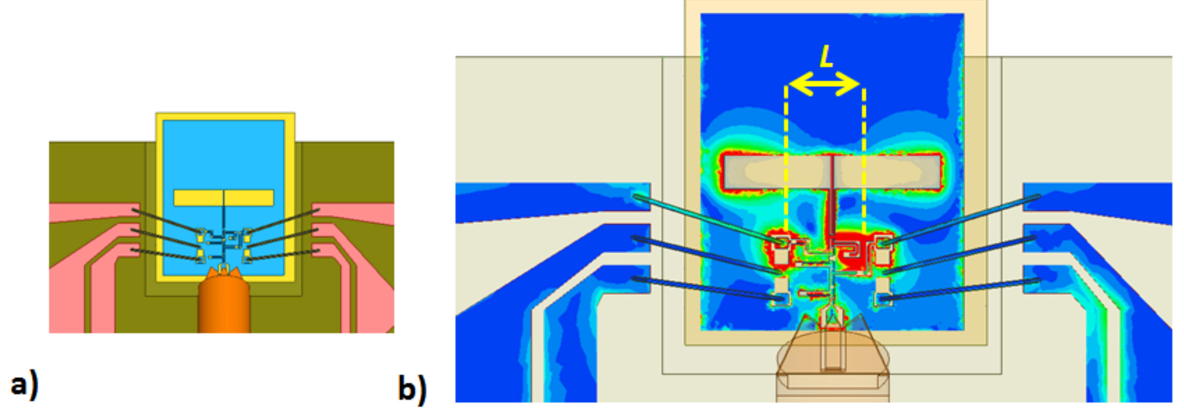

Figure 120 PA coupling to slot on support a) Top View of Chip + Support and b) Surface currents @ 67 GHz

Figure 121 shows the support impact for the co-design case. The matching performance of the antenna at 55 GHz is completely degraded. A matching level of -4 dB is now seen. In fact, the impedance has increased well beyond 15 Ω, and now has a value of 75 Ω. This is due to the chip boundary being modified by the addition of support. Coupling to the resonant PA element is still visible at 72 GHz. Consequently, change on the radiation properties of the antenna is expected and shown in Figure 121b. Realized Gain (Co and Cross) responses at θ = 180° are shown. At first hand, cross polarization levels have increased, which is normally due to the external metallic bodies as the DC routing, probe and wire-bonding surrounding the antenna. Secondly, co-levels have dropped which is normal due to the mismatch encountered. This gain reduction is also witnessed in measurements that follow.

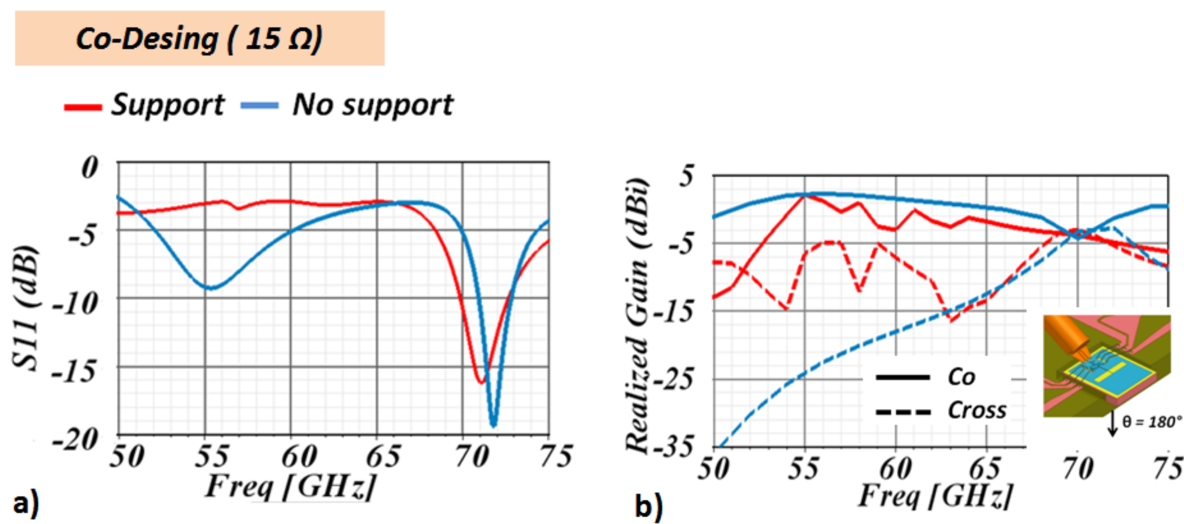

Figure 121 Co-Design: Support impact on antenna a) S11 b) Gain responses (θ = 180°): Co and Cross Pol

The radiation pattern has a higher F/B ratio than before with more or less 10 dB variation. The radiation is now concentrated to θ = 180° direction (Figure 122) for both Co-integration and Co-design. This is very important, as the gain measurement set-up must consider this energy relocation. The measurement set-up can be seen in Figure 123. A more detailed description is found in chapter 3.

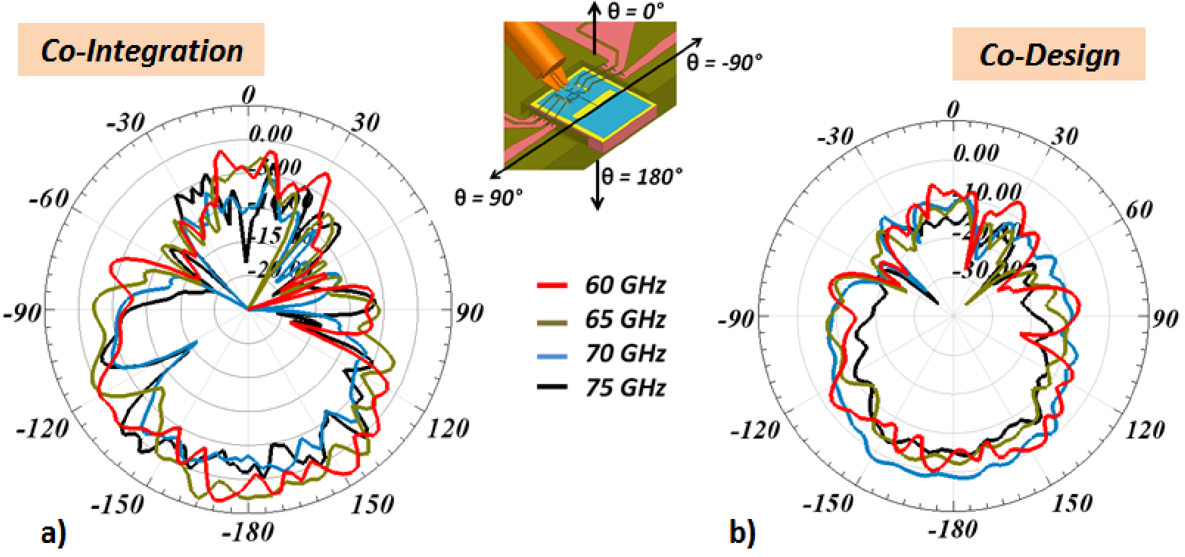

Figure 122 Energy relocation due to support presence. Gain Patterns for a) Co-Integration and b) Co-Design

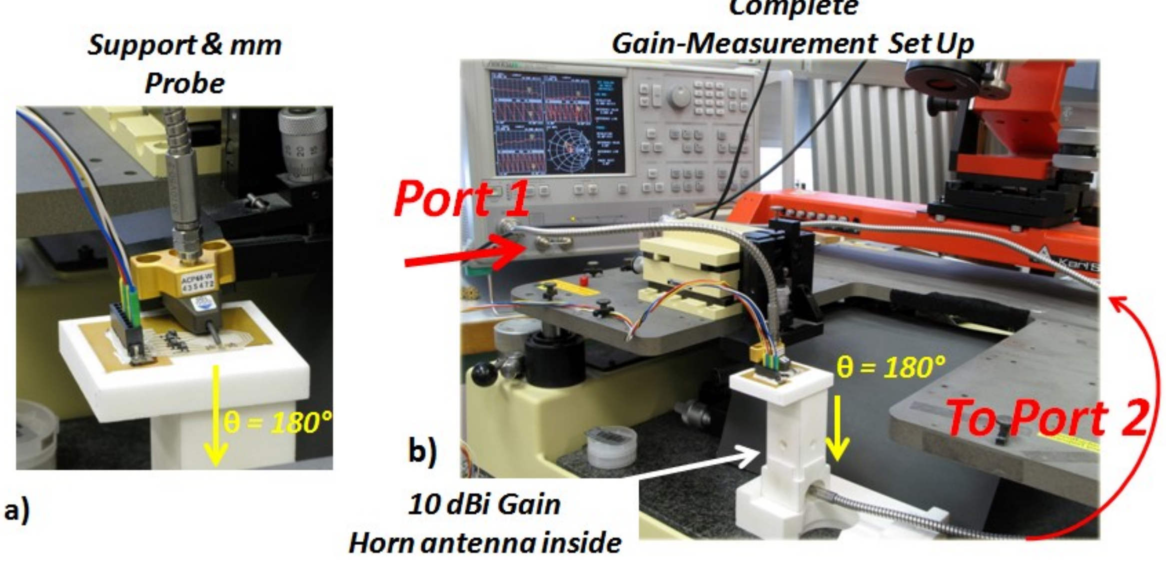

Figure 123 θ = 180° Gain Measurement Set-Up (Anritsu 65 GHz VNA) a) Close up on probe and circuit and b) complete chain

8.d) Gain Measurements

Gain measurements were done with Anritsu and ABmm analyzers. Expected simulated Gain levels shown before are included for comparison. The co and cross polarization levels show a good agreement up to 65 GHz. PA energy transfer to the antenna is evident; a gain increase at the end of the band of almost 15 dB was measured in the case of Co-Integration. Lower values are seen in the Co-design case, which can be explained by the lower antenna gain obtained in simulation and by the final chip location seen in Figure 125 b. The chip has slided to one of the receptacle sides and the glue use to fix the chip has modified the antenna boundaries (highlighted).

As the maximum amplification region of the PA is reached, a sudden gain drop is witness in measurement. Note that the “measured” antenna gain (PA Gain – Measurement: orange line) and simulation (green line) show the highest discrepancy between 65 and 70 GHz. Although a gain drop is seen in simulation for Co-Integration, the difference between measured and simulation is not until now explained. On both ABmm measurements (Co-Integration and Co-Design), almost 0 dB gain is measured on both designs.

One of the uncertainties of simulations done until now is the impossibility to take into account the real nature of the PA (not only the signal amplification aspect, but the real transistor and active parts on silicon presence). How will the transistors performance be modified by an external electromagnetic field? For example, the electromagnetic field generated by the slot? Due to this incapability, neither the impact of the radiation of the antenna on the transistor, nor the PA-Slot coupling phenomena can be taken into account. This could explain the gain drop witnessed before.

The simulated and measured values regain their agreement at the end part of the band (70 to 75 GHz), for Co-Integration as well as Co-Design.

Figure 124 Co-Integration gain measurements a) Co-pol and X-Pol for 50 - 65 GHz, b) Co-Pol for 50 - 75 GHz and c) Close up on bonded and glued chip

Figure 125 Co-Integration gain measurements a) Co-pol and X-Pol for 50 - 65 GHz, b) Co-Pol for 50 - 75 GHz and c) Close up on bonded and glued chip

9) Conclusions

SoC solutions offer some advantages in design flexibility that, as shown before, can increase the PA-Antenna path efficiency. 8.5 % increase was obtained when a co-design strategy was undertaken. Proper technology selection can also boost the performance of the system. In our case, high efficiency antenna is obtained (88 and 90 %) thanks to SOI.

Although PA-Antenna integration offers good opportunities for efficiency increase, it also renders the design more complex due to size reduction. From the previous work, several critical aspects regarding PA and Antenna integration have been put into evidence. At first hand, it is possible for the PA and Antenna to interact in a detrimental way. From the antenna point of view, the PA is an external element that interacts and modifies the performance of the antenna. As seen before, individual PA elements couple to the slot generated currents. Coupling through the antenna radiation can also be possible although it was not witnessed in our work. The PA location regarding the antenna radiating element is a key parameter. Secondly, devices introduced at measurement (probe and support) have a non negligible effect. The mm-probe close presence couples to the antenna radiation and clearly impacts its radiation and matching performance. Support, DC biasing and DC bonding affect as well. And last, the chip boundary becomes important for size-reduced solutions. Note, that the impact due to the substrate size is tied to the antenna radiation behavior. In our case, impedance and radiation characteristics are extremely dependent on the imposed boundaries of a required small-size solution.

Although a high gain solution compared to the state of the art was obtained (4dBi maximum gain), a higher value is needed to fulfill the application requirements. Values ranging between 6 and 7 dBi are specified. A different strategy is explored, where the antenna no longer resides on chip. This independence should allow diversifying the antenna selection possibilities, thus improving the antenna performance. This strategy is known as System in Package or SiP, and is presented in chapter 3.

Chapter 3 Dielectric Resonator Antenna: SiP solutions for enhanced performance

1) Introduction:

Two reasons give birth to this chapter. First of all, for an antenna to be considered as a complete solution in our application (high data rate download), the packaging of such component should be included. Secondly, a higher gain (6 - 7 dBi) is needed to be able to fulfill the application requirements.

Several packaging technologies were found to offer high performances at 60 GHz. (For example, multilayered technologies like LTCC (Low Temperature Co-Fired Ceramics) and HTCC (High Temperature Co-Fired Ceramics). Or technologies like eWLB (embedded Wafer Level BGA) or QFN (Quad Flat-Pack, No-Lead)). Micromachining possibilities are also present as for example, silicon cavity based solutions. All of these, present possibilities for packaging solutions but do not solve the antenna high gain requirement.

From the antenna point of view, one solution that was particularly attractive to us is the Dielectric Resonator Antenna or DRA. As seen in the study, DRA gain levels and bandwidth at (VSWR < 2) satisfy the requirements. As it will be shown, they are size compatible with active devices when high permittivity is used and their excitation is compatible with the CMOS process. The antenna study is presented next. PA-Antenna interconnection constraints are subsequently shown, and lastly, packaged PA-Antenna solutions presented.

2) The dielectric resonator antenna or DRA

A dielectric resonator antenna is composed of two elements: the dielectric resonator or DR and an excitation element. The DR is a three dimensional element made from a high permittivity material. To deliver energy to the DR, an excitation or “feeder” element has to be included in the configuration.

2.a) DRA state of the art

A DRA state of the art is presented next. Shape, excitation, permittivity and other characteristics as operating mode and gain are shown next in Table 6. Illustrations to these examples follow next where the DR and the excitation are shown. Special attention is made on the excitation mechanism.

Ref	Frequency (VSWR<2)	Shape	Excitation	ε_r	Gain (dBi)	Mode	Size (mm)
[97]	2.4	Cylindrical	CPW annular slot	20.8	2.8	TM^x_{110}	rad = 12.7 height = 8.5
[98]	2.4	Cylindrical	Probe	37	n/a	TM^x_{110}	rad = 5 height n/a
[99]	2.4 (25%)	Rectangular	MS excited Aperture	12	4.6	TM^x_{110}	Rad n/a height n/a
[100]	60 (21%)	Rectangular	CPW fed open slot	10.2	6	TM^x_{110}	L = 1.5, W = 2 height = 0.254
[101]	60 (15%)	Toroidal	Circular MS slot fed patch	10	11.9	$HEM_{51\delta}$	rad = 3.6 height n/a
[102]	36	Rectangular	SIW slot	10.2	5.7	TM^x_{110}	L = 3, W = 1.5 height = 1.27
[103]	28 (2.7GHz)	Cylindrical	Folded CPS	38	n/a	n/a	rad = 0.88 height = 0.93

Table 6 DRA state of the art: Frequency, shape, excitation, mode and gain

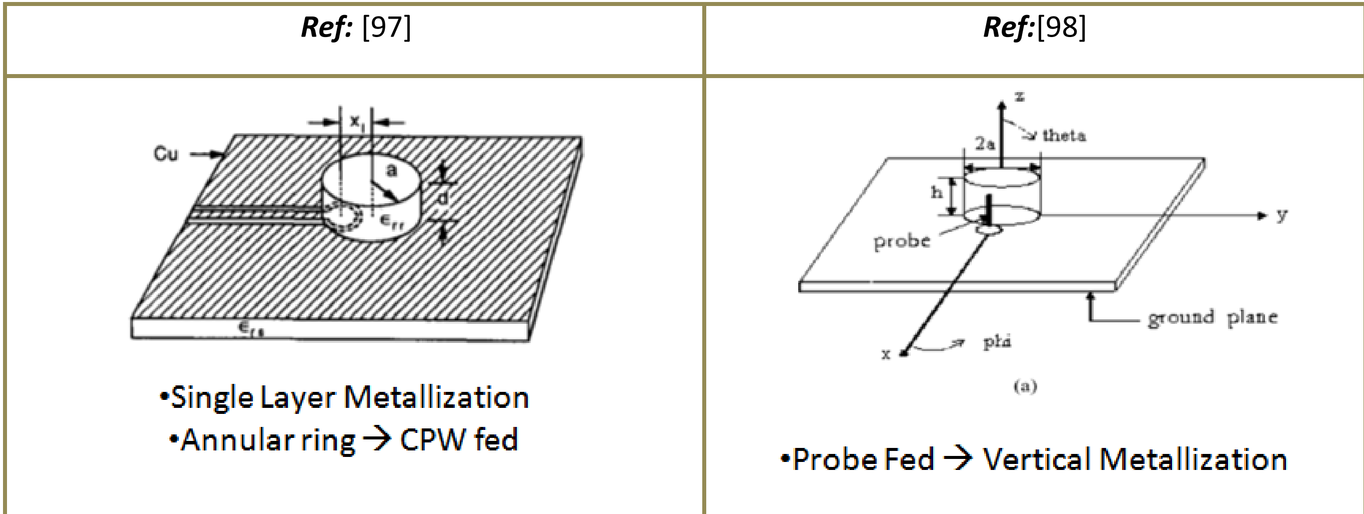

In these two examples, a single metallization layer is used. In [97], the CPW access line as well as the excitation are incorporated into the metallization, while in [98], an additional element is added: the probe. Although both designs are designed for a 2.4 GHz resonance, different dimensions are used. For example, the DR radius value is 12.7 mm and 5 mm for [97] in [98] respectively. The same resonant frequency can be obtained for different size configurations.

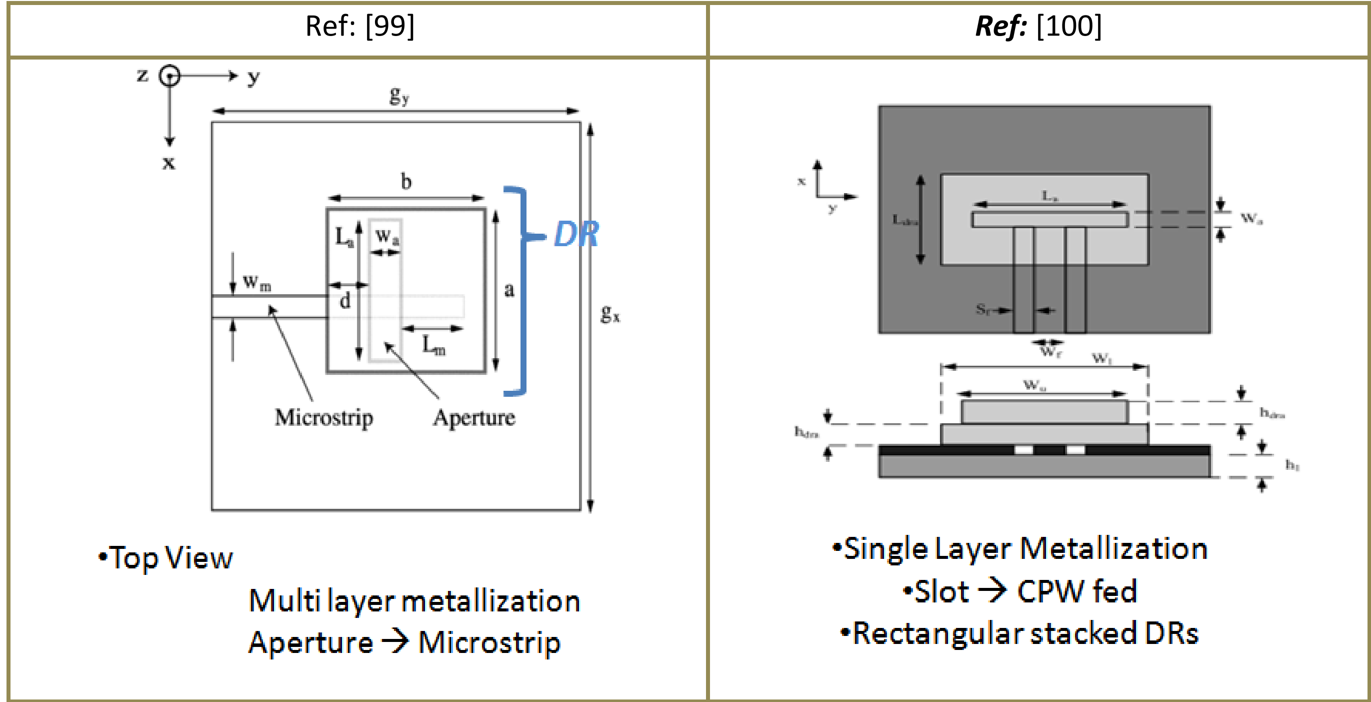

In [99], a microstrip aperture coupled DR is shown. The microstrip configuration demands a multilayer metallization. Special attention is given to the position of the aperture regarding the DR as well as its size (Slot length and width). 4.6 dBi Gain is obtained. A higher 6 dBi gain value is obtained in [100] by using a stacked DR configuration. CPW access is seen with a slot as the excitation element. Bandwidth values of 25 % and 21 % are reported for [99] and [100] respectively.

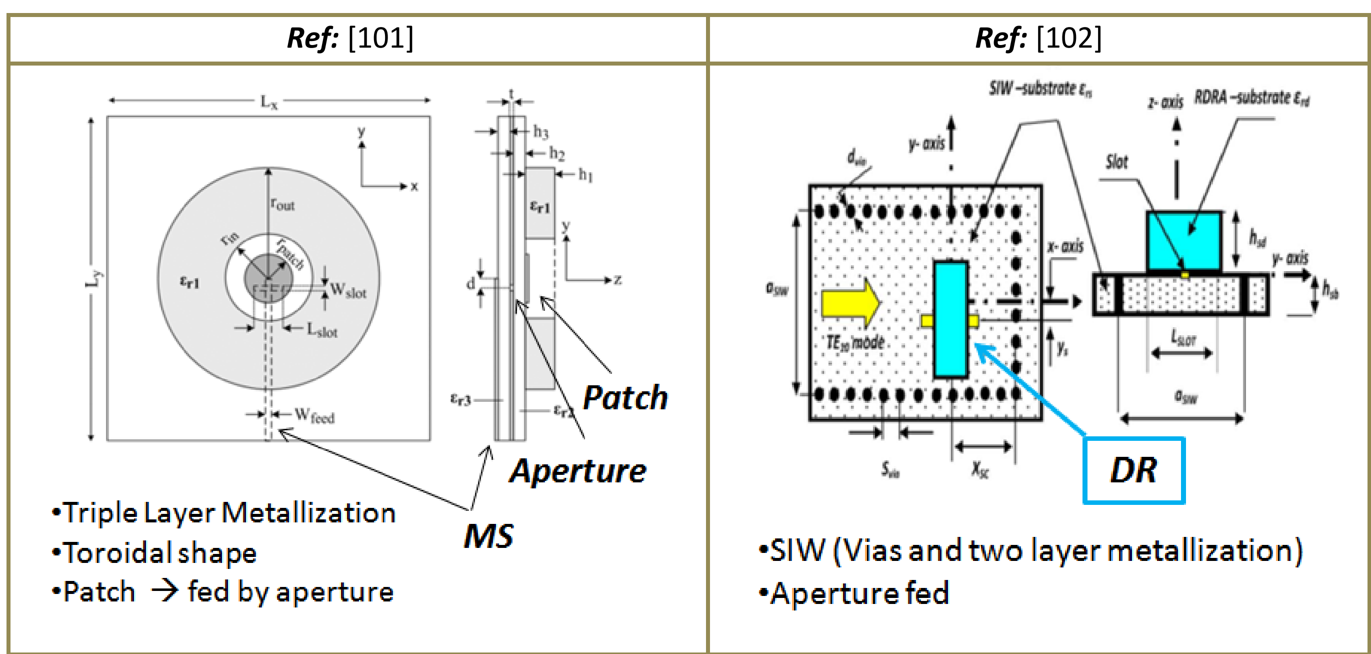

All previous solutions have shown the properties of the TM^{x}_{110}mode. In [101], the HEM^{x}_{51d} of a toroidal shaped DR for an increased gain; 11.9 dBi is obtained. Three layer metallization is

- **The** dielectric resonator antenna or DRA seen with a microstrip configuration that excites a circular patch through an aperture. The patch is used to excite the DR. In [102], the aperture fed DR is also used, but the access is now done through a SIW or Substrate Integrated Waveguide. Vias and two metallization layer needed. A gain level of 5.6 dBi is reported.

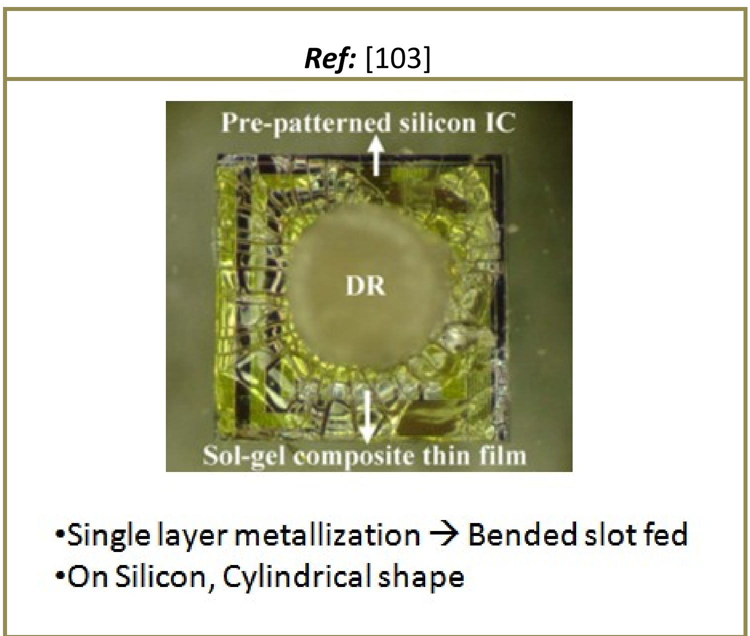

Finally, a one layer metallization configuration where a bended slot is used as the excitation element is presented in [103]. Differential excitation is achieved and a 10% bandwidth is obtained.

These examples give us a first view of some of the important characteristics and typical configuration for shape and excitation. Regarding shape, cylindrical and rectangular shapes are frequently found. Operation modes and excitation elements are well known for these configurations since they have been studied for quite some time now (beginning of the 80's according to [104]). For example in [105], approximate mathematical solutions for modes and frequencies of resonance have been developed and/or brought together from other sources for a complete solution to dielectric resonators.

For the excitation element, slots or annular rings, microstrip patches or simply, microstrip lines are commonly found. Probe excitation can also be achieved. The excitation element is indeed a very important characteristic of a dielectric resonator antenna solution and it will depend on the technological possibilities and constraints. One of the constraints for example is the transmission line configuration used to transmit the energy to the excitation. Typically,

- **The** dielectric resonator antenna or DRA

coplanar configurations as CPW line, microstrip or even SIW (Surface Integrated Waveguide) line are found. The excitation configuration is also important, as it should be compatible with measuring capabilities for the validation of the configuration.

In the following sections, we present the DR fabrication techniques, working principle, resonant modes and finally mode and excitation selection.

2.b) Fabrication of Dielectric Resonator Antennas

An important consideration to bear in mind is the fabrication process of the DR. Different fabrication methods have been identified in the literature and are presented next:

- **Milling (Drilling):** It consists of removing the unwanted parts of the element under elaboration by way of a mill powered by a drill. A +/- 10 µm tolerance can be achieved with this kind of machining.

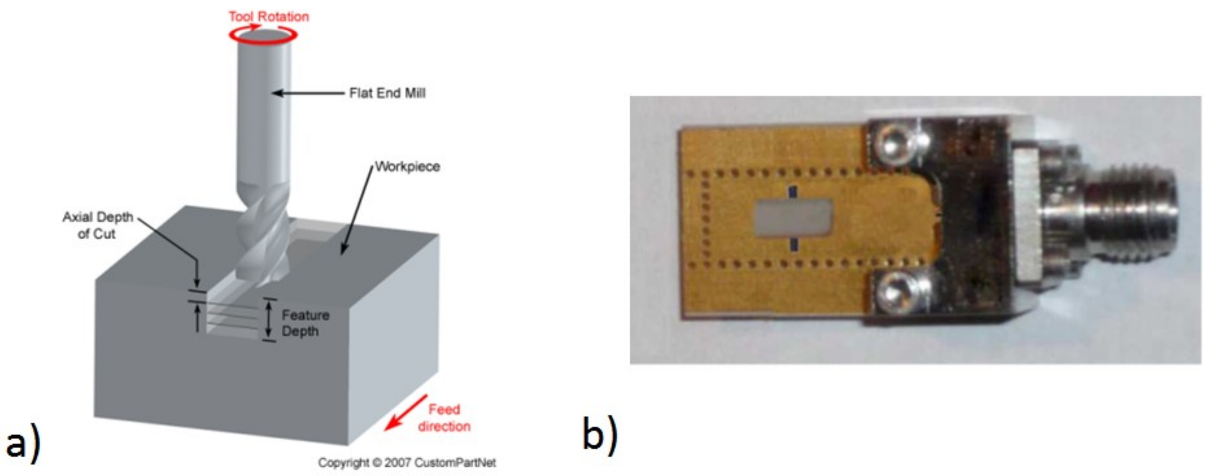

Figure 126 a) Milling process (Mill and substrate) b) Example of a milled DRA (excited by an aperture on a SIW) [102]

- **Laser machining:** With this procedure, ceramic substrates are easily cut or thinned. Depending on the power of the laser, wavelength and thickness of the substrate; some round edges can be obtained for the final product. Rapid prototyping is possible.

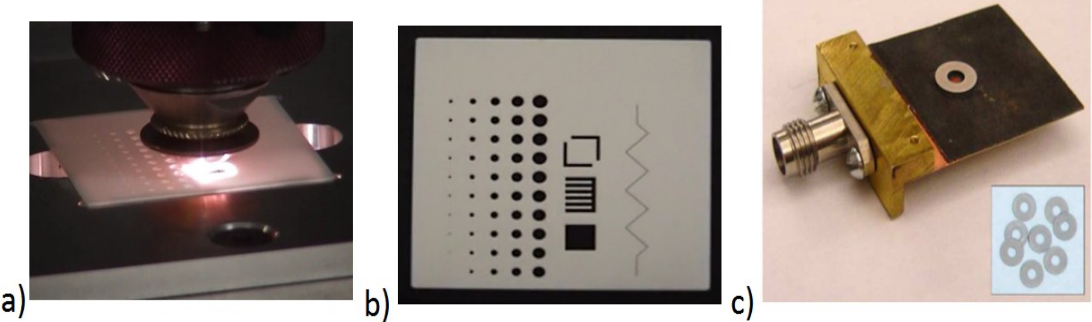

Figure 127 a) Laser and Ceramic substrate while being cut b) Finished sample[16] c) Example of a "lasered" DRA [101]

- **Sol-Gel composite film (growing the DR by a hydrothermal process):** In this fabrication process, the DR is grown from powder particles to form an interconnected microstructure. It is a crystallization process involving a sol-gel solution in a controlled atmosphere (13-15 atm). Dielectric properties are improved due to the controlled crystallization of the structure. In [103], the Sol-Gel based DR was successfully tested for compatibility with silicon technology (the DR excitation element resided on the M6 layer of technology).

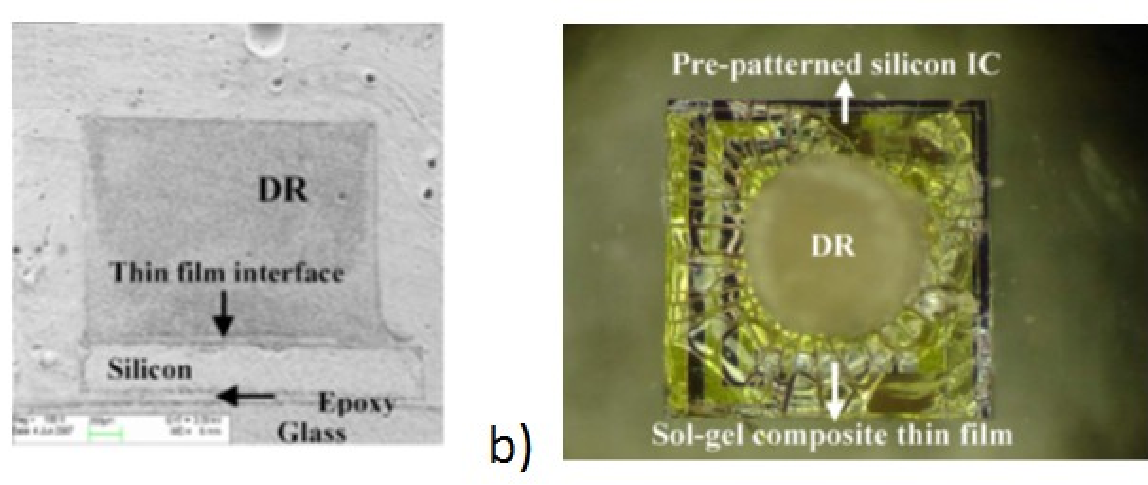

Figure 128 a) Transversal cut of the crystallized DR in the powder solution b) Top view of the DR and excitation element

- **Molding:** Industrial ceramic manufacturers are specialized in this process for ceramic manufacturing. It allows fabricating large number of samples. A powder of the ceramic element (alumine-oxide Al^2O^3 in many cases) is introduced into a metallic

[16] *http://www.cmslaser.com/laser-cutting.php*

- **The** dielectric resonator antenna or DRA

mould by way of a nozzle. It is then heated to melt and unify the powder. The simplified process is shown below as well as some samples obtained.

Figure 129 Molding process for ceramics. Samples taken from Friatek portfolio[17].

- **3D Printing:** It consists on the elaboration of an object by and additive process of dielectric layers. Several processes are part of the 3D printing technology. The basic idea behind 3D printing is to melt a granular compound and create the wanted object layer by layer. FDM, or Fused deposition modeling in Figure 130, is one method where the object is achieved by controlling the position of the nozzle. An also commonly used process is the Stereolithography in which liquid raw material is solidified by the use of laser. A platform and a piston are used to control the area of impact of the laser. Ceramics and plastics are typically used as basic materials.

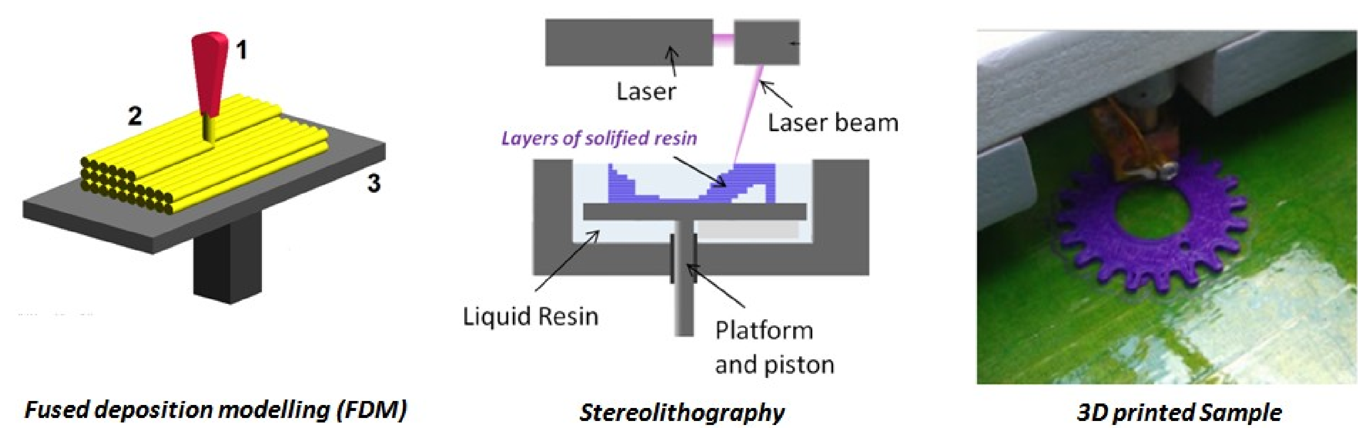

Figure 130 FDM[18] and Stereolithography[19] processes. An example of a 3D printed sample[20]

[17] http://www.friatec.com
[18] http://en.wikipedia.org/wiki/File:FDM_by_Zureks.png
[19] http://en.wikipedia.org/wiki/File:Stereolithography_apparatus.jpg#file
[20] http://www.squidoo.com

- **The** dielectric resonator antenna or DRA

- **LIGA:** It is a german acronym for Lithography (Lithographie), Electroplating (Galvanoformung) and Molding (Abformung) that describes a technological process for the fabrication of microstructures. Precision of 0.1 to 3 µm are obtainable depending on the mask elaboration procedure[21]. Large quantities of microstructures can be produced providing a mold for injection molding. Metal, ceramic or plastic structures can be fabricated.

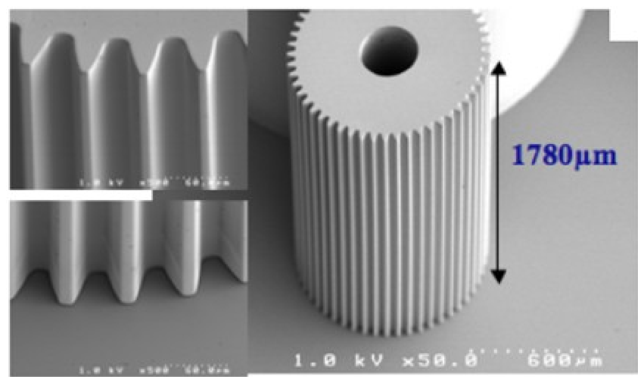

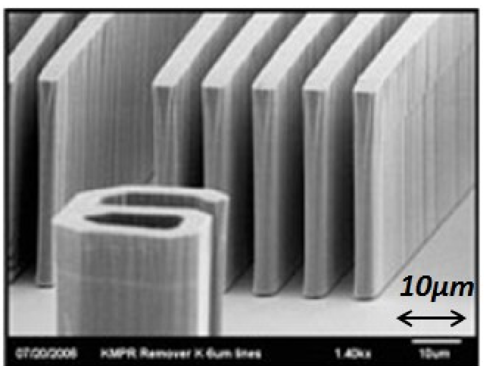

Figure 131 Structures fabricated by the LIGA process: rods[22] and metallic walls[23]

After the previous presentation of the DR fabrication possibilities, the functioning of the DR and the DR as an antenna is presented next.

2.c) How does the DRA works

To be able to understand the behavior principal of the DRA, the definition of modes has to be established. As any resonant element, electric and magnetic fields have specific distributions. This distribution is also called mode. Any given mode that could be established is identified according to its electromagnetic field distribution and appearing number.

2.c.i) Resonant modes in a cylindrical DR

To be able to define the modes in a DR, a nomenclature has to be defined. This nomenclature depends on the orientation of the fields (TM or TE field) and in the number of

---

[21] http://www.teltec.biz/

[22] http://www.memsnet.org/mems/fabrication.html
[23] http://www.teltec.biz/

- **The** dielectric resonator antenna or DRA

maximum-minimum field cycles found in the trajectories of ϕ and ρ (defining the index of the mode) as seen in Figure 132. If we take the first mode for instance (Figure 133), its E field distribution tells us that it is a TE mode, as it has no component in z direction. For the ρ index, we follow the trajectory described by the green line. Along this trajectory, one cycle has been completed so the index for ρ will be 1. For ϕ, no change is seen in field intensity when moving along the purple line. In this case, the index is 0. We have the TE_{01} mode.

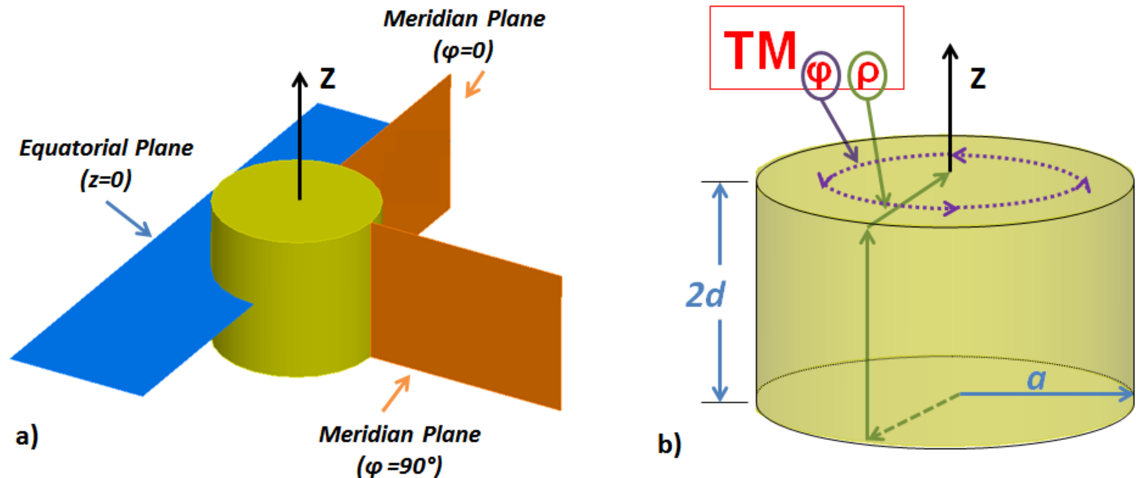

Figure 132 a) Equatorial and meridian planes b) Index trajectory definition

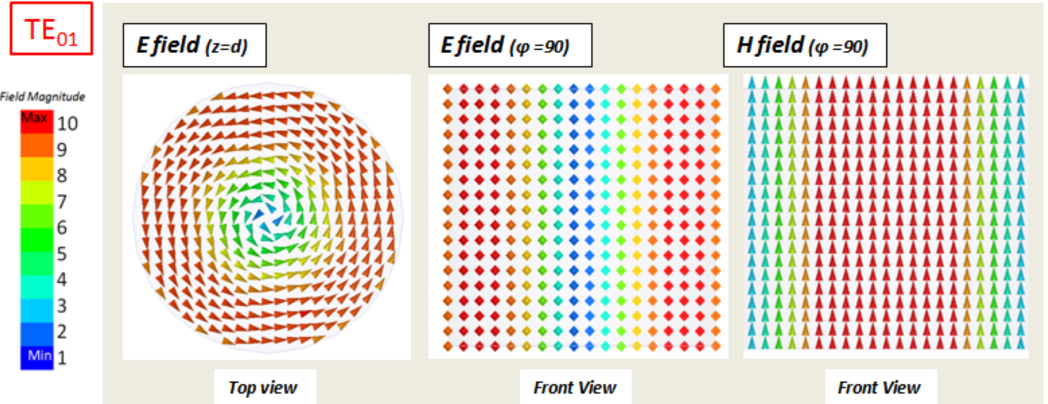

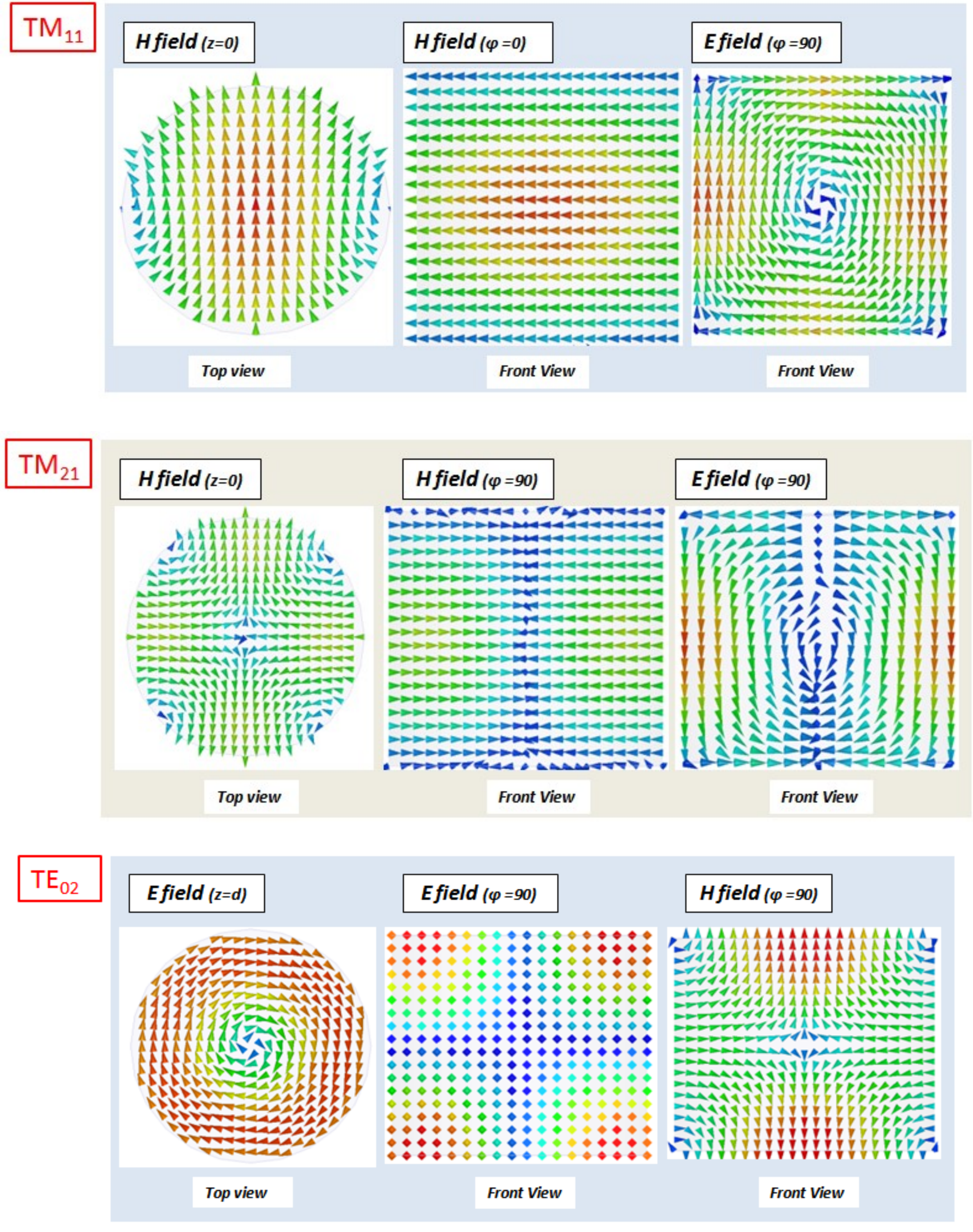
TM11
H field (z=0)
H field (φ =0)
E field (φ =90)
Top view
Front View
Front View
TM21
H field (z=0)
H field (φ =90)
E field (φ =90)
Top view
Front View
Front View
TE02
E field (z=d)
E field (φ =90)
H field (φ =90)
Top view
Front View
Front View

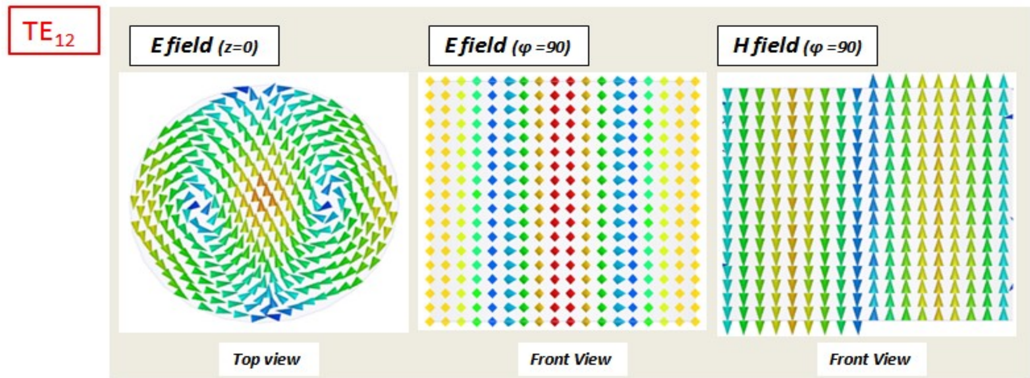

Figure 133 Field distribution for the first 5 modes of an isolated cylindrical DR.

All these modes are extracted for an isolated DR; no other element interacts with the DR. For the simulation environment, perfect magnetic frontiers have to be assigned to the lateral, top and bottom faces of the DR as seen in Figure 134 a). This has also been validated in [106]. However, another condition has to be added to include the metallic plane that will act as a support of the DR. The cylinder is thus analyzed with boundary conditions imposed for the electric fields components at z = 0: E_ρ and E_φ are equal to 0. (Figure 134 b)

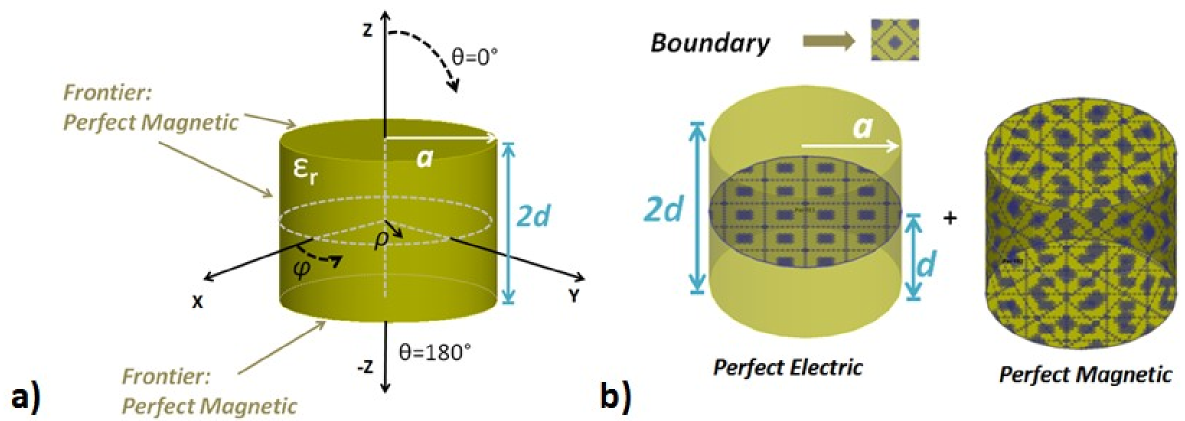

Figure 134 a) Dielectric cylinder with no ground plane described by equation 1 b) Equivalent DR with ground plane

By doing this, some of the modes presented before will not be able to appear. The perfect electric frontier eliminates modes that have tangential electrical components at z=0. By taking a look at the electric field distributions shown before, we can see that TE_{01} and TE_{12} modes will not be established. We could also reject the TE_{02} mode, due to its horizontal polarization of the E field. If we look closer to the E field at ϕ = 90°, it appears that the field has a minimum at z=0; this condition is compatible with the presence of the perfect electric

- **The** dielectric resonator antenna or DRA

border. This leaves TM_{11}, TM_{21} and TE_{02} as fundamental modes that could still be excited in the DR considering the inner perfect electric conductor.

2.c.ii) Mode selection

After this brief review of possible modes, a selection has to be made. One important difference between these modes is their quality factor. The quality factor is the ratio of the amount of energy stored to the amount of energy lost in a structure per period. Low loss structures have high quality factors. The loss component in the structure includes the energy lost through radiation. As we intend to use the DR as a radiation source, a low quality factor is expected. This characteristic is inversely related to the bandwidth. Taking into account the 12% bandwidth required for our application, the mode with the lowest quality factor should be chosen. According to [105], the mode with the lowest quality factor is the TM_{11}. A quality factor of 30.7 (for the TM_{11}) compared to 327 (TM_{21}) should offer us the best solution for a dielectric resonator antenna. Another particular advantage of this mode is the fact that it is the first one to be excited. This means that for a given frequency, the size of the DR will be the smallest possible compared to DR higher operating modes selection. Due to this, for a higher mode to be used at the same frequency as the TM_{11}, an increase in dimension will be the outcome.

2.c.iii) Resonance frequency of the TM_{11}

A first equation [106] is introduced for the resonance frequency of a cylindrical cavity, as seen in Figure 134 b). The X'_{11} factor has a value of 1.841 for the TM_{11} mode according to[106] . It makes part of the mathematical Bessel functions solutions.

$$f = \frac{1}{2\pi a\sqrt{\varepsilon\mu}}\sqrt{X'^{2}_{11} + \left(\frac{\pi a}{2d}\right)^{2}} \quad \textit{Eq. 16}$$

According to Eq. 15, the resonance frequency varies with the radius (a), height (d), permittivity (ε) and permeability (μ) of the material used. A comparison has been done between these theoretical predicted resonant frequencies and simulation. A variation of d (cylindrical height from 0.1 to 1 mm) and ε_r (dielectric permittivity, ε_r = 10, 20 and 40) can be seen in the following graph. (μ =1 and radius a = 0.56 mm are adopted for all iterations). The simulated structure has been configured as seen in Figure 135 b). A perfect magnetic frontier surrounds the entire structure and a perfect electric plane is located in the center. The Eigen

- **The** dielectric resonator antenna or DRA

mode solver of the simulator (HFSS^{TM}) is selected. This allows studying the modes inside the structure without the need of an excitation device. In this way, the possible impact of external elements like the excitation is avoided.

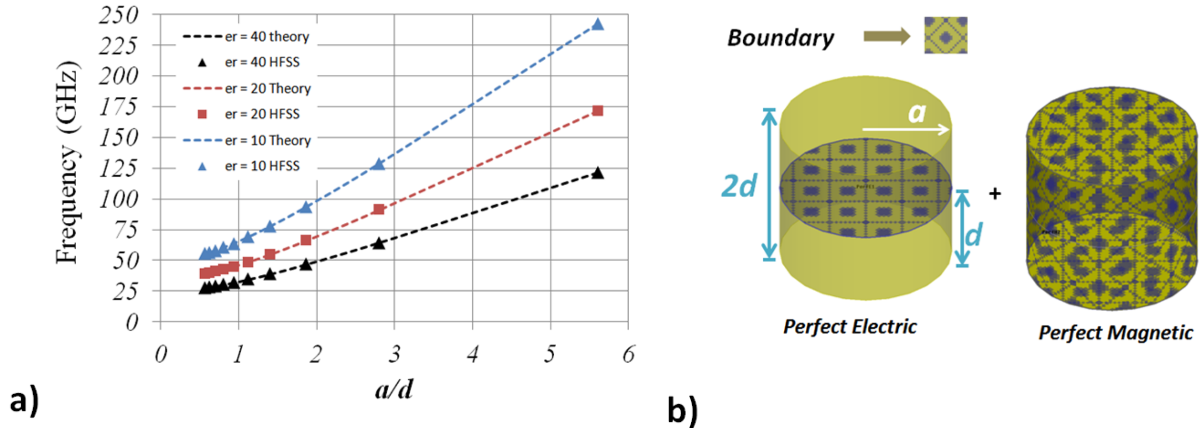

Figure 135 a) Comparison between theory and simulation b) Boundary configuration for simulator.

Simulation and theory agree perfectly. The frequency for an isolated DR can be calculated with no error margin. This is due to the same conditions imposed (boundaries) on the simulated cylinder as that used on the theoretical analysis [106]. A metallic ground plane should now be introduced to simulate the real environment in which the DR will be placed. The previous perfect electric boundary condition is replaced by the metallic ground and the image theory is applied; the DR height is reduced by two. The DR of height d is now located on top of a metallic ground plane. The field configuration resulting is shown next (Figure 136). The resonance frequency is exactly the same as that of the configuration shown before.

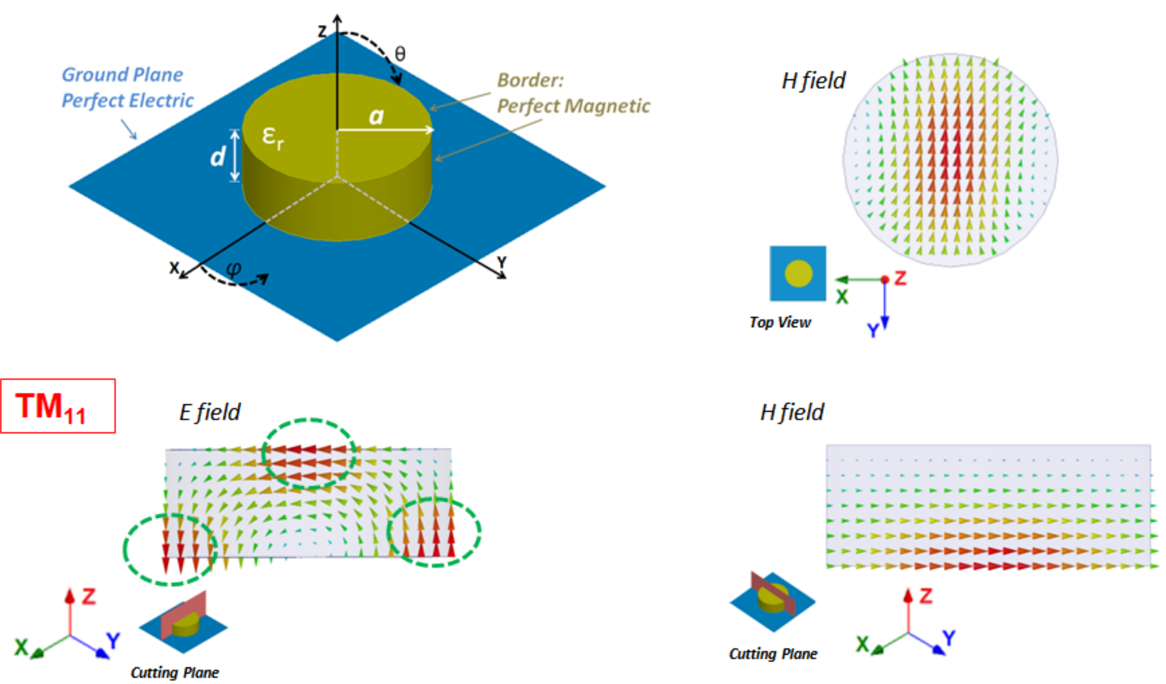

Figure 136 Field distribution for the TM_{11} mode including the ground plane

2.d) Selecting the excitation element

Once the expected mode is properly selected (i.e. when the field distribution inside the resonator is achieved), the excitation element of the antenna has to be selected. The excitation has to transfer as much energy as possible to the DR by electromagnetic coupling to the fields inside the DR. It could be ensured by either electric or magnetic coupling. According to [107], a higher coupling level can be achieved when the coupling elements are positioned at the region of their maximum field intensity. For the case of the DR, for a maximum magnetic field coupling, this should be in the center of the bottom face of the cylinder for the TM_{11} mode. Conveniently, this face is lying on top of the ground plane, which conducts to the implementation of the excitation element in the ground plane as part of the metallization. For an electric coupling, a maximum field region is found at the extremities (highlighted in Figure 136) of the DR for the TM_{11} and on the top face of the cylinder.

A typical element used to create a magnetic excitation is achieved by means of a slot. The slot magnetic field has the same distribution (linearly distributed along its length) as that of the magnetic field of the DR Figure 137.

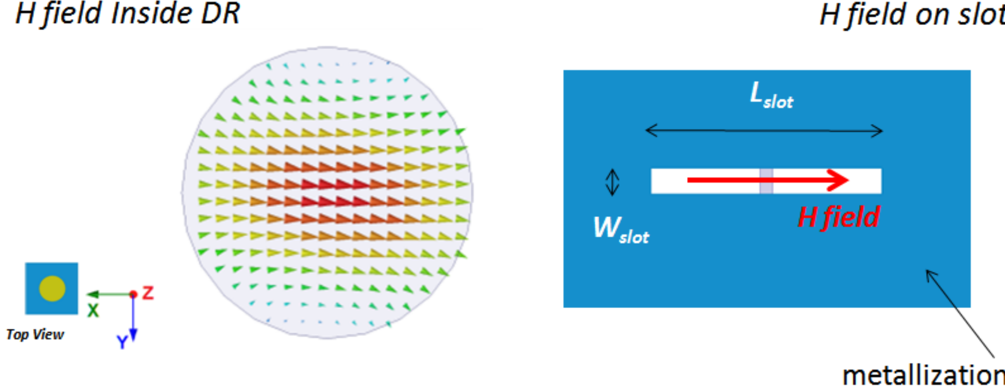

Figure 137 Magnetic field distribution on DR and slot

This excitation was used in [100] and [101]. No special orientation regarding the DR is needed for the slot due to the x-y plane symmetry of the DR. In fact, the slot will control the field distribution orientation in the x-y plane and thus, the polarization of the antenna. A slot is introduced in the ground plane as seen in Figure 138 a). A 0.508 mm height substrate is chosen with a permittivity of 9.9 from Al_20_3 based ceramic material. Different thicknesses (DR heights) are available for testing and it also offers a low loss (tan δ = 0.0001) characteristic. Using Eq. 1, a radius of 0.74 mm gives a resonance frequency of 60 GHz for the TM_{11} mode. Initial slot dimensions are 50 µm and 0.9 mm for W_{slot} and L_{slot} respectively. Position of the slot with respect to the DR can be seen in the top view of Figure 138 b). A first infinite ground plane is considered for simulation as depicted in c).

2.d.i) DR + Slot → Initial performances

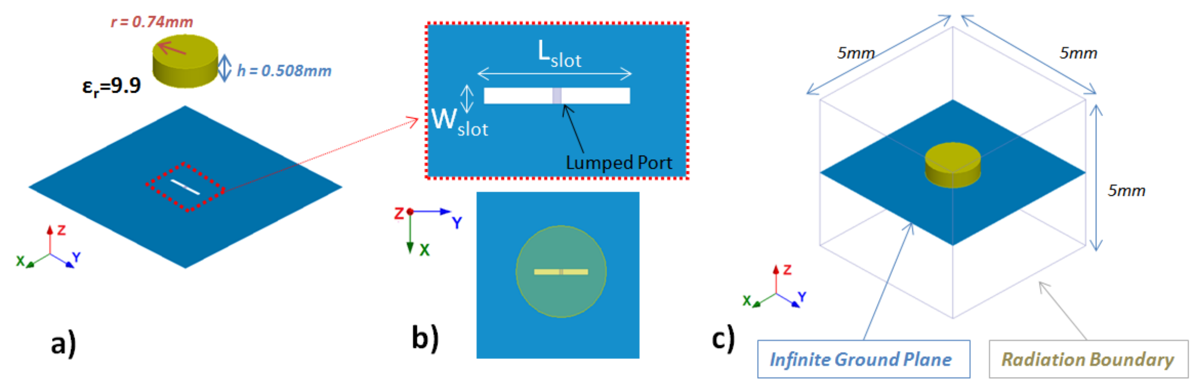

Figure 138 a) Slot in ground plane b) slot excitation and top view DR and slot c) Boundary conditions for simulation

An initial parametric study of the parameter L_{slot} shows several things. First of all, a slight frequency shift regarding the expected 60 GHz can be seen in the S11 response. This shift

- **The** dielectric resonator antenna or DRA

was expected as the previously presented frequency response (Figure 135) did not take into account the fields that exist outside the resonator for the TM_{11} mode. The magnetic boundary confines the studied volume to that of the resonator. In reality, the fields of the dielectric resonator extend outside the borders of the cylinder and the environment around it should be included. Another interesting thing is seen in the gain response, where almost no change in the gain is observed when changing the L_{slot} parameter. The L_{slot} value does not impact either the backward radiation performance (θ = 180°). The gain of the resonator does not depend on the dimensions of the slot that is exciting it. This is true only for a non resonant slot. However the matching response does change and it is taken into account in the Realized Gain response. A 5 GHz bandwidth (VSWR < 2) and 4.7 dBi max gain is obtained (for L_{slot} = 0.9 mm).

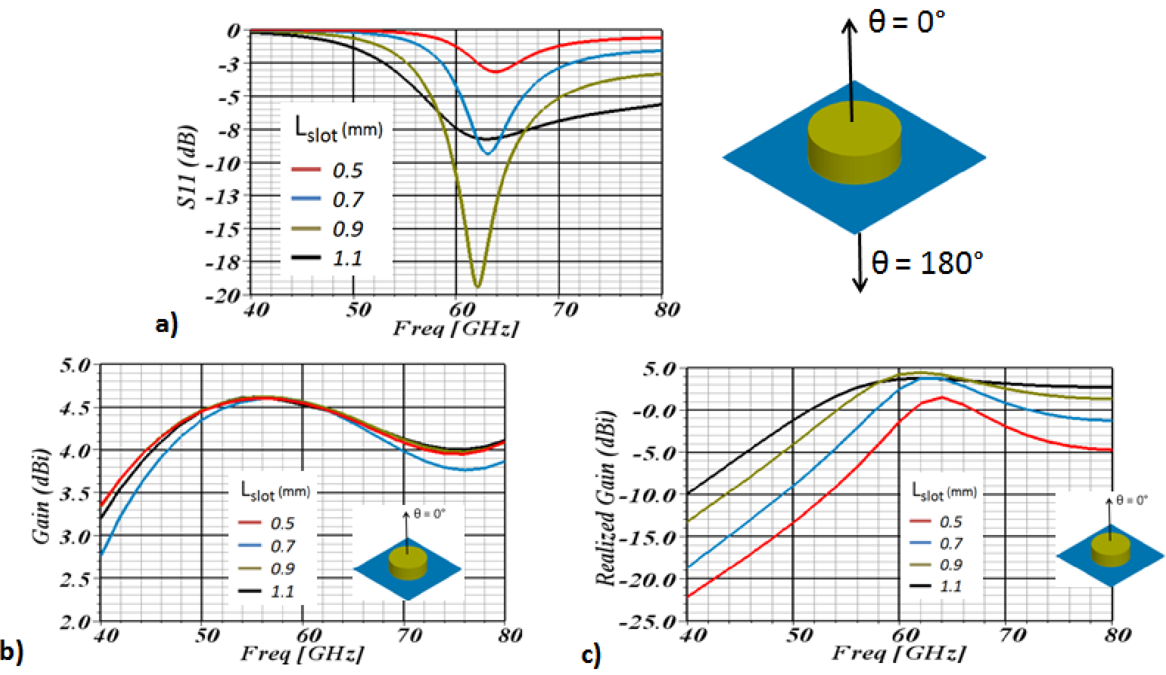

Figure 139 Infinite metal ground simulation a) Matching response b) Gain c) Realized Gain

2.d.ii) Finite ground plane effect

Another parameter that impacts the gain of the DR is the size of the ground plane. Anticipating practical realizations, a finite plane has to be introduced. A parametric study was done, where the size of the plane was varied. Values of 2 mm, 5 mm and 10 mm were taken, and compared to that of the infinite ground configuration. The gain radiation pattern

- **The** dielectric resonator antenna or DRA is also shown for these configurations. A configuration exhibiting a maximum gain at θ = 0° is the objective.

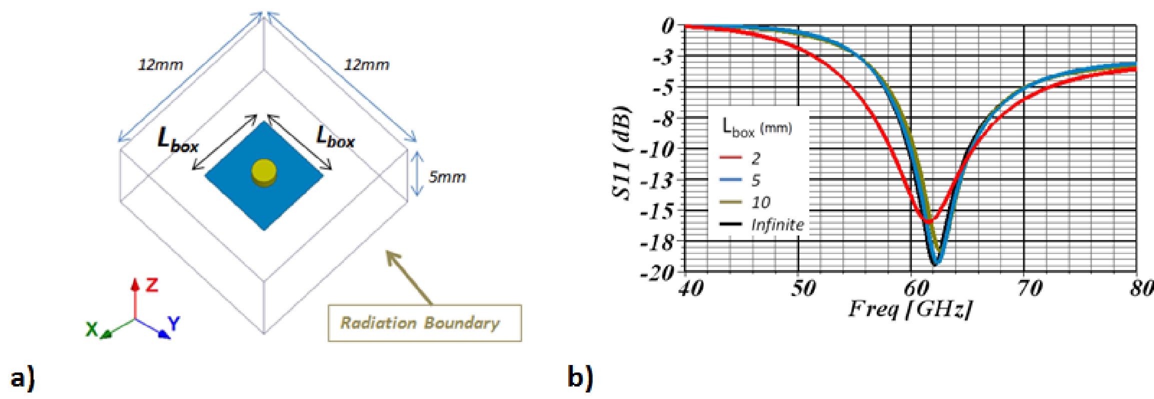

Figure 140 a) Simulation configuration for a finite size ground plane b) Matching response for a L_{box} variation

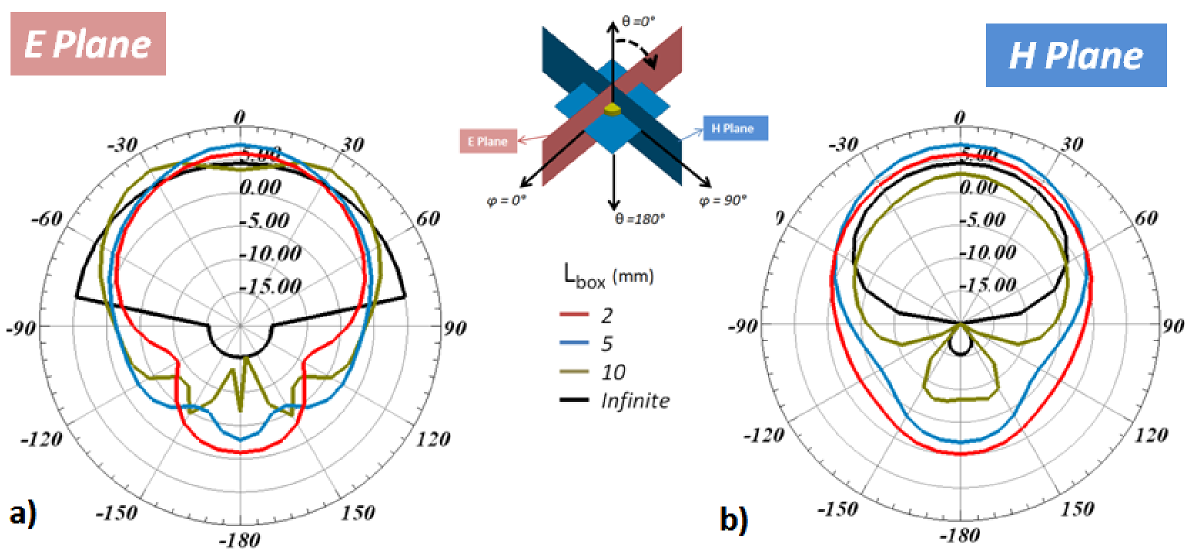

Figure 141 Gain pattern in a) the E Plane and b) the H Plane (the slot is longitudinally placed along the H plane)

The matching response exhibits an independence from the ground plane size except for a slight change for the 2 mm configuration. This S11 modification is explained by the change in the electric field seen in Figure 142 b). A higher field presence is observed in the backside θ = 180°) region consequently modifying the fields on the slot.

The gain pattern changes drastically for every size of the ground plane. As seen in the black line in the E Field gain response, a broadside almost omnidirectional pattern is expected for a DR placed on an infinite size ground. This was also seen in [106] for theoretical patterns. The electric field moves along the E field plane helped by the metallic ground plane. As

- **The** dielectric resonator antenna or DRA

there is no rupture of the ground plane, the radiation reaches the radiation boundary of the simulation configuration at angles from θ = -90° to 90°. This gives as result an almost omnidirectional pattern. This can be observed in Figure 142 a) for the E Plane field. As the finite ground plane is introduced, the omnidirected radiation is no longer obtained as can be seen in the 10 mm gain pattern. The energy that was before exiting the structure by the sides, begins now to be concentrated toward θ =0°. In this case (L_{box} = 10 mm), a maximum gain is obtained at θ = -30°and 30°. Optimum values can be obtained. For our case, a value of L_{box} 5mm was found to be optimum. As we pass this value, backside radiation starts to increase, leading to a lower broadside gain and a lower front to back ratio.

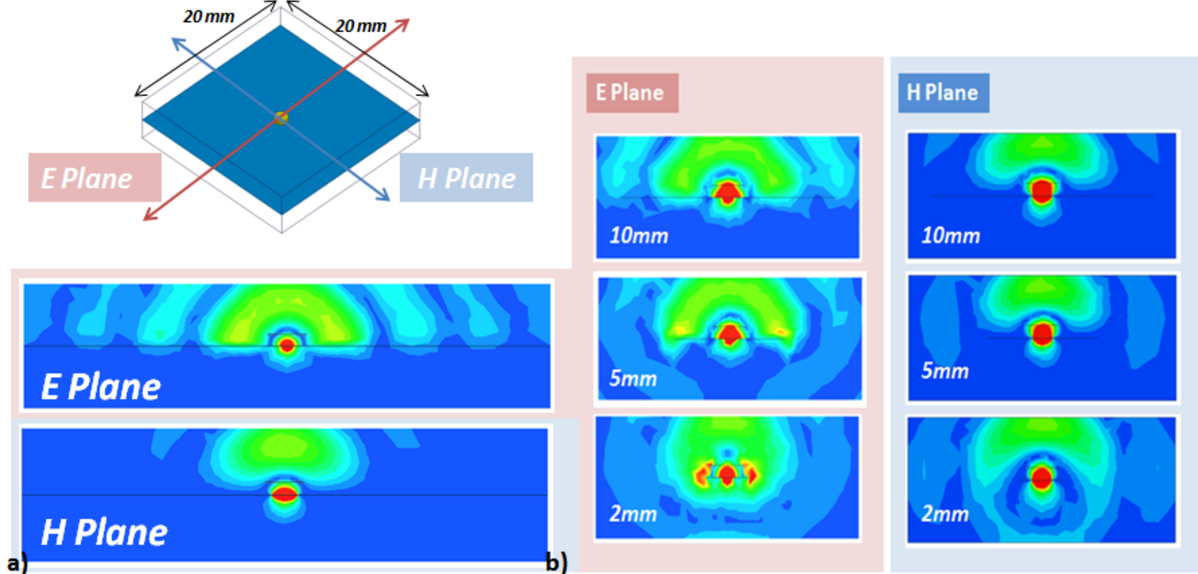

Figure 142 Magnitude E Field @ 62 GHz a) For a 20 x 20 mm^2 infinite ground plane b) For finite size ground plane

2.d.iii) The substrate effect

As the metallic plane needs a support, a substrate has to be also introduced in the configuration. With the introduction of this element, the slot size has to be adjusted due to the permittivity introduced by the substrate. The substrate material is the same as for the DR, with a permittivity of 9.9. A slight reduction of 0.15 mm was needed to regain a good matching with the DR; a new value of 0.75 mm was found to be optimum for a thickness of 0.1 mm for the substrate. Different values for the height of the substrate were studied to analyze its influence. The matching response for five different configurations (h_{subs} from 0.1 to 0.4 mm and no substrate) can be seen in Figure 143 b). As h_{subs} increases, a shift of the resonance frequency is seen, from 62 GHz (no substrate) up to 65 GHz for h_{subs} = 0.2 mm.

Another effect that is witnessed by the introduction of the substrate is the excitation of different modes inside the substrate as it becomes thicker. For hsubs = 0.4 mm, E Field magnitude is plotted for two different frequencies. We can observe how the field, originally concentrated in the DR passes from being concentrated in the DR (65 GHz) to be coupled to the substrate (72 GHz).

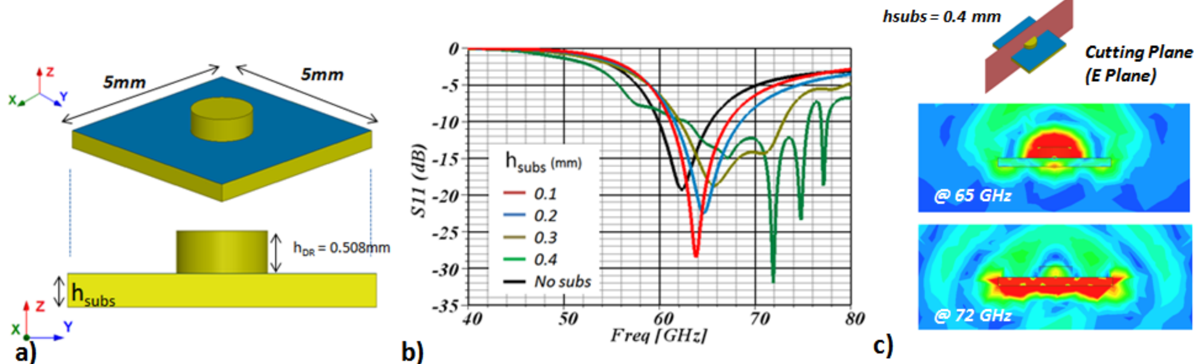

Figure 143 a) Substrate incorporated into the configuration b) Matching for different thicknesses c) E field Magnitude for hsubs = 0.4 mm.

Due to material availability, h_{subs} is chosen to a value of 0.381mm. It should ensure a good mechanical rigidity for any manipulation needed for measurements. For this value, we can expect to have some energy coupled to the substrate, but this coupling can be positioned outside the frequency band of interest. After these analysis steps, the resonance frequency is approximately shifted to 67 GHz due to the introduction of the substrate. The DR should now be lowered to our working frequency by increasing the radius of the DR. A value of 0.9 mm is taken for a.

2.e) DRA from lossy material and CPW feeder

Another element that has to be included is the excitation of the slot. A coplanar line has been chosen as it is completely compatible with the slot metallization without requiring additional technological layers and previewing the integration with the SOI based PA. The same metallization layer is considered with respect to the output stage of the PA.

Another important aspect of our research is concentrated on the high efficiency outcome for a PA-Antenna solution, and thus, losses have to be studied and minimized. Until now, the materials used are lossless. A final simulation including the loss factor of the dielectric and conductivity for the metallization is also shown (Figure 144). For these three cases, the

- **The** dielectric resonator antenna or DRA matching and gain can be seen in Figure 144. By taking a value of 0.9 mm for the DR radius, a resonant frequency of 58 GHz is obtained with a max realized gain of 7.8 dBi for the DR without CPW line feed. A 5 GHz bandwidth is obtained (VSWR <2). By adding the CPW, a frequency shift as well as a drop in gain is seen. The mismatch on the line, the portion of the line under the DR and the slight change of the slot shape due to the addition of the line have obviously an impact in the way the energy is coupled to the DR. A new gain value of 6 dBi is obtained after optimization of the slot dimensions to include the presence of the line. A slight drop in gain was expected when including the losses and was seen to be around 0.5 dBi. For this final lossy (real and fabricated) configuration, a gain of 5.5 dBi and a bandwidth (S11 @ -10dB) of 6 GHz is obtained.

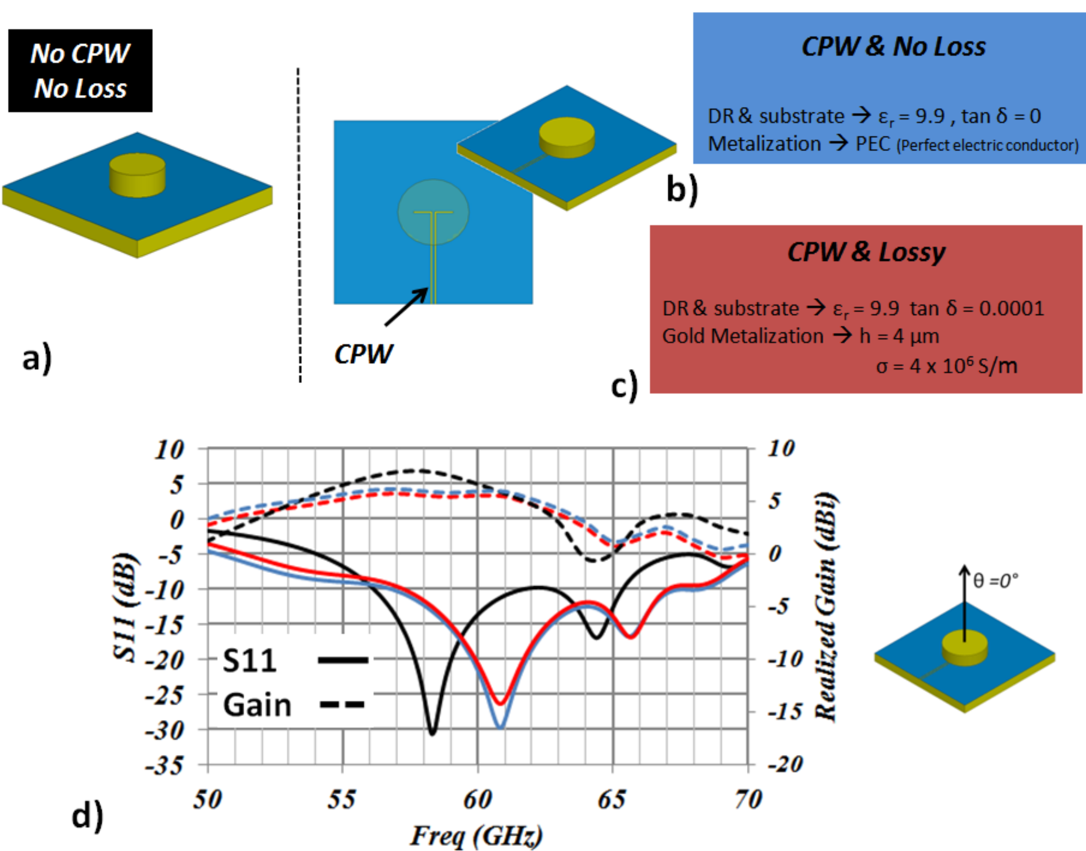

Figure 144 a) DR + substrate b) DR + Substrate + CPW (no loss) c) DR + Substrate + CPW (lossy) d) Matching and Realized Gain (dBi) @ θ = 0° for all configurations

For this last, a coupling at 66 GHz is observed that widens the bandwidth response of the antenna, but as it represents a coupling to the substrate, it is not taken into account. A reduction of the substrate height will reduce the coupling to the substrate as seen in Figure

- **The** dielectric resonator antenna or DRA

143. It is also outside of our frequency band so it shouldn't impact the performance of the antenna.

2.f) DRA radiation expected performance

The gain radiation patterns are shown next as well as a summary of the antenna performance. A -16.9 dB level difference (5.9 dBi for the Co-gain and -11 dBi for the Cross-gain values) remains an acceptable value, but shows the great impact that the CPW has on the configuration. For the no-CPW case, a -36 dB Co-Cross level was obtained. The CPW also affects the direction of maximum radiation. A significant 3-dB aperture variation was also seen when passing from the finite ground plane "no-substrate" to the finite ground plane "+ substrate" configuration for the E Plane. The substrate diminishes the radiation directed toward the θ = 0° (0.4 dBi drop in gain with respect the finite ground plane "no-substrate" configuration) and spreads it in a much wider angle than the finite ground "no-substrate" configuration does.

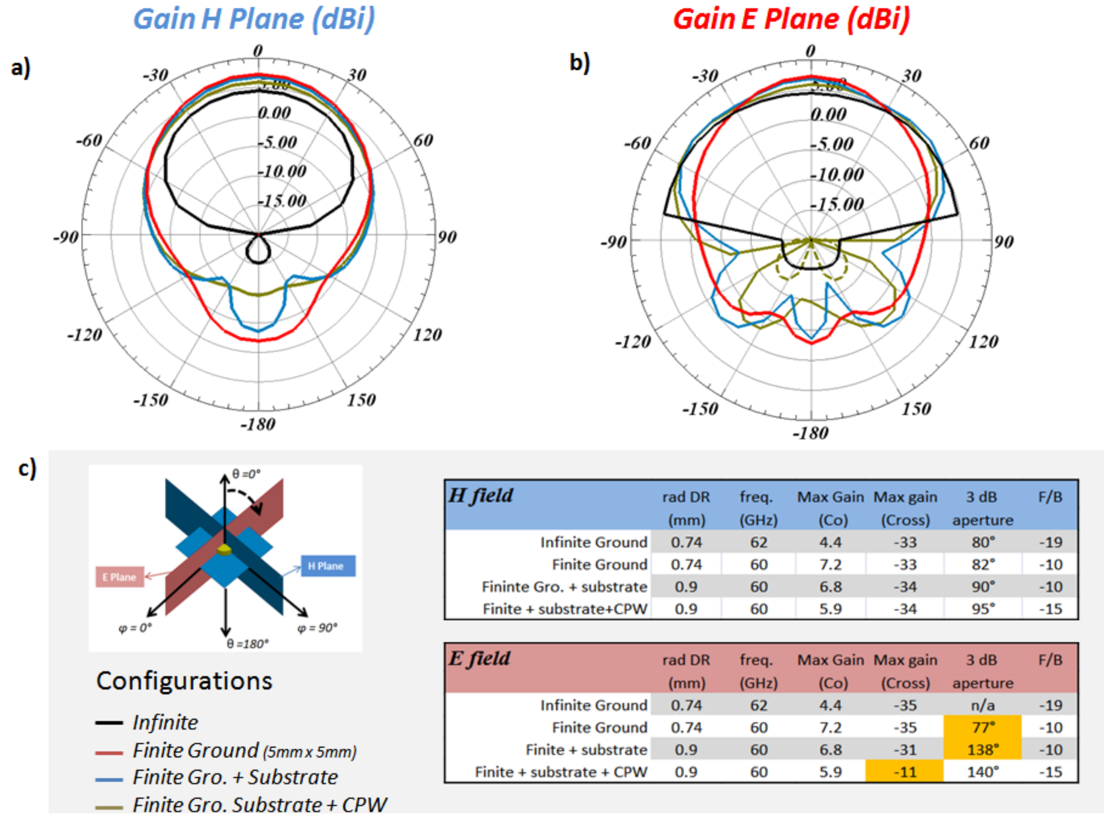

H field	rad DR (mm)	freq. (GHz)	Max Gain (Co)	Max gain (Cross)	3 dB aperture	F/B
Infinite Ground	0.74	62	4.4	-33	80°	-19
Finite Ground	0.74	60	7.2	-33	82°	-10
Fininte Gro. + substrate	0.9	60	6.8	-34	90°	-10
Finite + substrate+CPW	0.9	60	5.9	-34	95°	-15

E field	rad DR (mm)	freq. (GHz)	Max Gain (Co)	Max gain (Cross)	3 dB aperture	F/B
Infinite Ground	0.74	62	4.4	-35	n/a	-19
Finite Ground	0.74	60	7.2	-35	77°	-10
Finite + substrate	0.9	60	6.8	-31	138°	-10
Finite + substrate + CPW	0.9	60	5.9	-11	140°	-15

Figure 145 Gain patterns (dBi) for 4 configurations for a) H and b) E Plane (Co ——— Cross ---) c) Configurations and summary of antenna radiation performance.

2.g) DR Fabrication

Nine DR samples were fabricated from three different substrate thicknesses (508, 635 and 1000 µm) by laser. Fabricated samples are shown in Figure 146. A rather conical shape was obtained for the fabricated samples after fabrication. The top and bottom radii values are different and are shown next. An increase on the global shape of the DR was then obtained. Consequently, simulated expected frequency of 60 GHz is shifted downward to 54 or 56 GHz.

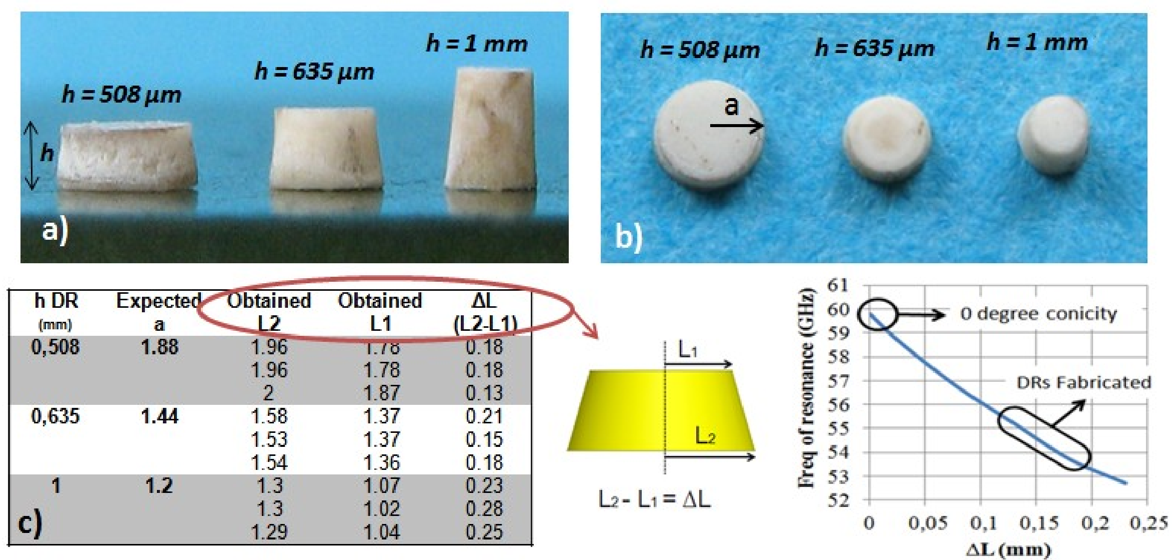

h DR (mm)	Expected a	Obtained L2	Obtained L1	ΔL (L2-L1)
0,508	1.88	1.96	1.78	0.18
		1.96	1.78	0.18
		2	1.87	0.13
0,635	1.44	1.58	1.37	0.21
		1.53	1.37	0.15
		1.54	1.36	0.18
1	1.2	1.3	1.07	0.23
		1.3	1.02	0.28
		1.29	1.04	0.25

Figure 146 Fabricated samples a) Front view b) Top view and c) Expected and obtained values for top and bottom radii and the frequency shift.

2.h) DR Measurement

A network analyzer Anritsu 37397C was used for characterization, with a receiving 10 dBi Gain V-Band horn antenna, positioned 8 cm apart from the DRA. At this distance, the far field region of the horn antenna (5 cm has been calculated according to its dimensions) is ensured. The positioning of the DR with respect to the slot was found to be difficult. For this, a positioning device based on a foam material was used to minimize the DR shift (Figure 147 b). The foam material has electric properties close to that of the air (εr = 1.04) and do not affect the DR radiation properties.

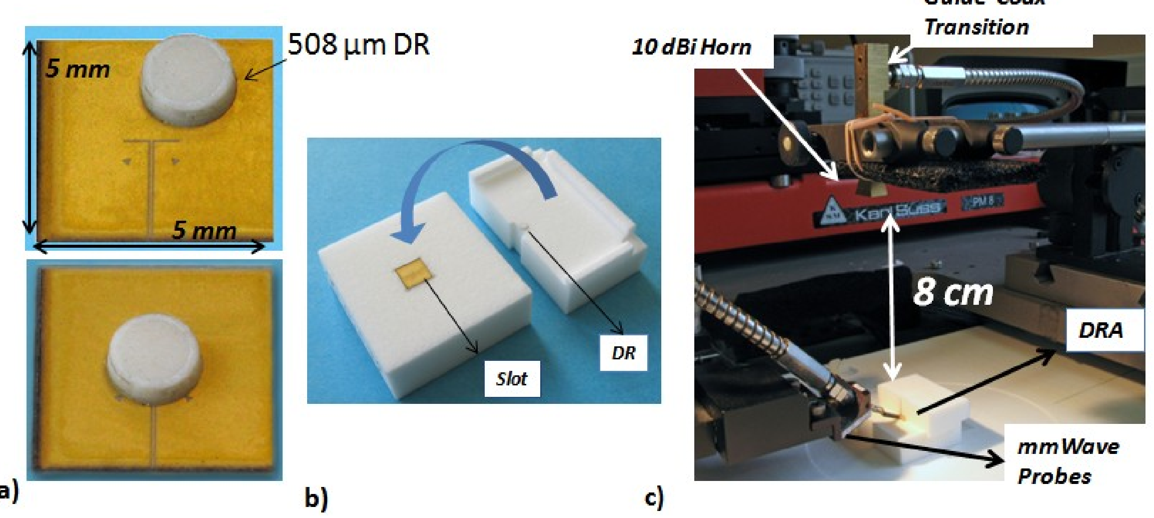

Figure 147 Measurement Bench a) DR and CPW fed slot b) Foam based support for DR positioning c) Antenna under Measurement

2.h.i) DR position shift impact

Although minimized, the DR position shift (with respect the CPW feeder) still exists and is studied next. A change is witnessed in the frequency of resonance as well as in the gain. As the DR center moves away from the slot center, the frequency of resonance shifts downwards (from 61 GHz to 58 GHz for x_shift equal to 0 and 0.3 mm respectively). The gain bandwidth is also compromised as seen in Figure 148d. Another effect is the shift in the direction of the maximum of radiation. For a 0.3 mm position shift, the maximum value is now found at θ = 40° instead of the 0° (value expected for a well centered DR). Clearly, the position of the slot regarding the maximum field of the H field on the TM^{11} mode is very important.

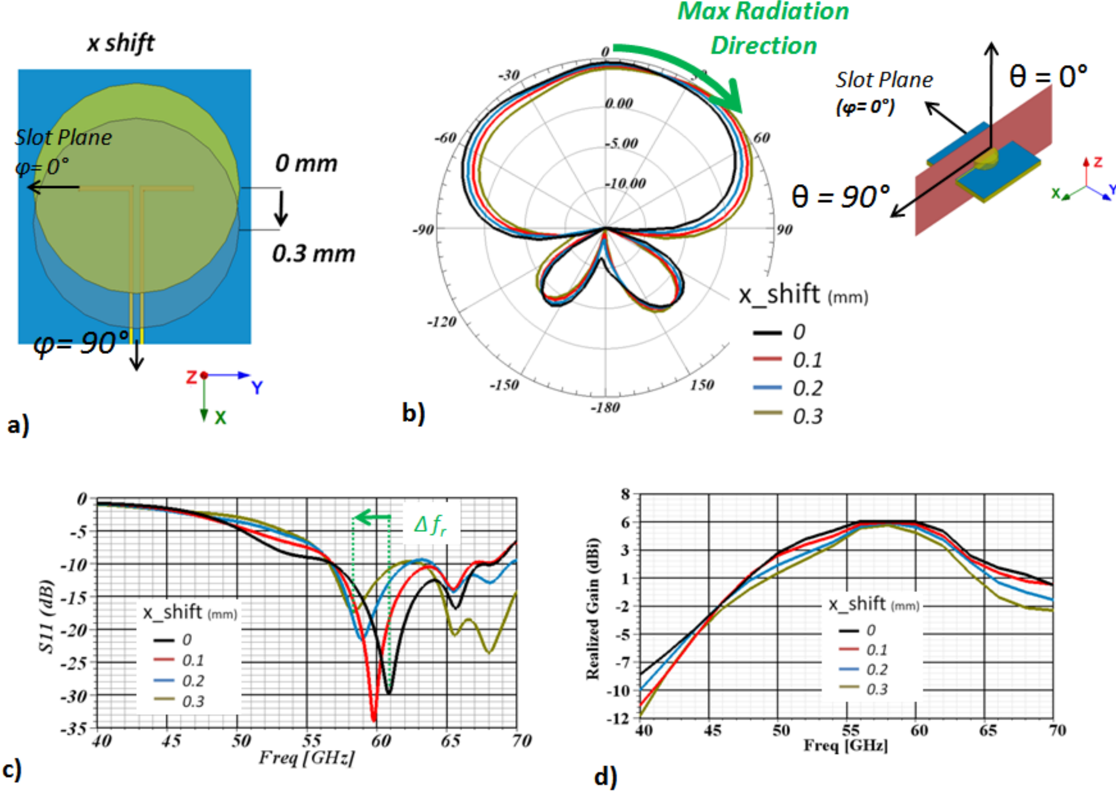

Figure 148 Study of DR misalignment. a) 0 to 0.3 mm DR shift b) Gain Pattern at 60 GHz for ϕ= 90°, c) and d) Matching and Realized Gain response (θ = 0°) .

The measured S11 and Gain results are shown in Figure 149. Six samples were measured, two for each fabricated height (508 µm, 635 µm and 1 mm). First of all, the matching response illustrate the conical shape impact on the resonant frequency. Values of 55 and 57 GHz are observed. The impact of the slot substrate is also seen in all measured results; a resonance in the higher part of the band (65 GHz) is obtained. Gain values of 5 dBi are measured for all samples at the resonating frequency and positive gain values obtained throughout the matched band. A drop on the gain response is also seen for all samples around 53 GHz as well as oscillations on the gain response, which come from unwanted reflections of parasitic elements of the measurement bench.

Figure 149 d) shows the gain measured in a single frequency point from 0° to 60° in two orthogonal planes. For the E plane, the gain of the antenna is much lower than that of the H plane. This difference is produced by the probe presence on that plane. A good agreement (measurement and simulation) is seen on the co and cross values for both planes. The expected 16 dB Co-Cross difference is seen.

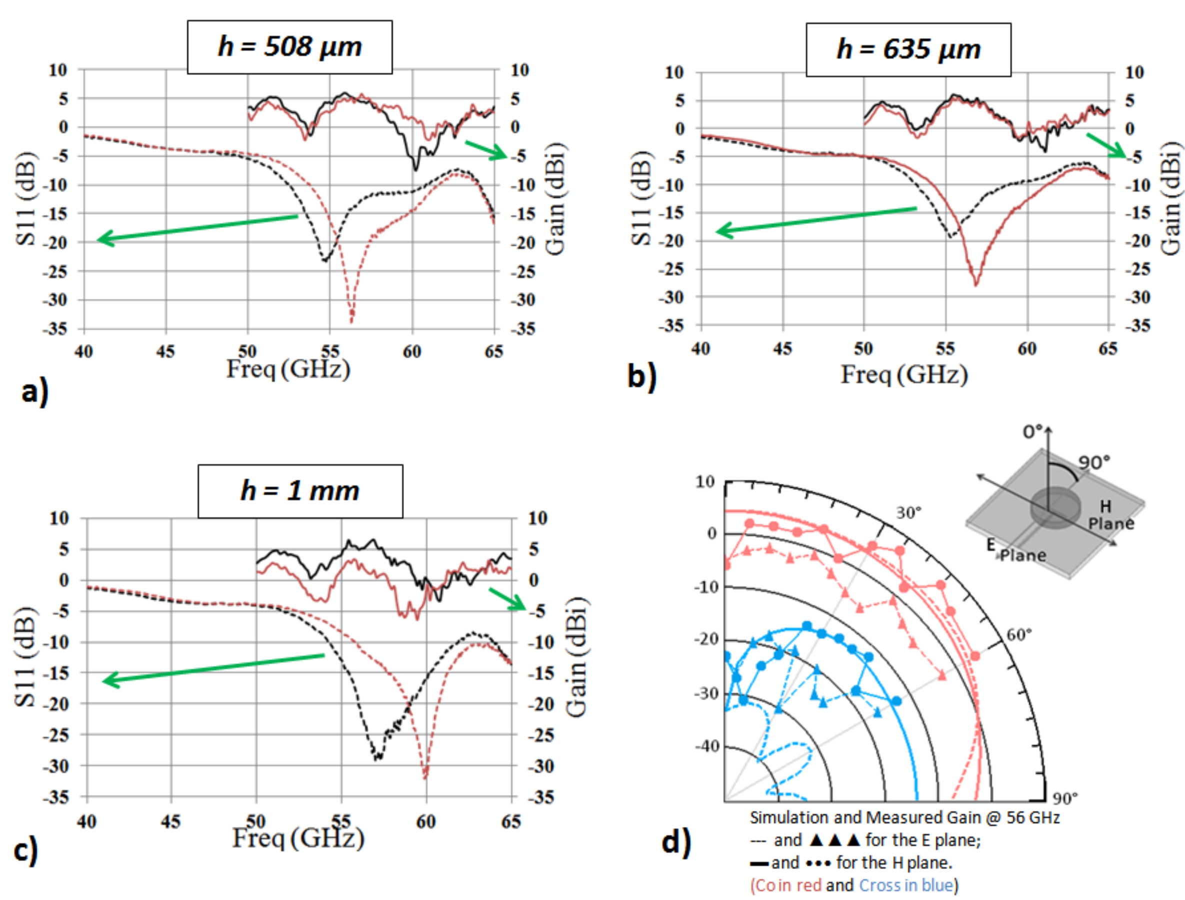

Figure 149 S11 response and Gain measurements for DR a) h = 508 µm b) h = 635 µm c) h = 1 mm and d) Radiation pattern: measured @ 56GHz for the h =508 µm DR

After the DRA measurement validation, the next step is the PA integration. In the following sections, different PA-DRA configurations are presented, exploring different packaging and interconnection possibilities.

3) PA and DRA integration

The first configuration is illustrated by Figure 150. The proposed configuration is based on the slot integration on the SOI structure. A cavity, where the chip will be introduced, is created in the alumina substrate. Once the chip inserted, the DR is positioned on top of the chip. Here, we take advantage of the small size of the slot. The length L_{slot} is reduced from 0.9 to 0.77 mm due to the higher permittivity of the silicon which is compatible with the SOI based PA dimensions (0.5 µm x 0.6 µm).

As seen before (Figure 143), coupling to the substrate limits the response of the antenna. For L_{box} = 5 mm, coupling to the substrate at 64 GHz can be seen in the S11 response. Due to

the higher permittivity of the chip, the mode established in the substrate lowered its frequency and entered into our working frequency. The excited substrate mode can be seen in Figure 151. The H field mode presents a field distribution parallel to the metallization of the substrate. It has components on the X and Y axis. Assuming field propagation along the Z axis, the mode is a TM (Transversal Magnetic). The denomination of the mode is obtained from the number of field maxima along the X and Y axis; they are shown in Figure 151 a). Two and three maxima are seen on the Y and X axis respectively rendering the mode the TM_{23}.

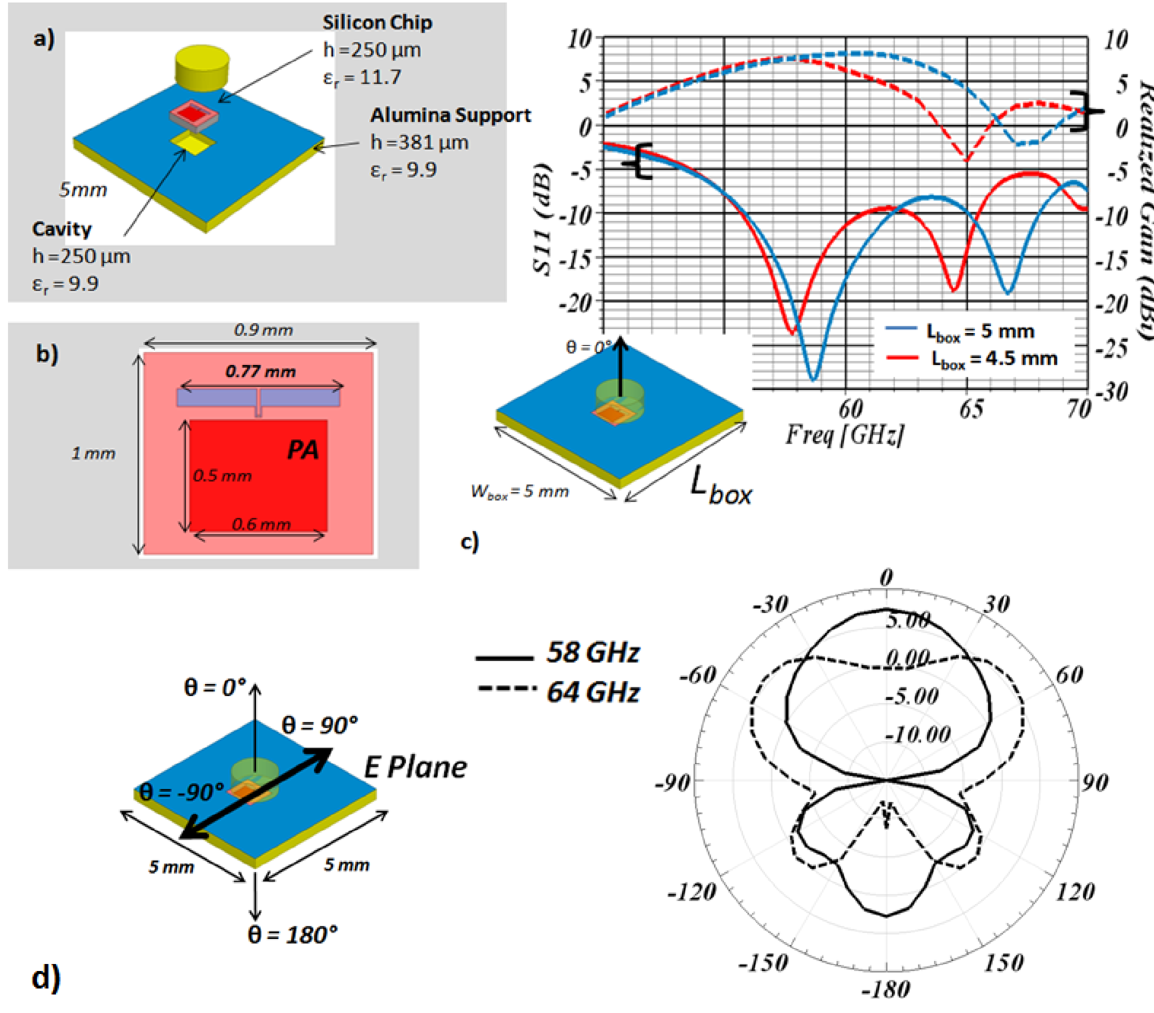

Figure 150 a) Cavity + PA+ DR → Packaging Strategy b) Dimensions of the Silicon Chip (PA + Slot) c) Gain (θ = 0°) and Matching response for L_{box} = 5 and 4,5 mm d) Gain Pattern (L_{box}= 5 mm) @ 58 and 64 GHz

The gain response is clearly affected on the higher part of the band. The gain patterns for both 58 and 64 GHz are shown in Figure 150 d). To maintain a stable radiation performance throughout the adapted band, L_{box} is lowered to 4.5 mm. This is due to the modes frequency

established on a rectangular cavity dependence on the dimensions of the cavity as explained in [12]. The substrate mode now appears at 67 GHz; radiation is reestablished on the whole band. Max gain of 8 dBi and a bandwidth of 6 GHz are obtained.

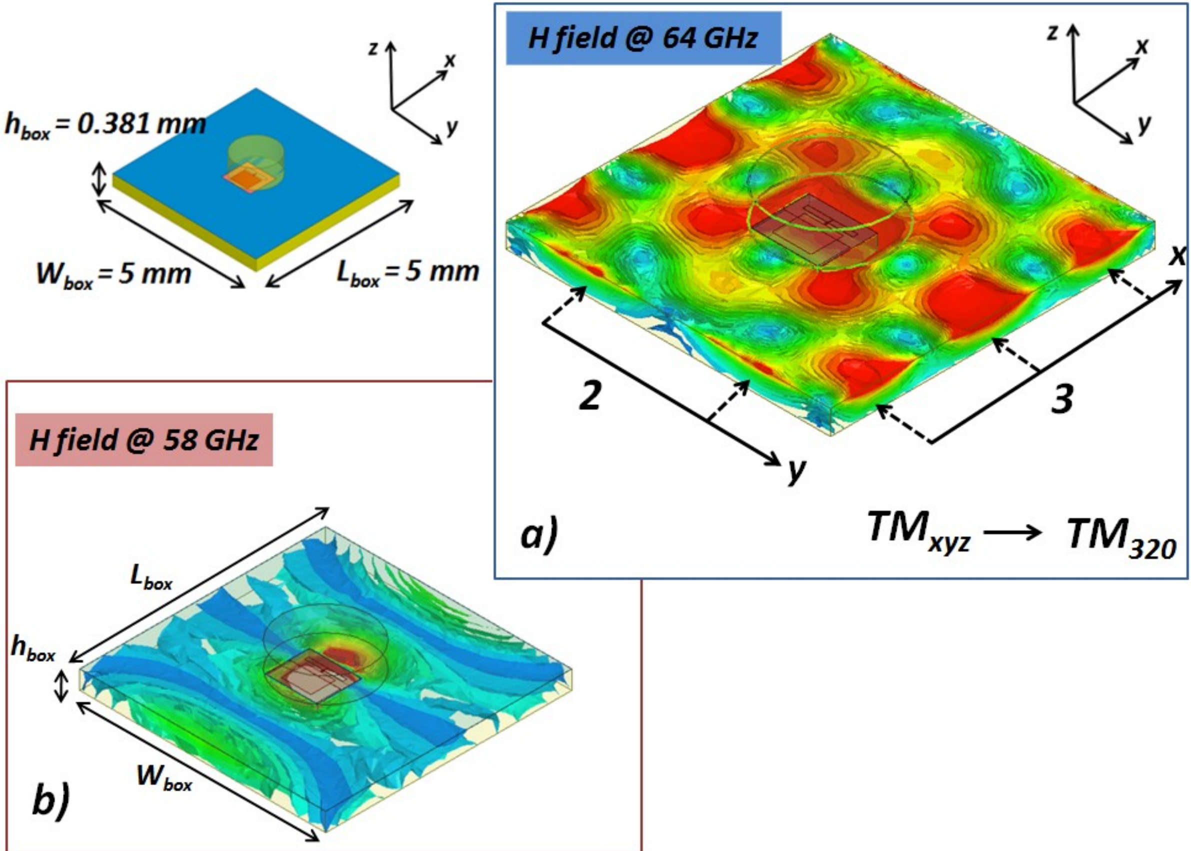

Figure 151 Substrate modes @ 64 GHz and L_{box} = 5 mm. H field in the substrate @ a) 64 GHz and b) 58 GHz

Although an acceptable performance (high gain 7 dBi, and 5 GHz bandwidth) from the antenna is obtained, the DC feeding of the PA remains difficult to access due to the presence of the DR on top of the PA. Another factor that has to be taken into account is that the high permittivity of the DR will impact the characteristic impedance of the CPW lines of the PA generating a change in the characteristic impedance of the line and consequently mismatch thus, an improved packaging of the PA + DRA has to be developed to take into account these constraints.

3.a) 1st DR incorporated in Package solution

A first solution has been investigated, where the DR is positioned on the backside of the cavity support. In this way, the access to the PA is available and mismatching due to the

presence of high permittivity elements (the DR) can be avoided. A complete solution can then be thought, with the introduction of the PCB. By introducing the PCB, the interconnections to the PA are taken into account and complete packaged solution is obtained. The proposed configuration can be seen in Figure 152.

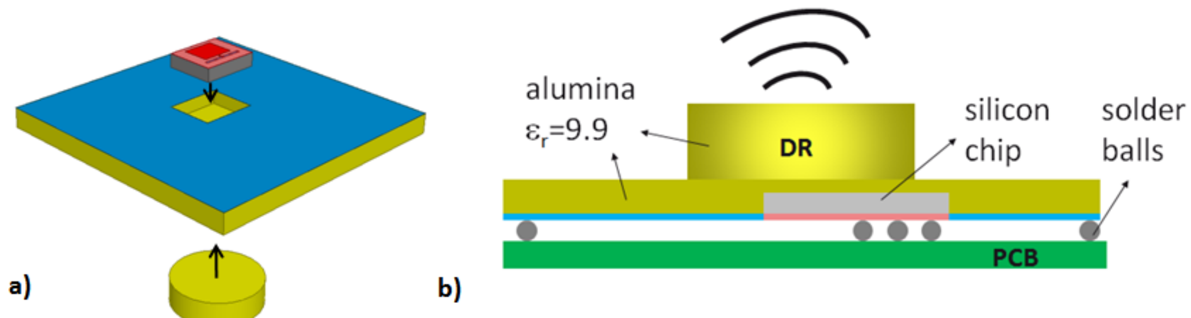

Figure 152 a) PA + Cavity + DR → Antenna and PA b) Cross view of the flip chipped Antenna- PA solution & Interconnections to PCB

The DR is placed under the on-Si slot for a proper excitation and the assembled structure flip-chipped on the PCB. Solder balls are used to carry DC biasing and RF signals to the PA (solder balls diameter impact is studied further above). The performance of the antenna is described next. One of the most important parameters for this configuration is the thickness of the substrate where the cavity is processed. The DR was previously placed in direct contact with the ground plane metallization. Now, it is separated by the thickness of the substrate. In fact, the height added by the substrate has to be added to the height of the DR, shifting the resonance frequency. As seen before, if the height is increased, a reduction of the radius is needed to maintain the same frequency. A new radius of 0.48 mm has been found by simulation to resonate at 60 GHz for a substrate height of 0.275 mm (h_{DR_new} = $h_{DR_Original}$ + h_{subs}; -Figure 153). The slot also suffers from an enlargement to be properly adapted to the dimension modification of the DR. A larger slot (length 0.9 mm) is now needed. Despite the chip dimensions increase (1.2 x 0.9 mm^2) regarding the previous solution, a small chip size is still achievable. High gain (6.1 dBi at θ=0°) with a F/B ratio of 10 dB and a bandwidth (VSWR < 2) of 7 GHz is obtained. These values make this solution very attractive as it fulfills the requirements of IEEE 60GHz application. The impact of h_{subs} on the antenna matching is also shown. As said before, the addition of the substrate increases the height of the DR, and the frequency of resonance shifts downward in frequency.

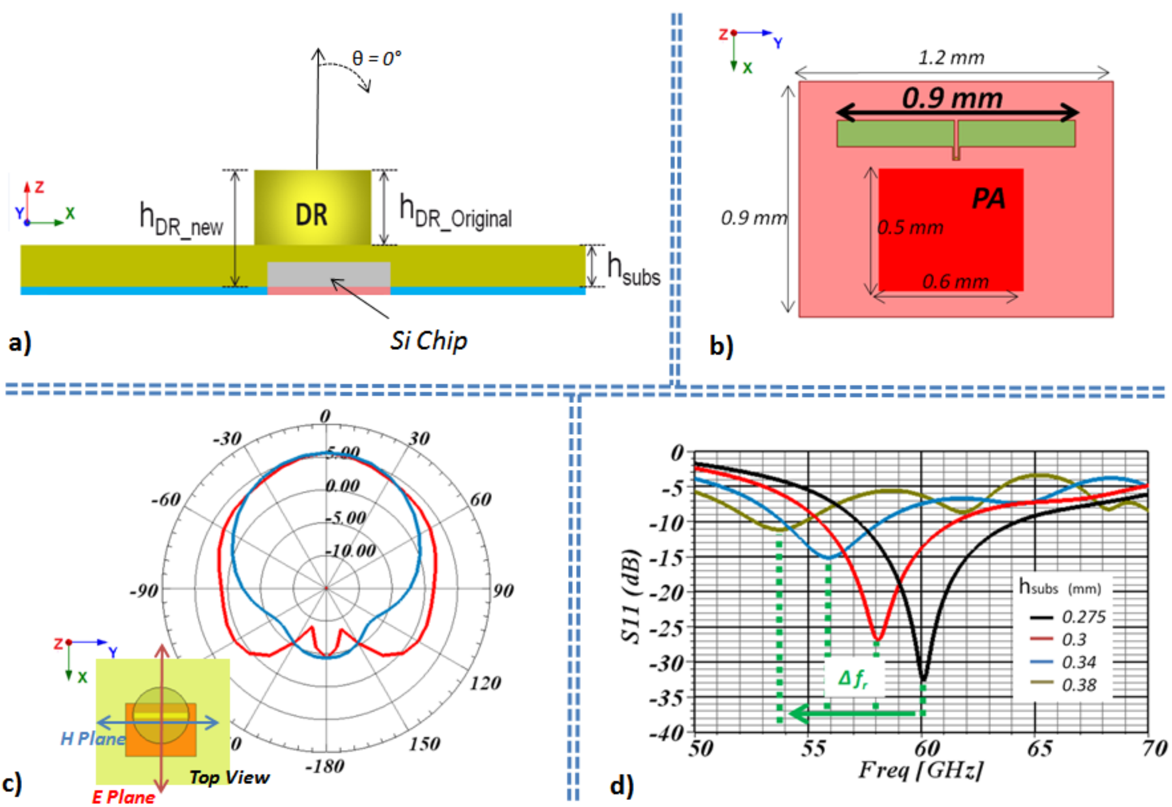

Figure 153 a) New height of the DR definition b) Modified slot dimensions c) Gain pattern for hsubs = 0.275 mm @ 60 GHz d) S11 response for hsubs variation.

To consider the whole package, the solder bumps and the PCB have to be taken into consideration in the simulation. The solder balls in charge of connecting electrically the PA and the PCB impose the distance between the PCB and the DRA. In Figure 154, the gain for several values of solder ball heights are simulated. The radiation pattern of the antenna is highly modified due to the presence of the PCB. The back radiation levels increase obtaining F/B levels of 4.3 up to 6.1 dB for 0.2 to 0.6 mm solder ball height values respectively. The maximum gain value (θ=0°) is also reduced as a logical side effect of the F/B ratio degradation. Although higher values of the solder ball height could be considered, another parameter that has to be taken into account is the losses due to such interconnection. For the 60 GHz signal, as it will be studied in more detail further ahead, the higher the solder ball the higher the losses.

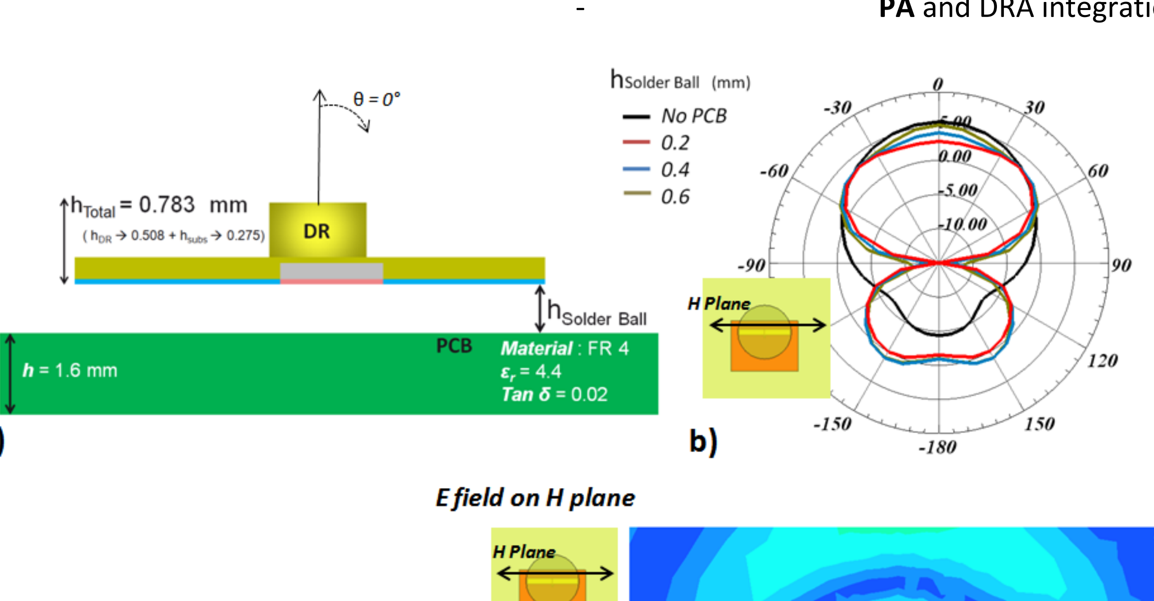

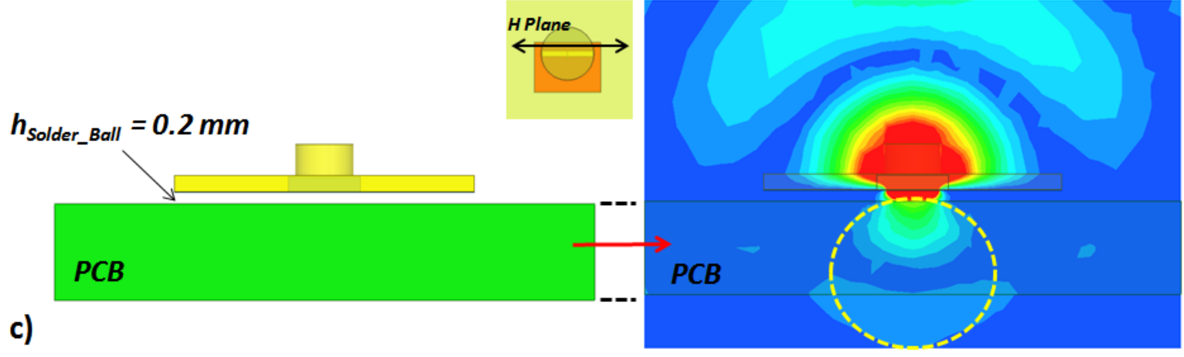

Figure 154 a) Addition of the PCB into the configuration b) Gain pattern (H plane) for different values of h_{Solder_ball} and c) E field on H plane for h_{Solder_ball} = 0.2 mm

3.a.i) Conclusions

From the previously presented interconnected PA-DRA solution, several conclusions can be extracted. First of all, the DRA continues to offer a high gain (6 dBi) and wide bandwidth (7 GHz @ VSWR < 2) response despite the relocation of the excitation slot. Secondly, the slot size has been verified to be compatible with SOI technology due to its small size. And finally, the impact of the packaging (PCB and interconnections) has been obtained from the point of view of the antenna radiation performance. Still, the DR remains as an independent element and its misalignment regarding the slot can impact the antenna performance as seen before. The solution presented next deals with this issue.

3.b) 2nd packaged solution → solving the DR alignment issue

Slot and DR alignment is a critical parameter to control, for maximizing the coupling to the DR, and thus obtaining the highest gain and retaining the expected resonance frequency. A new solution is now presented where the slot and the DR are fabricated in the same

elaboration process. This way, the positioning of the DR with respect to the slot is ensured. A miniature integrated non resonating slot structure is etched on the backside of the substrate where the DR is top-side processes (Figure 155). The DR is fabricated on the top face of the alumina using fine beam laser techniques. This resonant cylinder is excited by an integrated Coplanar (CPW) 50Ω fed slot etched on the backside of the DR supporting dielectric material, then acting as a conventional substrate. Co-integrating the DR and its excitation structure on the same mono-block substrate guarantees the critical and tedious alignment procedure between these elements during fabrication.

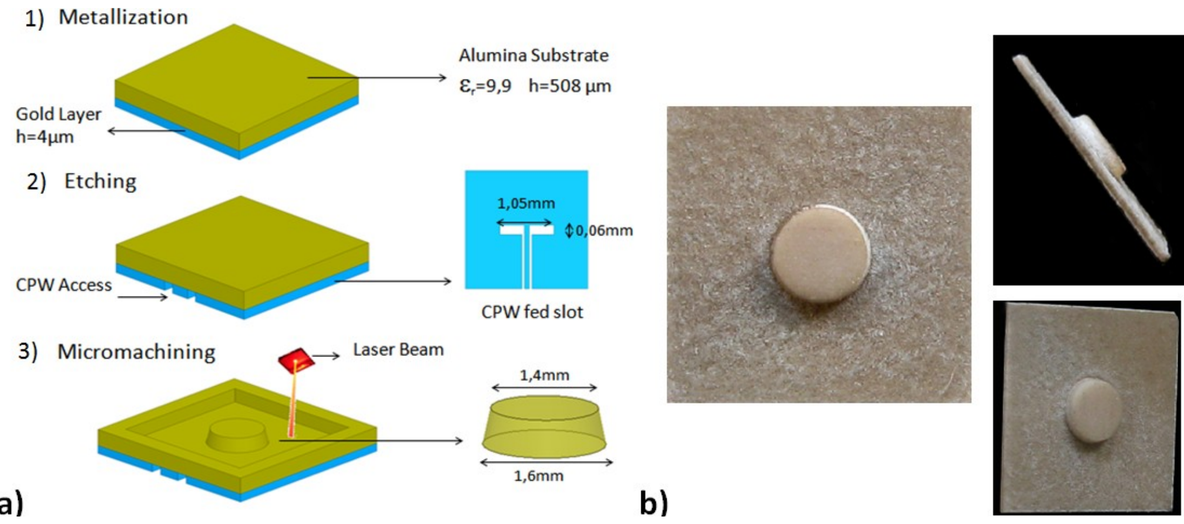

Figure 155 a) Fabrication Procedure 1) Metallization of the Substrate 2) CPW etching and slot dimensions 3) DR Laser Micromachining and DR dimensions b) Fabricated Samples

The proposed solution for the front end integration is depicted on Figure 156. The DRA, which is fabricated using fine beam laser techniques, is connected to the silicon chip through µ-bumps (height h=90µm). They will serve to deliver the 60 GHz signal to the antenna. DC bias and IF (intermediate Frequency) signals can also transit to the transceiver by way of solder bumps. These solder bumps will also be used as structural bases for the antenna, supporting in particular the DR. A good electrical isolation is consequently expected for the antenna element and the silicon device, as a metallic ground plane is placed between the DR and the Si die.

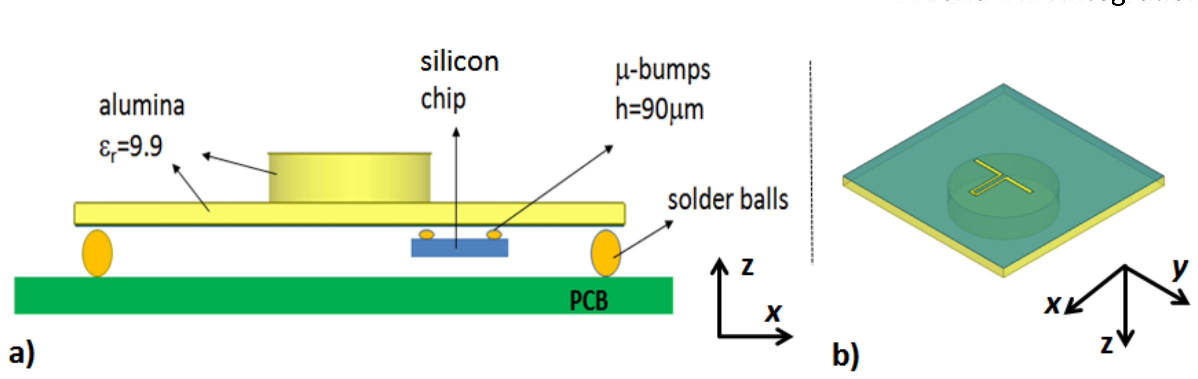

Figure 156 PA and DRA packaged integration a) Front view and b) View of the incorporated slot

As also seen, a substrate layer supporting the metallization still makes part of the DR; it does not contribute to the radiation. In fact, this substrate is vital for the performance of the system. It serves as base for the ground plane that will allow us to isolate the DRA from the active devices, which appears as one of the most important characteristics of the integration configuration.

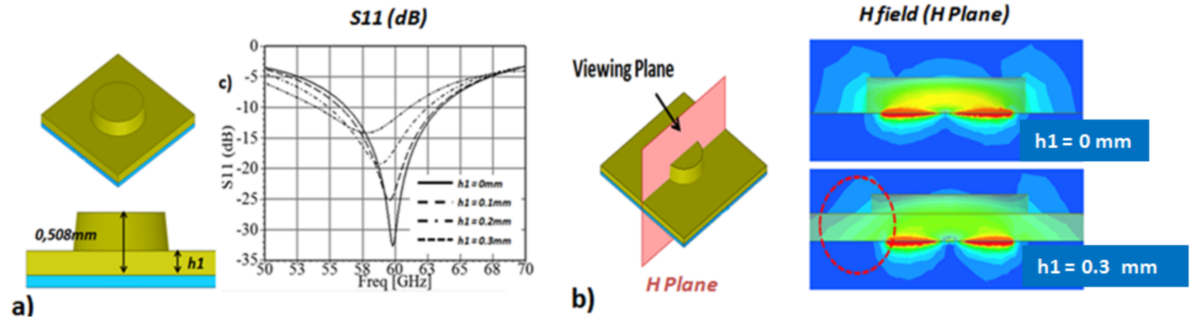

Figure 157 a) Frequency shift and mismatch caused by h1 b) E field for h1 = 0 and H1 = 0.3 mm.

The effect of this substrate is studied next. Several values of the substrate thickness (h1) were simulated and the reflexion coefficient is shown in Figure 157. The initial value of h1= 0 mm is the extreme case where only the DR is present. For our study, the DRA has been matched to this configuration. The CPW line characteristic impedance will also be influenced by the height of the substrate. To avoid this, the CPW line has been eliminated from the configuration and an internal port has been used to excite directly the slot. As h1 increases, a shift in the resonance frequency is observed. This frequency shift can also be seen when the radius of the DR increases; this is partially what is happening when we add a substrate layer to the configuration. The magnetic field has been plotted for h = 0 and h = 0,3 mm. The H field for h = 0 is mostly confined in the resonator contrasting with h = 0,3 mm

configuration, where fields partially laterally radiate (highlighted by a dashed red circle). The magnitude of h1 has almost no influence on the gain of the antenna. As the height of the substrate increases, an impedance change is clearly seen by the degraded value of the matching level. This is logically due to the disappearing shape of the DR each time h1 increases. Once h1 reaches the height of the DR, no cylindrical element will exist and the modes generated by the DR cylindrical boundaries will not be able to exist. Values from 6.3 to 5.9 dBi were found for variations of h1 from 0 to 0.3mm.

3.b.i) Backside radiation measurement bench

Another important characteristic of this antenna is the “clean” measurement conditions, due to the back-side position of the slot excitation plane and radiation characteristics of the antenna induced by the DR (Fig. 8). They are both radiating in different hemispheres separated by the ground plane of the slot. This results in reduced radiations of the antenna in the backward direction (θ = 0°, Figure 158), thus suppressing interferences with the inherent radiations of the mm feeding probe, as previously discussed in chapter 2 and studied in [108].

A new configuration for the measurement test bench is thus introduced. As seen in Figure 158, the access of the feeding probes (metallization layer) and the radiation of the antenna do not share the same side any longer. This forces the placement of the receiving antenna under the DRA. To achieve this, a foam based structure is fabricated. It will serve as support for the DRA and the receiving antenna. The receiving antenna is a 10-dBi gain horn antenna which is connected to a V Band Coax-guide transition. Absorbing material has been added to the surface of the horn antenna facing the DRA to suppress any reflexion that could interfere with the measurement results. As evidenced by the noise seen in the gain measurement results, this was not sufficient; the wide edge of the horn antenna still provides a large metallic region to reflect the energy from the DRA. The supporting structure will house these two elements and will ensure the proper alignment between the receiving and transmitting antenna. A specific receptacle is also fabricated to fix the DRA at the other end of the support. This will avoid the displacement of the DRA, thus to maintain the proper alignment between both antennas. The support is divided into two parts to allow the rotation of the receiving antenna and to measure co and cross polarization. In Figure 158c, we have a

complete view of the system and top view of the fabricated DR, respectively. The drawback is that no radiation pattern can be measured.

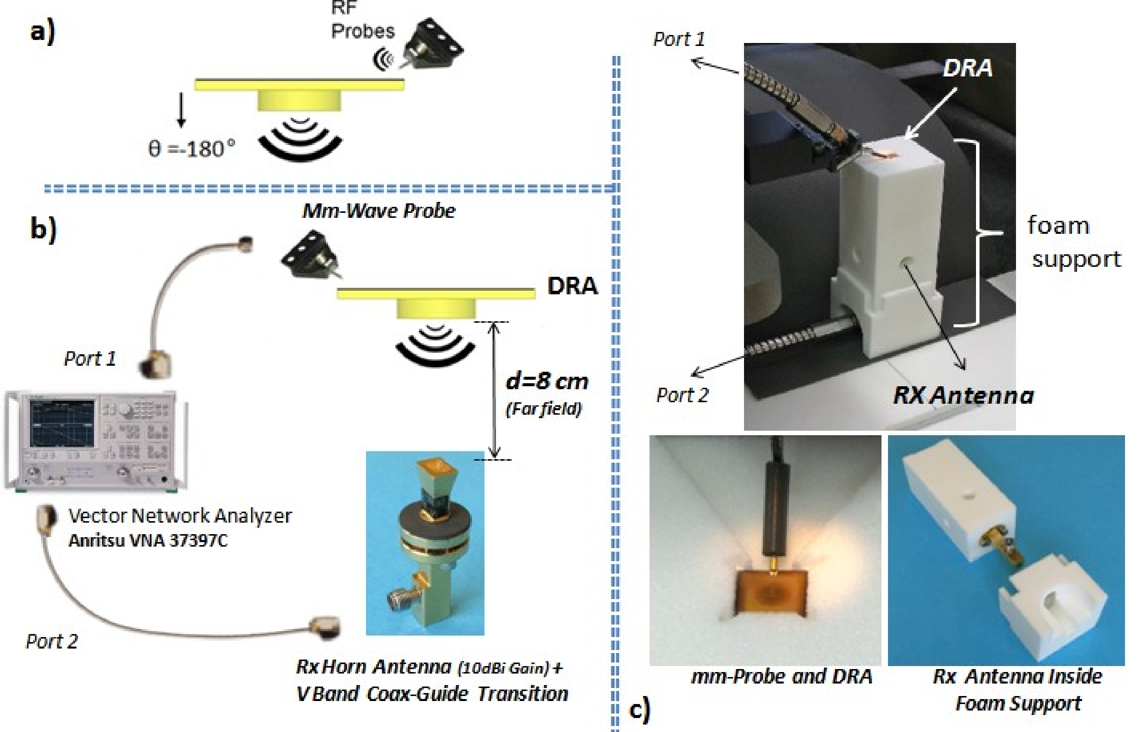

Figure 158 a) RF probes radiation b) Backside radiation measuring setup and c) Foam support for the implementation of the setup

3.b.ii) Measurement results

Due to fabrication tolerances, the desired shape of the resonator is slightly affected, as explained before. A conical resonator results due to the laser machining technique employed. This shape modification has been taken into account by retro simulations. A wider -10dB bandwidth (6.4 GHz instead of 4.7 GHz) is obtained, improving the performance with respect to the conventional cylindrical resonator. This shape modification results also in a resonant frequency shift of about 3 GHz due to a smaller top diameter of the cone. A lower gain is also encountered, from 6.7 to 5.4 dBi, but remains acceptable for the expected applications. Measurements have been performed and are in good agreement with simulation. A maximum 5.5 dBi gain value has been measured with a 6.2 GHz bandwidth. A simulated minimum efficiency of 59% was obtained within the properly matched frequency band of the antenna with a maximum efficiency of 95% @ 61.3 GHz.

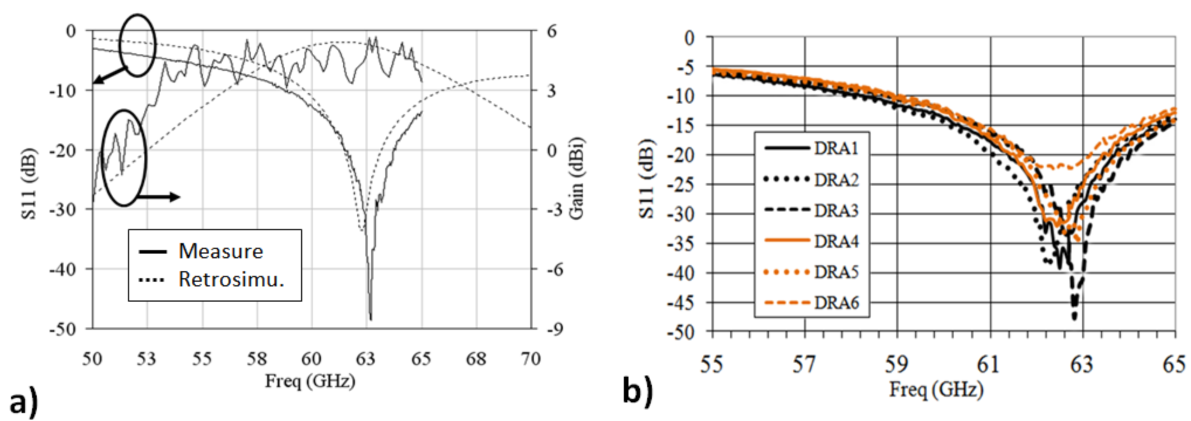

Figure 159 a) Matching and Gain measurement against Retrosimulation b) Matching response for all 6 fabricated DRA

Six DRA samples were fabricated to determine the repeatability and reliability of the laser micromachining; in Figure 159, the corresponding reflexion coefficient of each one is presented. Different matching levels were measured as could be expected due to different dimensions obtained by the fabrication procedure. Measured diameters ranging from 1.54 to 1.59 mm were micro machined. This difference in dimensions is also evidenced by a shift in resonance frequency as seen in the measured data. A maximum frequency shift of 0.6 GHz was found between the resonance frequency of the smallest and largest DRA. This value can be decreased if other fabrication techniques are used, like high-power laser machining technique or injection moulding techniques.

3.b.iii) Silicon Chip integration

As for the silicon chip integration, the use of µ-bumps is introduced. A study of the losses introduced by these µ-bumps is done for two configurations. Modern silicon technologies allow to obtain for CMOS processes bumps of 25 and 50 µm in diameter with pitch of 50 and 100 µm [109]. From 5 to 10 µm should be added to the height of the bump regarding its diameter. So in fact, the modelling of the solder ball for the 3D electromagnetic simulator will now be a cylinder. The µ-bumps will make part of a CPW - µ-bumps – CPW transition that will add some loss to the system. Two CPW lines (Alumina and Silicon) are simulated to obtain their loss. Then the transition is simulated for the dimensions of the µ-bumps given before.

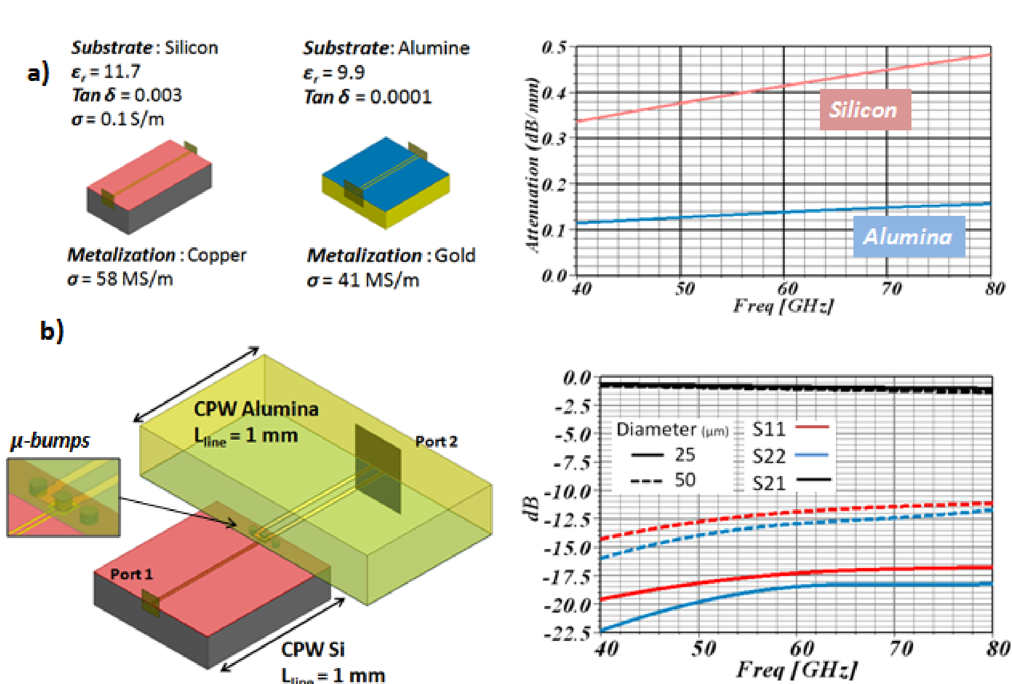

Figure 160 µ-bump loss extraction a) Silicon and Alumina CPW b) CPW - µ-bump – CPW transition and S parameters.

To obtain the loss due to the insertion of the µ-bump (Insertion Loss (IL)), the losses of the CPW lines are removed from the S21 value of the whole configuration. At 60 GHz -1 dB and -0.8 dB for the 50 µm and the 25 µm diameter case are observed. The losses in the CPW access line give a total of 0.56 dB (0.42 dB (Silicon) + 0.14 dB (Alumina)) which gives us an IL of 0.44 dB and 0.24 dB.

For the next analysis, the 50 µm solder bump has been used. The chip is now added to the configuration as seen in Figure 161. At first glance, we can see a slight frequency shift that can be corrected with a proper dimensionning of the slot. Secondly, a reduction in the bandwidth is also perceived. This reduction is also seen in the gain response.

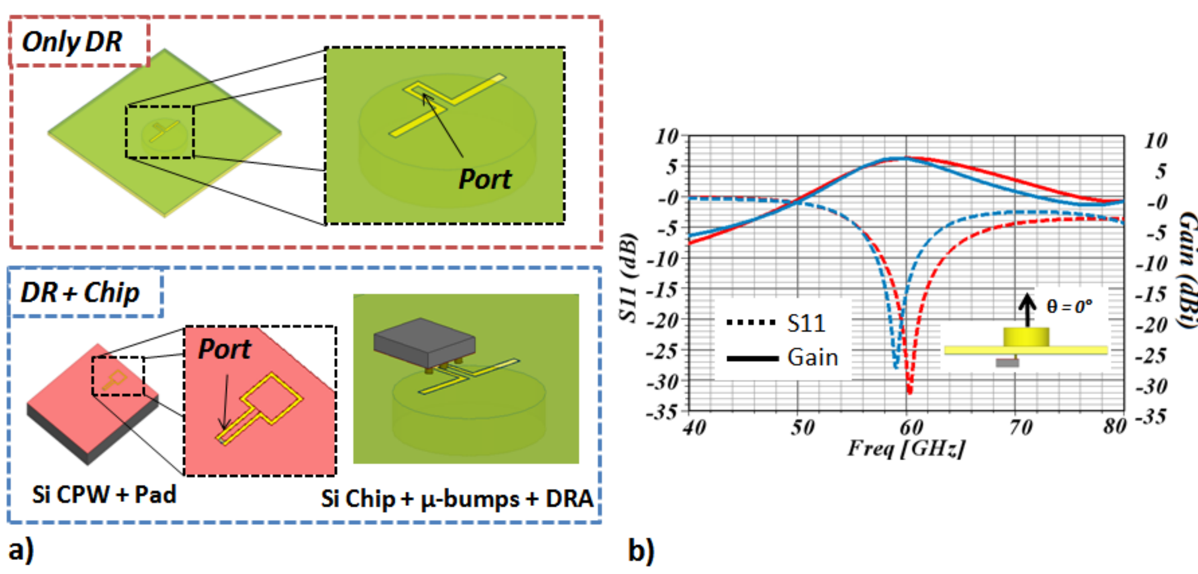

Figure 161 μ-bumping the chip to the DRA a) Only DR and DR + Chip Configuration b) S11 and Gain response

As mentioned before, a good electrical isolation is expected between the antenna and the silicon based devices due to the ground metallization layer separating both elements. Several integration configurations, as the one mentioned in [110], witnessed the influence of the Si Chip on the radiation of a nearby antenna. A decreased gain and some degradation of the radiation pattern were found. For SiP configurations, the antenna is separated from the Silicon die. As a result, the silicon die becomes part of the radiation environment of the antenna and will most probably affect its radiation performance due to its proximity. In our case, due to the slot plane, the radiation pattern should not be affected, at least in the intended direction of maximum radiation. Figure 162 shows the simulated radiation pattern of the DR taking into consideration the presence of the Si die compared to that of the DR alone.

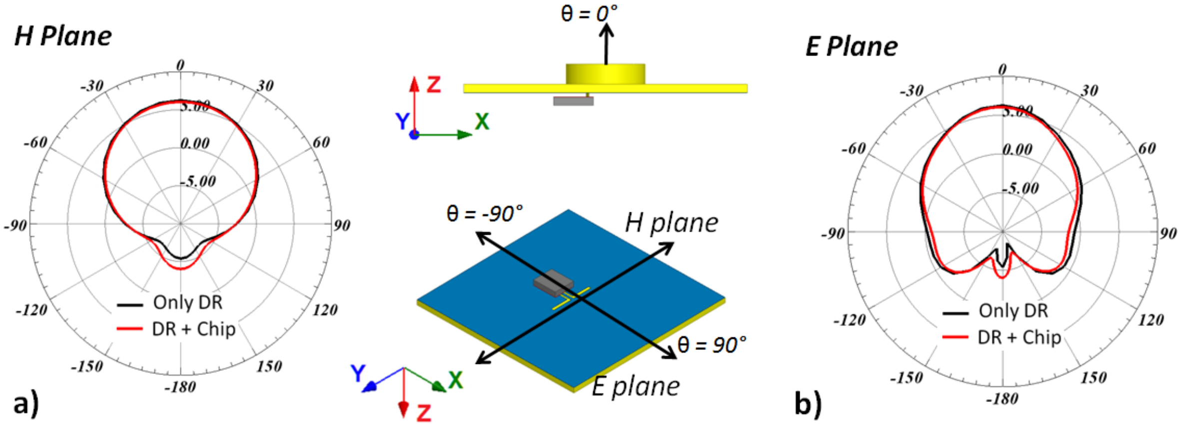

Figure 162 Radiation pattern for Only DR and DR + Chip configurations a) E Plane and b) H plane

A decrease of 0.2 dB on the maximum gain is seen for the case of the DR + Chip. This is only due to the μ-bumps IL described earlier. Another effect seen is a lower F/B ratio, from 11.6 dB for the DR alone case to 10.2 dB level. Certainly, the high permittivity of the chip attracts the radiation coming from the aperture of the slot. The impact of the chip appears to be higher in the E plane; a slight dissymmetry is seen in this plane more evidently in the backside radiation (θ = 180°). This is logically due to the presence of the chip in this plane. But despite the changes seen due to the presence of the chip, the performance of the antenna remains inside the specified criteria. The only drawback is the reduction of the bandwidth as seen before. To be able to increase the bandwidth, the ratio radius/height of the DR could be adjusted. A parametric study has been done for a DRA (DR + excitation slot) of radius of 1.1 mm and ε_r = 9.9. The height of the DR has been varied from 0.4 to 1.1 mm. As the frequency of resonance will shift, the relative bandwidth has been chosen as the control parameter. The definition of the relative bandwidth is seen in Figure 163. For our application, a relative bandwidth of 11.6% is required (7 GHz @ 60 GHz). As we can see, if the height of the DR is increased, a wider bandwidth is achievable. Values for radius (a) /height (d) in the order of 0.5 or 0.6 should give us a wide bandwidth response. The gain for all these values maintains a rather stable level of max gain at the broadside direction (θ = 0°), between 5.8 and 6.4 dBi.

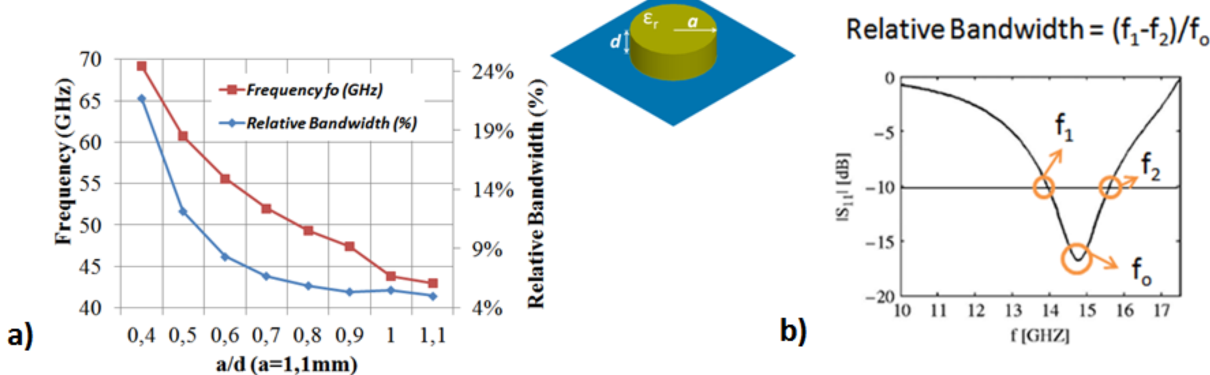

Figure 163 Parametric study of d (height of the DR) a) Frequency and Relative Bandwidth for varying d and b) Definition of relative bandwidth.

3.b.iv) Conclusions

Several conclusions can be extracted from the previously presented solution. First of all, by incorporating the DR and the excitation in a single element solve the misalignment issues presented before. The new configuration maintains a high gain (5.5 dBi) and wide bandwidth

response (6.2 GHz @ VSWR <2). In second hand, the new mono-block solution required a new measurement setup due to the antenna radiation direction and the mm-probe access plane. Consequently, a new measuring set up is presented for back-radiating antennas. Finally, the separation of the antenna excitation slot from the silicon chip required the introduction of interconnections. With this in mind, the whole system (PA-interconnections-Antenna) has been validated by simulation.

Although the PA-Antenna configuration is connected to the PCB and the chip is protected by the DR, it is not completely packaged as it is explained next. For this, a new completely packaged solution is presented.

3.c) 3rd packaged solution → *completely* packaged solution

For the previously mentioned solutions, the chip is not completely protected by the package. The use of solder balls as mechanical support will not fit entirely the definition of a packaged solution. According to [111], an IC package should provide electrical interconnection, mechanical support, environmental protection and heat dissipation. From the previous solutions, electrical interconnection and mechanical support have been achieved. Although temperature measurements have not been done, heat dissipation should not be a concern due to the low power levels managed by the chip. One last feature remains though, the environmental protection. In our previous packaged solutions, the chip is not completely isolated from the environment. The solder balls that make up the mechanical support will not provide the chip a complete shield from the environment. Having this in mind, a new solution has been designed and tested where the chip is completely protected from the environment. Knowing the good gain and bandwidth response of DR based antenna, a DR based packaging solution will now be presented.

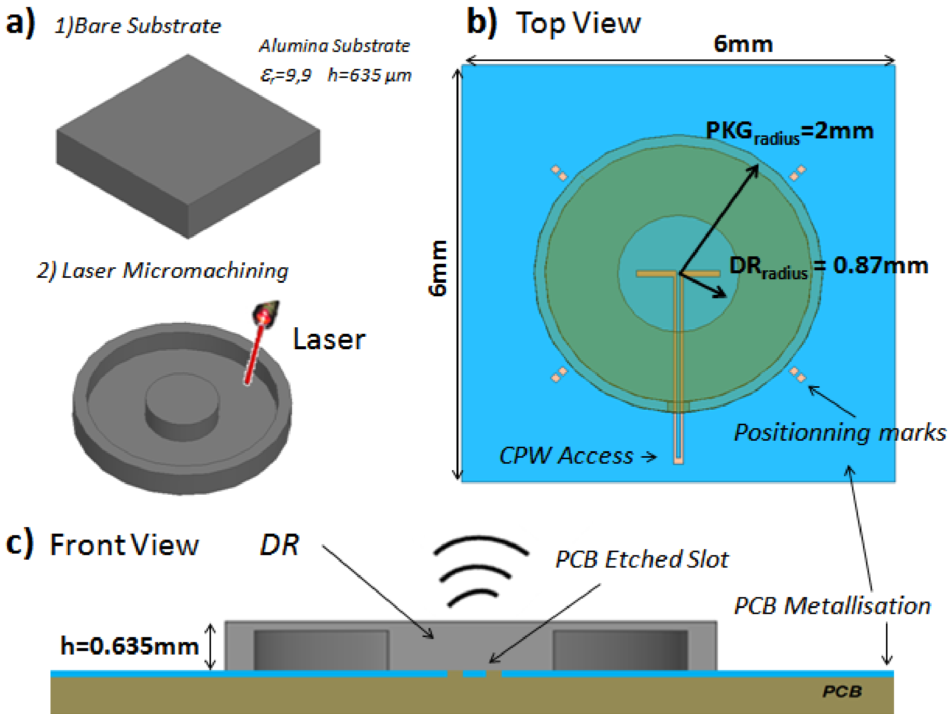

Figure 164 a) Micromachining process b) Top view of Package and PCB etched slot c) Front view for PCB and Antenna Integration

The antenna concept is presented first. From a bare alumina substrate, the DR and the package are shaped by a laser micromachining process. Then, the package is flip-chipped onto the PCB where a slot fed by a CPW line has been previously etched. A total package size of 36 mm^2 (6x6 mm^2) is obtained with a 0.635 mm thickness. This package size is in the same range of those found for example for industrial QFN (Quad Flat No-Lead) packages Figure 165, where 40 mm^2 (6.35x6.35 mm^2) or 57 mm^2 (7.62x7.62 mm^2) are commonly used dimensions [112]. The fabrication procedure and final antenna-PCB configuration can be seen in Figure 164.

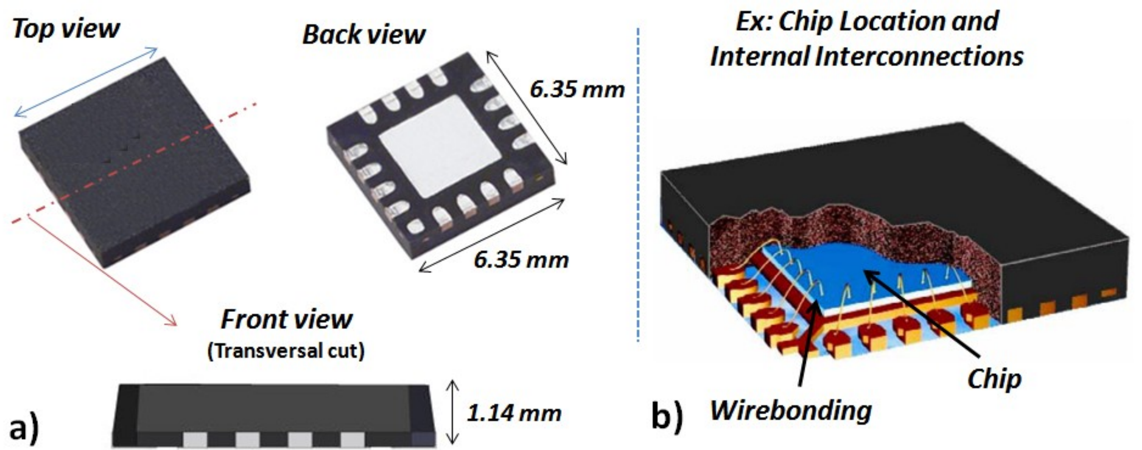

Figure 165 QFN example a) Kyocera 16 I/O package[24] and b) Internal view (chip and interconnections) [25]

To be able to study the package impact on the antenna, it is divided into three independent elements (Wall, DR and Lid) as seen in Figure 166. The first two elements, the lid and the DR are studied next. No CPW line is included. The slot is directly excited at its centre as it is shown in Figure 138.

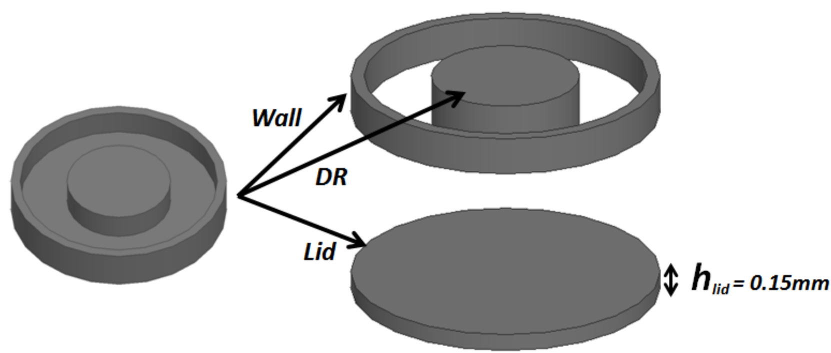

Figure 166 Elements of the DR based Package

3.c.i) The lid effect

The matching, gain and radiation pattern are shown for three different values for h_{lid} (Figure 167). The bandwidth (VSWR < 2) is increased considerably when the lid is added. Values increasing from 6.9 GHz (Only DR) to 9.2 GHz, 11.7 GHz up to 12.4 GHz (h_{lid} = 0.1, 0.2 and 0.3 mm respectively) are obtained. It can be observed that the matching value (S11 (dB) = -10dB) at the high end part of the bandwidth remains at the same frequency of 62.5 GHz. The

[24] http://www.pcb-3d.com/models/

[25] http://www.obs.u-bordeaux1.fr

bandwidth increase comes from the lower part of the band. As the lid is added and its thickness increased, a part of the electrical field for the resonant mode is located outside the DR leading to a resonant mode at a lower frequency. The same behaviour (bandwidth increase) is seen when varying the radius from 2 to 6 mm; we obtain a bandwidth variation starting from 6 to 9.5 GHz.

As h_{lid} tends toward 0.3 mm, a new mode appears in the high part of the band. This mode allows energy to propagate through the lid toward the edges. The E field @ 67 GHz for different phases is shown in Figure 167c. This mode exhibits a good coupling to the slot exciting the DR which gives us limit for the h_{lid} value. The impact of this coupling can be seen in the gain response (Figure 169a). For h_{lid} = 0.3 mm, a perturbation in the gain response is observed at 60 GHz. Regarding the gain and the bandwidth for values between 0.1 and 0.2 mm, a value of 0.15 mm has been chosen as it allows manipulating the object without fear of destroying it and gives us as much height as possible for the space necessary to locate the chip under the lid.

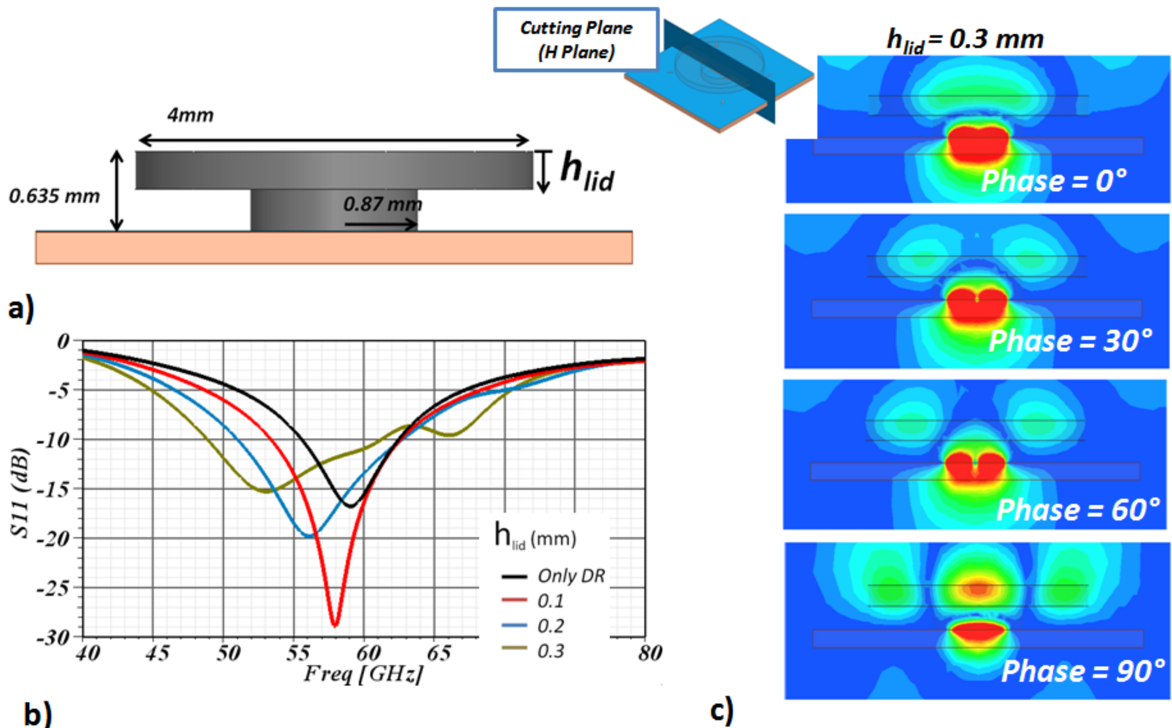

Figure 167 Lid Thickness study a) Configuration b) Matching response for different h_{lid} values and c) E field magnitude for h_{lid} = 0.3 for different phases (67 GHz)

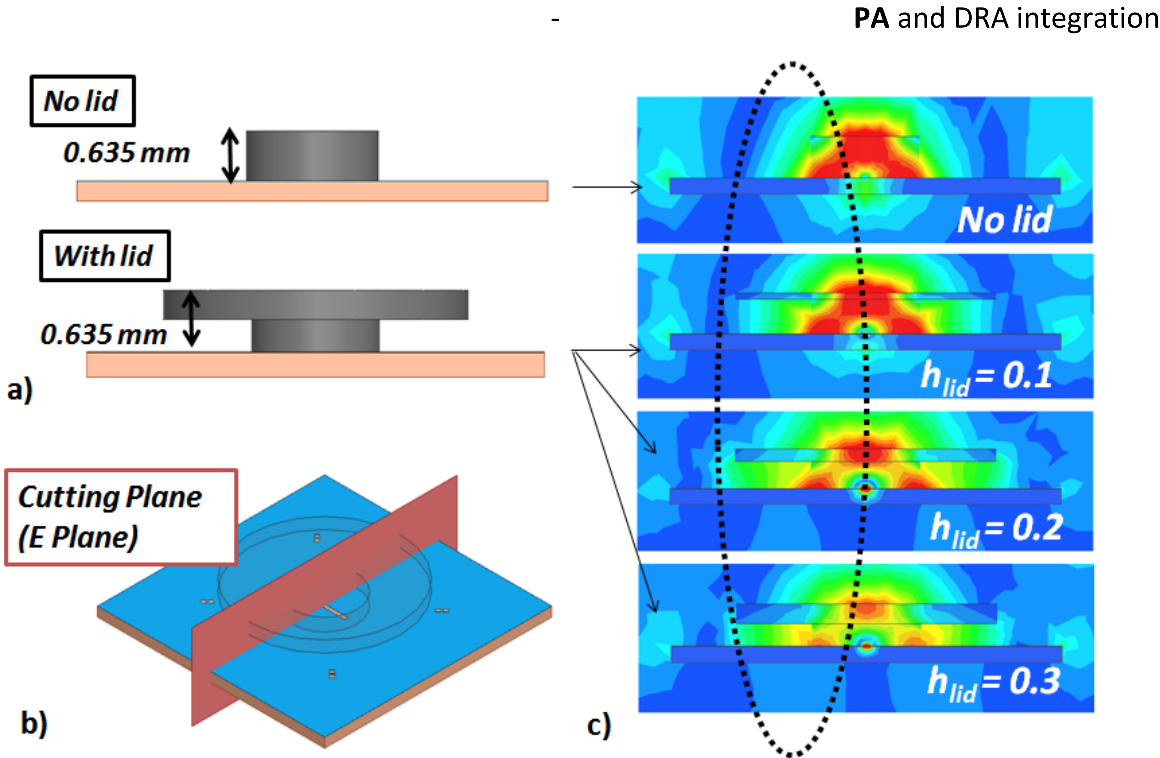

Figure 168 Increase in the frequency band study a) No lid and With lid configurations b) E field Cutting plane and c) E field magnitude for different heights of h_{lid} (Substrate and ground plane are finite)

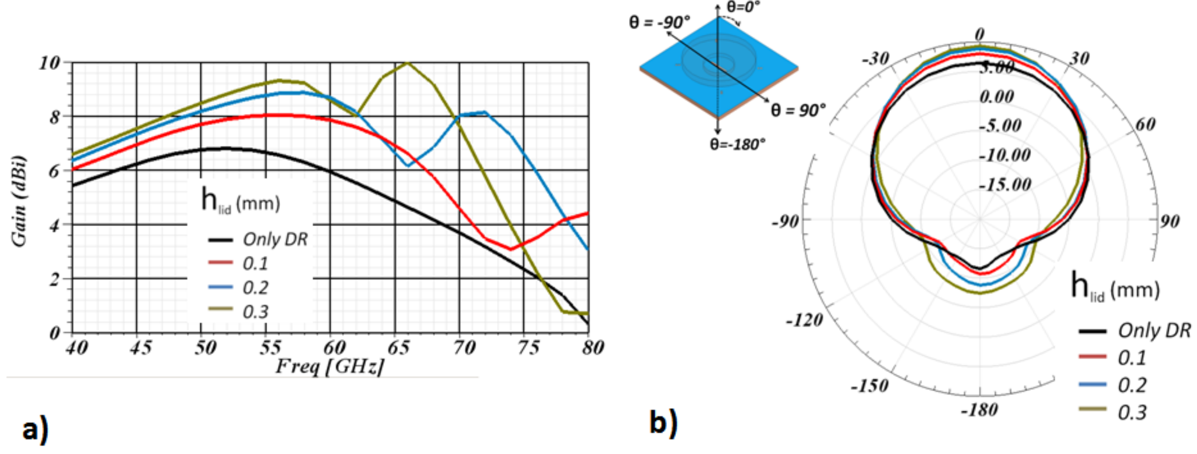

Figure 169 a) Gain and b) Gain pattern for h_{lid} variation @ 57 GHz

The gain increase can be explained with the help of the gain pattern for the H Plane seen in Figure 169b. The - 3 dB beamwidth values are 91°, 74° , 68° , 62° for Only DR, 0.1, 0.2 and 0.3 values of h_{lid} respectively. The lid concentrates the energy toward the broadside direction (θ = 0°), increasing the gain in this direction.

3.c.ii) The wall effect

As well as for the lid, for certain distances of the wall from the DR resonator (Wall_dist), an important decrease in gain is seen. As the Wall_dist parameter increases, the wall element in the configuration becomes more and more important. It begins to couple to the DR energy and two radiating elements start to appear at the extremities of the package. For 5 and 6 mm cases, the coupling to the wall is particularly strong, and changes completely the radiation pattern of the antenna (Figure 170c). Field that was directed in the broadside manner before, is now concentrated at the edges (θ = 0°). A low radiation (- 15dBi) point at θ = 0° is now obtained with radiation performance that decreases for our solution. A value of 4 mm for the wall distance is now selected, to be able to maintain a high broadside gain up to the higher part of the frequency band at 65 GHz as seen in Figure 170b.

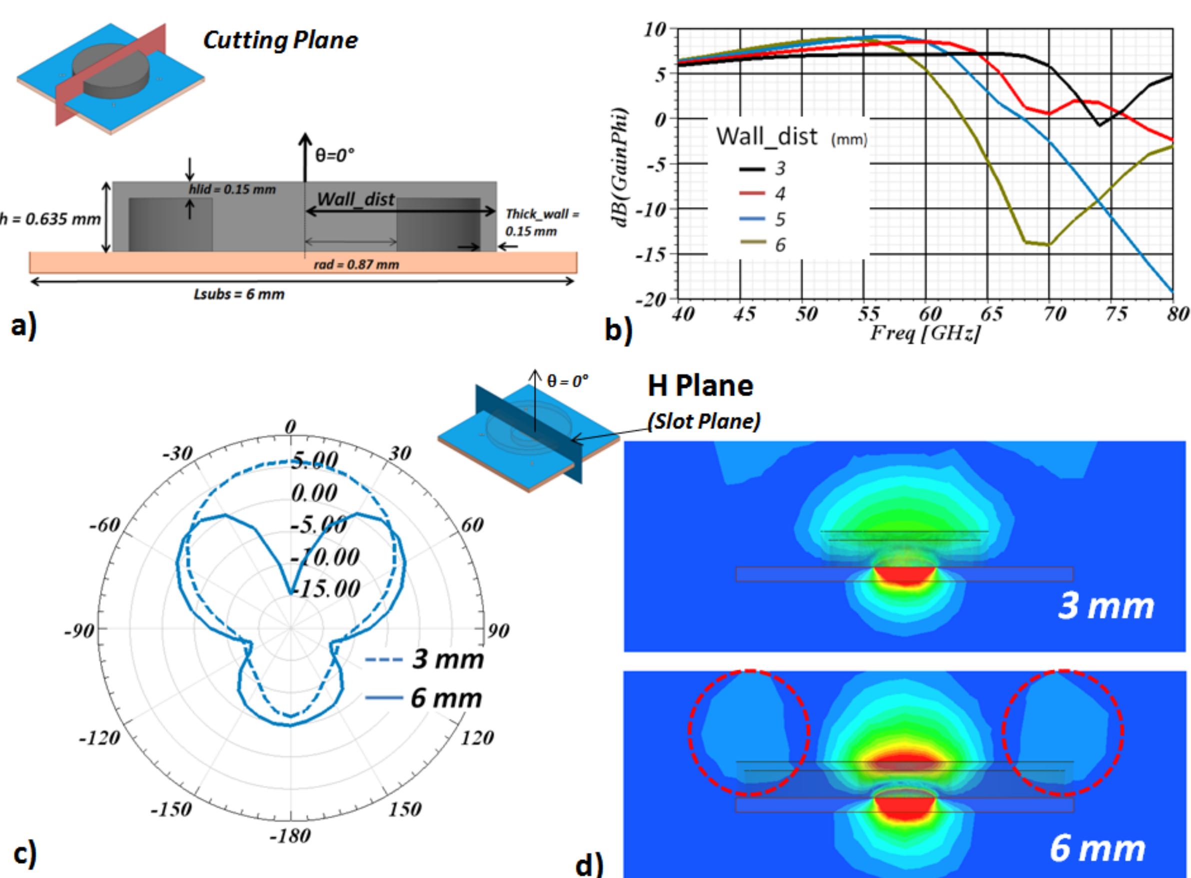

Figure 170 a) Parameter descriptions b) Gain (θ=0°) for different values of Wall_dist and c) Gain Pattern @ 70 GHz d) Magnitude of E field in the H field @ 70 GHz.

3.c.iii) The CPW coupling mechanism

Although the antenna is based on a slot excited DR, the coupling mechanism between the slot and the DR changes as the coplanar feed line is included. A single DR (that is, no package and no line), a DR fed by slot and coplanar line (no package), and the packaged DR are compared in Figure 171. Starting by the configuration of only the DR and the slot, a unique resonance is observed around 58 GHz. This is clearly the resonance of the DR coupled slot. A max gain of 6 dBi is found, that is in accordance with the value of the cylindrical DR presented previously. As we add the CPW line, three resonances appear; one for the DR that is shifted upwards in frequency (at 65 GHz) and two other (at 56 and 48 GHz) that are due to the coupling of the coplanar line to the DR. The coupling to the line can be seen in Figure 173a, where the E field magnitude for the three resonances is shown. For all cases, the phase of maximum intensity has been selected to be able to see the field at its maximum value. We can also observe how the magnitude at 65 GHz is lower than the other two cases, which can be verified in Figure 171b by the gain curve. Next, the package is added to the configuration. The three resonances are still present as seen in Figure 171c. A shift in frequency is witnessed for the resonance @ 56 GHz, increasing 4 GHz up to 60 GHz accompanied also by a 2 dBi increase in gain over almost all the matched band. This clearly indicates that the presence of the packaging impacts the performance of the DR. In Figure 173b, the E-field configuration for the DR and the DR with package is plotted. It can be clearly observed that radiation is not only due to the DR but to the whole structure. This may explain the gain as for any antenna it is dependent on its effective aperture area [8]. Finally, a 15 GHz operational bandwidth is obtained (47 GHz – 62 GHz) with a gain higher than 6 dBi and reflection coefficient lower than -10 dB. This value may seem high if the antenna 4 mm diameter is considered as the antenna aperture. In fact, the aperture of a DR based antenna is difficult to estimate due to the 3D nature of the radiating element. An additional dimension is thus needed.

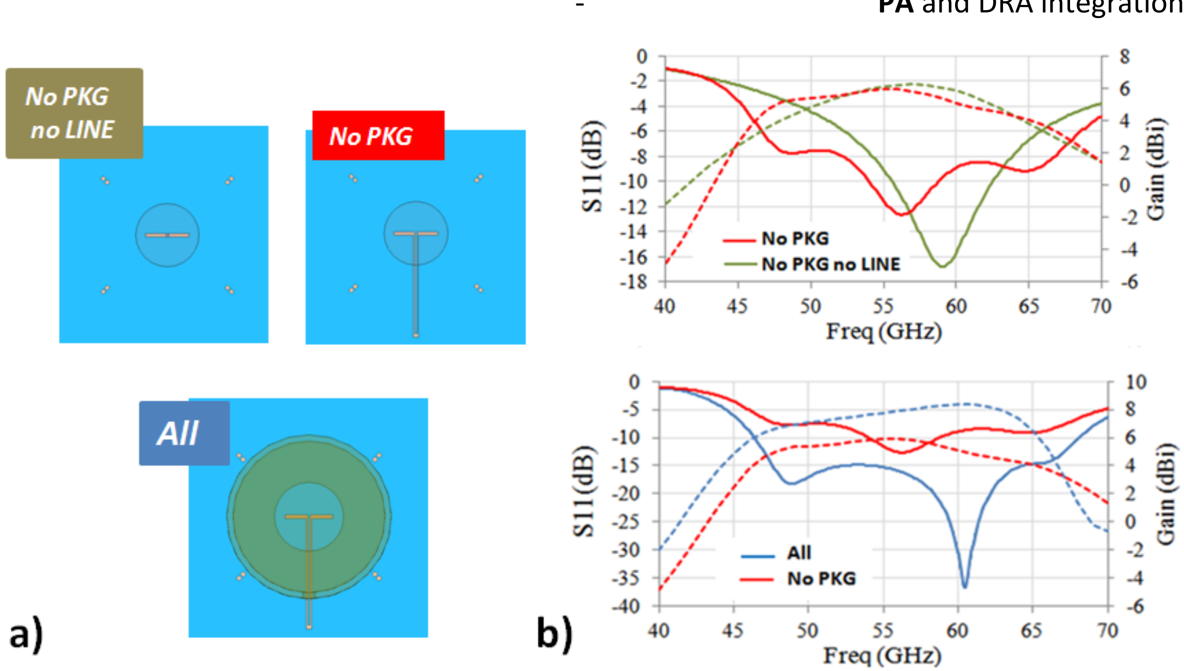

Figure 171 a) Simulated Configuration b) and c) Matching and Gain for different configurations (S11: Complete line, Gain: dashed line)

The variation of the gain patterns are shown next. A 15-GHz matched band (50 to 65 GH) is obtained over which a highly directive response is observed throughout. The gain reduction at the top of the band is also witnessed at 65 GHz. The proper excitation of the DR by the different elements (CPW and line) as explained previously is confirmed.

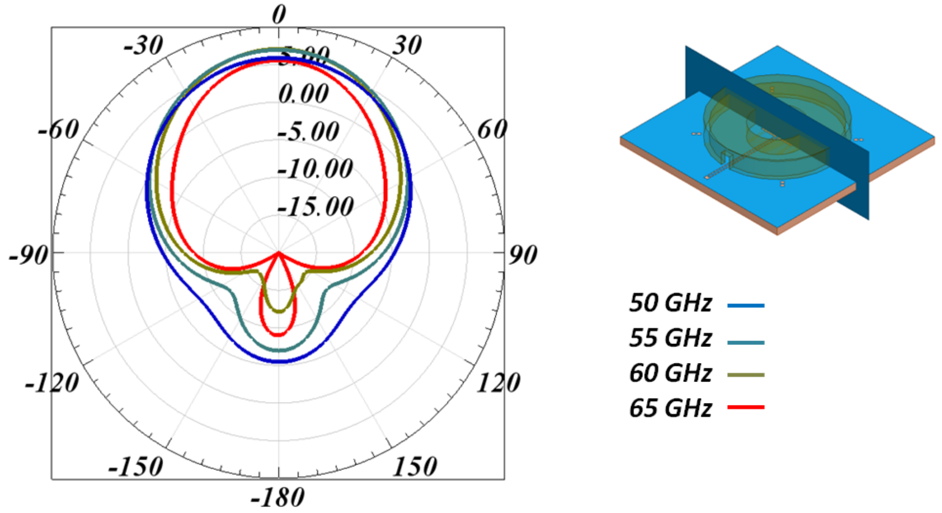

Figure 172 Gain patterns for the adapted band.

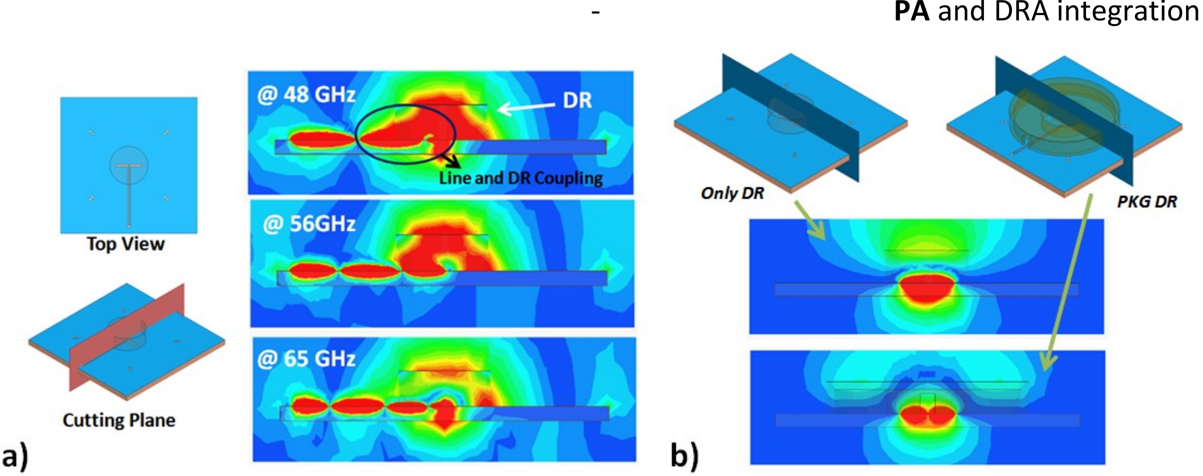

Figure 173 a) E field magnitude distributions a) Cut Planes for only DR and Packaged DR. b) E-field magnitude (H Plane) for only DR and Packaged DR

As mentioned before, the package was fabricated from a bare alumina substrate by laser micromachining. Figure 174 shows the fabricated sample as well as the foam support for its measurement. A small aperture was made on the package wall in order to minimize discontinuity effects on the CPW feed line. Without this opening, a tapered transition should be made, to account for the permittivity change over the CPW line due to the package wall. Note that the aperture has no impact in the overall radiation performance of the antenna.

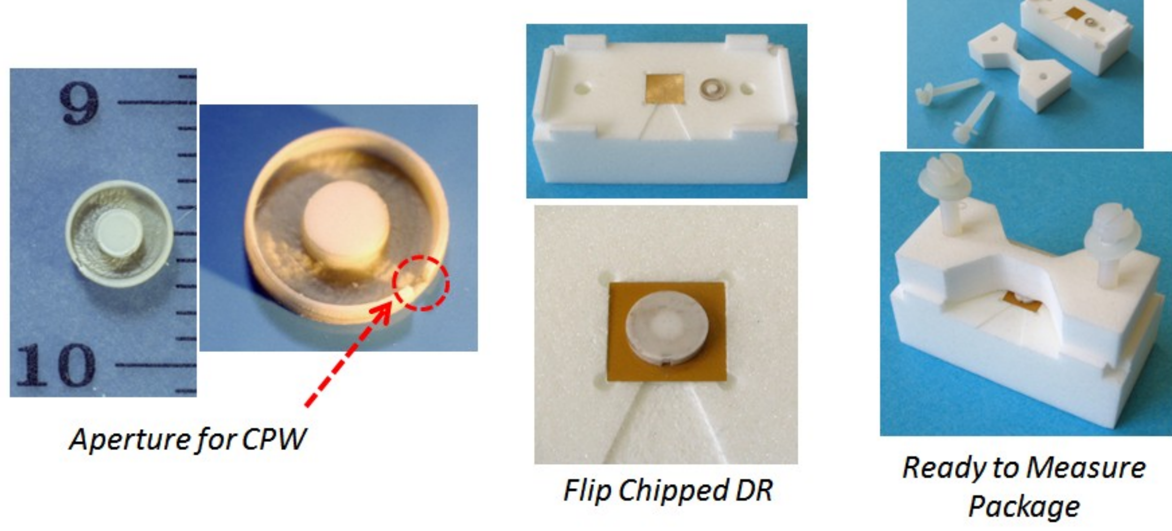

Figure 174 Fabricated sample and foam based measuring support

It should be mentioned that some particularities were obtained after fabrication due to the fixed point of rotation of the laser machine. For instance, the cylindrical DR shape used in simulations has a slightly conical form after fabrication. Retro-simulation runs showed little impact on the performance of the antenna. This conical shape is also seen in the exterior

side of the package wall. All of these unwanted variations due to the fabrication process can be avoided as said before, by the use of high power laser machining or industrial injection molding technique, with high precision.

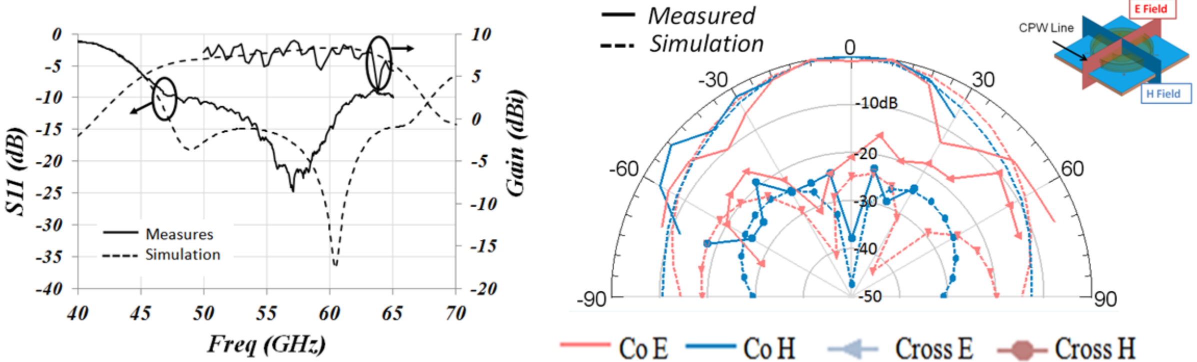

Figure 175 Measurement a) Matching and gain response b) radiation pattern

Good agreement can be seen for the measured and simulated responses for both S11 and antenna gain (Figure 175a). A slight shift in the resonance frequency is observed. This shift might be due to the miss-alignment between the etched slot and the package. Strong ripples are observed for the gain response, most probably due to interfering signals caused by reflected signals of the measuring bench. The radiation pattern was also measured (Figure 175b). Good agreement is also found for the Co- and Cross-polarization radiation measurements. As observed before, destructive interference was experienced due to reflected signals from the measurement bench. This can be seen for the measured Co-polarization component in the H-plane around 30°, where a 12 dB difference from simulation was measured. For the negative theta-angle values, rather good agreement is observed.

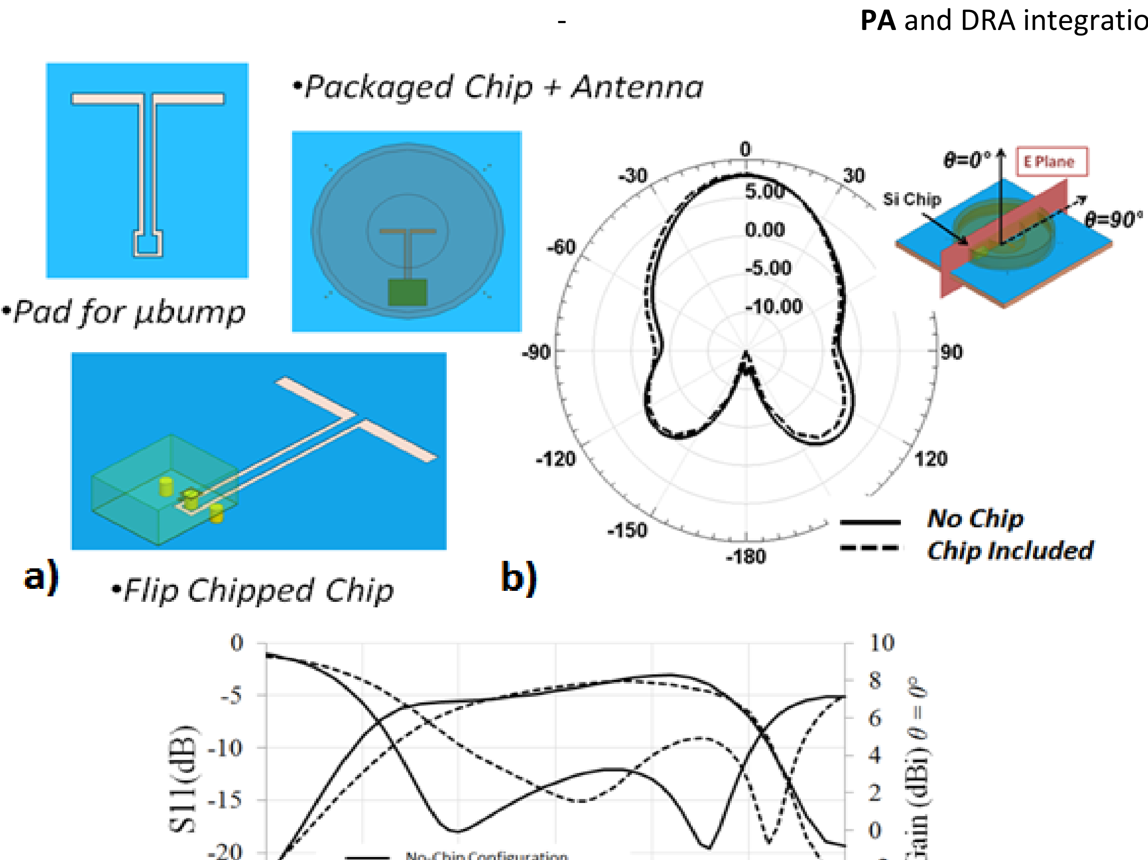

Figure 176 Including the Si Chip a) Flip Chipped Chip and b) E Plane Pattern @ 60 GHz and c) Matching + Gain (θ = 0°) for a No Chip and Chip Included configuration

The integration of the silicon chip and its influence on the performance of the antenna has been studied based on simulation results. In this case, a silicon chip of 0.36 mm^2 (basically the same size as the PA), was flip chipped onto the PCB (Figure 176). The chip is interconnected to the CPW feeding the antenna using µ-bumps (with 70 µm height). A total height of 0.32 mm is obtained in this configuration, compatible with the package cavity with a height of 0.485 mm. Two configurations are compared in Figure 176: *i*) a configuration where no chip is present and *ii*) insertion of the chip and the µ-bumps. The S_{11} results show a frequency shift of around 5 GHz due to the interconnection scheme. The presence of this shift is also seen in the realized gain response, for which the matching response was accounted for. Maximum gain values are observed under optimum match radiations. Still, good gain values are obtained over the expected bandwidth. Regarding the radiation performance, a slight shift toward the negative theta-angle values is witnessed due to the

presence of the chip. This should not compromise the integration of the front-end, as broadside radiation patterns are obtained with a 3 dB beamwidth of 64°.

3.d) 4th solution → eliminating interconnections

Due to the configuration of the previously proposed packaging solution, a very high precision assembly process is needed if the slot should be positioned under the DR to be able to assure contact between the two elements. A frequency shift of at least 3 GHz could be expected with a minimum separation of 5 µm between the slot and the DR according to simulations, thus underlying the significant incidence of the air – alumina interface. A lateral slot excitation is now introduced, where the slot is integrated on chip and positioned on the side of the DR (Figure 177). In this way, the slot - DR vertical configuration is eliminated and the impact of the air – alumina interface is reduced.

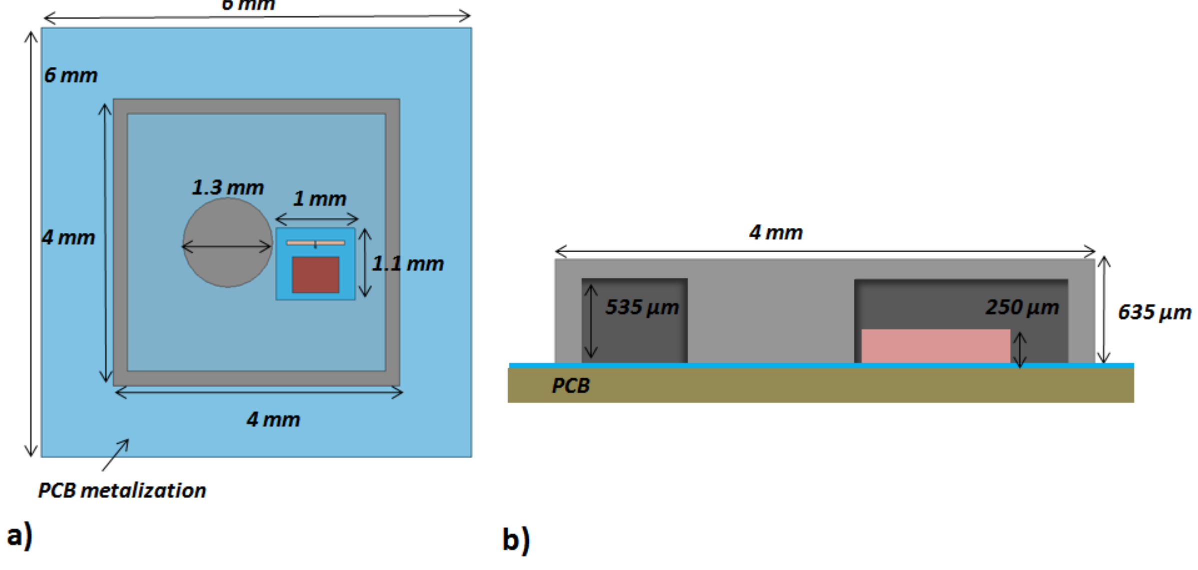

Figure 177 Side positioned slot configuration a) Top View and b) Front view

To be able to excite the DR, the slot has to be put in such a way that it corresponds with the magnetic field distribution of the resonant TM_{11} mode of the DR seen in Figure 178a. This induces a perpendicular position of the slot with respect the DR to obtain the maximum coupling. The slot plane has to be placed in the plane of maximum intensity of the field, that is, a plane crossing the center of the DR as seen in Figure 178b. A bottom metallic ground plane is needed for the DR to define proper conditions for the TM_{11} mode excitation. Thus, a metallization of the PCB has to be taken into account. By selecting the proper distance

between the DR and the Si chip, the excitation of the mode is accomplished. Simulation exhibits a bandwidth of 6.1 GHz (VSWR=2) and minimum gain of 5 dBi in the corresponding band, as seen in Figure 179.

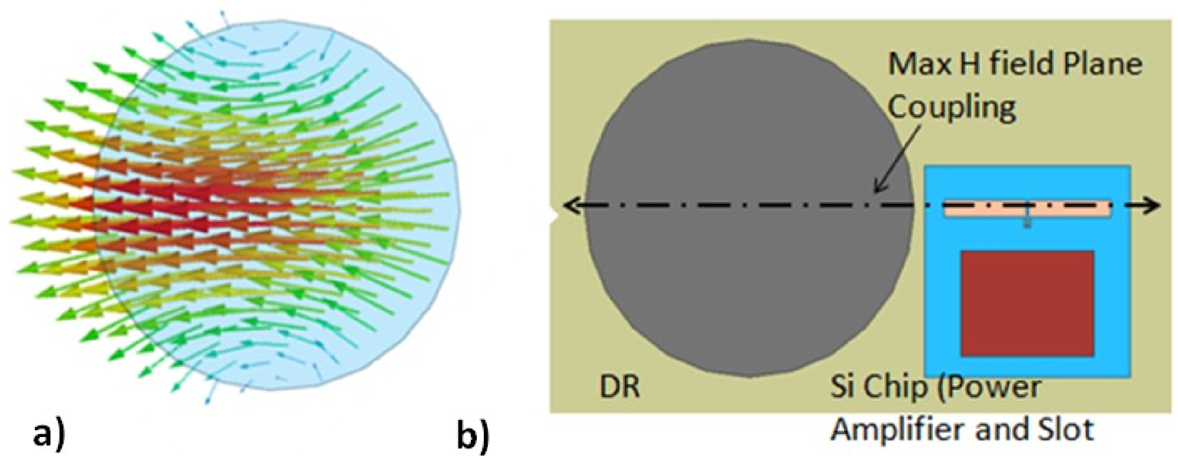

Figure 178 a) H field distribution in the DR. b) Example of DRA and Slot positioning

The slot has to be efficiently coupled to the DR. A maximum energy will be injected if resonance conditions are ensured from the slot. In this way, radiations from the slot can be expected due to its resonant behavior, rather than a classical near field capacitive coupling. Three different configurations were studied to be able to quantify the contribution of the slot to the radiation of the DR. On Figure 179, the gain and impedance matching for *i)* slot alone, *ii)* slot with DRA, and *iii)* slot with DRA and package (lid and walls), are compared. It can be observed how the coupling to the DR and the package improve the performance of the antenna. First of all, an increase in the bandwidth response can be observed, typically from 1.2GHz to 2.8 GHz with the "only slot" configuration and with the addition of the DRA configuration, respectively. This increase in bandwidth can also be seen in the gain response (wider frequency range covered with, for example, a +5 dBi minimum level). This underlines the incidence of the DRA, offering a wider "natural" radiation characteristic with respect the slot one. For the final configuration, the package is added, increasing even further the bandwidth response up to 6.1GHz. This is mostly due to the presence of the lid and its interaction with the DR which tends to improve the matching condition between the DR material properties and free space medium in terms of impedance as seen previously.

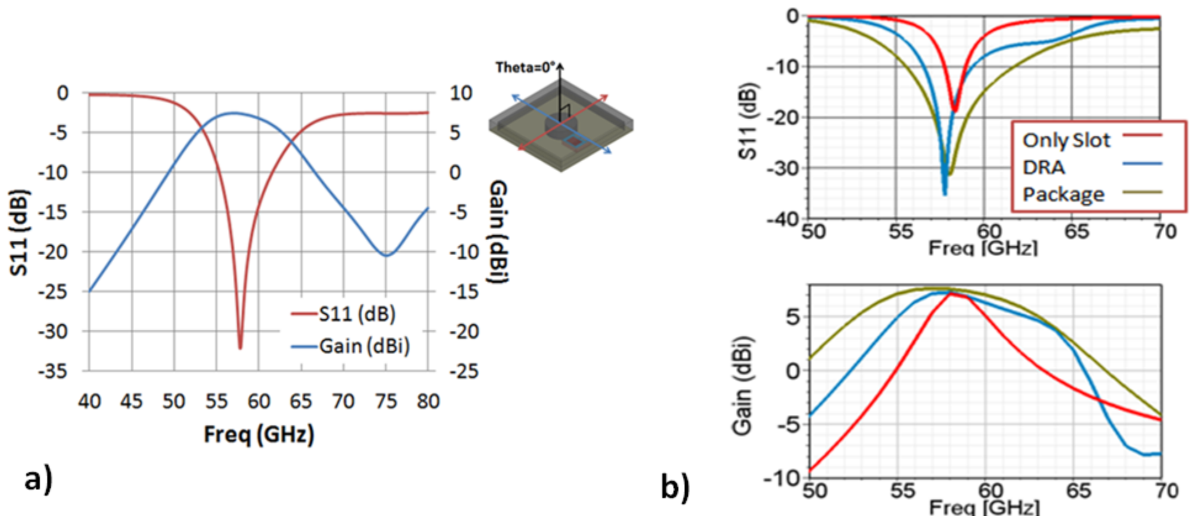

Figure 179 a) S11 and Gain (θ= 0°) and b) Simulated S11 (dB) and Gain (dBi) for *i)* slot alone, *ii)* slot with DRA, and *iii)* slot with DRA and package configurations

The interaction between the slot and the DR can be seen in Figure 180, where the magnetic field at 55GHz has been plotted. A high energy concentration can be found in the DR, and significantly contributes to the radiated energy.

The slot excitation element is completely compatible with standard Silicon technologies. Once input impedance control is ensured, integration with active devices can be foreseen, with significant advantages in terms of dimensions and global energy efficiency. A small size (0.88 mm^2) is achieved for the slot, as it takes advantage of the high permittivity of the silicon (ε_r = 11.7) which reduces its dimensions compared to those with lower permittivity substrates.

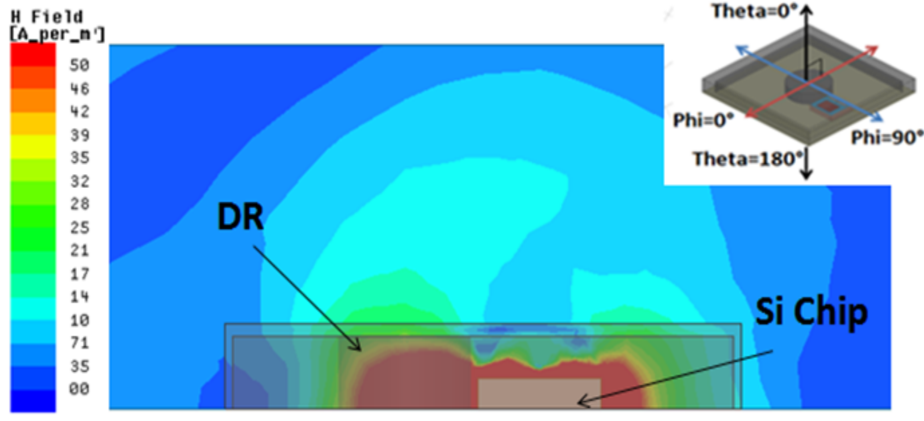

Figure 180 Coupling between slot and DR. (Magnetic Field Distribution at Phi = 90° @ 55GHz).

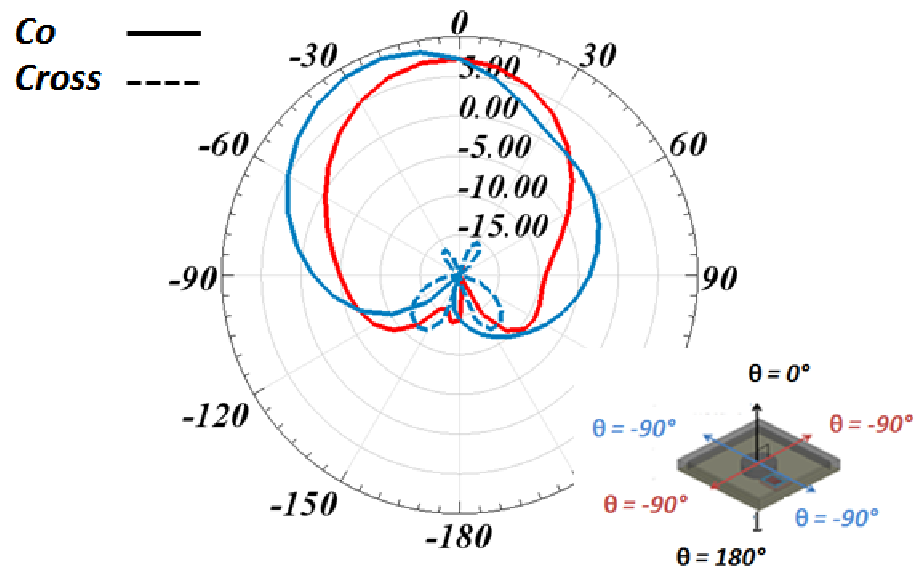

Figure 181 E-Plane and H-plane radiation patterns @ 58GHz

Due to the side positioned slot, a shift in the nominal maximum radiation direction (Phi=90°) can be seen on Figure 181. The slot element not only transfers energy form the active devices to the DRA but influences the radiation properties of this last. The chip presence introduces two new elements into the antenna configuration: a high permittivity substrate (silicon ε_r = 11.7) and a metallization plane (metallic layer, Si Technology). To discriminate the source of the radiation shift, two configurations are tested independently. As seen in Figure 182, the configuration of the underneath slot is retaken (Figure 164).

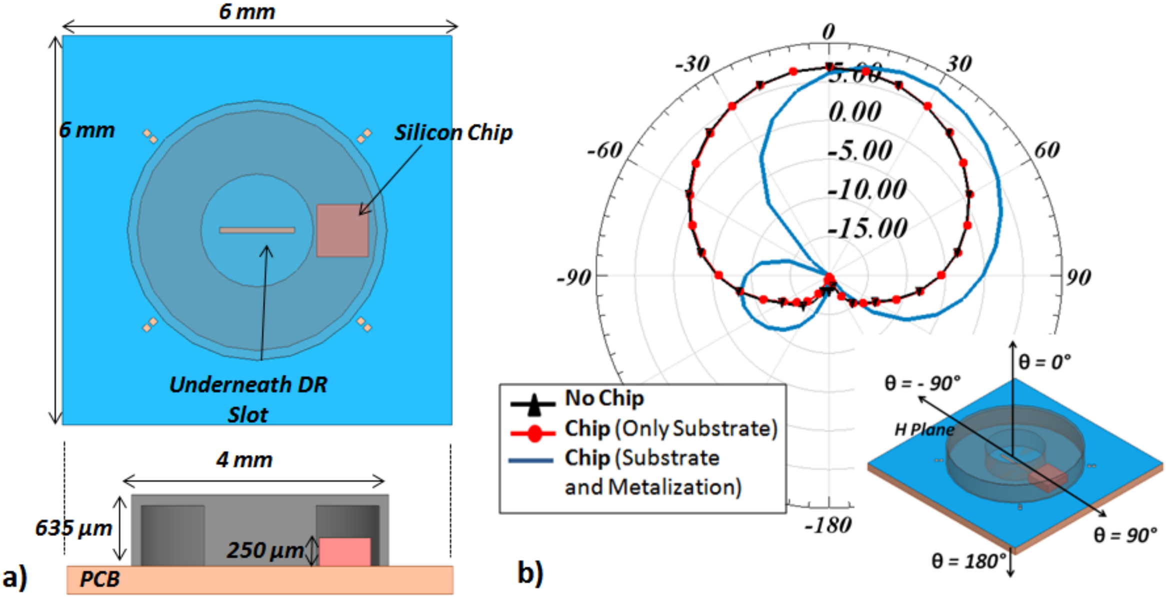

Figure 182 Side positioned Chip a) Top and Front view and b) Gain Pattern @ 58 GHz for “No Chip”, “Chip Only substrate” and “Chip Substrate and Metallization” configurations

A silicon chip is added next to the DR, where the side fed chip would be. The radiation pattern for three different configurations ("No Chip", "Chip Only Substrate" and "Chip Substrate and Metallization") is then compared. The side fed excitation cannot be used in this case as the excitation slot would disappear when the metallization layer is not included. It is observed that the presence of the high permittivity substrate doesn't impact the radiation behavior of the antenna; the gain pattern for "No Chip" and "Chip Only Substrate" does not exhibit any impact of the silicon substrate. When the chip metallization is included, the pattern suffers a drastic change in the H Plane radiation as seen in Figure 182 b. A shift of 40° for the maximum value is observed passing from $\theta = 0°$ to $\theta = 40°$. The same behavior is seen for the side fed DR of Figure 181. We can now conclude that the metallization of the chip is responsible for the field tilt.

Concluding remarks of this chapter are presented next.

4) Conclusions

In this chapter, a packaged and high gain PA-Antenna solution has been presented. Starting from the single high gain DRA solution, several configurations show the possibility of using the DRA in the millimeter band as efficient solution for the antenna element of the 60 GHz radio front end. Due to the low loss alumina substrate a high efficiency antenna can be obtained. The excitation positioning regarding the DR element was also evidenced to be primordial for the DRA configuration.

Original DR based solutions were possible by taking advantage of the laser machining. In this way, a first DR based “almost” packaged solution was presented. The interconnections allowed the PA and DRA to be part of the same solution. We could see how the interconnections play a fundamental role. The performance of the solution, specifically the efficiency (characterized by the Inserted Loss of the transition) and the bandwidth (VSWR >2) of the antenna are highly impacted. This configuration also included the PCB presence and its impact on radiation has been shown. A modification is then needed to be able to account for the imposed limitations of the interconnections and PCB presence.

Two final completely packaged configurations were then presented. These solutions share the same original DR based package, where the package and DR are fabricated at the same laser micromachining step. Higher bandwidth and higher gain are obtained with this solution. Specific study of the DR and the package dimensions has been presented. PA presence is also taken into account by way of simulation. For the first packaged solution, μ-bumps PA-DRA interconnection is used. It confirms the interconnection impact on gain and matching observed before. For the second one, a new DR excitation method is also introduced allowing the PA – DR interconnection to be avoided. The DR excitation is integrated on chip.

A measurement configuration is also introduced for backward radiation antenna. Trying to limit the impact of the measuring probe (due to its inherent radiation) and to offer a solution to back radiation antenna, these measuring setup is presented.

Chapter 4 - Multi-feed antenna for PA-Antenna efficiency enhancement

1) Introduction

As seen in chapter 2, PA passive losses were decreased through co-design. Modification of the PA output stage allowed passive element loss reduction regarding typically used 50 Ohm output impedance configurations. In this way, efficiency increase (decrease in PA IN-OUT signal path loss) was achieved. But PA-passive loss is not the only loss source that affects the PA performance. The typical PA response curve is seen in Figure 183. A maximum 13 dB gain level is obtained for low input power values. As the input power starts to increase and passes a certain value (2.5 W in the example), the output response can no longer maintain a 13 dB gain. Consequently, the output/input power linear relation depicted by the "ideal amplifier performance" is no longer achievable. The PA operation is limited by the finite biasing levels, which as explained in Chapter 1, clip (PA at saturation) the signal and add frequency harmonics to the output signal. The output signal frequency representation is observed in Figure 183 b).

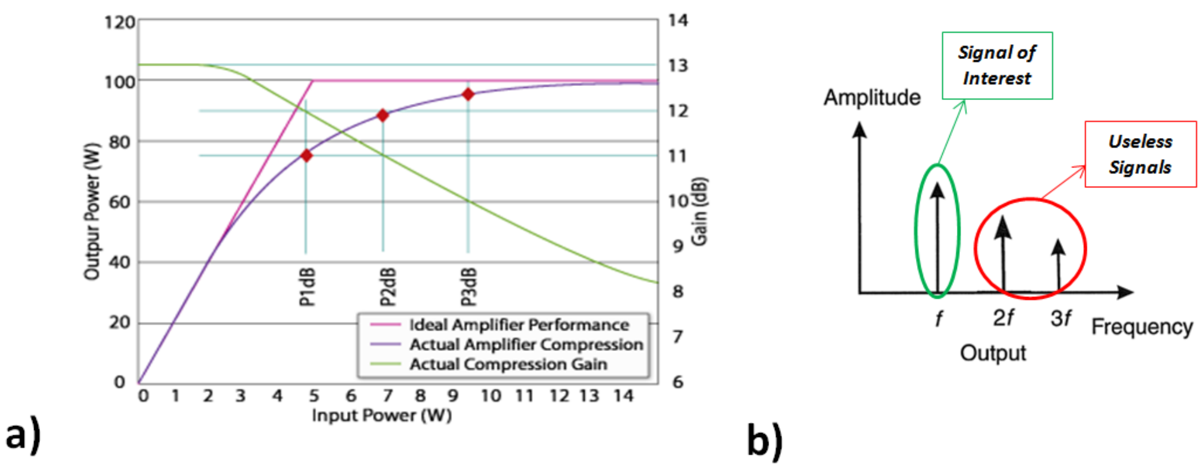

Figure 183 a) PA typical gain curve and 1, 2 and 3 dB compression points b) Output signal in the frequency domain

This means that energy is being relocated on higher harmonics (2*f*, 3*f* etc…) that do not carry useful information. An efficiency increase can be expected if higher harmonic signals are

suppressed. In other words, a higher linearity should increase the PA efficiency. The strategy proposed does not deal with PA internal operation and only aims the suppression of harmonics due to clipping as the efficiency increase strategy.

2) Multi PA solution

To avoid clipping (signal deformation due to transistor compression), the PA is limited to work in the linear region with no harmonic generation. In this way, high gain and linearity is possible. The drawback from limiting the PA region is the low output power. To increase this value, two PAs can be used considering a parallel configuration. Two linear-region-working PAs whose signal can then be added, obtaining a high output power and highly linear response are proposed, based upon a spatial radiated power recombination through multi-feed antenna. The antenna in this case is the key element, as it will not only act as the antenna, but will also be responsible of adding the independent low power signals.

2.a) Multi-feed antenna for Multi-PA solution.

An initial square patch configuration (Figure 184) has been chosen to show power addition capabilities as well as constraints and limitations of the two feed antenna. Regarding the patch dimensioning, L_{patch} parameter allow to control the resonant frequency of the patch. As a two feed configuration is foreseen, W_{patch} becomes the resonant frequency control parameter for the second feed. Due to this, a square patch ($L_{patch} = W_{patch}$) is chosen for the patch to resonate at the same frequency for both feeds.

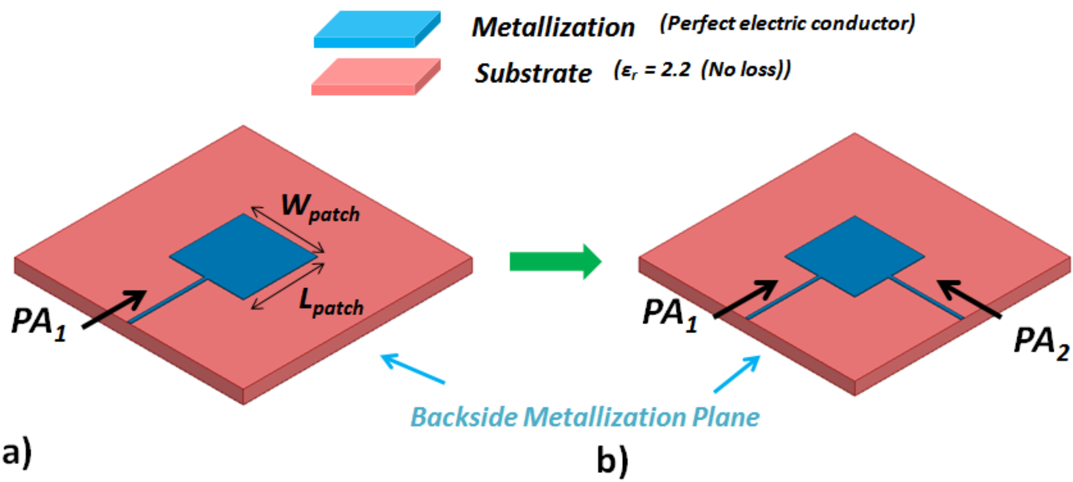

Figure 184 Passing from a) 1-feed Antenna to a b) 2-feed Antenna

2.b) Coupling constraint

For the two feed configuration, the S parameter response can be seen in Figure 185. Both feed share the same matching response (S_{11} and S_{22}) with 60 GHz resonating frequency. Due to the two feed configuration, energy transfer between feeders is possible. The energy coupling between the feeds is shown by S_{21} and S_{12} and it becomes a constraint of the system. For the patch, a -22 dB level coupling is obtained. A -20 dB level should be ensured to have an acceptable isolation level for multiple feeds, and also to prevent any degradation between PAs produced by such backward excitation.

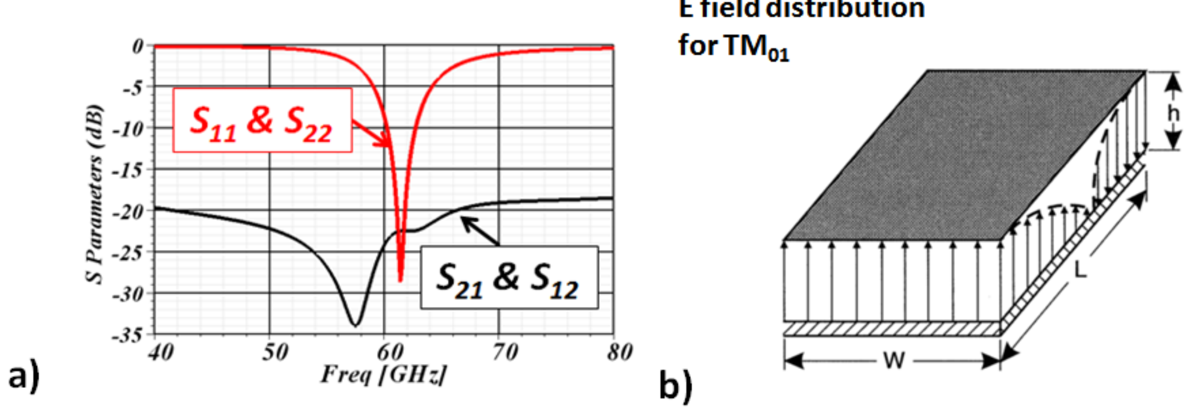

Figure 185 a) S Parameter response (2 feed configuration) and b) TM01 Electric field distribution

The field distribution for the patch TM_{01} mode is depicted by Figure 185 b. The patch mode excitation by the microstrip feed is done through the width (W) side of the patch. In this way, a maximum field level is encountered and the coupling from the microstrip line mode to the patch mode is maximal. Note that along the length (L) side of the patch, the TM_{01} patch mode offers a zero field magnitude along the center plane of the patch. As the second feed is added along the first resonant mode length side, it coincides with a zero value field of the mode excited by the first feed. In this way, the second microstrip line feed mode excites an independent TM_{01} mode. Consequently, a low coupling is obtained.

2.c) Vectorial addition

Electrical fields in the substrate are presented for: one and two feed configurations. The maxima and zero field region of the TM_{01} mode can be observed and this last is highlighted by the dashed black line. The second excited E field is rotated 90° regarding the first mode

due to the new feed position. For the two feeds configuration, the same maxima and zero field presence is observed although with a 45° rotation. The two orthogonal TM_{01} modes are excited simultaneously, generating 2 orthogonal polarizations resulting in a unique 45° vector after spacial recombination. This is the result of the vector addition of the 0° and 90° oriented vector. As we have good isolation (S_{21} and S_{12} < -20 dB) and good matching responses (S_{11} and S_{22} < -10 dB), then the energy from the two sources is now concentrated in a single one. The antenna is acting as a power combiner.

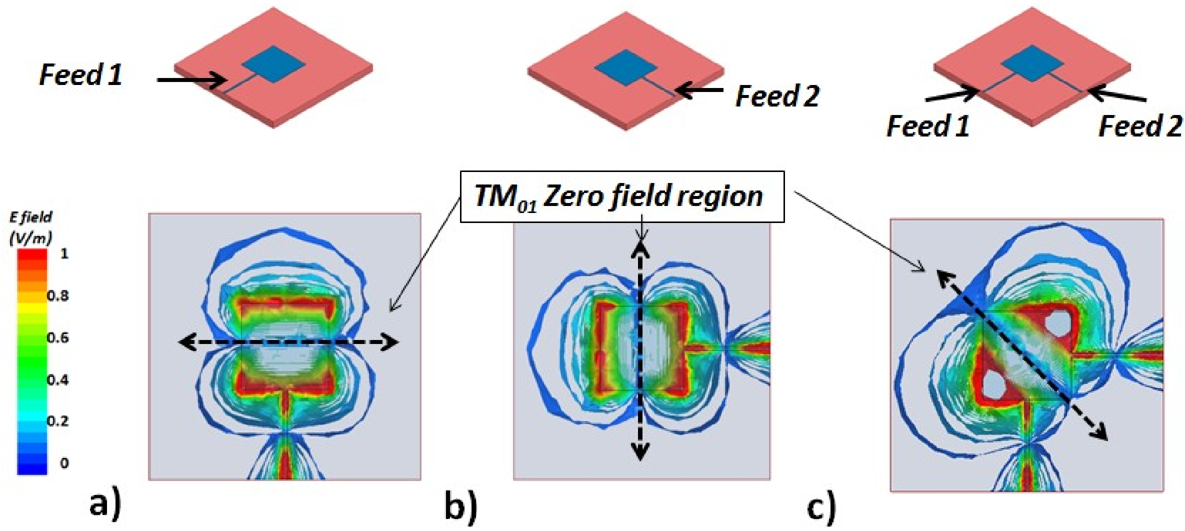

Figure 186 Electric field on substrate for a), b) 1 feed and b) 2 feed configurations

The vectorial addition (Figure 187) is done next by way of the magnetic field of the TM_{01} mode of the patch. The distribution of the magnetic field is parallel to the patch, distributed along x and y axis as shown in Figure 187. Depending on the excitation polarization, magnetic field for the near field of the patch is shown for the two individual feeds and the resulting two feed configuration. The vector addition presents the magnitude of the resulting field regarding the magnitude ($\boldsymbol{H_{field}}$) of each of the single feeds. The final obtained value has a $\sqrt{2}$ factor, that is, a $1.4 * \boldsymbol{H_{field}}$. A 0.6 difference from the expected 2*$\boldsymbol{H_{field}}$ total magnitude is obtained**.** This means that the antenna will introduce a loss of $0.6 * \boldsymbol{H_{field}}$ in the power addition mechanism. For a 2*$\boldsymbol{H_{field}}$ resulting magnitude, a single feed should have a $\sqrt{2} * \boldsymbol{H_{field}}$ magnitude. This means that the power combination mechanism does not operate without penalty and thus, introduces a power loss factor to the system. This loss should be covered by properly selecting the amplification level of the PA.

Despite of this, a reduction of the PA amplification level is still obtained (two 0.7*$\boldsymbol{H_{field}}$ signals are needed instead of a single $\boldsymbol{H_{field}}$ magnitude signal) maintaining the goal of a more linear solution.

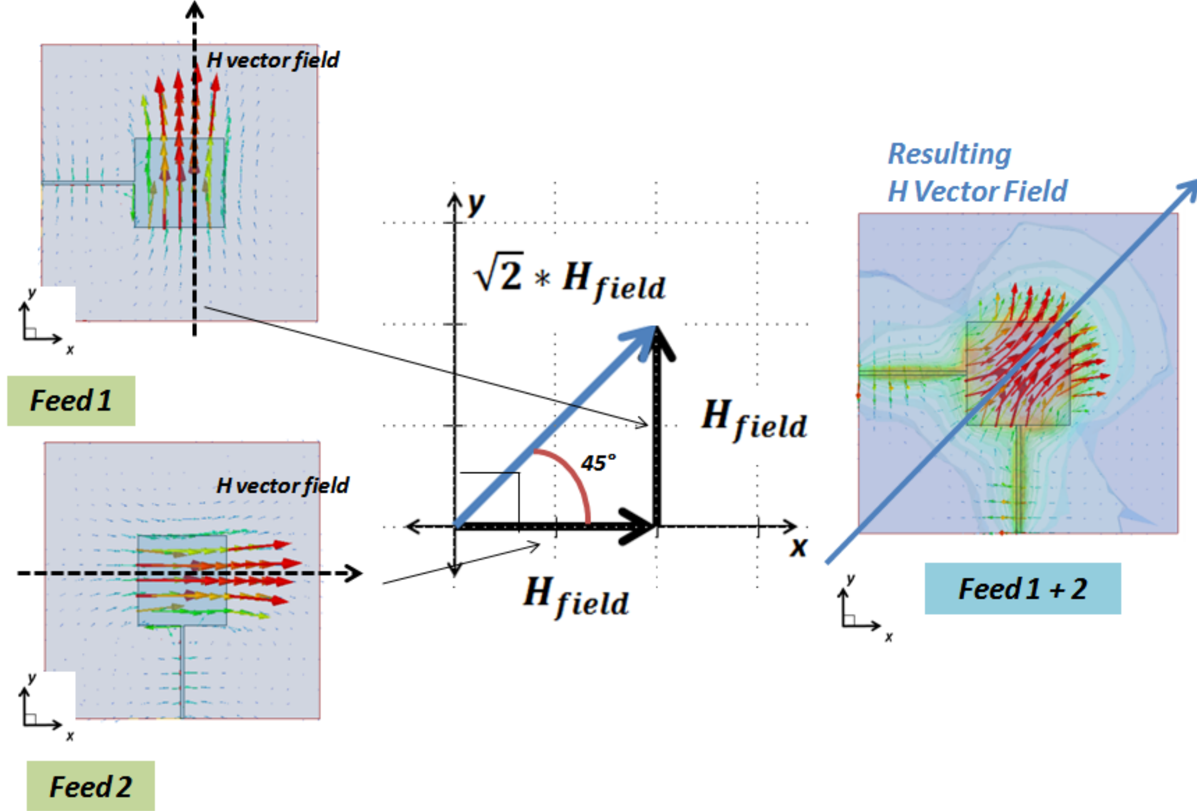

Figure 187 Vector addition of orthogonal (in phase) magnetic fields (and shown are in the substrate)

2.d) The impact of field rotation

Note that the resulting field implies a polarization change due to field rotation. A linear polarization is still obtained. Next, the field rotation is taken into account, and radiation properties for both, one and two feeds, configurations are shown (Figure 188). Same gain levels (6.4 dBi) are seen for both configurations at θ = 0°. A broadside radiation is still obtained for the two feed case. A major difference between both configurations is the H and E Plane orientation regarding the feed. For one-feed case, E Plane and microstrip feed line both share the same plane. The feed presence can be observed on the E plane gain pattern. The feed impact is different for the two-feed case. The 45° field rotation has displaced the field planes regarding the feed planes by the same angle. An increase on the cross polarization level is observed. Note that for the one-feed case, a higher cross pol level is

seen on the E plane while for the two-feed case, it is observed on the H plane. The microstrip mode field distribution interacts differently for both configurations and due to the field rotation regarding the feeds, the H plane radiation seems to interact more intensively with the feed.

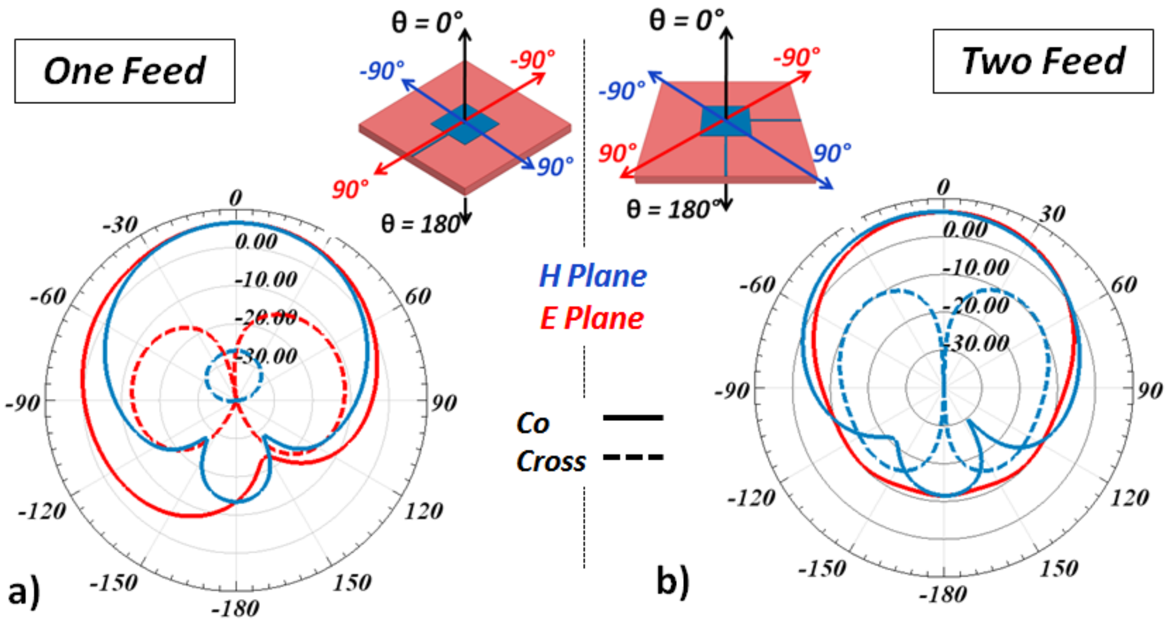

Figure 188 Gain Patterns a) One feed and b) Two feed @ 61.7 GHz

From the patch study, we can conclude several things. First of all, the double-feed patch configuration maintains the adaptation and radiation properties of the single patch: high broadside radiation levels, same half-beam aperture values and matched bandwidth. In a second hand, due to field rotation, the antenna-feed interaction changes from one configuration to the other. As seen, cross polarization levels change although they remain acceptable. Finally, low inter-feed coupling conditions have been identified.

Regrouping all the previous conclusions, the antenna working as a power combiner has been verified by simulation. Now, a compatible multi-feed antenna solution for PA-Antenna integration has to be chosen.

3) DRA for multi-feed PA-antenna solutions

The DR provides high gain performance for packaged mm-wave antenna solutions. For the previously used TM_{11} mode, it also presents a linear polarization that should allow to be used as a power combiner. The TM_{11} H field configuration is depicted by Figure 189. The

linear polarization of the mode can be seen especially at the center of the DR where the maximum field intensity can be seen oriented along the X axis. Along the Y axis, low H field components are expected. Consequently, an additional TM_{11} mode can be excited along the Y axis with a low inter-mode coupling.

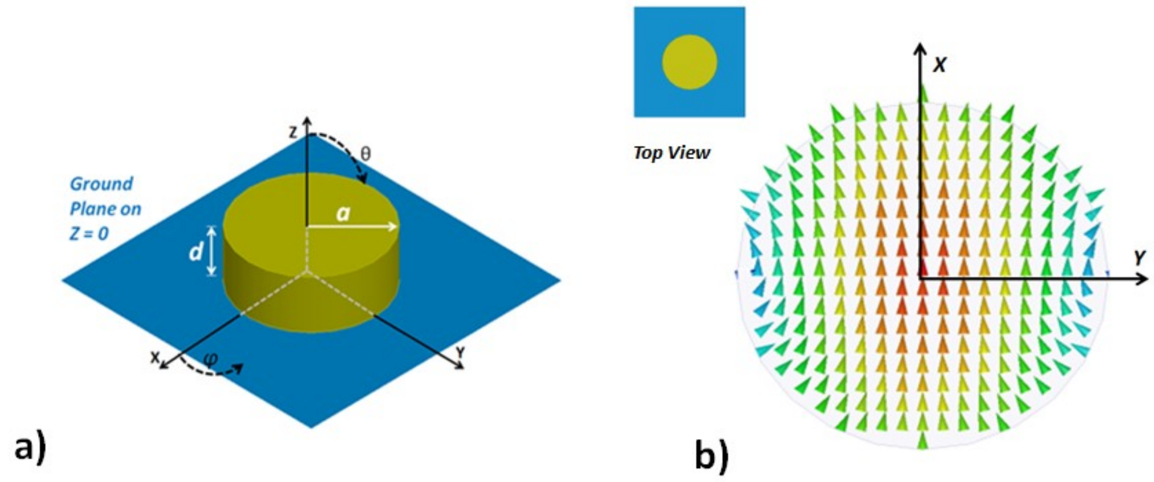

Figure 189 H field distribution for the TM_{11} mode (Hfield at Z = 0)

One of the difficulties of using the DR as a multi-mode power combiner is the excitation element. As seen in chapter 3, the proposed solutions use a ground plane with a slot as excitation element. Due to the central position of the slot, the second slot needed for the excitation of the orthogonal mode will interfere with the initial slot. Multi mode excitation becomes difficult for the central placed slot. A different excitation configuration is needed. From the patch solution, it is observed that the side feed is convenient due to the multiple sides of the patch. In a similar way, exciting the DR through its lateral side should resolve the feeding inconvenient. This brings us back to the side fed DR solution presented before (Figure 178).

3.a) Multiple lateral DR feed configuration

The displacement of the feed to one of the sides of the DR renders the whole DR perimeter as a possible feed location. Multiple simultaneous feeds are thus possible. Note that due to the mode orthogonality needed to avoid coupling between feeds, only two positions remain available; feeds should be directed along the DR X and Y axis (Figure 190). The S parameters

response shows a slightly wider matched band (> 5 GHz) with a -21 dB coupling level at least. The low coupling level confirms the expected orthogonal mode isolation.

A slight difference is observed between the two matching responses (solid and dashed red lines). This difference comes from the simulator meshing results which are not exactly the same for Feed 1 and Feed 2. The simulator treats each structure independently introducing the possibility of different meshing results.

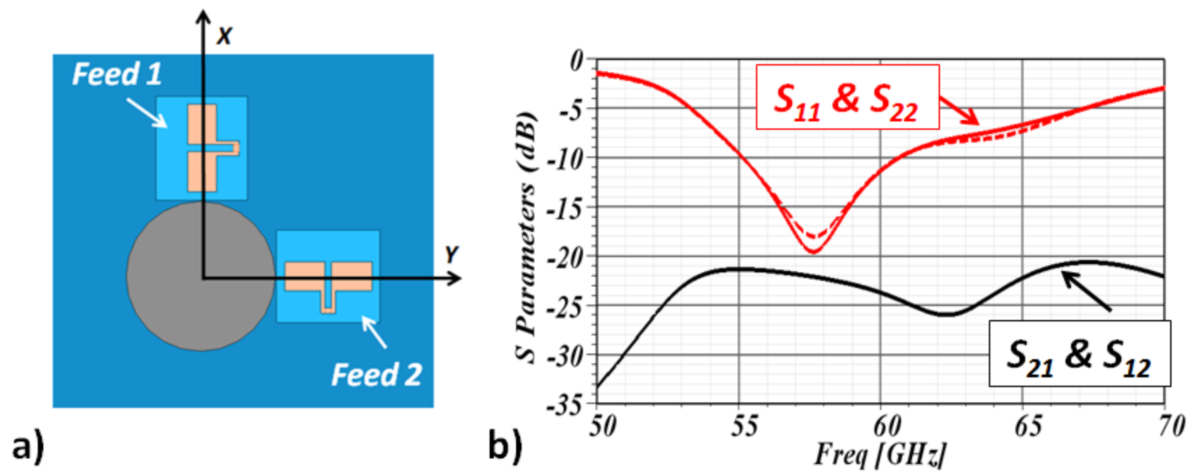

Figure 190 Two feed DR a) Top view configuration and b) S parameters

The H field in the resonator is depicted for several feed states in Figure 191. This allows seeing the individual DR excitation by each feed and the dual feed excitation. For the first two cases, the TM_{11} mode is excited independently for each feed. The resulting H field corresponds to a 90°rotation of the TM_{11} mode depending on the feed location. When the two feeds are simultaneously enabled, a 45° field rotation is obtained. The H Vector field depicted is the field on the bottom face of the resonator, that is, the face making contact with the metallization of the support.

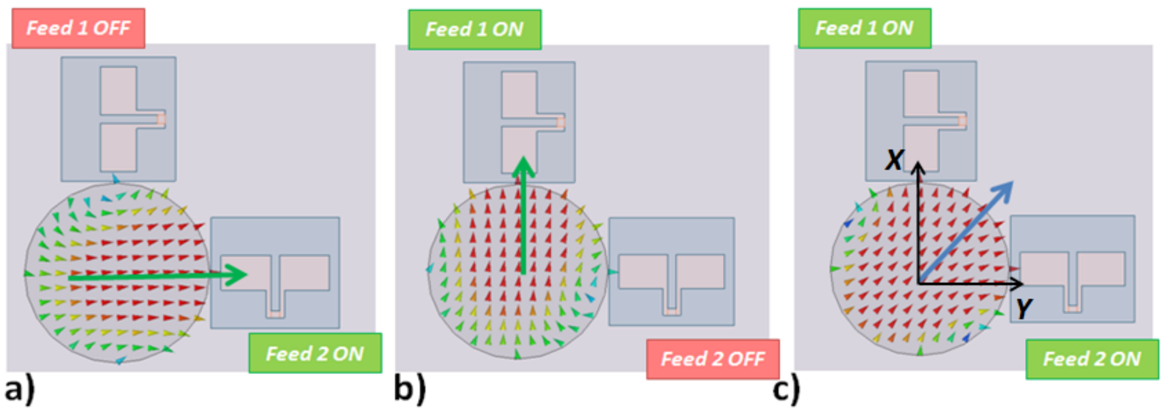

Figure 191 H Vector field in DR for a) Feed 1 OFF and Feed 2 ON, b) Feed 1 ON and Feed 2 OFF and c) Feed 1 ON and Feed 2 ON.

The TM_{11} mode is similar to the one seen in Figure 189. However, the higher field magnitude limited to the center of the DR is now seen reaching the borders of the DR. This is caused by the slot-on-chip mode excitation that is not the same as that for the underneath slot. This modifies the DR radiation performance as seen in chapter 3 and observed next in Figure 192.

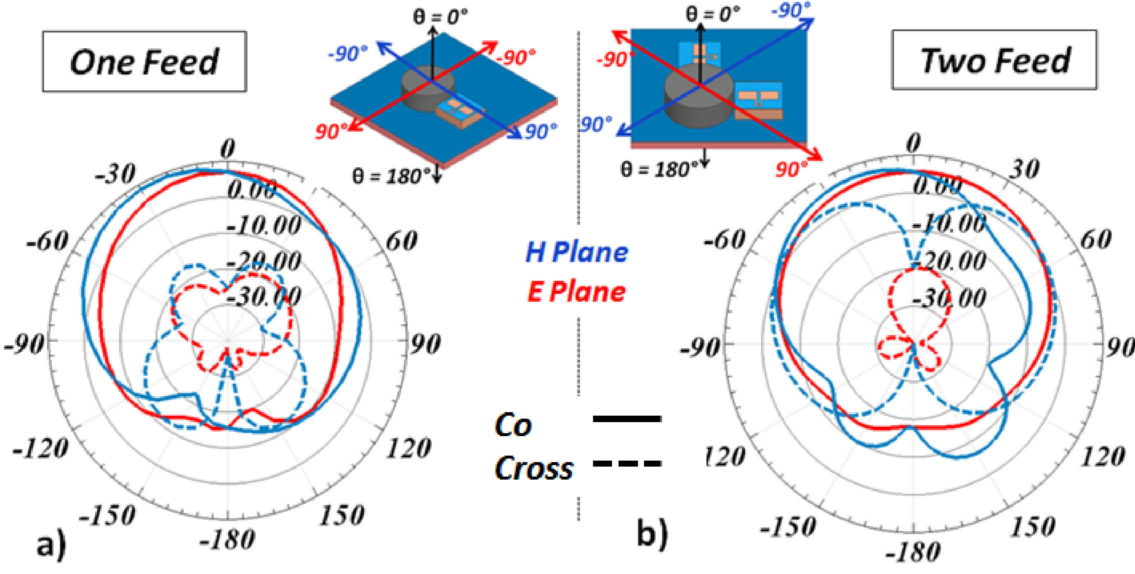

Figure 192 Gain Patterns for a) One feed and b) Two feeds @ 57 GHz

Gain patterns between one-feed and two-feed are compared. As before, one-feed case shows an H field displacement. The maximum is now seen at θ = -30° rather than 0°. This phenomenon is also seen on the two-feed configuration and also explained by the H vector

field concentration reaching out to the DR border. As also seen for the patch, the cross polarization levels are modified. A higher cross polarization level is seen on the H Plane. Positive gain values of 4 and 5 dBi are seen at θ = -60° and 60°. As seen in chapter 3, the slot-on-chip not only excites the DR, but radiates in a certain way. As the field rotates for the two-feed configuration, the polarization of the slot radiation is no longer directed along the same plane of the DR polarization as it was for the one-feed case. That is, the H field and E field distribution for the TM_{11} mode in the DR and the slot no longer share the same plane, thus increasing cross polarization and decreasing co-polarization.

4) Adapted feed for multi-fed DRA

From the previous study, we can conclude that the DR is adapted for the concept of antenna power addition. It offers multi-feed possibility and low feed coupling (S21 and S12 levels lower than -20 dB). Additionally, a relative large bandwidth (5 GHz) and high gain (6dBi) is maintained which renders the multi-fed DRA as an antenna solution for kiosk downloading applications. A new feeding mechanism, needs to be found to improve the cross polarization level encountered. The slot side-fed configuration is not adapted for the multi-feed due to the feed generated radiation that jeopardizes the radiation performance. A new DR excitation strategy is now introduced. For this new excitation and antenna solution, industrial multilayer packaging technology is foreseen and thus, presented next.

4.a) HTCC Packaging technology

LTCC or HTCC (Low or High Temperature Co-fired Ceramics) mm-wave packaging technology are multilayer technologies that allow the integration of semiconductor based devices and passive elements. An illustration of the fabrication process for LTCC is seen in Figure 193. The HTCC fabrication process differs from the LTCC process in that a higher co-firing temperature is needed. Vias and cavities are commonly found [113]–[115]. An example including a CMOS transceiver is also depicted by Figure 193. Bumping, vias, cavities and transmission lines are used for antenna and chip integration. The antenna is based on glass technology and interconnected to CMOS devices by an HTCC based CPW line.

HTCC technology consists on staking of multiple ceramic layers to obtain a final unique structure. It is based on A473 as ceramic tape material, offering ε_r = 8.6 and tan δ = 0.0021 at

60 GHz. The ceramic tape permittivity value allows thinking on elaborating the DR from the HTCC tape. A permittivity value of 9.9 was confirmed for high gain antenna in Chapter 3. These performances should be maintained for a 8.6 permittivity based DR with a slight increase in size expected though.

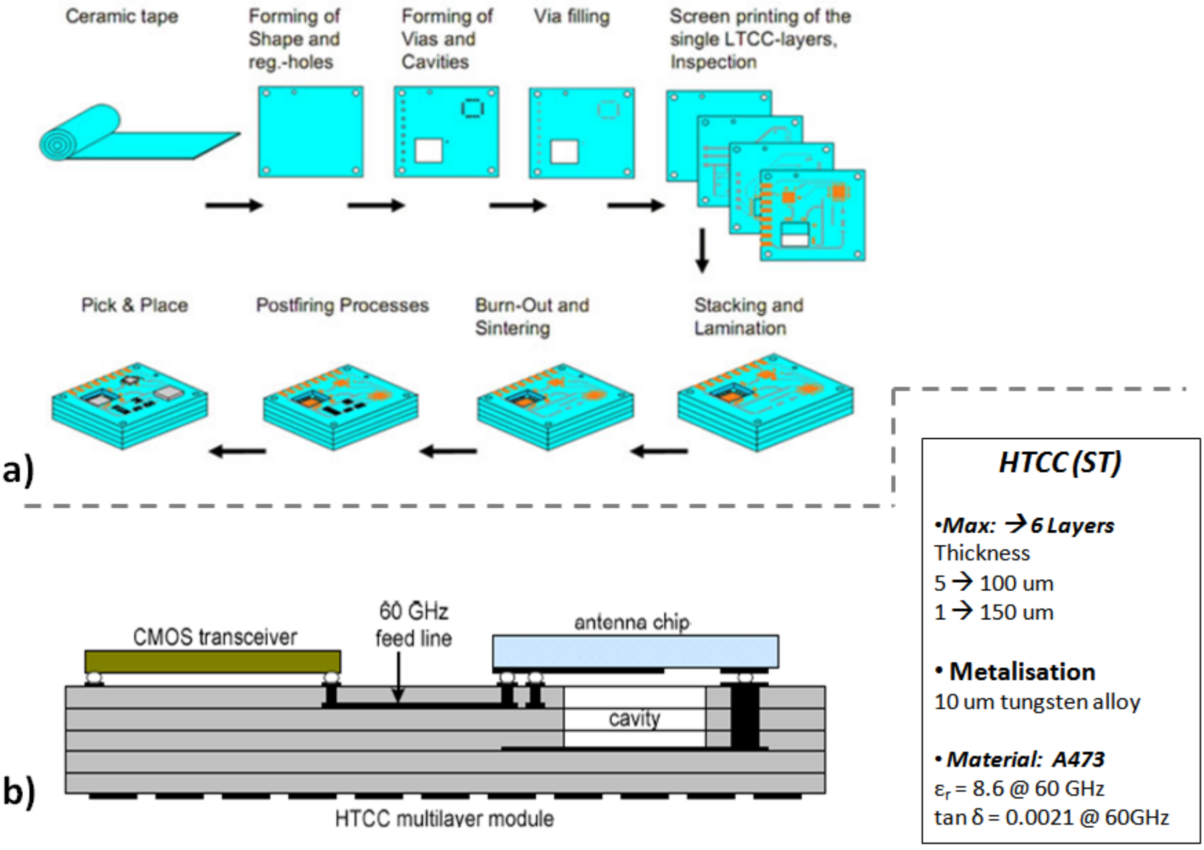

Figure 193 HTCC packaging technology a) LTCC Process[26] and b) Integration Example [116] and ST's HTCC technology description

4.b) DR Multilayer Fabrication

An initial HTCC based DRA solution is shown in Figure 194 a). This solution is based on the previously presented HTCC (ST) technology. A five-layer high DR that resides inside a cavity and is supported by the 0.15 µm thickness 1st layer is shown. For this initial configuration, the CPW fed slot already validated is used as the DR excitation element. No chip-antenna interconnection configuration is presented for the moment. The multilayer HTCC technology

[26] http://www.pass.com.hk/products/ltcc/

requires vias and cavity processed layer by layer. As an example, the 4th layer is shown Figure 194 b. This evidences a problem for the DR fabrication. The DR shape remains isolated from the rest of the structure. This would be the case for layers 2 to 6. As layers are stacked, DR individual elements center position cannot be ensured easily. Thus, the final cylindrical shape of the DR cannot be fabricated due to the alignment constraints. A supporting structure of some kind has to be included for the DR to remain positioned through the stacking stage of the fabrication process.

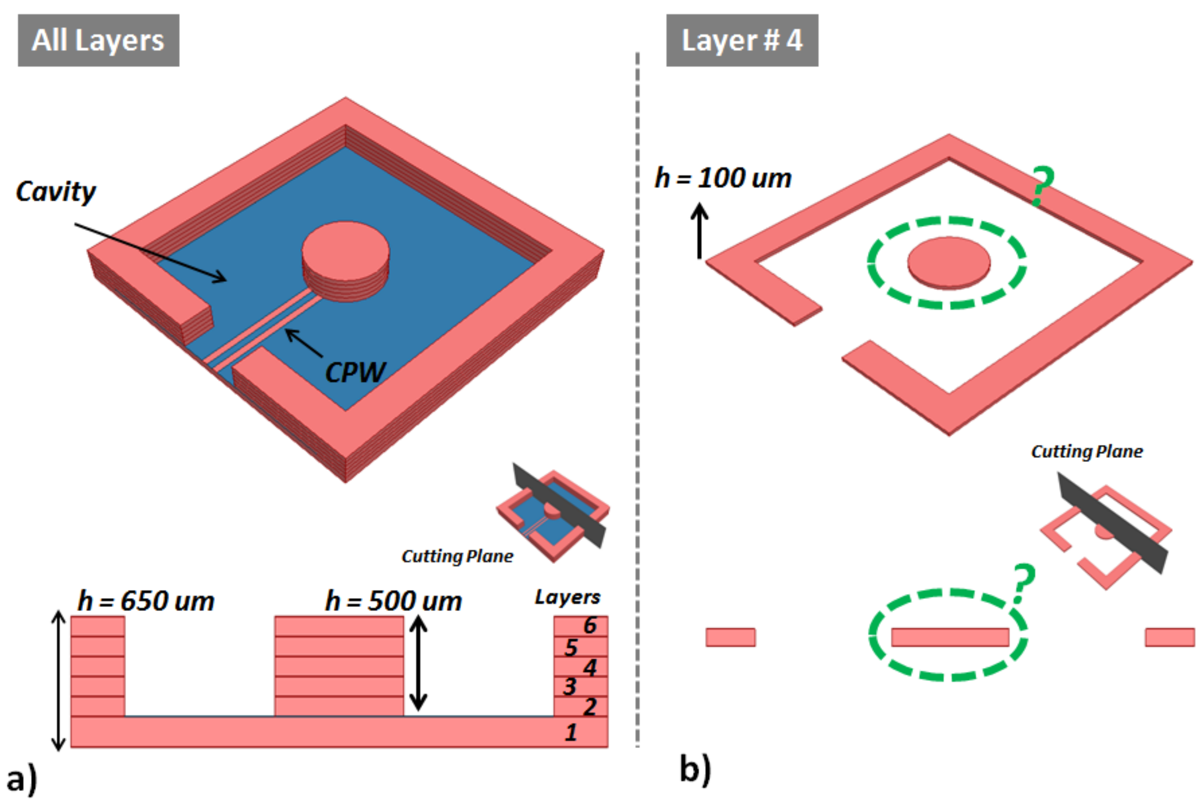

Figure 194 a) HTCC based DR (All layer solution) and b) Single layer

One way to fabricate the DR is by adding a holding element at one of the DR sides (Figure 195). Then, the DR makes part of the whole structure. This will ensure the correct DR position for each individual layer during fabrication. The CPW fed slot excitation can be used. As we can see, the support has direct access to one side of the DR. In other words, the support can be used to carry the signal and excite the DR through the side.

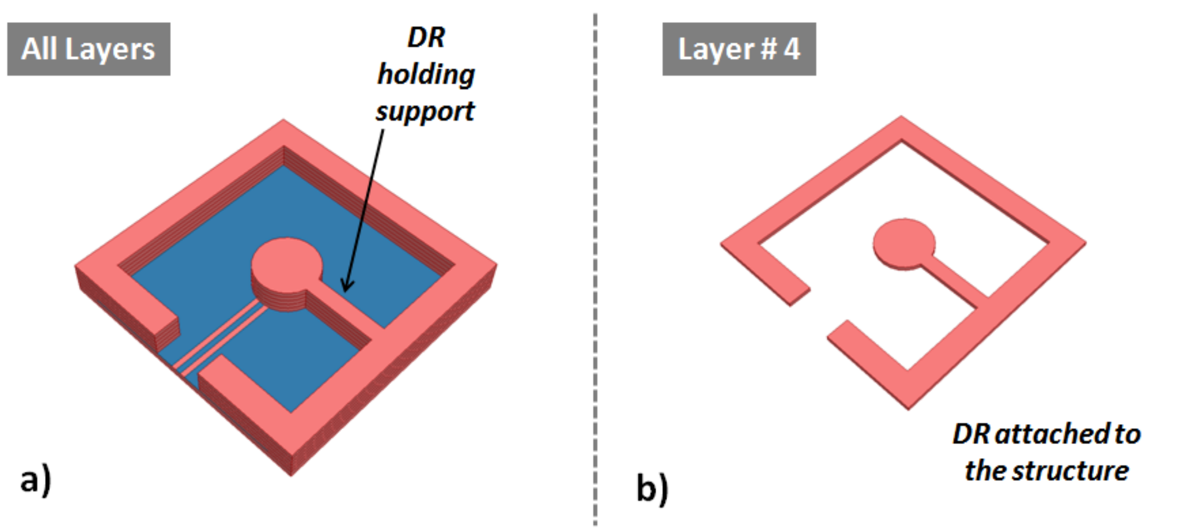

Figure 195 Holding element added for DR fabrication a) All layers view and b) Single Layer

4.c) Single Feed Waveguide Fed DR

The electric field distribution for the TM_{11} mode is depicted by Figure 196 a). The regions where a high field is located are highlighted. One sees high field intensity on the top as well as on the sides of the DR. A side-fed electrically-coupled DR can be foreseen. As shown by the field distribution, the side fed DR requires a vertical electrical field. This coincides with the TE_{01} mode field distribution for the rectangular waveguide (Figure 196 b). An initial waveguide-fed DR configuration is shown next. An additional microstripline has been added to excite the TE_{01} mode of the waveguide.

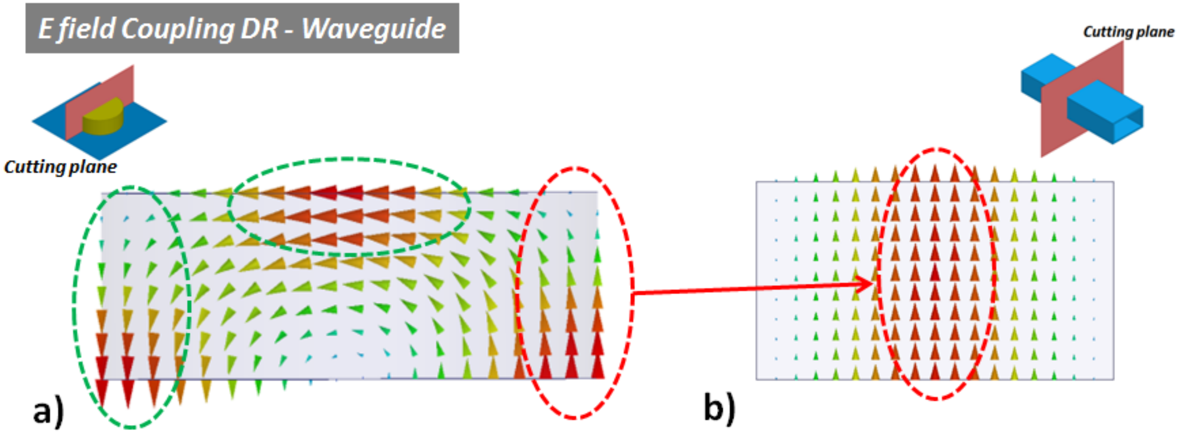

Figure 196 E vector fields for coupling mechanisms between DR and waveguide a) Cylindrical TM_{11} mode, b) Rectangular Waveguide TE_{01}

The complete structure is seen in Figure 197. Starting by the microstrip (MS) line which dominant mode is excited by the simulation port, the waveguide is then excited by the MS mode. The waveguide being assumed as a SIW structure due to the fine thickness of the substrate. The DR is attached by the waveguide to the rest of the structure and at the same time is excited. Due to the cylindrical shape of the DR, a tapered transition between the output of the waveguide and the DR is need for a suitable attachement of the DR to the supporting structure and to minimize the distance through a proper coupling phenomena with the DR.

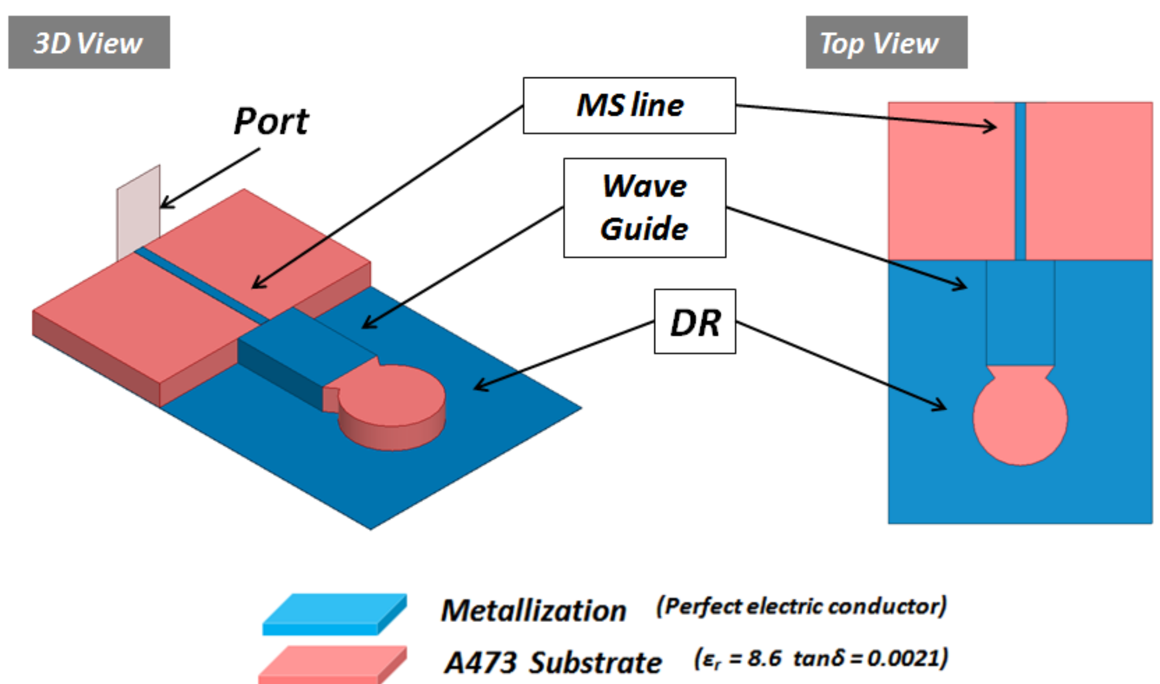

Figure 197 Wave guide fed DR + MS line configuration (3D and Top views)

4.a) Waveguide to SIW

Note that the waveguide is not feasible with LTCC or HTCC multilayer technology. The vertical metallization needed for the waveguide lateral walls cannot be fabricated. It should be replaced by the substrate integrated waveguide or SIW. The SIW (Figure 198) provides the conditions for the TE_{01} waveguide mode to propagate the same way as in a regular waveguide. The two metalized layer and the vias recreate the rectangular shape of the waveguide. The SIW used for Antennas and filters have already been fabricated and

validated [113], [117]–[119]. Low insertion loss (less than 1.5 dB/mm @ 50 GHz) has been measured. From here on the waveguide shown represents a SIW line.

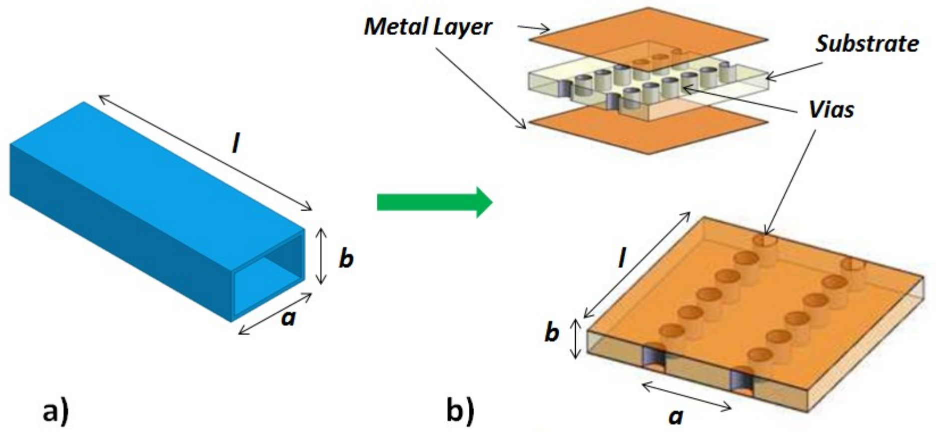

Figure 198 a) Waveguide and b) Substrate Integrated Waveguide[27]

4.b) Waveguide dimensioning and performance

First of all, the microstrip-waveguide transition is validated. A microstrip excited waveguide is first simulated. The cutting frequency for the waveguide TE_{01} mode is seen to be around 48 GHz. This should allow proper energy transfer to the DR at the 60 GHz band. The following equation has been used to calculate the dimensions of the waveguide.

$$f_c = \frac{1}{2a\sqrt{\varepsilon\mu}} \qquad Eq.\ 17$$

a stands for the waveguide width. Relative permittivity and permeability values are 8.6 and 1 respectively ($\varepsilon = \varepsilon_r * \varepsilon_0$ and $\mu = \mu_r * \mu_0$). The height value is fixed and depends on the packaging technology. In our case h = 0.5 mm. The microstrip line and the waveguide exhibit 0.05 dB/mm and 0.95 dB/mm attenuation respectively at 60 GHz.

[27] http://cassnewsletter.org/Volume3-Issue2/Technology_News_files/Figure1_1.jpg

- **Adapted** feed for multi-fed DRA

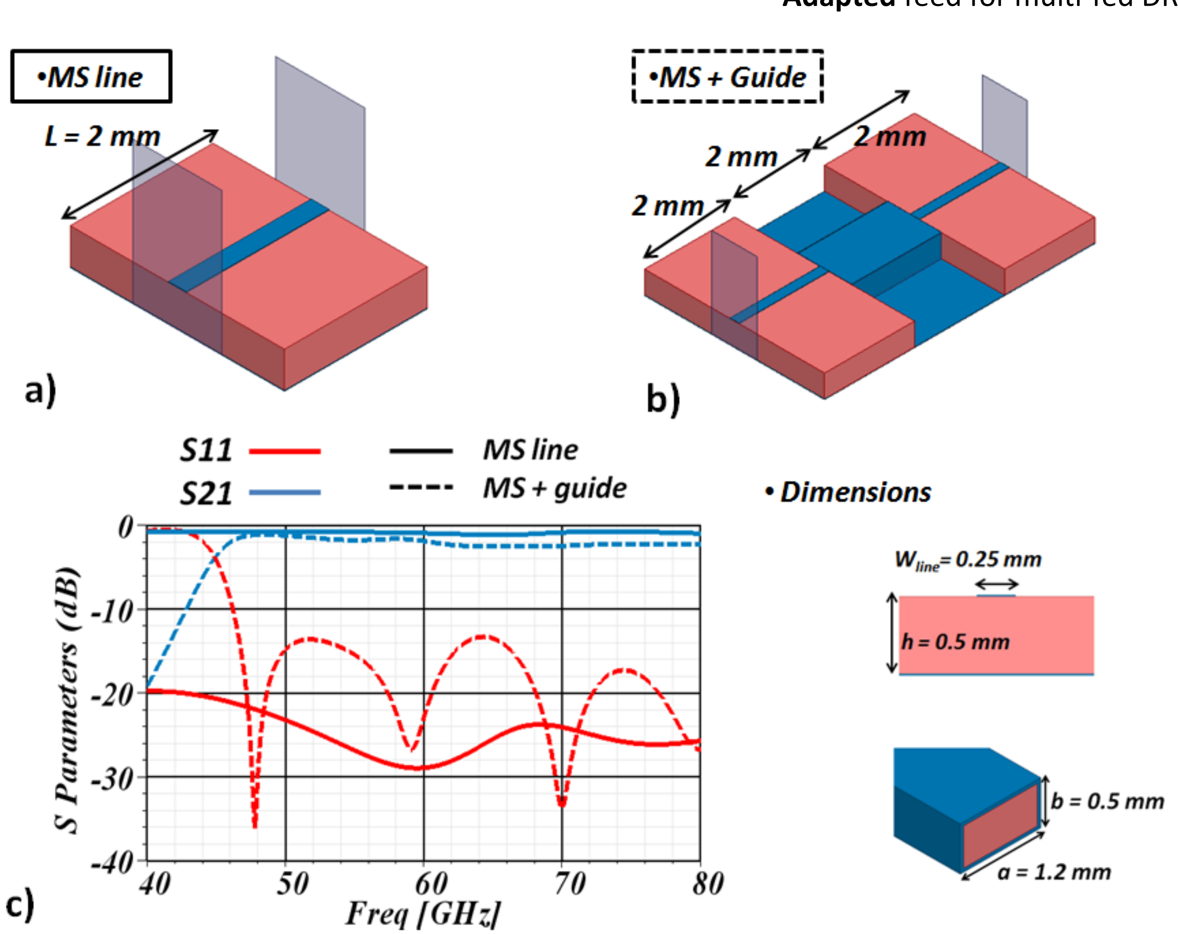

Figure 199 a) MS line b) MS line – Wave Guide – MS line Transitions and c) Matching and Transmission responses (S11 and S21)

The DR is added to the configuration as seen before in Figure 197. The DR size has increased as expected due to the lower material permittivity used. It has now a 0.9 mm radius compared to the 0.74 mm obtained with 9.9 permittivity. A 10 GHz bandwidth (S11 < -10dB) is obtained with a minimum 5dBi gain in the matched band (Figure 200 b). This increase in bandwidth compared to the solution presented in chapter 3 is due to the excitation element. The waveguide, as seen before, offers a natural wider transmission bandwidth. The DR will limit the operational bandwidth of the solution. This excitation also impacts the radiation behavior of the DR. The DR has no longer a perfect cylindrical shape and on one of the sides, the waveguide metallization modifies the near environment of the DR. The maximum is no longer seen at θ = 0° but a tilt of almost 45° is observed. A maximum of 7.2 dBi is obtained at 50°.

The radiation performance of a NO-DR configuration is also shown, that is, the radiation performance of the open ended waveguide. The open ended waveguide takes into account

the presence of the internal dielectric. The matching response is not accounted for. The gain is compared to that of the complete (WG + DR) configuration. It is observed that the open ended waveguide radiates and offers a maximum of 4 dBi gain (60 GHz Figure 200 a). A high cross polarization level of -2dB is also encountered. Its pattern is also shifted toward the positive theta values. The radiation pattern changes as the DR is added. The DR is now excited by the waveguide and the radiation performance of the DR takes over resulting in a new higher maximum gain of 7.2 dBi in accordance with DR gain values as seen in chapter 3. Cross levels also decrease to minimum of -30 dB at 55 GHz. The waveguide energy coupling to the DR prevents a high cross value from its open end. The fields are distributed according to the low cross polarization behavior of the TM_{11} mode.

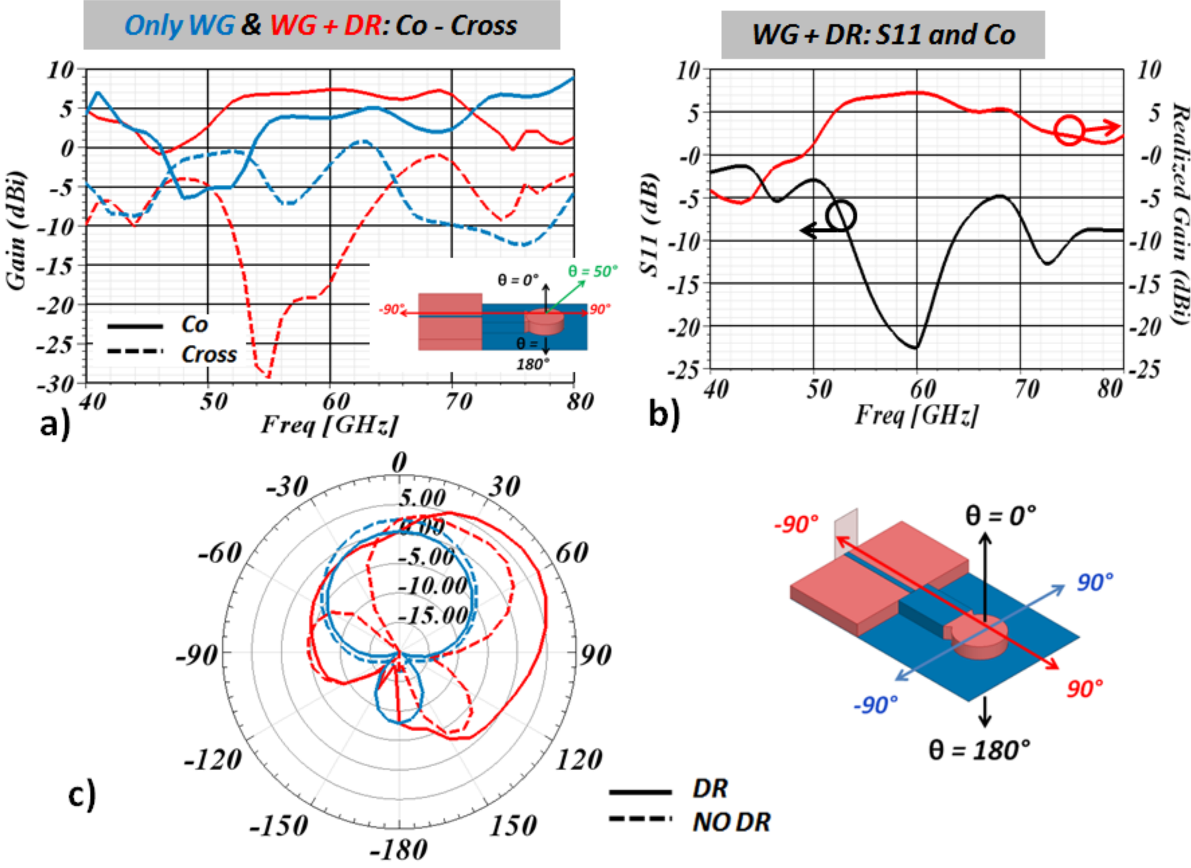

Figure 200 Waveguide fed DR a) Gain (Co & Cross) for DR and No DR waveguide configurations b) S11 and Realized Gain response @ θ = 50° for WG + DR and c) Gain Pattern for DR and No DR configurations

A parametric study has been done (Figure 201), to confirm the excitation of the DR and the impact of the DR- Waveguide distance. A clarification is done, regarding the properties of the joining DR-Waveguide element. The top face of the joining structure is metalized to maintain

the vertical electrical field from the waveguide open end to the DR lateral side. The previous matching and radiation responses include the top side metallization. Three DR-Waveguide distances are shown (0.1, 0.3 and 0.5 mm). The reduced matching response is observed as the DR separates from the open end of the waveguide. Good Co-Cross levels are observed in the adapted band.

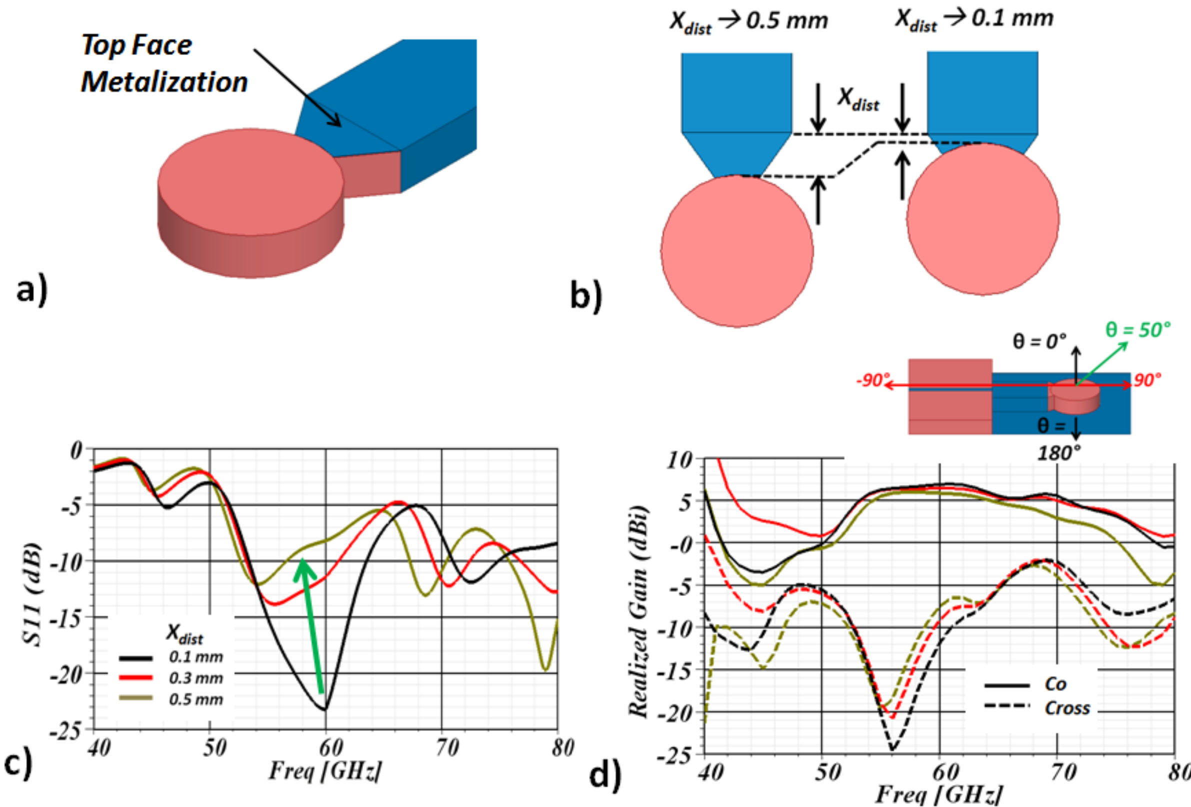

Figure 201 DR – Waveguide parametric study a) Metallization of the DR – Waveguide joining element b) Minimum and maximal distance taken and c) matching response and d) gain response

Nevertheless, a good radiation response is obtained for all covered distances. The following realized gain patterns are modified by the DR separation. A maximum gain value reduction is seen, from 7.1 to 5.6 dBi which can be explained due to the reduction of the matching response.

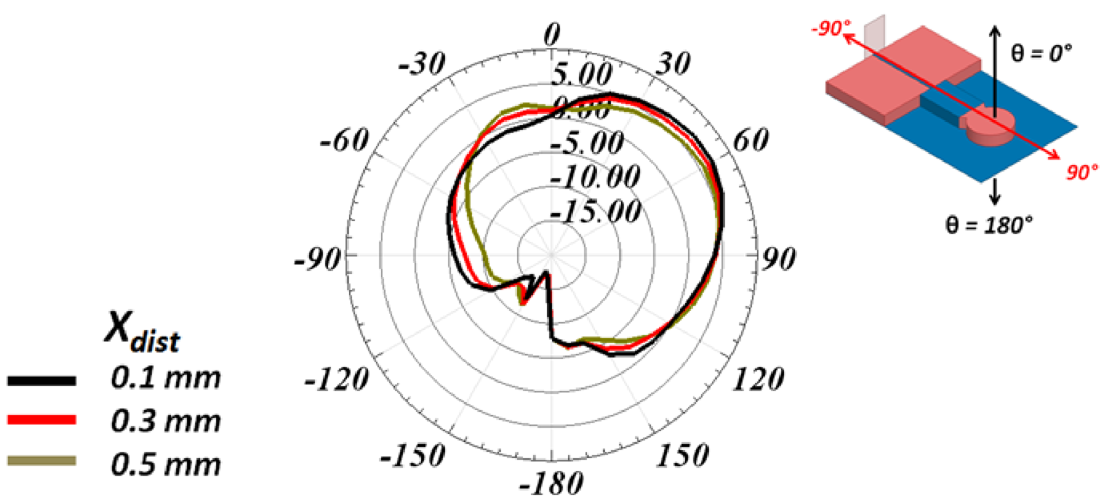

Figure 202 Gain pattern @ 60 GHz for several values of X_{dist}.

The DR excitation is also shown by way of the Electric vector field distribution of Figure 203. Electric fields are plotted for the entire structure, starting from the MS line up to the DR. The central and vertical oriented fields of the MS line and waveguide are shown. Several signal wavelengths appear on the MS and waveguide portions of the structure evident by the field polarity change. The TM_{11} DR mode is finally observed on the last portion of the figure. It can be compared to the field distribution of the mode seen at the right.

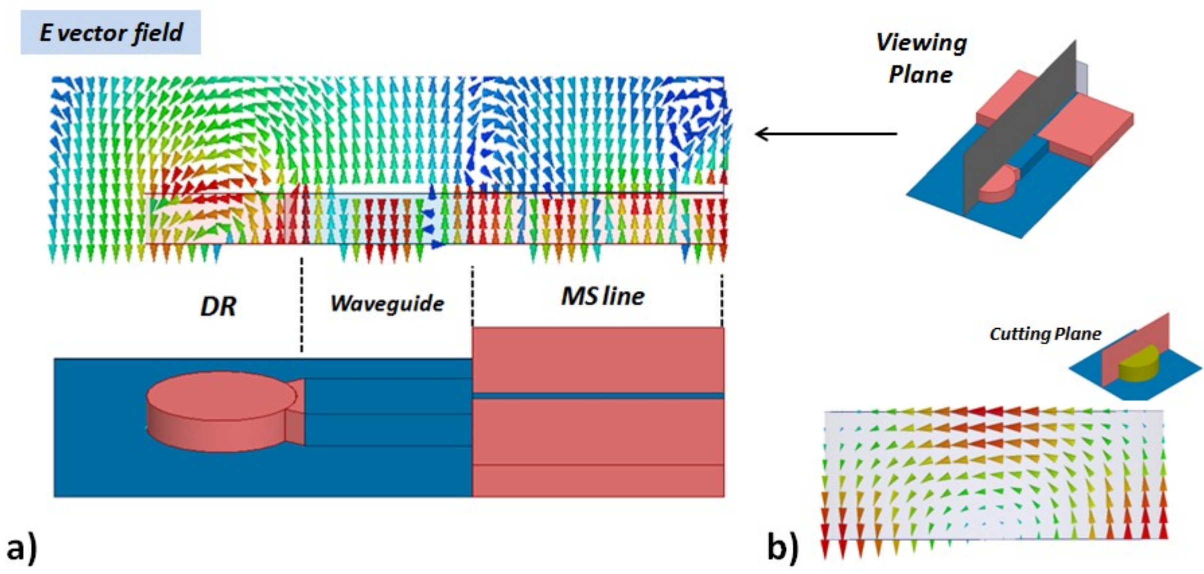

Figure 203 Electric Vector field @ 60 GHz a) from MS line to DR and in an b) Isolated DR

A high tilt (for all three X_{dist} values) degree of 50° has been obtained. By making use of the technology (HTCC) possibilities, the tilt degree could be controlled by inserting additional

elements to the configuration. Two types of element can be foreseen: isolated metallic barriers acting as reflectors or additional dielectric bodies that could couple to the DR radiation modifying its radiation properties. The WG coupling to the DR could also be controlled by the modification of the DR-WG interface. For example, the field exposed at the WG open end can be controlled with the incorporation of iris like element in the waveguide.

4.c) Multi feed DR

Finally, after obtaining the expected performance of the single side fed DR, the second feed is added to the configuration. Figure 204 depicts the two feed configuration as well as the matching and coupling responses. The matching response presents a 10 GHz bandwidth for both feeds. The same matching performance was observed for the single fed DR. Regarding the coupling response (S_{12} and S_{12}) a rather high -15 dB level is obtained and therefore a higher level compared to that of the slot-on-chip DR excitation seen in Figure 190.

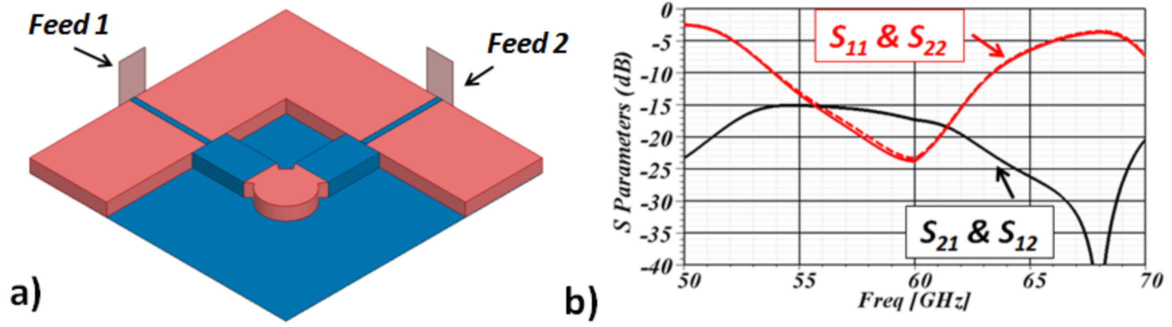

Figure 204 Multi-fed Waveguide excited DR a) Two feed configuration and b) S Parameters response.

Higher isolation levels could be obtained if the two sources are separated from each other. That is, if the DR is shifted as seen in Figure 201. Matching and coupling responses are seen next (Figure 205). Lower matching values are obtained as before, as the DR drifts apart from the waveguide. At the same time, the coupling between the two sources decreases. A 5 dB isolation level gain is obtained by passing from X_{dist} 0.1 to 0.5 mm. The radiation performance behaves similarly to that seen for one-Feed case (Figure 202). A good gain level is maintained for the different DR positions. This leads to think that if the matching response can be improved for a “far extended distance” DR position, a good isolation and radiation performance can be obtained. The coupling for a “No DR” configuration is also shown, where a -17 dB coupling level is obtained for the inherent waveguide radiation. The presence of the

DR does not seem to increase the coupling level between the two waveguides. The coupling level is generated by the proximity of the waveguide open end.

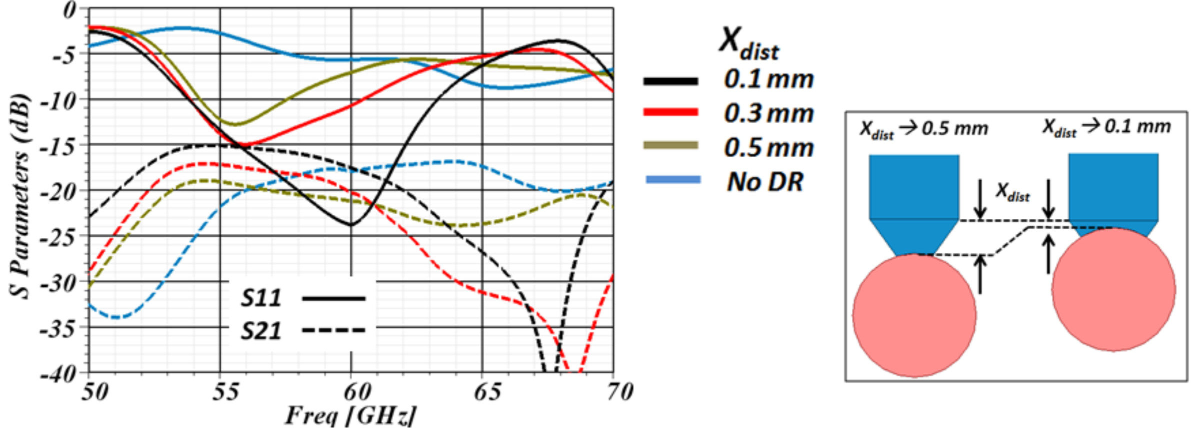

Figure 205 Matching (S11) and Coupling (S21) for X_{dist} values

As before, the magnetic vector fields inside the DR are plotted in Figure 206. Once again, feeds are enabled independently and the corresponding field is shown. The expected field rotation due to the orthogonal fields is observed. Radiation performance is seen next.

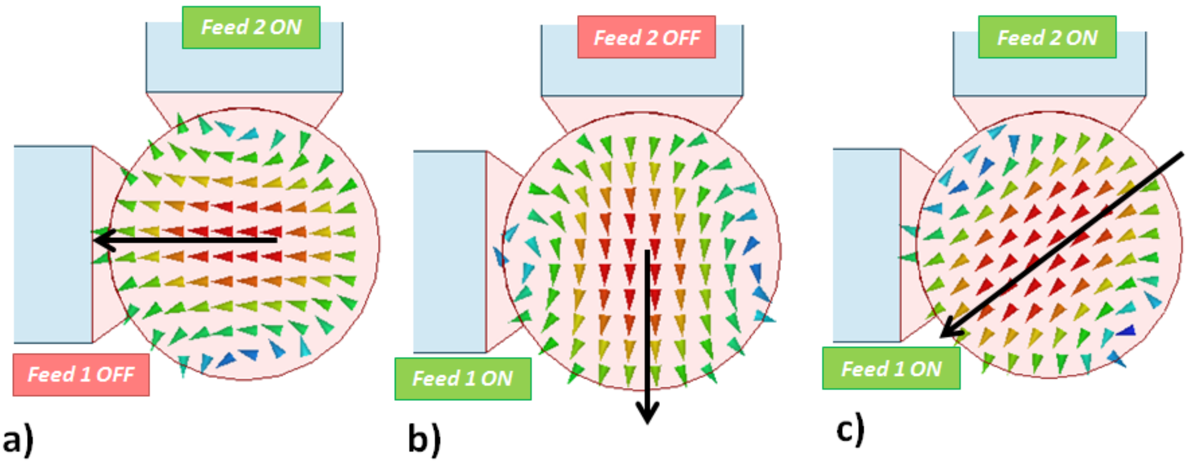

Figure 206 H Vector field in DR for a) Feed 1 OFF and Feed 2 ON, b) Feed 1 ON and Feed 2 OFF and c) Feed 1 ON and Feed 2 ON.

Good Co and Cross polarization levels are observed with level differences of more than 30 dB, which ensures a correct polarization. As expected, co and cross values are improved regarding the radiation performance of the on-chip-slot side-fed configuration previously shown in Figure 192. This can be explained by low radiation that escapes from the coupling component, in this case the waveguide. 3D visualization of the field is also shown for a

- **Adapted** feed for multi-fed DRA

complete field appreciation. Low backward radiation (θ = -90°) is seen which becomes relevant for the PA integration shown further ahead.

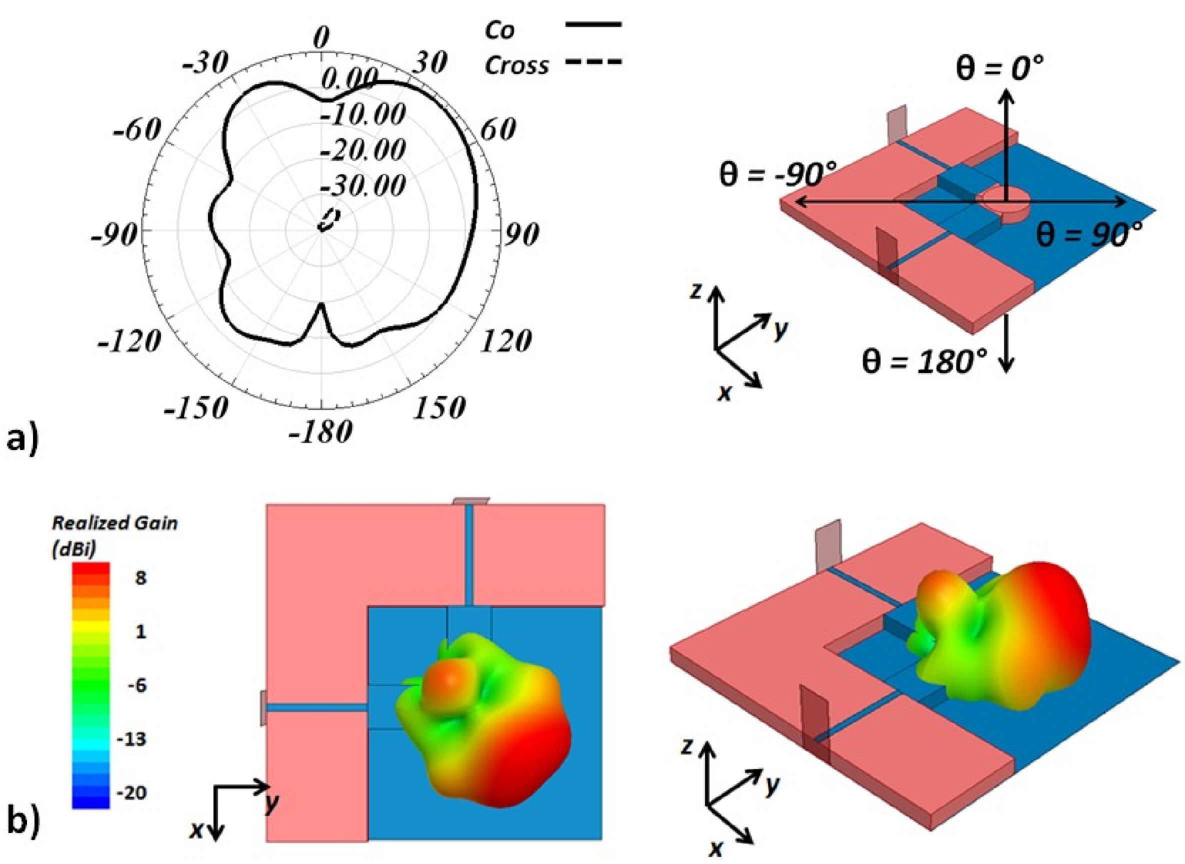

Figure 207 Two feed configuration radiation performance a) Co and Cross polarization @ 60 GHz b) 3D Total gain (Co + Cross components) visualization

4.d) SIW excitation

Although the MS line has shown a good performance (wide bandwidth and low insertion loss), is not well adapted for chip integration. As seen in chapter 2, a CPW configuration is preferred at the PA output. An additional CPW to MS transition would be required for a PA-Antenna interconnection. A different approach is taken, where the MS line is eliminated and the waveguide is directly excited by a CPW based element. In this way, a packaged chip-antenna configuration like the one seen in Figure 208 can be foreseen.

- **Adapted** feed for multi-fed DRA

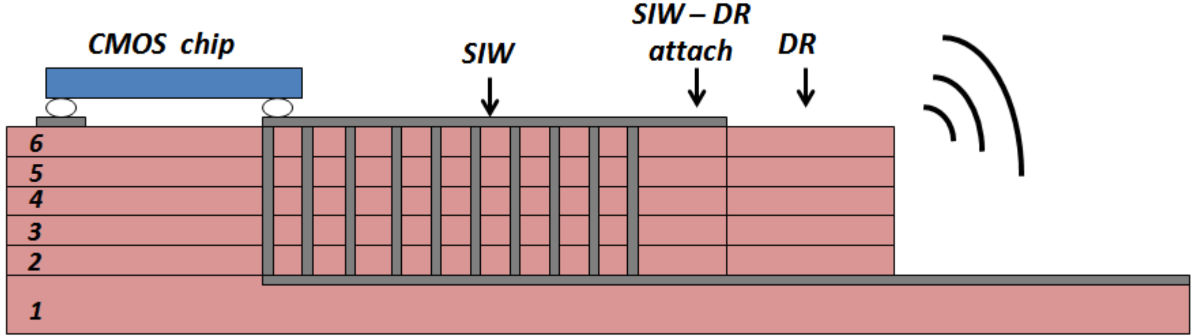

Figure 208 DR and Chip HTCC integration

The excitation is depicted by Figure 209 a). It has been validated in [120] where it was used as cavity mode excitation. The CPW access and field generator are highlighted. The excitation acts similarly as a CPW fed slot as seen in chapter 2 and 3, generating the vector H field shown. Dimensions L_x and L_y are used to control frequency and input impedance respectively. Next, the coupling from the excitation to the waveguide TE_{01} mode is highlighted. The waveguide horizontally distributed magnetic field is excited by the same horizontally directed field region of the excitation generated field.

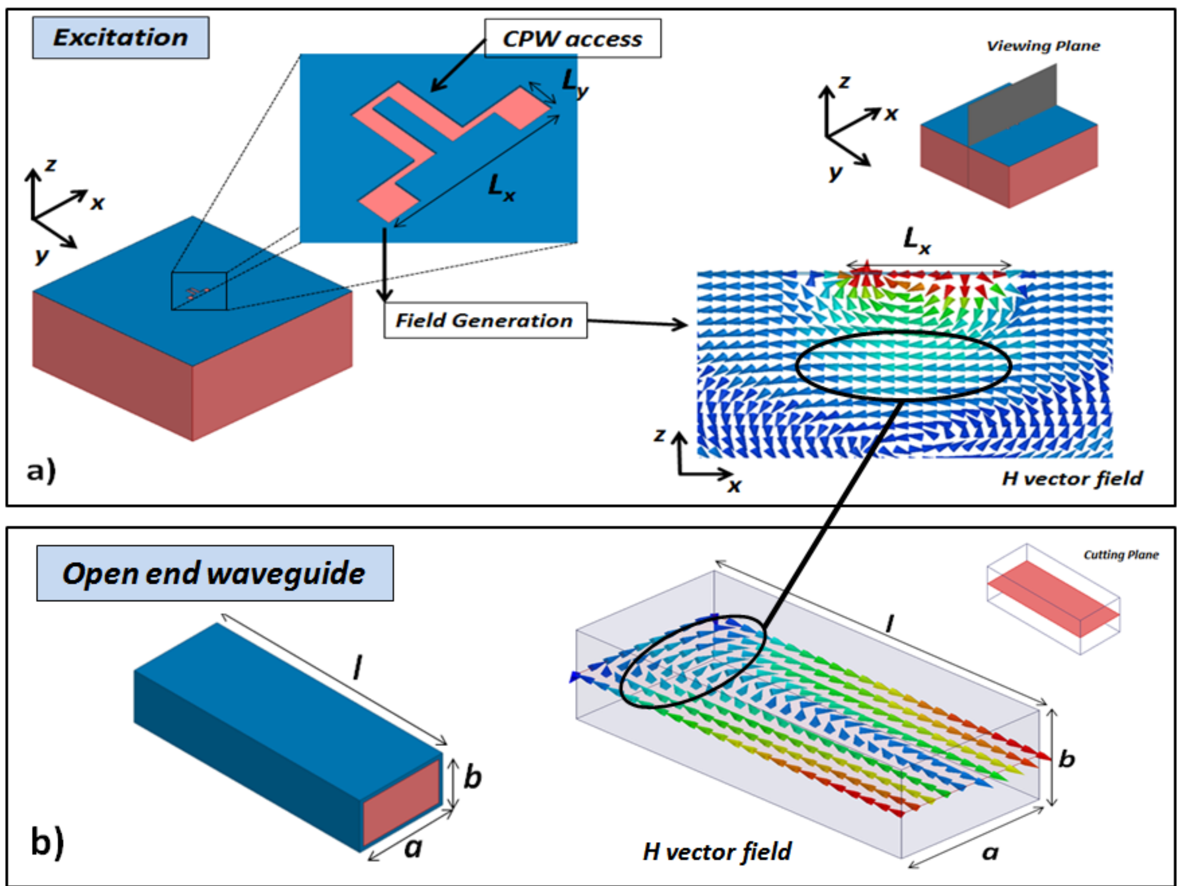

Figure 209 CPW Waveguide Excitation a) Excitation and front view of generated magnetic field. b) Magnetic fields of the open end waveguide. Coupling between excitation and waveguide mode is highlighted

The complete CPW accessed - Waveguide - DR configuration is shown next. The electric vector field is shown through the whole structure. The vertical waveguide field distribution is seen as well as the DR TM_{11} mode. As before, several phase changes on the TE_{01} mode are seen due to the length of the line. The magnetic field is also depicted by Figure 210 where the corresponding DR mode is also seen. The DR excitation by the integrated waveguide excitation has been validated by simulation. Radiation performance can be seen in Figure 211, where a high gain and low cross polarization is obtained. Similar behavior as that obtained with the MS line is seen (Figure 200); a high gain with corresponding pattern tilted due to the excitation. The length of the waveguide (3 mm) could be reduced for a more compact solution.

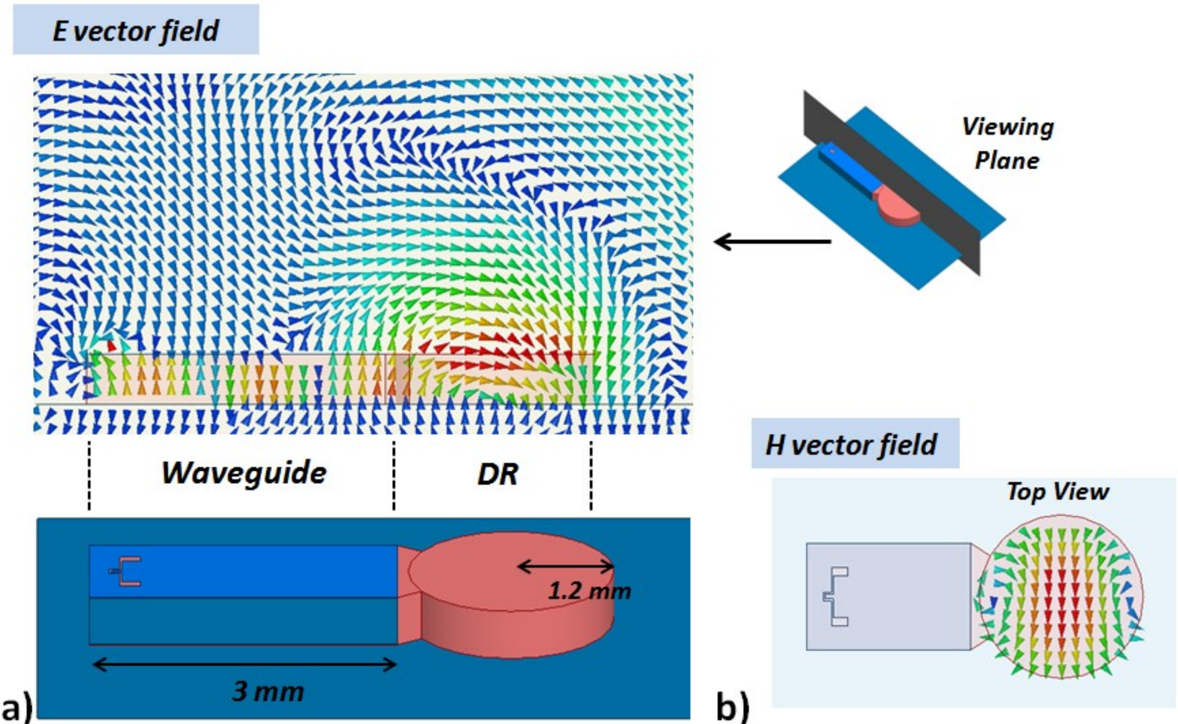

Figure 210 Complete configuration: excitation waveguide and DR a) Electric vector field and b) Magnetic vector field TM_{11} (Top view)

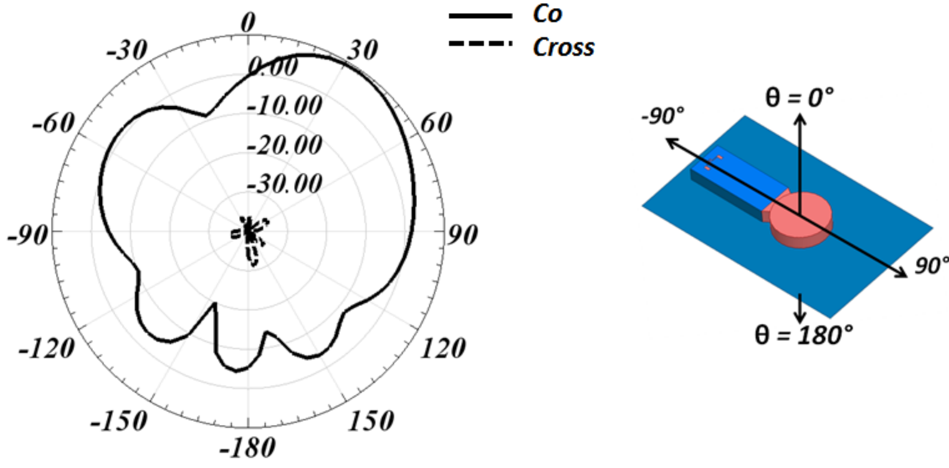

Figure 211 Gain Pattern for DR fed by waveguide + integrated excitation

4.e) PA incorporation constraints

From the PA point of view, the cost of adding an additional PA to the configuration remains to be specified. Two different scenarios could be foreseen: Two PA – Two chips or Two PA – One Chip. For the first case (Two PA – Two chips), the possibility of having two independent PA allows to control their localization depending on the antenna feeds positions. This will

alleviate the antenna feed design (Figure 211 a)). On the other hand, we have to recall that the PA makes part of a bigger structure as it is the transmitter (VCO-mixer-PA). Two independent PAs means two independent transmitters that will almost double the consumed power of the whole chain. Moreover, the existence of two chips will duplicate the interconnections and increase the size of the final solution.

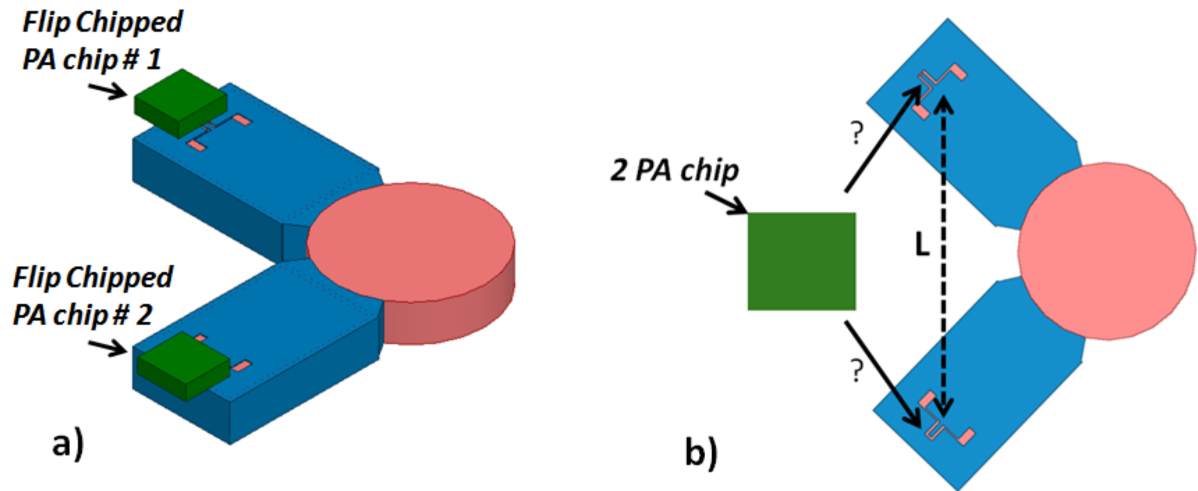

Figure 212 a) Two independent PA chip configuration and b) Single chip

For the second case (Two PA - One chip), a decrease on the number of interconnections is achieved as well as size and power consumption. A modification of the active devices design should be done to accommodate the additional PA and to assure impedance match at the input of the new parallel PA configuration. Note that antenna feed will now have an additional constraint. Due to the orthogonal feed, the punctual PA output location cannot be connected to both feeds as seen in Figure 212 b) A distance (L) separates both CPW SIW access.

Future studies should be done to incorporate SIW in the simulation. It should also render the Single-chip multi-feed antenna possible by using new SIW feeding possibilities like the one found in [117]. SIW bending is demonstrated (Figure 213), where a rotation of the open-end waveguide regarding the feed is achieved. In this way, both SIW CPW accesses could be redirected toward the position of the chip as seen in Figure 213 c).

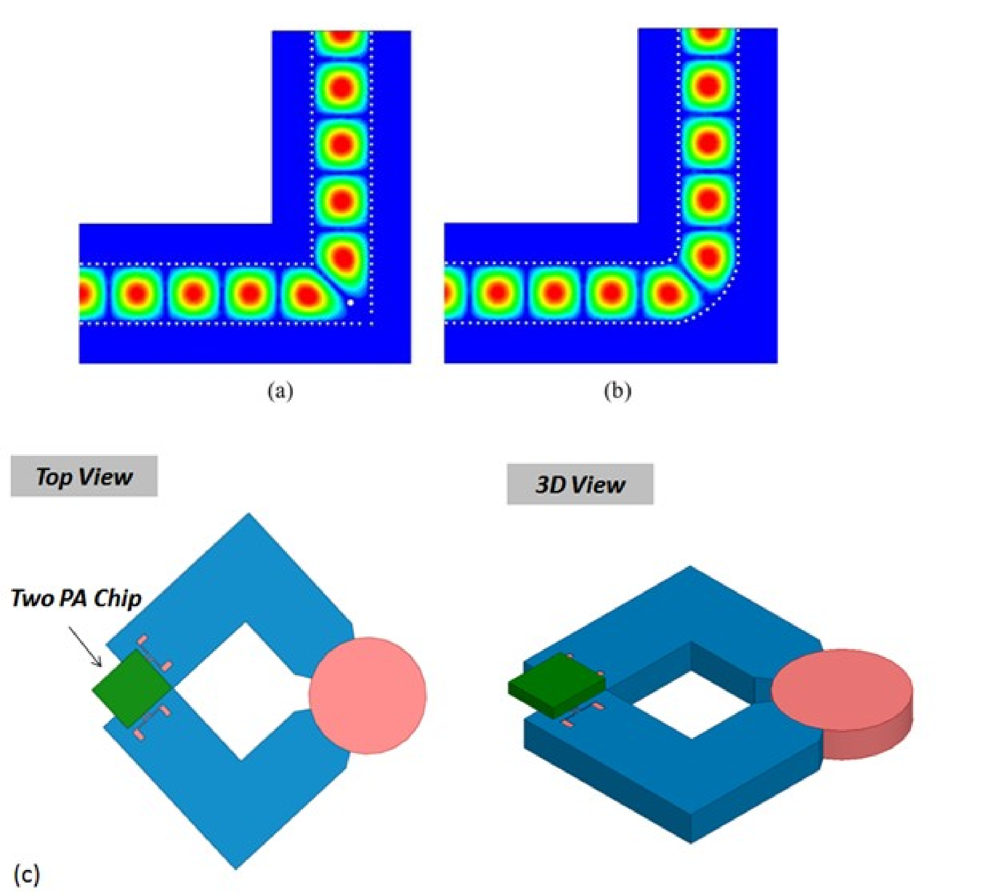

Figure 213 Electric field of bend structures proposed in [117] (a) Bend type 1: right angle corner + post insertion and b) curved corner. c) Two PA chip with bended SIW configuration

5) Conclusions

A new efficiency enhancement strategy is proposed in this chapter for the PA-Antenna transmitter configuration. The antenna is given a more important role than that of the radiating element. By becoming a power combiner, the high power and linearity requirements for the PA are alleviated. In this way, two low power but linear PAs will replace the single high power but “less” linear PA. The single-feed antenna becomes a multi-feed element.

From the antenna and its radiation performance point of view, two conclusions are extracted. First of all, coupling between feeds arises as a new constraint for the antenna design. Antenna operation mechanism and field distribution become key parameters for achieving high isolation between feeds. Secondly, the field rotation obtained after the orthogonal field addition increases the possibility for a higher cross-polarization level. The unwanted antenna feed radiation enter now into play. And in this new two feed scenario, the feed impact on the antenna performance should double regarding a single fed configuration. A good selection of the antenna excitation becomes primordial and should be reflected on a low cross polarization level.

The DRA and waveguide excitation were finally validated by simulation. Acceptable coupling levels were obtained and a low cross polarization level was achieved.

At the same time, industrial packaging technology was approached. DR fabrication constraints on multilayer technology were detected. A new DR feed solution is proposed where DR fabrication is solved. Multilayer based DR and multilayer waveguide were also confirmed as possible candidates for high gain mm-wave packaged PA-Antenna solution.

General Conclusions

A 60-GHz system for high data rate transfer was investigated. Focusing on the power amplifier and antenna integration, different solutions are presented. First, Silicon has been chosen as the technology for three reason: (*i*) the fabrication cost that continues to decline due to a large investment from the industry and government, (*ii*) the integration possibility due to the high die capability production compared to other technologies, and (*iii*), SOI technology presents an elevated substrate resistivity (3000 Ω/cm). This last property renders passive devices like capacitors, inductors and transmission lines more efficient components to be implemented. So, silicon CMOS seems the best choice to obtain low cost, high integrability and high efficiency solutions for RF applications.

The next point to be addressed was to manage the transmitter antenna integration to obtain efficiency increase.

Two different integration strategies were considered: SoC and SiP.

By incorporating the antenna on chip, a 8.5 % efficiency increase was achieved when a co-design strategy was taken. This demonstrates the possibilities offered by on-chip integration where the typical 50 Ω PA output and 50 Ω antenna input can be modified and matched as needed.

Although PA-Antenna SoC integration offers good opportunities for efficiency increase, it also renders the design more complex due to size reduction. First of all, the PA and antenna can interact in a detrimental fashion rendering the PA location regarding the antenna "radiating" element a key parameter.

Secondly, devices introduced at measurement (probe and support) have a non negligible effect. The mm-probe was seen to interfere with the radiation of the device under test. And last, the chip boundary (chip borders) becomes important for size-reduced solutions.

From a more ready-to-market scenario, the SiP offers some higher flexibility from the antenna point of view. Starting from the single high gain DRA solution, several configurations show the possibility of using the DRA in the millimeter band as efficient solution for the antenna element of the 60-GHz radio front end. Due to the low loss alumina substrate, a high efficiency antenna can be obtained. Original DR based solutions were possible by taking

advantage of the laser machining. In this way, a first DR based “semi” packaged solution was presented. We could see how the interconnections play a fundamental role. The performance of the solution, specifically the efficiency (characterized by the loss inserted by the transition) and the bandwidth (VSWR >2) of the antenna are highly impacted. Two final completely packaged configurations were then presented. These solutions share the same original DR based package, where the package and DR are fabricated at the same laser micromachining step. Wide bandwidth (10 GHz) and a minimum 5 dBi gain over the matched band were finally obtained. As a result, the application requirements were fulfilled.

Keeping in line with the thesis objective, another efficiency enhancement strategy is proposed and validated by simulations. The antenna is given a more important role than that of the radiating element. The single-feed antenna becomes a multi-feed element. In this way, two low power but linear PAs will replace the single high power but “less” linear PA. From the antenna and its radiation performance point of view two conclusions are extracted. First of all, coupling between feeds arises as a new constraint for the antenna design. Secondly, the field rotation obtained after the orthogonal field addition increases the risk for a higher cross-polarization level. After the constraint identification new solutions were proposed. They included the use of industrial packaging technology more precisely the multilayer HTCC. DR fabrication constraints on multilayer technology were detected and solved. Simulated results show a promising performance for multi-layered multi-fed DR solution.

Future Work

From the previously presented results, several axes can be identified to continue this research work. First of all, simulation tools are in constant evolution and offer new opportunities for circuit and antenna co-simulation. As we saw before, some aspects of PA and antenna solutions could not be taken into account by simulation. The co-integration and co-design solutions, both showed disturbances as the maximum PA output power was reached. These disturbances are not seen in simulation and only unverified coupling phenomena seem to explain the results. Having this in mind, new simulation tools could offer new possibilities to characterize the entire PA – Antenna chain and the interaction between them.

Secondly, multilayer technology (HTCC) is ideal for dielectric resonator-based antennas. The relatively high permittivity of ceramic tape allows the resonator size to be compatible with mm-wave active devices. It also offers a low tan δ value that allows increasing the antenna efficiency. Having solved the fabrication constraint, a completely compatible antenna solution can be foreseen for a PA-antenna packaged solution. Beside the radio front-end integration, the flexibility of the fabrication procedure allows one to carry out experiments on the antenna. For example, the DR could be given different shapes (rectangular, oval) that could enhance its performance. The DR boundary can also be modified by the metallization possibility of the technology introducing shielded antenna solutions.

Finally and as mentioned before, future studies should be done on SIW technology to confirm the compatibility with the SIW fed DR and the constraint that could arise from the PA circuit design.

References

[1] "IEEE 802.15 Task Group 3c." [Online]. Available: http://ieee802.org/15/pub/TG3c.html. [Accessed: 21-Jun-2011].

[2] R. Fisher, "60 GHz WPAN Standardization within IEEE 802.15.3c," in *International Symposium on Signals, Systems and Electronics, 2007. ISSSE '07*, 2007, pp. 103–105.

[3] "What is unlicensed spectrum? What frequencies are they in?" [Online]. Available: http://www.wimax.com/wimax-regulatory/what-is-unlicensed-spectrum-what-frequencies-are-they-in. [Accessed: 09-May-2012].

[4] D. Liu, U. Pfeiffer, J. Grzyb, and B. Gaucher, *Advanced Millimeter-Wave Technologies: Antennas, Packaging and Circuits*. Wiley-Blackwell (an imprint of John Wiley & Sons Ltd), 2009.

[5] S. Yong and C.-C. Chong, "An Overview of Multigigabit Wireless through Millimeter Wave Technology: Potentials and Technical Challenges," *EURASIP Journal on Wireless Communications and Networking*, vol. 2007, no. 1, p. 078907, Dec. 2006.

[6] H. Singh, Su-Khiong Yong, Jisung Oh, and Chiu Ngo, "Principles of IEEE 802.15.3c: Multi-Gigabit Millimeter-Wave Wireless PAN," in *Proceedings of 18th Internatonal Conference on Computer Communications and Networks, 2009. ICCCN 2009*, 2009, pp. 1–6.

[7] "Information (Rohde & Schwarz International - Technologies - Wireless Connectivity - WiGig / WiHD)." [Online]. Available: http://www2.rohde-schwarz.com/en/technologies/Wireless_Connectivity/mmwave/information/. [Accessed: 03-Apr-2012].

[8] C. A. Balanis, *Antenna Theory: Analysis and Design, 3rd Edition*, 3rd ed. Wiley-Interscience, 2005.

[9] P. Njissang and J. Johnson, "WirelessHD® 60GHz CE Products Arrive in Europe." Wireless HD, Sep-2009.

[10] "Qualcomm News and Events - Press Releases Qualcomm Atheros and Wilocity Announce Tri-band Wi-Fi: Industry's First Standards-compliant, Multi-gigabit Wireless Chipset," *Qualcomm*.

[11] A. M. Niknejad and H. Hashemi, Eds., *mm-Wave Silicon Technology: 60 GHz and Beyond*, 1st ed. Springer, 2008.

[12] C.-H. Wang, Y.-H. Cho, C.-S. Lin, H. Wang, C.-H. Chen, D.-C. Niu, J. Yeh, C.-Y. Lee, and J. Chern, "A 60GHz transmitter with integrated antenna in 0.18 um SiGe BiCMOS technology," in *Solid-State Circuits Conference, 2006. ISSCC 2006. Digest of Technical Papers. IEEE International*, 2006, pp. 659 –668.

[13] B. Heydari, M. Bohsali, E. Adabi, and A. M. Niknejad, "A 60 GHz Power Amplifier in 90nm CMOS Technology," in *Custom Integrated Circuits Conference, 2007. CICC '07. IEEE*, 2007, pp. 769 –772.

[14] D. Chowdhury, P. Reynaert, and A. M. Niknejad, "A 60GHz 1V + 12.3dBm Transformer-Coupled Wideband PA in 90nm CMOS," in *Solid-State Circuits Conference, 2008. ISSCC 2008. Digest of Technical Papers. IEEE International*, 2008, pp. 560 –635.

[15] H. Mendez, "Silicon-on-insulator SOI technology and ecosystem Emerging SOI applications," 29-Apr-2009.

[16] M. Kaynak, I. Tekin, and Y. Gurbuz, "A matching circuit tuned, multi-band (WLAN and WiMAX), Class A power amplifier using 0.25 um-SiGe HBT technology," in *Research in Microelectronics and Electronics, 2008. PRIME 2008. Ph.D.*, 2008, pp. 169 –172.

[17] M. Chang and G. M. Rebeiz, "A wideband high-efficiency 79-97 GHz SiGe linear power amplifier with > 90 mW output," in *Bipolar/BiCMOS Circuits and Technology Meeting, 2008. BCTM 2008. IEEE*, 2008, pp. 69 –72.

[18] H. Mendez, "Low-Power Design with Material Impact on Silicon on Insulator Technology," 29-Apr-2009.

[19] B. Martineau, "Potentialités de la technologie CMOS 65nm SOI pour des applications sans fils en bande millimétrique," Thèse de doctorat, [S. n.], [S. l]., 2008.

[20] D. Axelrad, “Application des technologies CMOS sur SOI aux fonctions d’interface des liens de communication haut débit (>10Gbit/s),” Thèse de doctorat, [s.n], [S.l.], 2005.

[21] C. Pavageau, “Utilisation des technologies CMOS SOI 130 nm pour des applications en gamme de fréquences millimétriques,” Université des Sciences et Technologies de Lille, 2005.

[22] D. M. Pozar, *Microwave Engineering*, 2nd ed. Wiley, 1997.

[23] F. Gianesello, “Technologies CMOS SOI pour applications RF et millimétrique,” Paris, 02-Nov-2009.

[24] M. Helaoui and F. M. Ghannouchi, “Optimizing Losses in Distributed Multiharmonic Matching Networks Applied to the Design of an RF GaN Power Amplifier With Higher Than 80% Power-Added Efficiency,” *Microwave Theory and Techniques, IEEE Transactions on*, vol. 57, no. 2, pp. 314 –322, Feb. 2009.

[25] F. Ellinger, *Radio Frequency Integrated Circuits and Technologies*. Springer, 2008.

[26] Y. S. Ng, L. Leung, and K. N. Leung, “A 3-GHz fully-integrated CMOS Class-AB power amplifier,” in *Circuits and Systems, 2009. MWSCAS ’09. 52nd IEEE International Midwest Symposium on*, 2009, pp. 995 –998.

[27] M. Kaynak, I. Tekin, and Y. Gurbuz, “A matching circuit tuned, multi-band (WLAN and WiMAX), Class #x2014; a power amplifier using 0.25 #x03BC;m-SiGe HBT technology,” in *Research in Microelectronics and Electronics, 2008. PRIME 2008. Ph.D.*, 2008, pp. 169 –172.

[28] D. Chowdhury, P. Reynaert, and A. M. Niknejad, “A 60GHz 1V + 12.3dBm Transformer-Coupled Wideband PA in 90nm CMOS,” in *Solid-State Circuits Conference, 2008. ISSCC 2008. Digest of Technical Papers. IEEE International*, 2008, pp. 560 –635.

[29] W. L. Chan, J. R. Long, M. Spirito, and J. J. Pekarik, “A 60GHz-band 1V 11.5dBm power amplifier with 11% PAE in 65nm CMOS,” in *Solid-State Circuits Conference - Digest of Technical Papers, 2009. ISSCC 2009. IEEE International*, 2009, pp. 380–381,381a.

[30] M. Tanomura, Y. Hamada, S. Kishimoto, M. Ito, N. Orihashi, K. Maruhashi, and H. Shimawaki, “TX and RX Front-Ends for 60GHz Band in 90nm Standard Bulk CMOS,” in *Solid-State Circuits Conference, 2008. ISSCC 2008. Digest of Technical Papers. IEEE International*, 2008, pp. 558–635.

[31] B. Heydari, M. Bohsali, E. Adabi, and A. M. Niknejad, “A 60 GHz Power Amplifier in 90nm CMOS Technology,” in *Custom Integrated Circuits Conference, 2007. CICC ’07. IEEE*, 2007, pp. 769 –772.

[32] D. Dawn, S. Sarkar, P. Sen, B. Perumana, D. Yeh, S. Pinel, and J. Laskar, “17-dB-gain CMOS power amplifier at 60GHz,” in *Microwave Symposium Digest, 2008 IEEE MTT-S International*, 2008, pp. 859 –862.

[33] E. Cohen, S. Ravid, and D. Ritter, “60GHz 45nm PA for linear OFDM signal with predistortion correction achieving 6.1% PAE and #x2212;28dB EVM,” in *Radio Frequency Integrated Circuits Symposium, 2009. RFIC 2009. IEEE*, 2009, pp. 35 –38.

[34] J. Lee, Y. Huang, Y. Chen, H. Lu, and C. Chang, “A low-power fully integrated 60GHz transceiver system with OOK modulation and on-board antenna assembly,” in *Solid-State Circuits Conference - Digest of Technical Papers, 2009. ISSCC 2009. IEEE International*, 2009, pp. 316 –317,317a.

[35] S. Aloui, E. Kerherve, D. Belot, and R. Plana, “Design Techniques and Modeling for 60GHz Applications With a 65nm-CMOS-RF Technology,” in *Millimeter Waves, 2008. GSMM 2008. Global Symposium on*, 2008, pp. 241 –244.

[36] W. L. Chan, J. R. Long, M. Spirito, and J. J. Pekarik, “A 60GHz-band 1V 11.5dBm power amplifier with 11% PAE in 65nm CMOS,” in *Solid-State Circuits Conference - Digest of Technical Papers, 2009. ISSCC 2009. IEEE International*, 2009, pp. 380 –381,381a.

[37] C. Marcu, D. Chowdhury, C. Thakkar, L.-K. Kong, M. Tabesh, J.-D. Park, Y. Wang, B. Afshar, A. Gupta, A. Arbabian, S. Gambini, R. Zamani, A. M. Niknejad, and E. Alon, “A 90nm CMOS low-power 60GHz transceiver with integrated baseband circuitry,” in *Solid-State Circuits Conference - Digest of Technical Papers, 2009. ISSCC 2009. IEEE International*, 2009, pp. 314 –315,315a.

[38] N. Kurita and H. Kondoh, “60GHz and 80GHz wide band power amplifier MMICs in 90nm CMOS technology,” in *Radio Frequency Integrated Circuits Symposium, 2009. RFIC 2009. IEEE*, 2009, pp. 39 –42.

[39] U. R. Pfeiffer, “A 20dBm Fully-Integrated 60GHz SiGe Power Amplifier with Automatic Level Control,” in *Solid-State Circuits Conference, 2006. ESSCIRC 2006. Proceedings of the 32nd European*, 2006, pp. 356 –359.

[40] S. Aloui, E. Kerherve, D. Belot, and R. Plana, “A 60GHz, 13 dBm fully integrated 65nm RF-CMOS power amplifier,” in *Circuits and Systems and TAISA Conference, 2008. NEWCAS-TAISA 2008. 2008 Joint 6th International IEEE Northeast Workshop on*, 2008, pp. 237 –240.

[41] A. Siligaris, Y. Hamada, C. Mounet, C. Raynaud, B. Martineau, N. Deparis, N. Rolland, M. Fukaishi, and P. Vincent, “A 60GHz power amplifier with 14.5dBm saturation power and 25% peak PAE in CMOS 65nm SOI,” in *ESSCIRC, 2009. ESSCIRC ’09. Proceedings of*, 2009, pp. 168 –171.

[42] Y. Jin, M. A. T. Sanduleanu, E. A. Rivero, and J. R. Long, “A millimeter-wave power amplifier with 25dB power gain and +8dBm saturated output power,” in *Solid State Circuits Conference, 2007. ESSCIRC 2007. 33rd European*, 2007, pp. 276 –279.

[43] T. Suzuki, Y. Kawano, M. Sato, T. Hirose, and K. Joshin, “60 and 77GHz Power Amplifiers in Standard 90nm CMOS,” in *Solid-State Circuits Conference, 2008. ISSCC 2008. Digest of Technical Papers. IEEE International*, 2008, pp. 562 –636.

[44] M. Tanomura, Y. Hamada, S. Kishimoto, M. Ito, N. Orihashi, K. Maruhashi, and H. Shimawaki, “TX and RX Front-Ends for 60GHz Band in 90nm Standard Bulk CMOS,” in *Solid-State Circuits Conference, 2008. ISSCC 2008. Digest of Technical Papers. IEEE International*, 2008, pp. 558 –635.

[45] J.-L. Kuo, Z.-M. Tsai, K.-Y. Lin, and H. Wang, “A 50 to 70 GHz Power Amplifier Using 90 nm CMOS Technology,” *Microwave and Wireless Components Letters, IEEE*, vol. 19, no. 1, pp. 45 –47, Jan. 2009.

[46] S. Montusclat, F. Gianesello, D. Gloria, and S. Tedjini, “Silicon integrated antenna developments up to 80 GHz for millimeter wave wireless links,” in *Microwave Conference, 2005 European*, 2005, vol. 3, p. 4 pp.

[47] H. F. Pues and A. R. Van de Capelle, “An impedance-matching technique for increasing the bandwidth of microstrip antennas,” *Antennas and Propagation, IEEE Transactions on*, vol. 37, no. 11, pp. 1345 –1354, Nov. 1989.

[48] M. Barakat, “Dispositif radiofréquence millimétrique pour objets communicants de type Smart Dust,” 2008.

[49] S.-S. Hsu, K.-C. Wei, C.-Y. Hsu, and H. Ru-Chuang, “A 60-GHz Millimeter-Wave CPW-Fed Yagi Antenna Fabricated by Using 0.18-um CMOS Technology,” *Electron Device Letters, IEEE*, vol. 29, no. 6, pp. 625 –627, Jun. 2008.

[50] R. Garg, *Microstrip Antenna Design Handbook*. Artech House, 2001.

[51] A. Shamim, L. Roy, N. Fong, and N. G. Tarr, “24 GHz On-Chip Antennas and Balun on Bulk Si for Air Transmission,” *Antennas and Propagation, IEEE Transactions on*, vol. 56, no. 2, pp. 303 –311, Feb. 2008.

[52] E. Seok, C. Cao, D. Shim, D. J. Arenas, D. B. Tanner, C.-M. Hung, and K. K. O, “A 410GHz CMOS Push-Push Oscillator with an On-Chip Patch Antenna,” in *Solid-State Circuits Conference, 2008. ISSCC 2008. Digest of Technical Papers. IEEE International*, 2008, pp. 472 –629.

[53] P.-C. Kuo, S.-S. Hsu, C.-C. Lin, C.-Y. Hsu, and H.-R. Chuang, “A 60-GHz Millimeter-Wave Triangular Monopole Antenna Fabricated Using 0.18 um CMOS Technology,” in *Innovative Computing Information and Control, 2008. ICICIC ’08. 3rd International Conference on*, 2008, p. 237.

[54] Y. P. Zhang, M. Sun, and L. H. Guo, “On-chip antennas for 60-GHz radios in silicon technology,” *Electron Devices, IEEE Transactions on*, vol. 52, no. 7, pp. 1664 – 1668, Jul. 2005.

[55] P. Park and C. P. Yue, “A feasibility study of on-wafer wireless testing,” in *VLSI Design, Automation and Test, 2008. VLSI-DAT 2008. IEEE International Symposium on*, 2008, pp. 299 –302.

[56] S. K. Padhi, N. C. Karmakar, and C. L. Law, “CPW fed MMIC slot dipole for MM-wave applications,” in *Antennas and Propagation Society International Symposium, 2002. IEEE*, 2002, vol. 1, pp. 414 – 417 vol.1.

[57] Y. Su, J. Jau Lin, and K. O. Kenneth, “A 20 GHz CMOS RF down-converter with an on-chip antenna,” in *Solid-State Circuits Conference, 2005. Digest of Technical Papers. ISSCC. 2005 IEEE International*, 2005, pp. 270 –597 Vol. 1.

[58] C. Cao, Y. Ding, X. Yang, J.-J. Lin, H.-T. Wu, A. K. Verma, J. Lin, F. Martin, and K. K. O, “A 24-GHz Transmitter With On-Chip Dipole Antenna in 0.13 um CMOS,” *Solid-State Circuits, IEEE Journal of*, vol. 43, no. 6, pp. 1394 –1402, Jun. 2008.

[59] P. M. Mendes, A. Polyakov, M. Bartek, J. N. Burghartz, and J. H. Correia, “An integrated folded-patch chip-size antenna using high-resistivity polycrystalline silicon substrate,” in *Advanced Semiconductor*

Devices and Microsystems, 2004. ASDAM 2004. The Fifth International Conference on, 2004, pp. 311 – 314.

[60] U. Johannsen, A. B. Smolders, R. Mahmoudi, and J. A. G. Akkermans, “Substrate loss reduction in antenna-on-chip design,” in *Antennas and Propagation Society International Symposium, 2009. APSURSI ’09. IEEE*, 2009, pp. 1 –4.

[61] F. Gutierrez, K. Parrish, and T. S. Rappaport, “On-Chip Integrated Antenna Structures in CMOS for 60 GHz WPAN Systems,” in *Global Telecommunications Conference, 2009. GLOBECOM 2009. IEEE*, 2009, pp. 1 –7.

[62] J.-J. Lin, L. Gao, A. Sugavanam, X. Guo, R. Li, J. E. Brewer, and K. K. O, “Integrated antennas on silicon substrates for communication over free space,” *Electron Device Letters, IEEE*, vol. 25, no. 4, pp. 196 – 198, Apr. 2004.

[63] M. Barakat, C. Delaveaud, and F. Ndagijimana, “Performance of a 0.13 um SOI integrated 60 GHz dipole antenna,” in *Antennas and Propagation Society International Symposium, 2007 IEEE*, 2007, pp. 2526 – 2529.

[64] N. Segura, S. Montusclat, C. Person, S. Tedjini, and D. Gloria, “On-wafer radiation pattern measurements of integrated antennas on standard BiCMOS and glass processes for 40-80GHz applications,” in *Microelectronic Test Structures, 2005. ICMTS 2005. Proceedings of the 2005 International Conference on*, 2005, pp. 107 – 111.

[65] S. Montusclat, F. Gianesello, and D. Gloria, “Silicon full integrated LNA, filter and antenna system beyond 40 GHz for MMW wireless communication links in advanced CMOS technologies,” in *Radio Frequency Integrated Circuits (RFIC) Symposium, 2006 IEEE*, 2006, p. 4 pp. –80.

[66] S. Montusclat, F. Gianesello, D. Gloria, and S. Tedjini, “Silicon integrated antenna developments up to 80 GHz for millimeter wave wireless links,” in *Microwave Conference, 2005 European*, 2005, vol. 3, p. 4 pp.

[67] C. D. Moussa Barakat, “Conception d’Antenne Spirale intégrée sur SOI à 60 GHz,” *Journées Nationales Microondes*, p. 3, Mai 2009.

[68] I.-S. Chen, H.-K. Chiou, and N.-W. Chen, “V-Band On-Chip Dipole-Based Antenna,” *Antennas and Propagation, IEEE Transactions on*, vol. 57, no. 10, pp. 2853 –2861, Oct. 2009.

[69] R. Pilard, S. Montusclat, A. Elwertowska, D. Gloria, F. Le Pennec, and C. Person, “Size reduction and input impedance increase in advanced MMW silicon integrated double-slotted antenna using fractal and director slot layout,” in *Antenna Technology: Small Antennas and Novel Metamaterials, 2008. iWAT 2008. International Workshop on*, 2008, pp. 294 –297.

[70] U. R. Pfeiffer, J. Grzyb, D. Liu, B. Gaucher, T. Beukema, B. A. Floyd, and S. K. Reynolds, “A chip-scale packaging technology for 60-GHz wireless chipsets,” *Microwave Theory and Techniques, IEEE Transactions on*, vol. 54, no. 8, pp. 3387 –3397, Aug. 2006.

[71] J. A. G. Akkermans, M. I. Kazim, Y. Yu, M. H. A. J. Herben, P. G. M. Baltus, and P. F. M. Smulders, “Flip-chip integration of differential CMOS power amplifier and antenna in PCB technology for the 60-GHz frequency band,” in *Antennas and Propagation, 2009. EuCAP 2009. 3rd European Conference on*, 2009, pp. 2818 –2822.

[72] Y. P. Zhang, M. Sun, K. M. Chua, L. L. Wai, D. Liu, and B. P. Gaucher, “Antenna-in-Package in LTCC for 60-GHz Radio,” in *Antenna Technology: Small and Smart Antennas Metamaterials and Applications, 2007. IWAT ’07. International Workshop on*, 2007, pp. 279 –282.

[73] R. Suga, H. Nakano, Y. Hirachi, J. Hirokawa, and M. Ando, “Cost-Effective 60-GHz Antenna Package With End-Fire Radiation for Wireless File-Transfer System,” *Microwave Theory and Techniques, IEEE Transactions on*, vol. 58, no. 12, pp. 3989 –3995, Dec. 2010.

[74] M. Al Henawy and M. Schneider, “Integrated antennas in eWLB packages for 77 GHz and 79 GHz automotive radar sensors,” in *Radar Conference (EuRAD), 2011 European*, 2011, pp. 424 –427.

[75] N. Hoivik, D. Liu, C. V. Jahnes, J. M. Cotte, C. Tsang, C. Patel, U. Pfeiffer, J. Grzyb, J. Knickerbocker, J. H. Magerlein, and B. Gaucher, “High-efficiency 60 GHz antenna fabricated using low-cost silicon micromachining techniques,” in *Antennas and Propagation Society International Symposium, 2007 IEEE*, 2007, pp. 5043 –5046.

[76] J. Laskar, S. Pinel, S. Sarkar, P. Sen, B. Perunama, M. Leung, D. Dawn, D. Yeh, F. Barale, K. Chuang, G. Iyer, J.-H. Lee, and P. Melet, “60GHz CMOS/PCB co-design and phased array technology,” in *Custom Integrated Circuits Conference, 2009. CICC ’09. IEEE*, 2009, pp. 453 –458.

[77] W. M. A. Wahab, D. Busuioc, and S. Safavi-Naeini, “Low Cost Planar Waveguide Technology-Based Dielectric Resonator Antenna (DRA) for Millimeter-Wave Applications: Analysis, Design, and Fabrication,” *Antennas and Propagation, IEEE Transactions on*, vol. 58, no. 8, pp. 2499 –2507, Aug. 2010.

[78] A. Babakhani, X. Guan, A. Komijani, A. Natarajan, and A. Hajimiri, “A 77GHz 4-Element Phased Array Receiver with On-Chip Dipole Antennas in Silicon,” in *Solid-State Circuits Conference, 2006. ISSCC 2006. Digest of Technical Papers. IEEE International*, 2006, pp. 629 –638.

[79] H.-C. Lien, H.-C. Tsai, Y.-C. Lee, W.-F. Lee, and W.-F. Lee, “A Circular Polarization Microstrip Stacked Structure Broadband Antenna,” *PIERS Online*, vol. 4, no. 2, pp. 259–262, 2008.

[80] H.-C. Lien and H.-C. Tsai, “A Wide-band Circular Polarization Stacked Patch Antenna for the Wireless Communication Applications,” *PIERS Online*, vol. 4, no. 2, pp. 255–258, 2008.

[81] A. Sharma, V. K. Dwivedi, and G. Singh, “THz Rectangular Patch Microstrip Antenna Design Using Photonic,” in *PIERS*, 2008.

[82] J.-G. Kim, H. S. Lee, H.-S. Lee, J.-B. Yoon, and S. Hong, “60-GHz CPW-fed post-supported patch antenna using micromachining technology,” *Microwave and Wireless Components Letters, IEEE*, vol. 15, no. 10, pp. 635 – 637, Oct. 2005.

[83] T. Zwick, D. Liu, and B. P. Gaucher, “Broadband Planar Superstrate Antenna for Integrated Millimeterwave Transceivers,” *Antennas and Propagation, IEEE Transactions on*, vol. 54, no. 10, pp. 2790 –2796, Oct. 2006.

[84] K. W. Leung, W. C. Wong, K. M. Luk, and E. K. N. Yung, “Annular slot-coupled dielectric resonator antenna,” *Electronics Letters*, vol. 34, no. 13, pp. 1275 –1277, juin 1998.

[85] B. Pan, Y. Li, G. E. Ponchak, J. Papapolymerou, and M. M. Tentzeris, “A 60-GHz CPW-Fed High-Gain and Broadband Integrated Horn Antenna,” *Antennas and Propagation, IEEE Transactions on*, vol. 57, no. 4, pp. 1050 –1056, Apr. 2009.

[86] A. Buerkle, K. Sarabandi, and H. Mosallaei, “Compact slot and dielectric resonator antenna with dual-resonance, broadband characteristics,” *Antennas and Propagation, IEEE Transactions on*, vol. 53, no. 3, pp. 1020 – 1027, Mar. 2005.

[87] G. Felic and S. Skafidas, “Flip-Chip Interconnection Effects on 60-GHz Microstrip Antenna Performance,” *Antennas and Wireless Propagation Letters, IEEE*, vol. 8, pp. 283 –286, 2009.

[88] A. Fischer, Z. Tong, A. Hamidipour, L. Maurer, and A. Stelzer, “A 77-GHz antenna in package,” in *Microwave Conference (EuMC), 2011 41st European*, 2011, pp. 1316 –1319.

[89] A. Parsa and B. Razavi, “A New Transceiver Architecture for the 60-GHz Band,” *Solid-State Circuits, IEEE Journal of*, vol. 44, no. 3, pp. 751 –762, Mar. 2009.

[90] J. Lee, Y. Huang, Y. Chen, H. Lu, and C. Chang, “A low-power fully integrated 60GHz transceiver system with OOK modulation and on-board antenna assembly,” in *Solid-State Circuits Conference - Digest of Technical Papers, 2009. ISSCC 2009. IEEE International*, 2009, pp. 316 –317,317a.

[91] A. Arbabian, B. Afshar, J.-C. Chien, S. Kang, S. Callender, E. Adabi, S. D. Toso, R. Pilard, D. Gloria, and A. Niknejad, “A 90GHz-carrier 30GHz-bandwidth hybrid switching transmitter with integrated antenna,” in *Solid-State Circuits Conference Digest of Technical Papers (ISSCC), 2010 IEEE International*, 2010, pp. 420 –421.

[92] M. Tanomura, Y. Hamada, S. Kishimoto, M. Ito, N. Orihashi, K. Maruhashi, and H. Shimawaki, “TX and RX Front-Ends for 60GHz Band in 90nm Standard Bulk CMOS,” in *Solid-State Circuits Conference, 2008. ISSCC 2008. Digest of Technical Papers. IEEE International*, 2008, pp. 558 –635.

[93] S. Pinel, S. Sarkar, P. Sen, B. Perumana, D. Yeh, D. Dawn, and J. Laskar, “A 90nm CMOS 60GHz Radio,” in *Solid-State Circuits Conference, 2008. ISSCC 2008. Digest of Technical Papers. IEEE International*, 2008, pp. 130 –601.

[94] A. Valdes-Garcia, S. Reynolds, and J.-O. Plouchart, “60 GHz transmitter circuits in 65nm CMOS,” in *Radio Frequency Integrated Circuits Symposium, 2008. RFIC 2008. IEEE*, 2008, pp. 641 –644.

[95] C. Marcu, D. Chowdhury, C. Thakkar, L.-K. Kong, M. Tabesh, J.-D. Park, Y. Wang, B. Afshar, A. Gupta, A. Arbabian, S. Gambini, R. Zamani, A. M. Niknejad, and E. Alon, “A 90nm CMOS low-power 60GHz transceiver with integrated baseband circuitry,” in *Solid-State Circuits Conference - Digest of Technical Papers, 2009. ISSCC 2009. IEEE International*, 2009, pp. 314 –315,315a.

[96] T. Lertwiriyaprapa, C. Phongcharoenpanich, and M. Krairiksh, “Investigations of a rectangular cavity backed slot antenna excited by a probe,” *Journal of King Mongkuts University of Technology*, p. 7, 2007.

[97] R. A. Kranenburg, S. A. Long, and J. T. Williams, “Coplanar waveguide excitation of dielectric resonator antennas,” *Antennas and Propagation, IEEE Transactions on*, vol. 39, no. 1, pp. 119 –122, Jan. 1991.

[98] Z. Peng, H. Wang, and X. Yao, “Dielectric resonator antennas using high permittivity ceramics,” *Ceramics International*, vol. 30, no. 7, pp. 1211–1214, 2004.

[99] A. Buerkle, K. Sarabandi, and H. Mosallaei, “Compact slot and dielectric resonator antenna with dual-resonance, broadband characteristics,” *Antennas and Propagation, IEEE Transactions on*, vol. 53, no. 3, pp. 1020 – 1027, Mar. 2005.

[100] Y. Coulibaly, M. Nedil, L. Talbi, and T. A. Denidni, “Design of a mm-wave broadband CPW-fed stacked dielectric resonator antenna for underground mining communication,” in *Antennas and Propagation Society International Symposium (APSURSI), 2010 IEEE*, 2010, pp. 1 –4.

[101] A. Perron, T. A. Denidni, and A.-R. Sebak, “High-Gain Hybrid Dielectric Resonator Antenna for Millimeter-Wave Applications: Design and Implementation,” *Antennas and Propagation, IEEE Transactions on*, vol. 57, no. 10, pp. 2882 –2892, Oct. 2009.

[102] W. M. A. Wahab, D. Busuioc, and S. Safavi-Naeini, “Low Cost Planar Waveguide Technology-Based Dielectric Resonator Antenna (DRA) for Millimeter-Wave Applications: Analysis, Design, and Fabrication,” *Antennas and Propagation, IEEE Transactions on*, vol. 58, no. 8, pp. 2499 –2507, Aug. 2010.

[103] P. V. Bijumon, A. P. Freundorfer, M. Sayer, and Y. M. M. Antar, “Ultralow Temperature Processing and Integration of Dielectric Resonators on Silicon Substrates for System-on-Chip Applications,” *Electron Devices, IEEE Transactions on*, vol. 55, no. 7, pp. 1727 –1732, Jul. 2008.

[104] A. Petosa and A. Ittipiboon, “Dielectric Resonator Antennas: A Historical Review and the Current State of the Art,” *Antennas and Propagation Magazine, IEEE*, vol. 52, no. 5, pp. 91 –116, Oct. 2010.

[105] D. K. and P. Guillon and Editors, *Dielectric Resonators*, Har/Dis. Noble Pub, 1998.

[106] S. Long, M. McAllister, and L. Shen, “The resonant cylindrical dielectric cavity antenna,” *IEEE Transactions on Antennas and Propagation*, vol. 31, no. 3, pp. 406 – 412, mai 1983.

[107] D. M. Pozar, “Microstrip antennas,” *Proceedings of the IEEE*, vol. 80, no. 1, pp. 79 –91, Jan. 1992.

[108] K. Mohammadpour-Aghdam, S. Brebels, A. Enayati, R. Faraji-Dana, G. A. E. Vandenbosch, and W. DeRaedt, “RF probe influence study in millimeter-wave antenna pattern measurements,” *International Journal of RF and Microwave Computer-Aided Engineering*, vol. 21, no. 4, pp. 413–420, 2011.

[109] S. L. Wright, R. Polastre, H. Gan, L. P. Buchwalter, R. Horton, P. S. Andry, E. Sprogis, C. Patel, C. Tsang, J. Knickerbocker, J. R. Lloyd, A. Sharma, and M. S. Sri-Jayantha, “Characterization of micro-bump C4 interconnects for Si-carrier SOP applications,” in *Electronic Components and Technology Conference, 2006. Proceedings. 56th*, 2006, p. 8 pp.

[110] A. Fischer, Z. Tong, A. Hamidipour, L. Maurer, and A. Stelzer, “A 77-GHz antenna in package,” in *Microwave Conference (EuMC), 2011 41st European*, 2011, pp. 1316 –1319.

[111] Asm, *Electronic Materials Handbook: Packaging*. ASM International, 1989.

[112] “Packages and Lids for Evaluation (Standard Product Lists) | Semiconductor Components | Products | KYOCERA,” 22-Jun-2012. [Online]. Available: http://global.kyocera.com/prdct/semicon/semi/std_pkg/index.html. [Accessed: 17-Aug-2012].

[113] G.-H. Lee, C.-S. Yoo, J.-G. Yook, and J.-C. Kim, “SIW (substrate integrated waveguide) quasi-elliptic filter based on LTCC for 60-GHz application,” in *Microwave Integrated Circuits Conference, 2009. EuMIC 2009. European*, 2009, pp. 204 –207.

[114] Y. C. Lee, W. Chang, and C. S. Park, “Monolithic LTCC SiP transmitter for 60GHz wireless communication terminals,” in *Microwave Symposium Digest, 2005 IEEE MTT-S International*, 2005, pp. 1015 –1018.

[115] S. B. Yeap, Z. N. Chen, A. C. W. Lu, V. Sunappan, and L. L. Wai, “60-GHz LTCC antenna array with microstrip to CPW transition,” in *Microwave Conference, 2009. APMC 2009. Asia Pacific*, 2009, pp. 1938 – 1941.

[116] J. Lanteri, L. Dussopt, R. Pilard, D. Gloria, S. D. Yamamoto, A. Cathelin, and H. Hezzeddine, “60 GHz antennas in HTCC and glass technology,” in *2010 Proceedings of the Fourth European Conference on Antennas and Propagation (EuCAP)*, 2010, pp. 1 –4.

[117] Y. J. Cheng, K. Wu, and W. Hong, “Power Handling Capability of Substrate Integrated Waveguide Interconnects and Related Transmission Line Systems,” *IEEE Transactions on Advanced Packaging*, vol. 31, no. 4, pp. 900 –909, Nov. 2008.

[118] H. Yousef, S. Cheng, and H. Kratz, “Substrate Integrated Waveguides (SIWs) in a Flexible Printed Circuit Board for Millimeter-Wave Applications,” *Journal of Microelectromechanical Systems*, vol. 18, no. 1, pp. 154 –162, Feb. 2009.

[119] J. C. Bohorquez, B. Potelon, C. Person, E. Rius, C. Quendo, G. Tanne, and E. Fourn, “Reconfigurable Planar SIW Cavity Resonator and Filter,” in *Microwave Symposium Digest, 2006. IEEE MTT-S International*, 2006, pp. 947 –950.

[120] P. Ferrand, M. Chatras, D. Baillargeat, P. Blondy, S. Verdeyme, J. Puech, L. Lapierre, J. Galiere, and E. Estebe, “Compact quasi planar silicon bandpass filters based on metallic periodic structure for Q and V band applications,” in *Microwave Symposium Digest, 2004 IEEE MTT-S International*, 2004, vol. 3, pp. 1459 – 1462 Vol.3.

Publications

International Conferences

[1] J. P. Guzman, C. Calvez, R. Pilard, F. Gianesello, M. Ney, D. Gloria, and C. Person, "Silicon integrated dielectric resonator antenna solution for 60GHz front-end modules," in *IEEE 12th Topical Meeting on Silicon Monolithic Integrated Circuits in RF Systems (SiRF)*, 2012, pp. 53 –56.

[2] J. P. Guzman, C. Calvez, M. Ney, C. Person, R. Pilard, and F. Gianesello, "Mono-block Dielectric Resonator antenna with incorporated excitation for 60 GHz integrated systems," in *6th European Conference on Antennas and Propagation (EUCAP)*, 2012, pp. 3260 –3263.

[3] J. P. Guzman, M. Ney, and C. Person, "Packaged antenna solution for the Radio front end @ 60 GHz based on a dielectric resonator," in *15th International Symposium on Antenna Technology and Applied Electromagnetics (ANTEM)*, 2012.

Awarded SEE Innovation Prize

[4] J. P. Guzman, S. A. Muhammad, M. Ney and C. Person. "Cylindrical Dielectric Resonator coupled to a nearby on-chip integrated slot for a completely packaged 60 GHz front-end," in *42nd European Microwave Week (EuMW)*, 2012.

Co-authored Papers

[1] S.A. Muhammad, J. P. Guzman, C. Person, M. Ney, R.Pilard. "Dielectric Resonator Antenna inside a Package for Millimeter Wave Transmitter System". *7th European Conference on Antennas and Propagation (EUCAP)*, 2013.

[2] S.A. Muhammad, J. P. Guzman, M. Ney, C. Person, R. Pilard, E. Kerhervé, N. Demirel "System in Package Solution with Dielectric Resonator Antenna and Power Amplifier for a 60 GHz High Data Rate Transmitter" *7th European Conference on Antennas and Propagation (EUCAP)*, 2013.

National Conferences

[3] J. P. Guzman, M. Ney, C. Person. "Antenne Basse Impédance de type Résonateur Diélectrique encapsulée pour une co-conception PA-Antenne à 60 GHz ». *17emes Journées Nationales Microondes (JNM)* 2011, pp. 1 -4.